SIMULATION AND DESIGN OF A HYDROGEN ARCJET THRUSTER SEEDED WITH CESIUM

by

Darrel Kim Robertson

B.Sc. Physics with Space Science and Technology, Leicester University, 1995
S.M. Aeronautics and Astronautics, Massachusetts Institute of Technology, 1998

Submitted to the Department of Aeronautics and Astronautics
in partial fulfillment of the requirements for the degree of

DOCTOR OF PHILOSOPHY IN AERONAUTICS AND ASTRONAUTICS

AT THE MASSACHUSETTS INSTITUTE OF TECHNOLOGY

June 2001

Signature of Author Darrel Robertson

Department of Aeronautics and Astronautics

May 25, 2001

Certified by M. Martinez-Sanchez

Professor Manuel Martinez-Sanchez, Thesis Supervisor

Department of Aeronautics and Astronautics

Certified by Chathan M Cooke

Lecturer, Dr. Chathan Cooke

Department of Electrical Engineering

Certified by Mark Drela

Professor Mark Drela

Department of Aeronautics and Astronautics

Certified by

Professor Jaime Peraire

Department of Aeronautics and Astronautics

Certified by Rudrapatna V. Ramnath

Professor Rudrapatna Ramnath

Department of Aeronautics and Astronautics

Accepted by Wallace E Vander Velde

Professor Wallace Vander Velde

Chairman, Department Graduate Committee

Simulation and Design of a Hydrogen Arcjet Thruster Seeded with Cesium

by

Darrel Kim Robertson

Submitted to the Department of Aeronautics and Astronautics

on May 25, 2001, in partial fulfillment of the requirements for the degree of

Doctor of Philosophy in Aeronautics and Astronautics

ABSTRACT

In conventional arcjets the largest loss in efficiency is the energy required to ionize the propellant. Adding a small amount of a readily ionizable material should provide adequate electrical conductivity, without the main propellant being ionized, thereby reducing this frozen loss.

To study the effects of seeding a hydrogen arcjet with cesium, a two-dimensional numerical model was developed. The ions and atoms are treated as one fluid and the electrons as a second. The flow was modelled by Navier-Stokes equations modified to account for thermal and chemical non-equilibrium. The equations were numerically integrated by MacCormacks predictor-corrector scheme and a TVD scheme. The electric potential was solved by successive over-relaxation.

Results show that the seeded arcjet can be run with the cesium fully ionized but the hydrogen having minimal dissociation or ionization. When the flow passes through the high current density region of the anode arc attachment, the hydrogen was found to not ionize as previously feared even when run at comparatively high currents. The cesium is fairly uniformly spread throughout the constrictor, as is the current density, so there is no formation of a narrow arc as in conventional thrusters. Consequently the constrictor must be an insulator or else the arc will not extend down the constrictor as desired. Modelling predicts that seeding can cut the frozen losses from fifty percent to less than one percent.

Following this an experiment to test a prototype was designed. Performance mapping was done using a lower order model which was shown to be consistent with the full two dimensional code. Varying the parameters mapped out the performance range and provided a design for a prototype. A thermal model led to a structural design including regenerative cooling. Supply and extraction of the cesium was examined and the pumping requirements determined. Finally a mission analysis showed that a seeded arcjet is the best choice for LEO-GEO orbit raising with transfer times between 30 and 160 days.

Author: Darrel Kim Robertson
E-mail: dkr@alum.mit.edu

Thesis Supervisor: Manuel Martinez-Sanchez
Professor of Aeronautical and Astronautical Engineering

Acknowledgements

I would first like to thank my thesis supervisor Professor Manuel Martinez-Sanchez for the opportunity to work on such an interesting and exciting project. I would especially like to thank him for his help in understanding the physics involved in arcjet operation, particularly as to which phenomena were important and which could be neglected. When I occasionally got stuck, he proved to be a great source of new ideas on how to tackle problems with the modelling of the physics.

Secondly I would like to thank Guy Benson for his explanations of how the numerical model of conventional arcjets that I inherited worked, and of why things were done in the code the way that they were. I would also like to especially thank Folusho Oyerokun for his insights into how the addition of cesium changed the behaviour of an arcjet, and together with Prof. Manuel Martinez-Sanchez, as to what were the important questions to be answered in the research. Even though I never spoke to him in person I'd also like to thank Scott Miller, whose code I inherited and whose thesis was an invaluable resource.

I also owe a debt of gratitude to all the professors who served on my thesis committee, Chathan Cooke, Mark Drela, Jaime Peraire, and Rudrapatna Ramnath. I am very grateful to the Engineering and Physical Sciences Research Council (EPSRC) for providing me with the studentship that enabled me to come and study at MIT.

Next I would like to thank everyone in the Space Systems Lab, especially Peggy Edwards and SharonLeah Brown for all their administrative help, and my colleagues in the propulsion group, James Szabo, Tatsuo Onishi, Paulo Lozano, Nuria Margarit, Stephanie Thomas, Luis Fernando Velasquez Garcia, Anne Pacros, and Shannon Cheng.

I don't think I can get away without thanking all my friends here especially Rebecca Rogers and her family, April Smith and Eric Knopp, Kerstein Audette, Amy Gresser and everyone at New England Canoe Polo, and Tech Squares.

Lastly and perhaps most importantly I'd like to thank my Mum and Dad (Valerie and Peter) and my brother Ian for their endless support and encouragement.

"Wark."

– Yakky.

"Maauuuu."

– Mau.

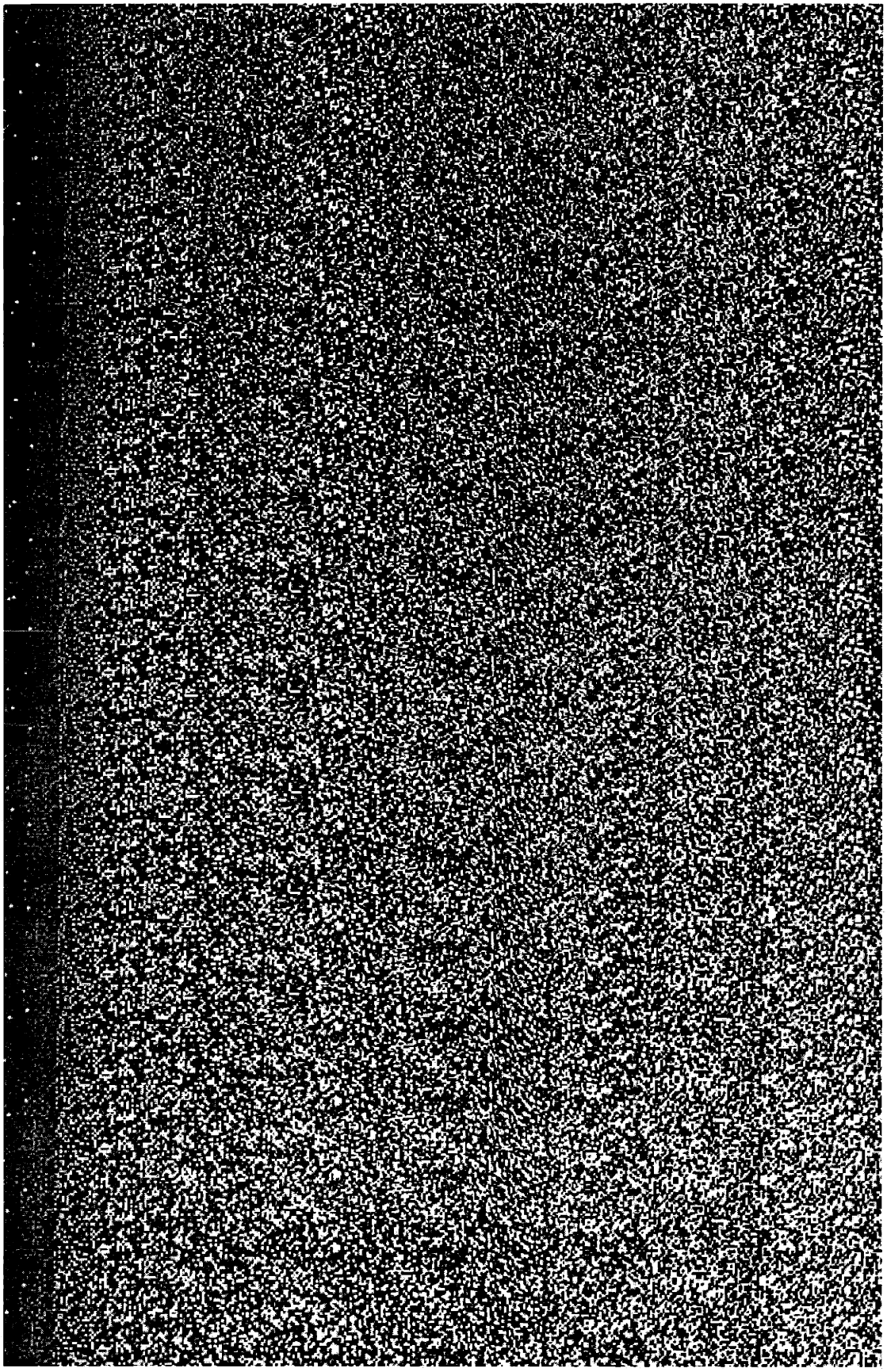

Contents

List of Figures

List of Tables

List of Symbols

c	Sound speed $[\mathrm{m\,s^{-1}}]$
$\hat{c}_{v,s}$	Constant volume specific heat of species s $[\mathrm{J\,mol^{-1}\,K^{-1}}]$
e	Electron charge [C]
e_d	Characteristic dissociation energy [J]
e_i	Characteristic ionization energy [J]
e_v	Characteristic vibrational energy [J]
$e_{s,int}$	Species internal energy per unit mass $[\mathrm{J\,kg^{-1}}]$
f_s	Distribution function of species s
g_e	Gravitional acceleration at earth's surface $[\mathrm{m\,s^{-1}}]$
g_l	Degeneracy of energy level l
h	Planck's constant [J s]
h_s	Enthalpy of particle of species s [J]
$\vec{j}$	Current Density $[\mathrm{A\,m^{-2}}]$
$\vec{j}_s$	Species current density $[\mathrm{A\,m^{-2}}]$
k	Boltzmann's constant $[\mathrm{J\,K^{-1}}]$
$\dot{m}$	Mass flow rate $[\mathrm{kg\,s^{-1}s}]$
m_s	Mass of particle of species s [kg]
m_{sr}	Reduced mass of species s and r
n_s	Species number density $[\mathrm{m^{-3}}]$
$\hat{n}_s$	Molar concentration $[\mathrm{mol\,m^{-3}}]$
p	Total scalar pressure [Pa]
p_s	Species scalar pressure [Pa]
$\overline{\overline{p}}$	Pressure tensor
q_a	Partition function of species a per unit volume

q_s	Charge of species s [C]
$\vec{q}_s$	Heat flux of species s $[\mathrm{J\,m^{-2}\,s^{-1}}]$
$\vec{u}$	Mass-averaged flow velocity $[\mathrm{m\,s^{-1}}]$
$\vec{u}_s$	Species velocity $[\mathrm{m\,s^{-1}}]$
$\vec{v}$	particle velocity $[\mathrm{m\,s^{-1}}]$
v_B	Bohm velocity $[\mathrm{m\,s^{-1}}]$
x_s	Species mole fraction
$\vec{B}$	Magnetic field [T]
D_a	Ambipolar diffusion coefficient $[\mathrm{m^2\,s^{-1}}]$
D_i	Effective diffusion coefficient $[\mathrm{m^2\,s^{-1}}]$
D_{ij}	Binary diffusion coefficient $[\mathrm{m^2\,s^{-1}}]$
$\overline{D}_{ij}$	Multicomponent diffusion coefficient $[\mathrm{m^2\,s^{-1}}]$
$\vec{E}$	Electric field $[\mathrm{V\,m^{-1}}]$
E_l	Elastic collisional energy transfer $[\mathrm{J\,s^{-1}\,m^{-3}}]$
E_s	Total species energy per unit mass $[\mathrm{J\,kg^{-1}}]$
$\mathbf{F}$	Flux vector in z direction
$\vec{F}_s$	External force [N]
$F^{(l,s)}$	Non-dimensional Coulomb collision integral
$\mathbf{G}$	Flux vector in r direction
H_s	Total species enthalpy per unit mass $[\mathrm{J\,kg^{-1}}]$
I	Current [A]
I_{sp}	Specific Impulse [s]
J	Jacobian of coordinate transformation
$\vec{J}$	Flux of a quantity
K_p, K_n, K_c	Equilibrium constants
N_A	Avogadro's number $[\mathrm{mol^{-1}}]$
Q_a	Partition function of species a
Q_{ij}	Collision cross section $\left[\mathrm{\AA^2}\right]$
$\hat{R}$	Universal gas constant $[\mathrm{kJ\,kmol^{-1}\,K^{-1}}]$
$\dot{R}$	Radiative energy transfer per unit volume $[\mathrm{J\,s^{-1}\,m^{-3}}]$
R_s	Species ordinary gas constant $[\mathrm{J\,kg^{-1}\,K^{-1}}]$

$\mathbf{S}$	Source vector
T	Thrust [N]
T_s	Species temperature [K]
$\mathbf{U}$	State vector
V	Volume $[\mathrm{m}^3]$
$\vec{V}_s$	Species diffusion velocity $[\mathrm{m\,s}^{-1}]$
Z_s	Charge magnitude of particles of species s
β	Hall parameter
β_0	Ratio of fluid pressure to magnetic pressure
δ_s	Inelastic correction factor of species s
ϵ_0	Permittivity of vacuum $[\mathrm{F\,m}^{-1}]$
κ_s	Species thermal conductivity $[\mathrm{J\,s}^{-1}\,\mathrm{m}^{-1}\,\mathrm{K}^{-1}]$
μ_a	Chemical potential of species a $[\mathrm{J\,mol}^{-1}]$
μ_0	Permeability of vacuum $[\mathrm{H\,m}^{-1}]$
μ_s	Species viscosity $[\mathrm{kg\,m}^{-1}\,\mathrm{s}^{-1}]$
ν_{ij}, ν'_{ij}	Stoichiometric coefficients
$\overline{\nu}_{sr}$	Average collision frequency between species s and r $[\mathrm{s}^{-1}]$
φ	Arbitrary quantity
ϕ	Electrical potential [V]
ρ	Total mass density $[\mathrm{kg\,m}^{-3}]$
ρ_c	Charge density $[\mathrm{C\,m}^{-3}]$
ρ_s	Species mass density $[\mathrm{kg\,m}^{-3}]$
ψ	Electron mobility $[\mathrm{m}^2\,\mathrm{ohm}^{-1}\,\mathrm{C}^{-1}]$
ψ_{ij}	Non-Dimensional parameter used in Coulomb collision integrals
σ	Electrical conductivity $[\mathrm{mho\,m}^{-1}]$, collision parameter $\left[\mathrm{\AA}^2\right]$
σ_{ij}	Effective hard sphere collision radius $\left[\mathrm{\AA}^2\right]$
$\overline{\overline{\tau}}$	Viscous stress tensor
θ_d	Characteristic dissociation temperature [K]
θ_r	Characteristic rotational temperature [K]
θ_v	Characteristic vibrational temperature [K]

χ	Collision deflection angle
ω_s	Species mass fraction
Φ	Viscous dissipation function $[\mathrm{J\,s^{-1}\,m^{-3}}]$
$\Omega_{ij}^{(l,s)}$	Collision integral $\left[\mathrm{\AA}^2\right]$
$\langle\Omega_{ij}^{(l,s)}\rangle$	Average effective collision integral $\left[\mathrm{\AA}^2\right]$
Δv	Change in velocity $[\mathrm{m\,s^{-1}}]$
∇	Gradient operator in coordinate space $[\mathrm{m^{-1}}]$
∇_v	Gradient operator in velocity space $[\mathrm{s\,m^{-1}}]$
$<>$	Average value of a quantity
$\ln\Lambda$	Spitzer logarithm

Chapter 1

Introduction

1.1 Why Electric Propulsion?

At present most propulsion needs in space are fulfilled by chemical thrusters such as hydrazine monopropellant for stationkeeping, MMH and nitrogen tetroxide for attitude control, liquid oxygen and hydrogen for launchers like the space shuttles main engine, and powdered aluminium and ammonium perchlorate for solid propellant boosters.

The thrust of a rocket is given by the mass flow rate times the effective exhaust velocity.

$$F = \dot{m} u_{eq} \tag{1.1}$$

where

$$u_{eq} = u_e + \left(\frac{p_e - p_a}{\dot{m}} \right) A_e \tag{1.2}$$

p_a being the ambient pressure, p_e the pressure of the flow at the nozzle exit, $\dot{m}$ the mass flow rate, u_e the nozzle exit velocity, and A_e the area of the nozzle exit.

The exhaust velocity of a chemical thruster is limited by the energy stored within the chemical bonds of the propellants. Reacting hydrogen with oxygen gives an exhaust velocity of about 4500 ms^{-1}. To achieve a higher exhaust velocity more energy could be supplied by using nuclear reactions or by adding energy from an external source such as electrical power.

Electric propulsion systems utilize a power source unrelated to the propellant such as solar panels or radioisotope thermal generators, and then use power conditioning equipment

to regulate the current or the voltage supplied to the thruster. Unfortunately current power generation and conditioning equipment tends to be heavy resulting in a low thrust to weight ratio for the system compared to chemical thrusters as can be seen in figure 1-1. This means electric propulsion would be unsuitable for launch craft, but in a microgravity environment the higher I_{sp} would make electric thrusters the optimal choice for missions such as stationkeeping, orbital manoeuvreing, and interplanetary travel.

$$I_{sp} = \frac{u_{eq}}{g}, \tag{1.3}$$

where g is the acceleration due to gravity at sea level.

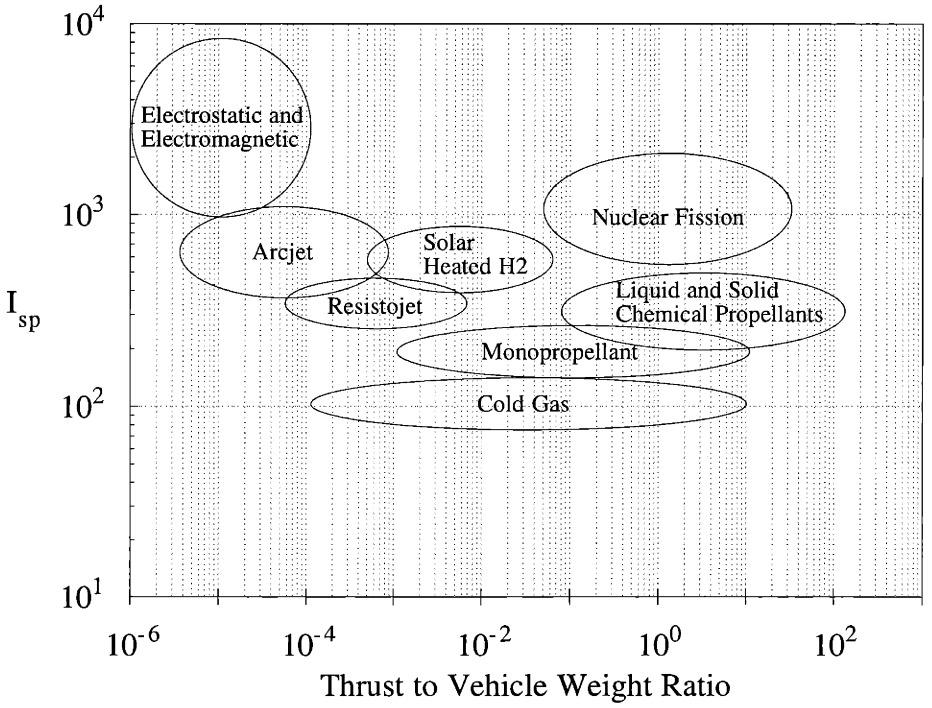

Figure 1-1: *Specific Impulse versus Thrust-to-Weight Ratio of Various Propulsion Systems*

1.2 Why Arcjets?

Most electric thrusters use one of three general principles: electrothermal, electromagnetic, or electrostatic. Electrothermal thrusters such as resistojets and arcjets use electricity simply to heat up the propellant. The thermal energy is then converted to kinetic energy by expanding the gas in a nozzle. Resistojets pass electric current through a wire in the

flow, and the heat created by resistive work is transfered to the propellant. Arcjets heat the propellant by passing an electric arc through the working fluid itself. Other concepts include heating by microwaves, radio waves, or laser. The thrust attainable by electrothermal thrusters is limited by the melting point of the thruster walls, which limits the temperature of the propellant and hence the thrust. Typical specific impulses for electrothermal thrusters are in the range 300 to 1600 seconds.

Resistojets are also electrothermal, and can be highly efficient, so the question arises as to why one would use a seeded arcjet over a resistojet. The simple answer is that arcjets have a higher specific impulse for a given power supplied. Another point is that resistojets since they only supply energy by heating from the walls, which therefore have to be hotter than the flow, require a very long constrictor with a length to diameter ratio of order of a thousand. Arcjets however, heat the gas internally so the fluid is hotter than the walls, and the energy is deposited in a much shorter span, so the constrictor need only have a length to diameter ratio of order ten. This results in much lower viscous losses, since the boundary layer doesn't have as much distance in which to grow. Wall temperature is a limiting factor in thruster design due to the limitations of materials. This leads to the important point that for a given wall temperature, since the arcjet can have a hotter internal flow, whereas the resistojet must have a cooler internal flow, that the arcjet will have a higher specific impulse. The long length of resistojets also means that a high pressure difference is required to drive the gas through the thruster, whereas in arcjets a much smaller pressure drop is required.

Electromagnetic thrusters overcome the limitations of electrothermal thrusters by accelerating ions with magnetic fields. An example of such a thruster is a Magnetoplasmadynamic (MPD) thruster which works in a similar manner to arcjets, but at much higher power and lower pressure, so that the radial current between the anode and cathode induces a magnetic field in the azimuthal direction. The Lorentz force $\vec{E} \times \vec{B}$ accelerates ions in the axial direction, and collisions between ions and neutrals create a bulk axial motion of the propellant which can provide specific impulses up to 5000 seconds.

An example of an electrostatic thruster is the ion engine which operates by ionizing the propellant and then accelerating the ions through a large potential difference between perforated grids. The ion beam created is then neutralised by some device that emits electrons. Ion engines can provide specific impulses of 2000 to 10000 seconds, but tend to

have very low mass flow rates due to space charge limitations between the grids.

Different missions will have different optimum specific impulses. Figure 1-2 from Sutton [124] shows the typical missions where different electric thrusters provide the optimum specific impulse.

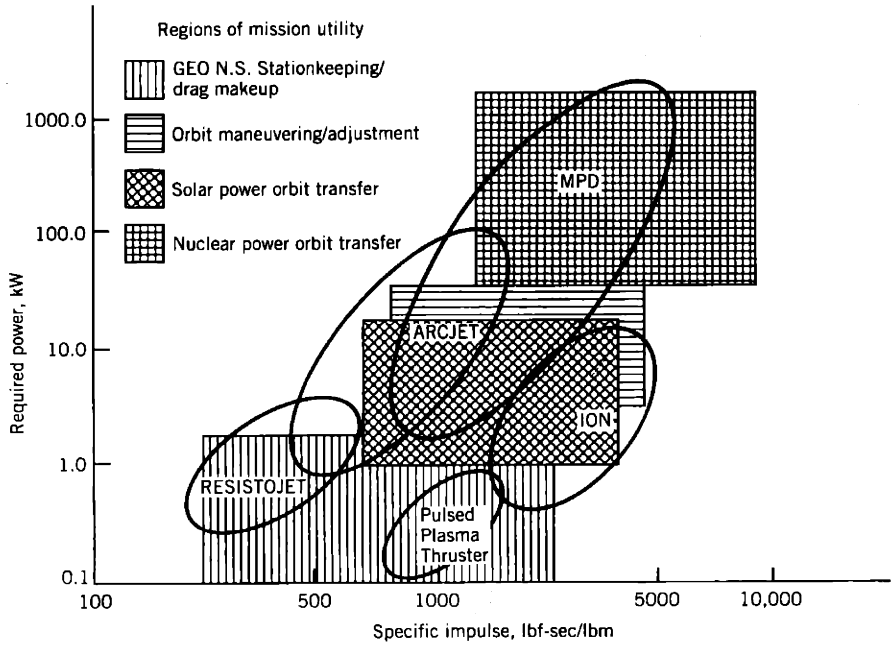

Figure 1-2: *Approximate Regimes of Application of Various Electric Propulsion Systems (from Sutton)*

1.3 Conventional Arcjets

1.3.1 Arcjet Physics

Figure 1-3 shows the entire assembly of the Olin Aerospace MR-508 1.8 kW hydrazine thruster including the propellant feed. The full system also requires a power conditioning unit. The nozzle section is only a small part of the whole assembly.

Figure 1-4 shows a simplified diagram of an arcjet. The basic principle is to heat the gas by passing an electric current between the anode and the central cathode. The arc is created by a high voltage spike which breaks down the propellant creating ions and electrons which can carry the current. The power conditioning unit then adjusts the current or voltage to its desired level. The potential difference strongly accelerates the electrons which transfer their energy to the ions and neutral species through collisions, heating the gas to temperatures

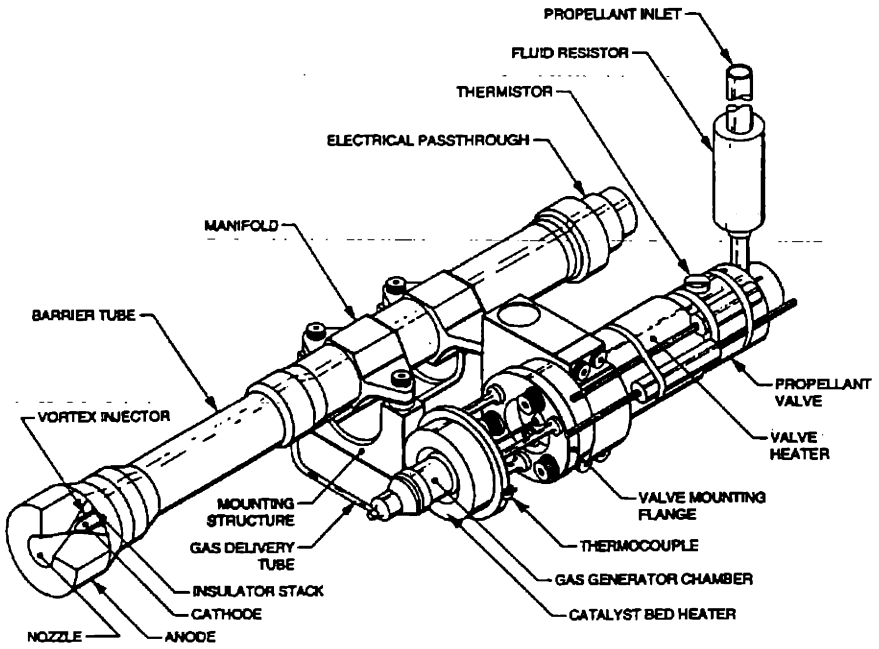

Figure 1-3: *Olin Aerospace MR-508 1.8kW Hydrazine Thruster*

of up to 30000 Kelvin in the core of the constrictor. Expanding the plasma through the nozzle converts the thermal energy to kinetic energy i.e. thrust.

The anode is contoured to create a narrow passage called the constrictor, through which the arc passes, and the nozzle for accelerating the gas. The cathode is a cylindrical rod with a conical tip. The constrictor stabilizes the arc in a central position, and injecting the propellant with azimuthal swirl is also thought to stabilize the arc. The electrodes are typically made of tungsten due to its high melting point of 3680 K. The cathode is often impregnated with two percent thorium to decrease the work function, and the conical tip focuses the current attachment to a small region enhancing the thermionic emission of electrons.

In a conventional arcjet the electric arc passes along the core of the constrictor creating high current density, electrical conductivity, and temperature. In the outer flow near the walls the temperature will be much lower at about 1000 K. Within the core the gas is highly dissociated and ionized, whereas it will be nearly all molecular in the outer region. Steep gradients in the properties occur in a transition region between the core and outer flow. Most of the propellant flows through the outer region, whereas most of the energy is deposited in the core. Figure 1-5 shows the gas temperature profile in the constrictor as modelled by Scott Miller [85], and figure 1-6 shows the density profile.

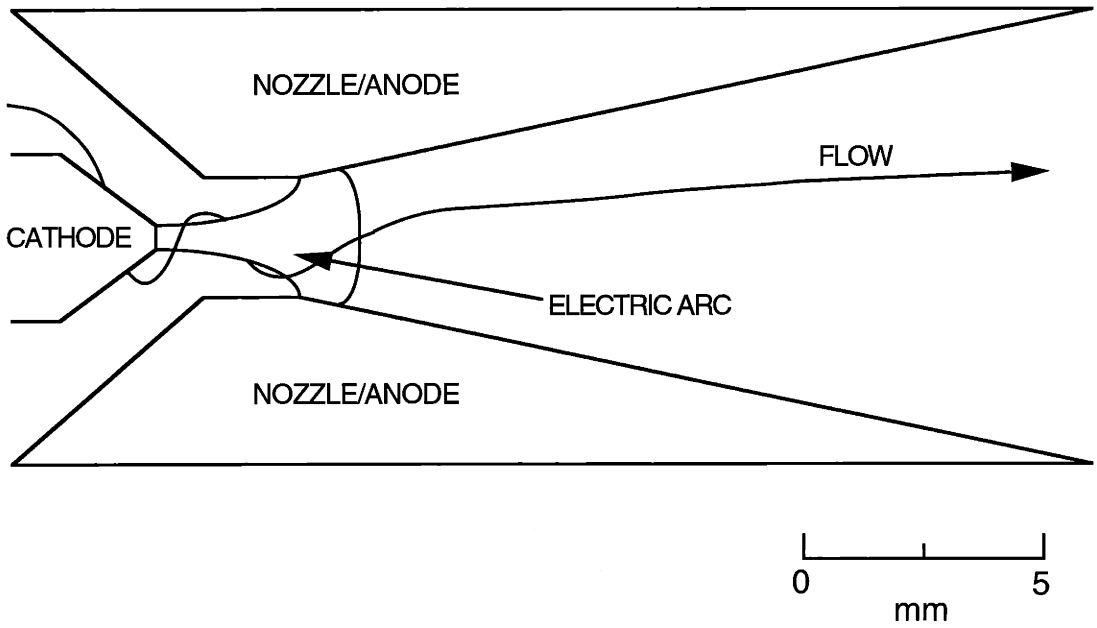

Figure 1-4: *Basic Arcjet Thruster Diagram*

Since the fluid inside the constrictor is partially ionized, plasma sheaths will be present at the walls. Large potential drops can exist across the plasma sheaths as in figure 1-7. The near-electrode regions I and V are the potential drops across the sheaths, and are on the order of a debye length in width. Inside the sheaths quasineutrality does not hold and the net space charge can create an electric field orders of magnitude greater than in the arc column *III*. Regions *II* and *IV* are transition regions between the sheaths and the arc column, where quasineutrality holds but comparatively large potential gradients still exist. In region *III* (the arc column), gradients in plasma properties are much lower [95].

In a conventional arcjet, where the arc is localised in the core, gradients in properties of the plasma between the core and outer region cause outward diffusion of ions and electrons and heat conduction. In steady state to maintain the density, neutrals diffuse inwards and a balance is set up between the ionization rate in the core and the loss of charged particles by outward diffusion and subsequent recombination.

An electric arc can attach itself to an electrode in either a diffuse attachment or a spot attachment. With diffuse attachment the electric arc is spread over a relatively wide area, so the current density is moderate, whereas spot attachments are characterized by high ($10^9 - 10^{12}\,\mathrm{Am}^{-2}$) current densities at a very localized attachment region, sometimes with rapid motion of the arc foot. Arc attachment on arcjet cathodes is usually spot

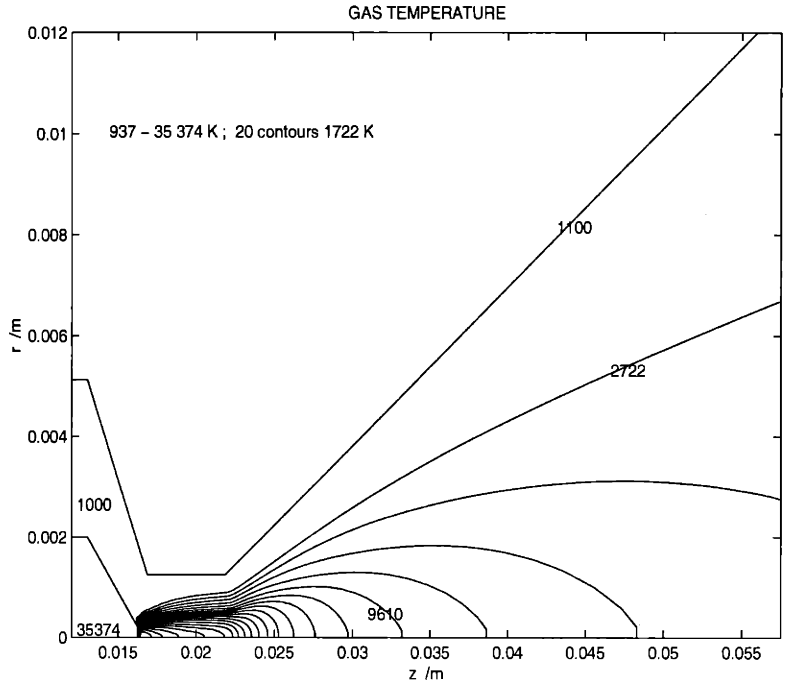

Figure 1-5: *Temperature Profile in an Arcjet Constrictor.*

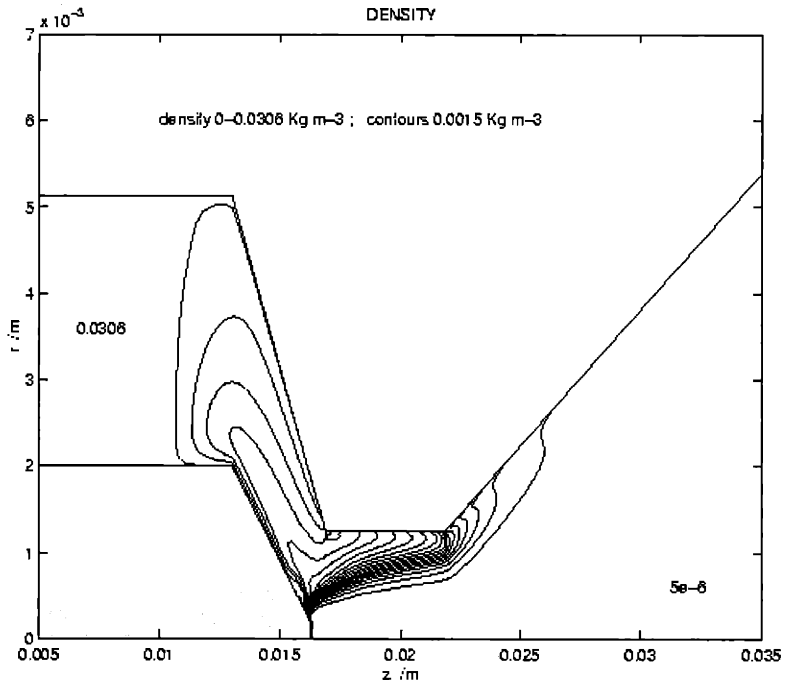

Figure 1-6: *Density Profile in an Arcjet Constrictor.*

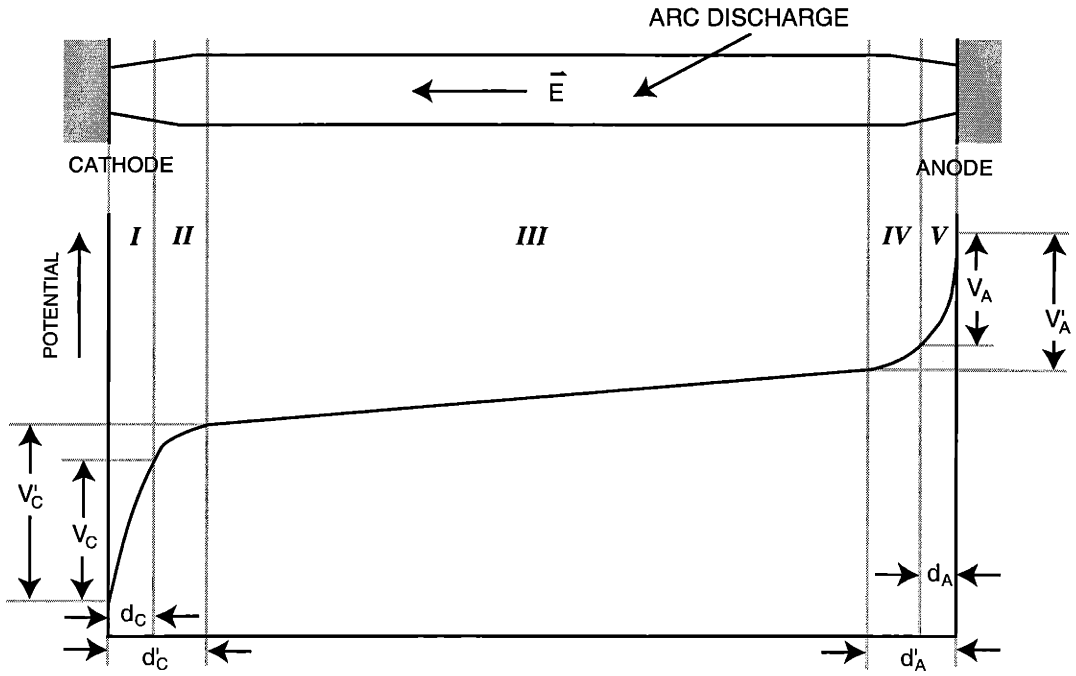

Figure 1-7: *Potential Drops within an Arc Discharge*

attachment, and the conical tip intensifies the local electric field since the field lines must remain perpendicular to the cathodes equipotential surface. The main intensification of the electric field however occurs at the foot of tiny mini-arcs at the foot of the main arc. This enhanced electric field increases the thermionic emission of electrons from the cathode tip, and accelerates the electrons away from the tip which constricts the current flow. The very intense currents experienced during startup heat the cathode tip, boiling some of it away and reducing the electric field intensity and creating a stable arc attachment condition.

In addition to the thermionic and field emission of electrons at the cathode tip ions contribute to the current as well, providing about 15-20% of the total current. Tungsten is a good thermionic emitter, due to its relatively low surface work function of 4.5 volts, and alloying with thorium which has a work function of 3.35V reduces the work function further. The enhanced field thermionic emission is given by the Richardson-Dushman equation as modified by Schottky [95],

$$j_S = 6 \times 10^5 \, T_c^2 \exp\left[-\frac{1}{kT_c}\left(e\phi_c - \sqrt{\frac{e^3 E}{4\pi\epsilon_0}}\right)\right], \quad \left[\mathrm{A/m^2}\right] \tag{1.4}$$

where E is the electric field strength in Vm^{-1}, T_c is the temperature of the cathode in K, and ϕ_c is the work function of the cathode material, in volts. The magnitude of the current

due to pure field emission is given by the Fowler-Nordheim equation [95]

$$j_{FN} = 1.54 \times 10^{-6} \frac{E^2}{e\phi_c} \exp\left[-\frac{6.83 \times 10^9 \left(e\phi_c\right)^{\frac{3}{2}}}{E} f\left(\frac{3.79\sqrt{E}}{e\phi_c} \times 10^{-5} \right) \right], \quad \left[\mathrm{A/m^2}\right] \quad (1.5)$$

where E is in units of V/m, $e\phi_c$ is in eV, and f is a function which decreases from $f(0) = 1$ to $f(1) = 0$.

The anode within an arcjet is a passive collector of current, and the current attachment at the anode can be of either the spot or the diffuse kind. Diffuse attachment can be the result of a constant low current density discharge, while the spot kind of attachment can come in the form of a sporadic high current density discharge. It has been postulated that the current attachment at the anode may be a 3-dimensional effect, as current "spokes" may appear, with rotation of the spokes occurring due to the applied swirl velocity and due to motion of the high temperature area of the arc discharge with respect to the gas [78, 81]. This phenomenon has some theoretical basis, but, at this time, it is difficult to prove this phenomenon experimentally, although there is some data from segmented anodes. The anode sheath region is very similar to the cathode sheath region, with the notable exception that the current is carried almost exclusively by the electrons, resulting in a net negative space charge. The voltage drop in the anode sheath, V_C, can be positive or negative, depending on the magnitude of the collected current.

The performance is strongly dependent upon the propellant used. Firstly, for a given amount of energy deposited the thrust will be higher for propellants of low mass, and secondly, less energy is required to ionize the propellant if it has low dissociation and ionization energies.

$$E = \frac{1}{2} m v^2 \quad (1.6)$$

$$F = \dot{m} v = \dot{m} \sqrt{\frac{2E}{m}} \quad (1.7)$$

Hydrogen gives the highest specific impulse due to its low weight, but carries with it the problem that as a cryogenic fuel it requires heavy and costly storage and refrigeration equipment. Hydrazine (N_2H_4) has no storage problems since it is a liquid at room temperature, and is also highly volatile. Therefore it is currently the most commonly used propellant for arcjets.

1.3.2 Sources of Loss in Efficiency

Potential Drops at Electrodes

There are two main sources of loss in efficiency in arcjets. The first is the voltage drops at the electrodes, which can be comparable to that across the main arc column. The drop at the cathode (ΔV_C) is mostly due to the drop in the ionization layer in front of it, and at the anode (ΔV_A) due to a resistive drop in the gas in front of it. In the numerical model by Miller [85] of a radiation cooled arcjet running on hydrogen at a flow rate of $0.1gs^{-1}$ with an applied current of $100A$ generating a voltage of $115V$ hence a power input of $11.50KW$, the potential drop was calculated as $14.6V$ causing a power loss to the anode of $1.46KW$. This is nearly 13% of the total potential drop and power input.

Frozen Losses

The largest source of loss in efficiency is frozen losses. To be able to pass a current through the working fluid, it first needs to be dissociated into its component atoms, which in turn need to be ionized to create electrons and ions which can conduct the current. The ions and dissociated atoms are blown out the back of the thruster before they have time to recombine, so the energy required to dissociate and ionize the propellant is lost, and cannot be converted into thrust. More specifically, as the gas is expanded and accelerated in the nozzle it cools, but the residence time in the nozzle is significantly shorter than the recombination timescale, so the atomic and charged species in the plasma do not have time to relax to their equilibrium values and the gas is said to be in frozen flow. In Miller's baseline simulation [85] he calculated that 30.0% of the exit plane energy flux was in the form of dissociation energy, and 17.5% in the form of ionization energy. Thus fully 47.5% of the energy was lost in frozen losses. With thermal energy at 12.7%, only 39.2% of the exit plane energy flux was in the form of axial kinetic energy.

One strategy that has been employed to reduce frozen losses is to run the arcjet at high pressure, which lowers the chamber dissociation level and increases the recombination rate in the nozzle [56]. Figure 1-8 shows the effect of pressure on frozen flow efficiency calculated using a simplified one dimensional model [55], where the frozen flow efficiency has been defined as the ratio of enthalpy converted to jet kinetic energy to that imparted

in the chamber assuming no recombination in the nozzle.

$$\eta_{frozen} = \frac{h_c - h_e}{h_c} \tag{1.8}$$

where h_c is enthalpy in the chamber and h_e is the enthalpy at the exit.

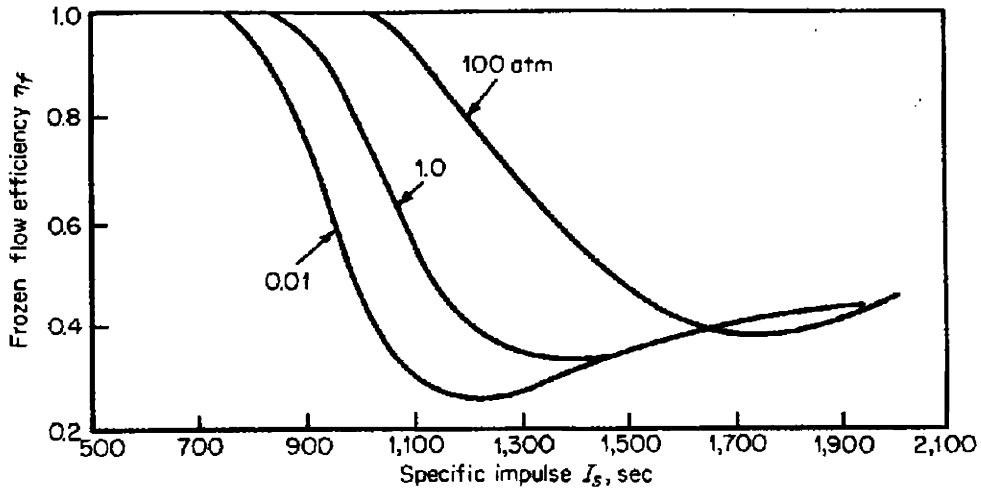

Figure 1-8: *Theoretical Variation of Frozen Flow Efficiency with Specific Impulse for Hydrogen at Various Pressures.*

However this model is not directly applicable to conventional arcjets since it assumes all the flow experiences the same conditions whereas in an arcjet most of the mass slips by in the cool outer layers while only a small proportion is heated in the central arc. There are also disadvantages of operating at high pressure such as increased stress on the hot chamber walls and erosion of the nozzle throat. Smaller orifices are also required which leads to higher arc temperatures and thus increased radiation losses.

1.4 Seeding Arcjets with an Alkali Metal

The frozen losses in an arcjet create the largest loss of efficiency in the system. The idea of seeding is to add a small amount of an easily ionizable material to the flow which produces the electrons required to pass the electric current. This concept is commonly used in magnetohydrodynamic power conversion to obtain good electrical conductivity without ionizing the working gas [112]. Figure 1-9 shows the variation of the conductivity of hydrogen seeded with a 0.1% cesium mole fraction as a function of temperature at various pressures.

Using cesium as an example of an alkali metal, in the gas phase it is atomic so has no

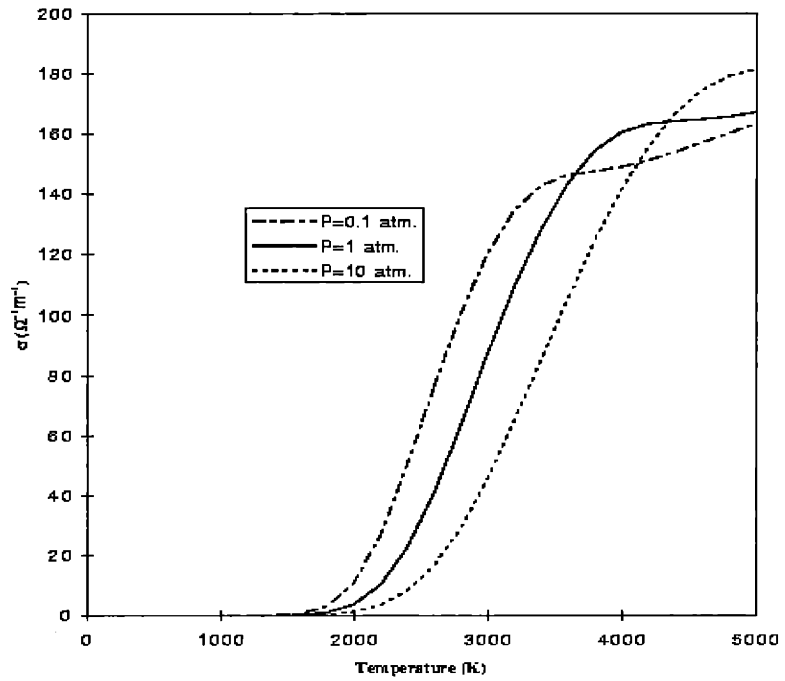

Figure 1-9: *Conductivity of Hydrogen Seeded with 0.1 percent Cesium per Mole*

dissociation energy and is readily ionizable with an ionization energy of $3.89eV$ compared to hydrogen with a dissociation energy of $4.5eV$ per hydrogen molecule and an ionization energy of $13.6eV$ per hydrogen atom. The difference in ionization energies means that cesium will effectively be fully ionized at temperatures above $4000K$ whilst hydrogen will not start to ionize until the temperature reaches $7000K$. If the arcjet can be run at electron temperatures between these limits then the buffer hydrogen should remain at least atomic whilst the cesium seed is fully ionized. In arcjets the electrons and heavy species are typically not in thermal equilibrium with the heavy species such as ions, atoms, and molecules possessing a lower temperature. This means that if the temperature of the heavy species can be kept lower than that of the electrons then it should be possible to keep the hydrogen molecular with no significant dissociation. Since the alkali metal is much more easily ionized and only a very small amount of it would be used, the amount of energy put into dissociating and ionizing the gas is greatly reduced. Quasi one-dimensional simulations of cesium seeded hydrogen arcjet thrusters by Oyerokun [93] in some cases predict frozen losses of less than one percent compared to the near fifty percent frozen losses in a conventional arcjet. Although the specific impulse is slightly reduced due to the presence of the heavy alkali metal in the flow, Oyerokun predicted a specific impulse of about $850s$ with negligible frozen losses using

a two percent cesium mass fraction.

1.5 Research Objectives

The quasi one-dimensional numerical model of Oyerokun [93] predicted the effective eradication of frozen losses, making alkali seeding a very promising concept, but left a number of questions unanswered. To address these questions a stability analysis of the governing equations was done by Oyerokun and for this research a fully two dimensional numerical model was developed.

One drawback of operating the arcjet at a lower temperature was a reduced specific impulse. It was felt that raising the temperature and allowing some hydrogen to dissociate would improve the specific impulse, but might lead to ionization instabilities which would cause the arcjet to undergo a transition back to conventional operation. Oyerokun's stability analysis of the system predicted the ceiling on electron temperature of approximately $7000K$, and that when operating the seeded arcjet at higher gas temperatures, whilst raising the specific impulse it reduced the electron temperature at which hydrogen ionization instability occurred,making ionization more likely.

With the level of approximation used in Oyerokun's models the physics modelled did not address several issues one of which was in the physics near the electrodes, in particular the possibility of a buffer ionization instability when passing though the electric arc attachment region. The electric arc has to attach to the anode at some point downstream of the constrictor, where there will be a region of high current density and therefore of strong heating as can be seen in figure 1-10 showing the electron temperature of a conventional arcjet as modelled by Miller. [85]

There was an important question as to whether the buffer hydrogen would ignite (i.e. dissociate and ionize) when it passed through the arc attachment region. If the hydrogen did ignite then the thruster might convert back to conventional operation and all the frozen losses would be back again.

Another important concern is the effect of viscosity which was left out of the quasi 1-D model in favour of a restriction on the channel length. Since seeded arcjets are designed to be run at much lower temperatures, and thus lower electrical conductivity, the ohmic power deposited per unit volume is lower. Consequently, to deposit a comparable amount

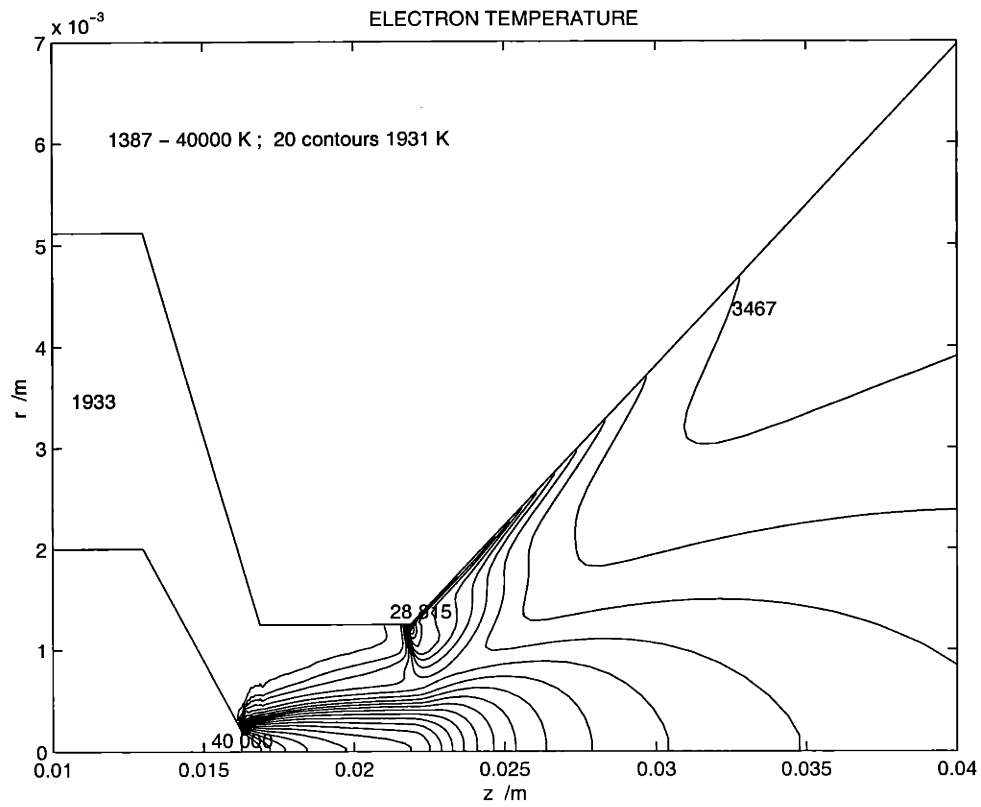

Figure 1-10: *Electron Temperature in the Arc Attachment Region of a Conventional Arcjet Thruster*

of energy into the flow as a conventional arcjet, the constrictor must be longer to give more distance over which power is deposited. Oyerokun [93] in his quasi 1-D model, integrated the equations until the flow reached sonic conditions, and obtained constrictor length to diameter ratios of around ten. With such long constrictors viscous effects may well become important.

The quasi 1-D model assumed equilibrium chemistry, but the work of Miller [85] showed significant non-equilibrium effects, so these should be incorporated into future models. Losses from radiation were also neglected in the 1-D model.

Finally, the quasi 1-D model assumed that since the charged species were provided by the near fully ionized cesium, rather than ionization of the buffer gas, that electrical conductivity would be relatively even throughout the constrictor, and hence the current density would be uniform through the channel and not form into a narrow arc core in the centre of the constrictor. Whether or not a constriction to form a core will occur requires a fully two dimensional model.

The two dimensional model was to address these issues and provide a reasonably accurate prediction of seeded arcjet performance and internal plasma physics.

Beyond writing a numerical code to predict seeded arcjet performance, an experiment to test a prototype seeded arcjet was to be designed. Firstly this would require the range of operation of the thruster to be examined with the view to creating an optimal design for a prototype seeded arcjet. This could be done by mapping the performance variation with operating parameters such as mass flow rate, current, power supplied, and thruster geometry.

For the design of the arcjet itself a thermal model of the temperature distribution within a suggested structure would need to be written. Other issues to be addressed would be the propellant feed system, the apparatus for measuring the its performance, the vacuum equipment required, and finally the handling of the cesium including its injection into the flow and extraction from the exhaust because of cesium being toxic and explosive in the presence of water vapour.

Finally, given the predicted performance of the seeded arcjet, a mission study was to be done to compare the use of the seeded arcjet to a conventional hydrogen or ammonia arcjet, Hall thrusters, and any other relevant thrusters.

1.6 Thesis Overview

The multi-fluid non-equilibrium numerical model of Miller [85] with some of the adaptations of Benson [5] was initially rewritten to include just a cesium ion species, since it was believed at the time that the cesium would be ionized very rapidly to nearly full ionization as soon as it entered the thruster.

The cesium ions were originally included as a separate fluid with their own momentum equations as there was a question over whether due to its much higher mass, the cesium ions would be centrifuged to the outside of the channel. The cesium ions were also originally given their own energy equation, but calculations quickly showed that all heavy species (not electrons) were very strongly coupled in their temperature, and that departures in their temperatures would be damped out on timescales much faster than the flow equations. Consequently a separate energy equation is not required, and the cesium ions can be treated as having the same temperature as the hydrogen fluid. The momentum of the cesium ions

were similarly found to be very strongly coupled to the hydrogen species in all regions of the flow. The coupling caused severe problems with numerical stability and consequently the three fluid model which had been developed was abandoned in favour of a two fluid model with an electron fluid and a heavy species fluid. At this time the stability analysis of Oyerokun [93] was predicting a significant fraction of unionized cesium at the entrance to the constrictor so in writing the two fluid model an atomic cesium species was included.

The code itself accounts for hydrogen molecules, atoms, and ions and cesium atoms and ions. The electrons are treated as one fluid and the heavy species as a second, with separate temperatures and a heat transfer rate between the two. The flow was modelled by Navier-Stokes equations for each fluid, modified to account for thermal and chemical non-equilibrium. The finite differenced flow equations were then integrated by McCormack's method, and the electric potential equation was solved by successive over-relaxation.

After results from a couple of nominal runs were obtained, the numerical integration scheme was changed from an explicit predictor-corrector scheme to a Total Variation Diminishing scheme to avoid the excessive problems encountered with stability and highly restrictive timestep required.

Miller [85] found that the addition of an anode heat balance had no significant effect on the overall performance and minimal effect on the internal flow, so this was left out until converged solutions were obtained, to save on computational effort. Similarly, to accurately model the radiative losses by including a radiative transfer model is computationally expensive, and is not a dominant heat transfer mechanism, so was left for later. The thermal code was written with more of a view to the design of the prototype, and its predicted wall temperatures can then be used iteratively to improve the accuracy of the internal fluid model.

The performance mapping in the end was done using Oyerokun's [93] quasi 1-D code, after its main features were verified using the fully 2-D code. This was done because the quasi 1-D code was much faster allowing thousands of runs to be done, rather than just a handful.

Next the other issues relating to the prototype design and experimental setup were examined, and finally a mission study demonstrated that a seeded arcjet would provide the most payload delivered into orbit for a couple of missions.

Chapter 2 of this thesis gives an overview of previous research that has been done on

arcjet thrusters and arcjet simulations.

Chapter 3 gives the derivation of the governing equations, and chapter 4 details the numerical scheme and discretised equations. Chapter 5 then details the results obtained by the fully 2-D model.

Chapter 6 goes on to present the experimental design starting with mapping out the performance using a reduced order model. Next a search for some suitable materials from which to make the seeded arcjet is presented, followed by the theory and results of a thermal model of a proposed structure. The experimental design is then concluded with a mechanical layout for a laboratory prototype, sizing of the vacuum tank and pumps, and diagnostic equipment, and a look at the supply and extraction of the cesium.

Chapter 7 gives the mission analysis showing a couple of missions where a seeded arcjet would be the thruster of choice. Finally chapter 8 gives a summary, conclusions and suggestions for future work.

Chapter 2

Summary of Previous Research

2.1 Introduction

This chapter deals with the history of arcjets, their improvements, and modelling. For the information up to 1994 most of what is written below comes from Miller [85], who did a good job of detailing the research up to that point.

Research on arcjet thrusters began in the late 1950's, starting with simple analytical models and unconstricted arc experiments, and leading to the fully developed prototypes which were tested at many operating points for relatively long firing durations. Due to a lack of an appropriate mission nearly all work on arcjets stopped by 1966, as there was at that time insufficient power available in space to make arcjet thrusters a viable option for propulsion such as in stationkeeping and orbital manoeuvres. Research on arcjets continued mainly for use as heaters.

By the mid 1980's the growth in size of satellites and the ever increasing demand for power had made it possible for one to two kilowatts of power to be available for periodic firing of electric thrusters. Electric propulsion could be used to gain much greater performance than monopropellant thrusters, and so arcjet research began again in earnest. Since then there have been many experimental programs and numerical simulations have become increasingly complex and accurate.

In the mid 1990's extensive experiments and modelling of the plume and its interactions with the spacecraft began. Arcjets underwent flight qualification tests, and in 1999 a 30 kW ammonia arcjet was flown to demonstrate its capabilities.

2.2 Experimental Arcjets

Early work was mainly undertaken by three companies in the United States: Giannini Scientific/Plasmadyne, General Electric, and Avco. Giannini focused on the development of 2 kW and 30 kW arcjets either radiatively or regeneratively cooled and using hydrogen as a propellant [30],[128]. Measurements of thrust, specific impulse, efficiency, chamber pressure, and power radiated were taken during a 500 hour lifetime test of the 30 kW arcjet.

General Electric built a 30 kW radiation cooled AC arcjet, and tested it using hydrogen and ammonia as propellants [106]. Avco built water cooled and radiation cooled 30 kW arcjets and also used hydrogen and ammonia as propellants [60],[61], and also made measurements of electrode erosion. Spectroscopic measurements were taken through a quartz window in the constrictor and showed that the temperature in the core was in excess of 20000 Kelvin.

This early research gave the basic trends in performance, such as the negative slope of the voltage-current curve, as was also seen in earlier DC arc discharge columns. This occurs primarily because the conductivity of the breakdown gas increases as current is increased. This was observed in arcjet thrusters up to a saturation point beyond which the voltage remained nearly constant.

When arcjet research began again in the 1980's NASA's Jet Propulsion Laboratory tested a 30 kW radiation cooled ammonia arcjet, of a similar design to most radiation cooled arcjets used today. Initial work was aimed at the optimal geometry and consider things such as cathode tip geometry, cathode placement, and nozzle contour. Important operational characteristics can be seen from their test data [38] shown in figure 2-1.

The voltage-current curve displays the negative slope, and increases with mass flow rate. This is due to the increased difficulty for the arc to penetrate the cooler outer region, because the heat diffusivity is inversely proportional to density ($\alpha = \kappa/\rho c_p$). Specific impulse increases with input power but decreases with mass flow rate. When plotted against the specific power (power per mass flow rate) the data collapses onto a single line for a thruster geometry and propellant.

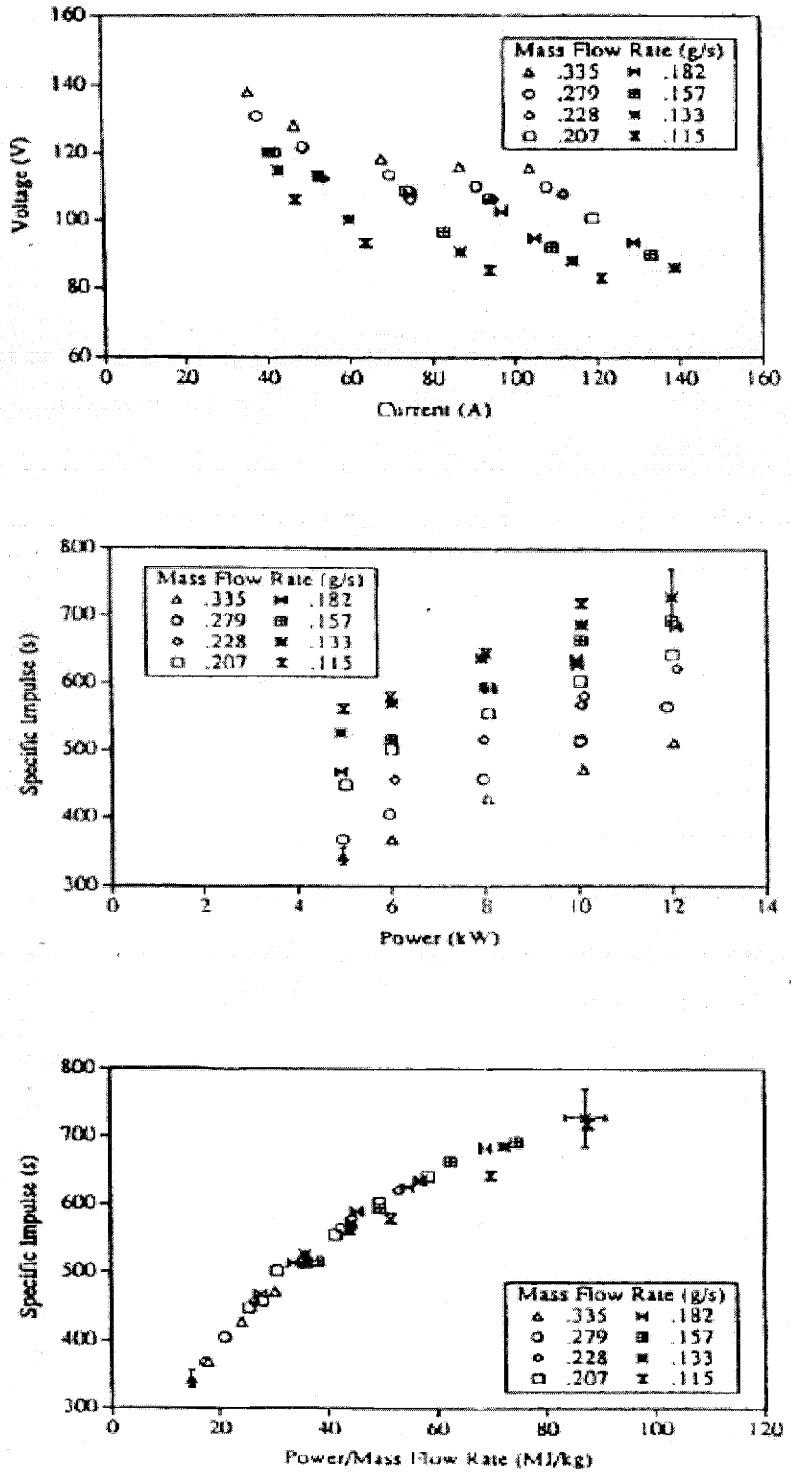

Figure 2-1: *Operational Trends of a 30 kW Ammonia Arcjet. (From Goodfellow and Polk, 1991)*

Long duration testing of 600 to 1500 hours showed that the primary cause of failure was erosion of the cathode tip, and damage to the anode surface around the arc attachment region, in general being from the midpoint of the constrictor to about one constrictor length into the nozzle for that thruster [98] [99]. Damage to the anode was due to both tracking of the foot of the arc where it attached to the anode, and also due to deposition of molten material burnt off the cathode. Eventually the boron nitride injector suffered erosion and fracture. Thruster lifetime was observed to decrease roughly linearly with increasing current.

In 1984 NASA Lewis began investigations into arcjets using the Giannini 1 kW radiation cooled thruster using hydrogen, nitrogen, ammonia, and hydrazine as propellants [24] [88]. After initial testing they built a new low power arcjet and tested it with ammonia and hydrazine [22] [42]. One thousand hour lifetime tests showed no greater damage than on short duration tests for cathode degradation, and micro-cracks and molten deposition on the anode. Consequently electrode degradation was concluded to not be a limiting factor over realistic mission lifetimes for that thruster.

Five different nozzle configurations were tested to determine the effect on thrust and efficiency [26]. Sharply contoured bell-shaped nozzles gave the poorest performance. When compared to a baseline nozzle, short trumpet-shaped nozzles gave the same thrust, but a 25% higher discharge voltage and therefore a lower efficiency. A test of three different constrictor diameters showed that smaller constrictors could produce a modest 1 to 2 percent increase in efficiency [25]. Comparisons of different cooling mechanisms showed a ten to fifteen percent increase in efficiency when regenerative cooling was used in an otherwise radiation cooled design [114].

Finally a thruster with the anode split into five electrically insulated segments was tested to determine the current distribution on the anode as shown in figure 2-2 [23]. The discharge voltage was measured to be about 35 V higher than with a solid anode for a low power arcjet though trends with current were similar. The current was found to attach fairly evenly over the anode, and as the mass flow rate was increased the bulk of the current attached further downstream in the nozzle. (Figure 2-3).

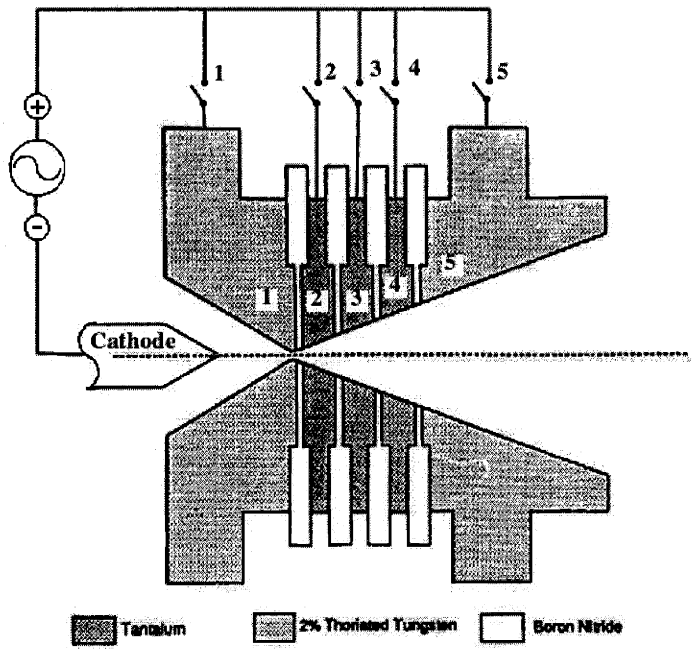

Figure 2-2: *Schematic of segmented anode with simplified diagram of electrical circuit overlaid. (From Curran, Manzella, and Pencil.)*

Typical operating characteristics with $\dot{m} = 4.97 \times 10^{-5}$ Kg s^{-1}.
(Switch position: 0=open, 1=closed. See figure 2-2 for circuit diagram.)

configuration	segment	1	2	3	4	5
1	switch position	1	1	1	1	1
	voltage /V	134.0	134.0	134.0	134.0	134.0
	current /A	0.2	1.1	1.4	2.6	4.9
	current density /A cm^{-2}	39.5	23.1	15.1	18.1	2.8
2	switch position	0	0	0	0	1
	voltage /V	56.1	93.6	116.8	124.5	138.9
	current /A	0.0	0.0	0.0	0.0	10.0
	current density /A cm^{-2}	0.0	0.0	0.0	0.0	5.8
3	switch position	1	1	1	1	0
	voltage /V	139.3	139.3	139.3	139.3	123.5
	current /A	0.4	2.7	6.0	1.2	0.0
	current density /A cm^{-2}	79.0	57.0	63.7	8.5	0.0

Figure 2-3: *Typical operating characteristics of segmented anode. (From Curran, Manzella, and Pencil.)*

NASA Lewis researchers also built a 30 kW arcjet similar to the University of Stuttgart's TT1 thruster [41], which suggested that narrower constrictors and shorter nozzle improved performance.

The Rocket Research Company built a flight qualified low power hydrazine arcjet for stationkeeping of geosynchronous satellites, and started with research on optimization [65]. The qualification was for the General Electric GE 7000 Telstar 4 series of communication satellites [66] [119], and involved thermal and vibration testing, an 800 hour life test, power conditioning unit efficiency tests, leakage tests, and a system mass minimization requirement.

The University of Stuttgart built an extensive electric propulsion laboratory and tested arcjets with various propellants at power levels from 1 to 80 kilowatts. The first design to be built was the TT1 water cooled 15 kW class arcjet [34], which has a segmented anode with three segments upstream on the constrictor, one for the constrictor itself, and four in the nozzle. Both the current and heat flux into each segment were measured and performance characteristics were recorded over a range of currents and mass flow rates using argon, nitrogen, hydrogen, and hydrazine as propellants. In general the arc was observed to attach upstream of the constrictor for argon, in the constrictor and first portion of the nozzle for nitrogen and hydrazine, and in the first 20 to 30 percent of the nozzle for hydrogen. A quartz window was inserted in the constrictor for some experiments which allowed measurements of the arc diameter and estimations of the arc temperature from spectral analysis [32]. Depending on the propellant, operating point, and axial location, temperatures of 12000 to 28000 Kelvin were measured in the core, and 5000 to 10000 K in the edge of the arc.

Stuttgart also built a radiation cooled 15 kW TT1 arcjet and fired it using hydrogen and hydrazine [35], and in addition to performance characteristics the temperature at different locations on the outer casing were measured during operation [33]. In addition a 1 kW radiation cooled hydrazine arcjet named ARTUS and a 50 kW water cooled hydrogen arcjet named HIPARC were constructed and tested [37] [69]. The high power arcjet was designed with a four segment nozzle and at a mass flow rate of $0.1 gs^{-1}$, fifty percent of the current attached in the first nozzle segment and thirty percent in the second nozzle segment. As the mass flow rate was increased the current spread out over the entire nozzle.

In Japan there has been research at the Institute for Space and Astronautical Science (ISAS) and in a joint program between Osaka University and Ishikawajima-Harima Heavy

Industries. ISAS built and tested a low power (3 kW) radiation cooled hydrazine arcjet [134] and at Osaka both a low power radiation cooled arcjet and a high power water cooled arcjet were tested [125] [126] [137]. The lower power thruster was run for 50 hours and given a multiple startup test igniting it 600 times using hydrazine propellant in order to assess electrode erosion rates and identify possible failures modes. For the high power arcjet performance was measured with a variety of propellants, and the arc attachment behaviour found to be upstream of the constrictor for argon, and downstream for the rest. Transmission spectra taken through a quartz window gave temperatures of 10000 K in the plenum chamber and 7000 to 13000 K in the constrictor for argon and nitrogen.

The University of Pisa with a company called BPD built both medium and low power radiatively cooled arcjets [20] [19]. Tests included runs with different propellants, currents, and mass flow rates, voltage-current characteristics, anode temperatures, and erosion measurements.

In the 1990's efforts began to measure the number density, temperature, and velocity distributions in thruster plumes. Several techniques such as plasma probes, emission spectroscopy, and laser induced fluorescence have been demonstrated. Manzella and Capelli used atomic absorption spectroscopy to measure the ground state atomic hydrogen number density in a 1 kW hydrogen arcjet [79] and found a peak number density greater than $3 \times 10^{19} m^{-3}$ was indicated in the core of the plume. Liebeskind et al. [73] used LIF to take velocity measurements and found an axial velocity profile with a peak of 13000 ms^{-1} on axis at a distance of 0.13 diameters from the exit plane. Hoskins et al. [51] used emission spectroscopy to measure the electron temperature and number density profiles over the exit plane of a 10 kW hydrogen arcjet. The electron temperature was found to only vary between 0.2 eV at the nozzle wall to 0.35 eV on the centreline, where the electron number density peaked at $4 \times 10^{20} m^{-3}$. Lichtin and Janson et al. used emission spectroscopy and time-of-flight mass spectrometers to examine a 1 kW ammonia arcjet [58] [72].They measured peak N_2 velocities of 6000 ms^{-1}, N_2 translational temperatures of 3000 - 4000 K, and NH rotational and vibrational temperatures of 3000 - 7000 K. Pivirotto and Deininger took velocity measurements of a 30 kW ammonia arcjet and found an axial velocity of 21000 ms^{-1} at a specific impulse of 800 s [97]. NASA Lewis examined the plume of a low power hydrazine arcjet [80] [113] and found electron temperatures of 0.2 - 0.3 eV and electron number densities of $10^{16} - 10^{17} m^{-3}$ three to fifteen centimeters downstream of the exit

plane. At the exit plane itself the electron number density was found to be $2 \times 10^{19} m^{-3}$ and rotational temperatures of 750 K, 1750 K, and 2500 K for N_2, N_2^+, and NH respectively.

In 1994 Olin Aerospace did a detailed comparison of regenerative cooling in arcjets [50] and managed to improve the efficiency of a baseline thruster five percent by using regenerative cooling and a bi-angled nozzle. This work was extended in 1997 by the Electric Propulsion Laboratory, Inc. of Colorado who built and tested a prolific number of arcjets incorporating numerous exotic design features [3]. Features included arc energy recovery chambers, hot gas heat exchangers, extensive regenerative cooling, by-pass flow, novel cathode shapes. The energy recovery chamber concept is an extension of the bi-angle nozzle idea where the gas is allowed to expand rapidly from the constrictor whereupon expansion is then halted in a large diameter, constant area chamber, where the pressure is less than the constrictor but still much greater than the exit plane as shown in figure 2-4. Due to the intermediate pressure and extended time the gas spends in the chamber, there is significant conversion of excited modes back to kinetic energy. The flared arc attaches to the large surface area in the energy recovery chamber so heat loading at the arc attachment point is reduced which should improve efficiency and longevity. The longer arc column also means a higher voltage for a given power input, and the resulting lower current also decreased heat loading.

The heat exchanger was conceived as a way of increasing the heat transfer from the areas around the arc. Thermally isolating the heat exchanger was found to force it to operate at a high, relatively uniform temperature, which promoted more effective convective heat transfer to the gas stream, and reduced thermal stress. With regenerative cooling using a thin wall with ridges normal to the flow seemed to give best results as it maximized heat transfer to the cooling stream as shown in figure 2-5. Finally completely insulating the outer body with 2 cm of a polycrystalline mullite fibre blanket, covered with a thin titanium shroud, prevented virtually any heat from escaping the regenerative paths, leading to higher efficiency.

In 1999 the USAF Research Laboratory and TRW launched a 30 kW ammonia arcjet to demonstrate the feasibility and compatibility of a high power arcjet system [10]. In-flight diagnostics included four thermo-electrically cooled quartz crystal micro-balances (TQCMs), four radiometers, eight gallium-arsenide solar array cells, electromagnetic interference an-

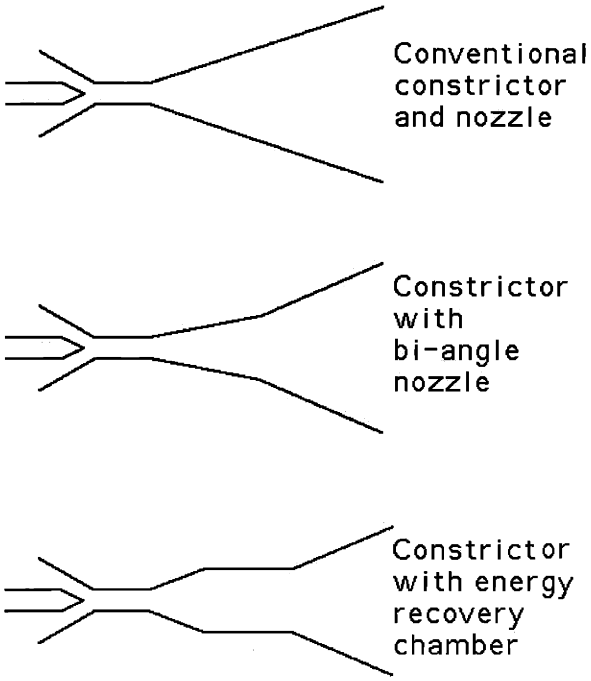

Figure 2-4: *Different arcjet constrictor and nozzle geometries. (From Aston and Aston)*

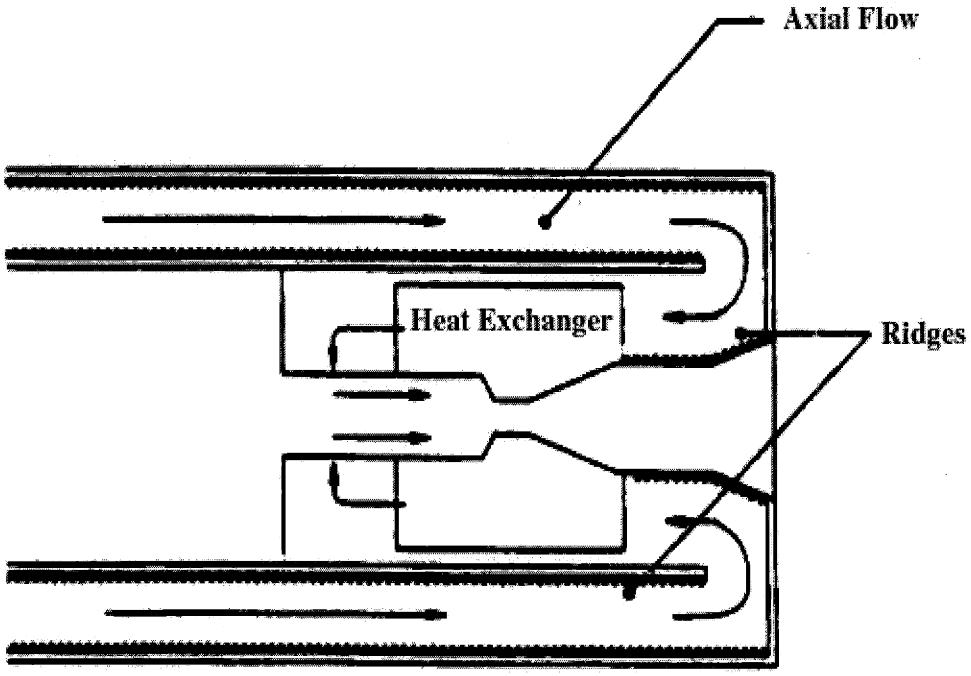

Figure 2-5: *Regenerative cooling path with heat exchanger, thin nozzle walls, and an insulating blanket. (From Aston and Aston)*

tennas, and accelerometer, and a video camera. Eight firings were conducted over 60 days for a total duration of 2023 s. Using an accelerometer the I_{sp} was measured as $786 \pm 50\,s$; the thrust as $1.93 \pm 0.09\,N$; and the efficiency as $26.7 \pm 2.7\,\%$.

The optical measurements were the first chance to observe a high power plume expansion under molecular flow conditions as ground based tests have all been performed at considerably higher background pressure. The spectral line of the NH (A-X) transition was closely examined to determine vibrational and rotational temperatures.

The EMI antennas measured the radiated emission from the arcjet in the lower gigahertz communication frequencies and found no differences between firing and quiescent periods. A bit error rate test also found no significant difference in bit error rate when the arcjet was fired.

The TQCMs measured the mass deposition at different locations, and no measurable deposition was observed that was attributable to the steady state operation of the arcjet. Surprisingly TQCMs within line of sight of the arcjet actually showed a slight removal of previously deposited material with each firing.

The radiometers measured the heat transfer through a coating of S13-GLO which degrades when subjected to the spectral emission of the arcjet. Only those placed with a view of both the plume and body showed any degradation, and the thermal analysis of the heat flux to the spacecraft has not been published to date.

Solar cell segments placed near the thruster exhaust showed increasing degradation including a 3% decrease in power over the 60 days of firing. This is due to the exhaust plasma partially shorting the solar cell load and the reduction in solar transmissivity of the cover glass. No deleterious effects were noticed on the main solar arrays however.

Overall the results are very promising since sensors behind the arcjet or behind the thermal shield showed no deleterious effects, and those which did, in a realistic setting would not be placed so close to the arcjet exit plane.

2.3 Arcjet Modelling

The physical processes involved in arcjet operation can be very complex, making analytical insight difficult and numerical simulations time consuming. The widespread availability of computers in the 1960's and 70's allowed significant progress with semi-analytical and simplified numerical models. As computers have become faster and cheaper, numerical models have become increasingly detailed and accurate.

2.3.1 Semi-Analytical Techniques

Much of the early analytical work on arcjets was done by Avco Research [59]. The basic principles of thermal energy addition were examined using experimental data from a 30 kW arcjet and one dimensional modelling in which the flow was divided into three regions; the arc core, a transition layer, and the outer flow. The importance of loss mechanisms such as frozen flow, wall drag, flow non-uniformities, finite area ratio, angular momentum losses, and power radiated from the anode were all estimated.

Culham Laboratory in England derived a one dimensional model which reduced to two ordinary differential equations, one for the velocity, and another for the degree of dissociation [120]. The model was composed of axial momentum and energy equations, a dissociation rate equation, the thermodynamic relations. Hydrogen, nitrogen, and hydrogen/nitrogen mixtures such as hydrazine were simulated, although nitrogen dissociation was ignored as peak temperatures predicted were only 6000 Kelvin. Assuming fully developed flow wall friction, conductive heat loss and radiation losses were estimated. The two differential equations were simultaneously integrated downstream until the flow became choked, signalling the sonic point and the end of the constant area constrictor. The arc was assumed attach at that point so no heat was added beyond that point. Once a solution was obtained by space marching from the initial conditions, the inlet total pressure was varied until the chocked mass flow rate matched experimental values. Results were then compared to experiment for ammonia at 5 to 30 kW and for hydrogen and hydrazine at 1 to 3 kW. The predicted specific impulses and efficiencies were in error by as much as 25 to 50 percent, but the specific impulse did increase with specific power, albeit at a lower gradient than in experiments as seen in figure 2-6.

The University of Stuttgart created a two channel model with the solution marched from

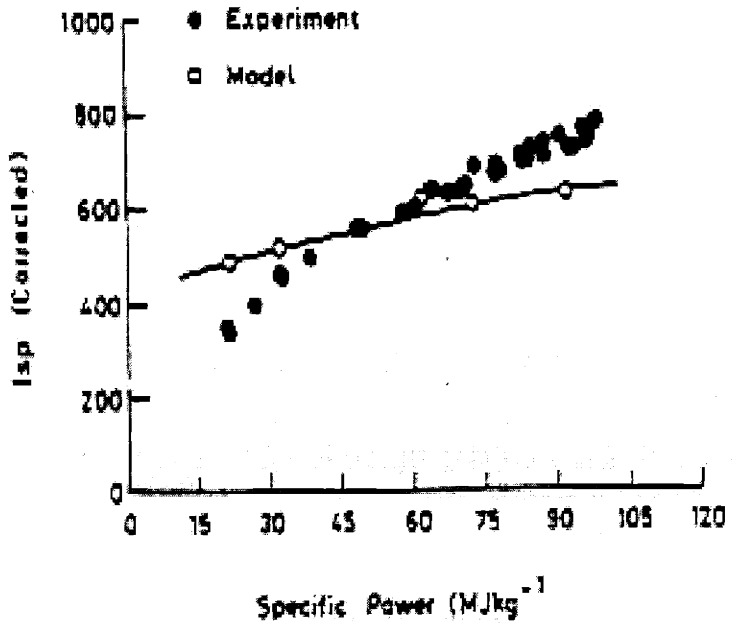

Figure 2-6: *Comparison of Predicted and Experimental Specific Impulse for a 30 kW Ammonia Arcjet. (From Spurrett and Bond, 1991)*

the constrictor inlet to nozzle exit with radial profiles determined at each axial location from integral relations [36]. Within the constrictor the core velocity was assumed to be sonic and the outer cold gas velocity calculated assuming it is adiabatic. Ionization was assumed to be in equilibrium so any molecular propellants were fully dissociated, such as for hydrogen, nitrogen, and hydrazine. Argon was also modelled. Temperatures in the arc core were calculated from an energy equation which included ohmic heating, radial heat conduction, and radiation. In the outer flow the temperature was determined by balancing the energy conducted outward from the arc with the enthalpy convected downstream. The pressure is assumed to be constant radially over both regions, and the mass flow rate enforced in an integral manner. The arc was assumed to attach at the constrictor exit so there is no heating in the nozzle, which was considered to be in frozen flow with the inner and outer velocities determined from a quasi-1D expansion. As with the Culham Laboratory model, it predicted the right trends but the slope was incorrect, and the error ranged up to 50 percent. Discharge voltage was calculated from a power balance between enthalpies of inner and outer flows and the electrical power input, and found to be 10 to 20% higher than experimental values.

Sakamoto at M.I.T. in 1993 also developed a two stream quasi-1D model [82], where

the inner and outer regions are analysed separately, although are connected through the assumption that the arc expands radially as heat conducted outward is absorbed by gas in the outer region flowing into the arc. Average values of the flow variables are obtained by integration radially through the arcjet, and the pressure is assumed to be constant over the cross-section. In the core ohmic dissipation and radial conduction are used being the dominant effects whereas the outer flow is assumed to be isentropic. The gas is also assumed to be in equilibrium with relations between enthalpy, internal energy, heat flux potential, and electrical conductivity linearized. The solution is integrated axially by a Runge-Kutta scheme until the sonic point is reached, and the total pressure at the inlet is varied until the location of the sonic point matches the position of the constrictor exit for the thruster being simulated. As in the Stuttgart model there is no heating in the nozzle and frozen flow is assumed. The current attachment point, anode wall temperature, and voltage drop at the anode, are all quantities specified by the user to give the best match to experimental data for a given thruster and propellant. Specific impulse was predicted to within 1-25% and voltage within 1-40%.

2.3.2 Simplified Axisymmetric Numerical Schemes

The first significant numerical model of an arcjet was developed at NASA Ames in 1967 [133], and calculates the flow through a constricted arc. The flow is assumed to be axisymmetric and the electric potential is assumed to be constant and perpendicular to axis of symmetry. Convection, radial heat conduction, ohmic heating, radiation, and viscous shear are all incorporated into the model, and the transport coefficients and enthalpy at determined from tables of equilibrium states as a function of temperature and pressure. The governing equations are an energy equation, and axial momentum equation, and continuity is ensured by iteration at each axial location until the proper mass flow rate is achieved. The computation domain is a number of concentric cells in the radial direction and the solution is space marched from the inlet to the constrictor exit, which is defined as the point where the flow becomes choked. The arc is considered to be carried only by those cells with temperatures above a threshold for electric conduction. The results follow the right trends although accuracy varies considerably, and although it delivers good insight into constrictor physics no details of arc attachment are included and no nozzle calculations are made either.

The CSIRO Division of Applied Physics in New South Wales developed a model of flow in an argon plasma torch which can be applied to arcjets since the main difference is just the operating point [67]. (One atmosphere ambient pressure and subsonic flow for a plasma torch). The governing equations used are radial, axial, and azimuthal momentum, density, energy, and electric potential. The gas is assumed to be in local thermodynamic equilibrium with ohmic dissipation, viscous shear, heat conduction, and radiative transfer included. The arc is taken to start at the cathode and attach at a particular spot on the anode. Artificially high gas temperatures are specified at each attachment point in order for the arc to be stable and fixed. Results are given for laminar and turbulent flow and underpredicts the discharge voltage by about forty percent.

2.3.3 Numerical Models with More Complex Physics

In the early 1990's the Rocket Research Company developed an inviscid axisymmetric model using finite rate chemistry [13] [14] [64]. Governing equations include global mass continuity, two species continuity equations, radial and axial momentum, energy conservation, and a magnetic field equation. Physical effects accounted for include ohmic heating, viscous dissipation, Bremsstrahlung radiation, thermal conduction, and finite rate chemistry, with realistic geometries. The numerical scheme used is total variation diminishing (TVD), semi-implicit, and includes both Eulerian and Lagrangian integration phases. This solver was originally developed at Los Alamos National Laboratory for solving magnetohydrodynamic flow problems. The model overpredicted the voltage by a factor of two, which was overcome by a heuristic fix in which a minimum electrical conductivity was imposed in order to alter the pattern of current attachment on the anode. Although this brought the voltage into line with experimental values, the specific impulse was still overpredicted by up to 20%, which is shown in figure 2-8. It also caused the current to attach throughout the constrictor and nozzle, which does not match the arc induced heat transfer to the anode seen in hydrogen arcjets.

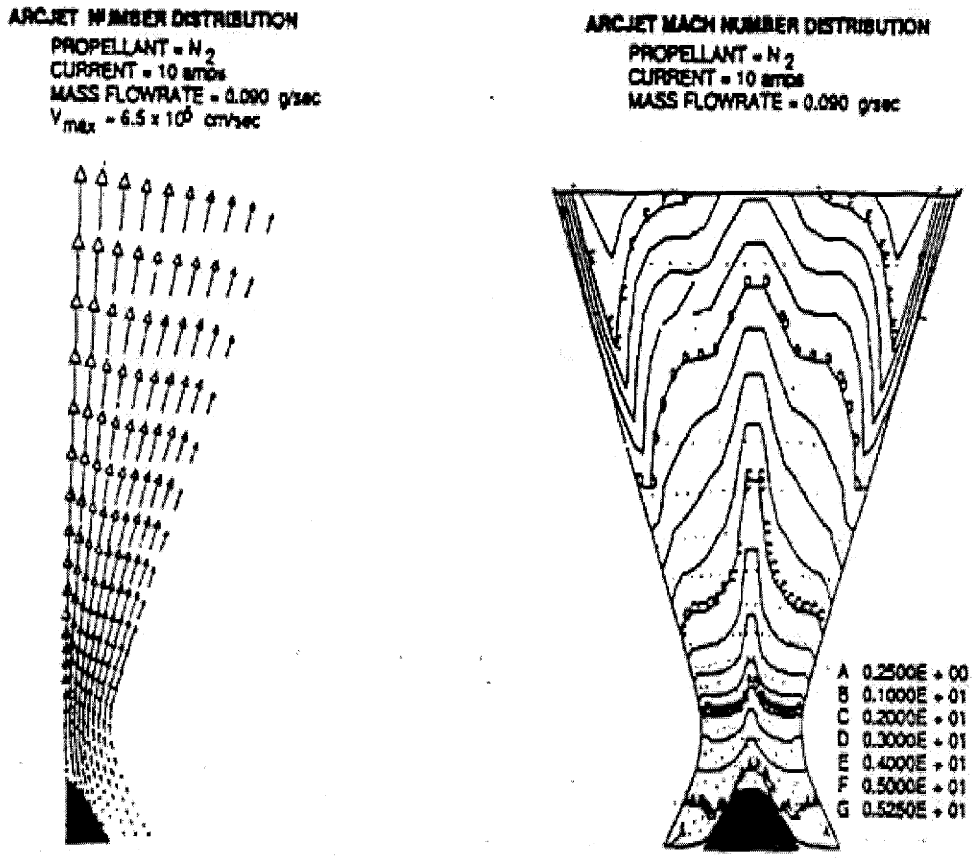

Figure 2-7: *Predicted Velocity and Mach number using Nitrogen (From Butler and King)*

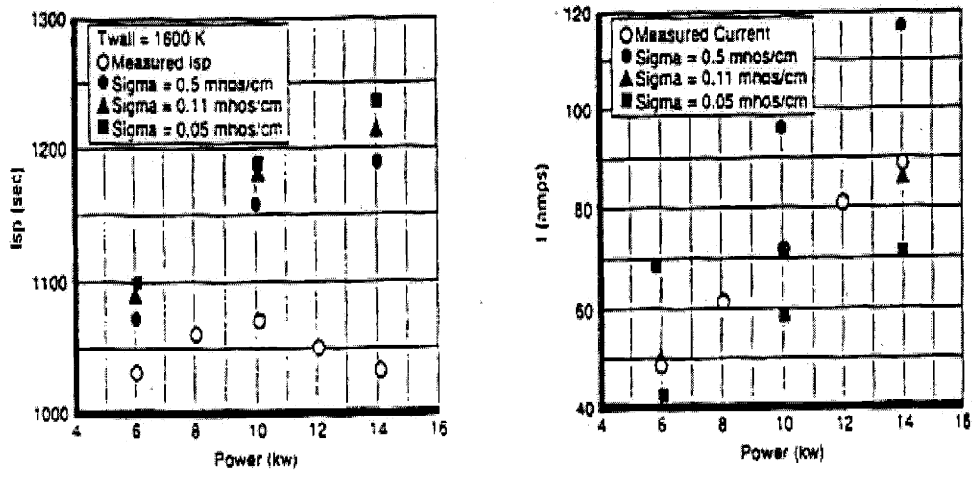

Figure 2-8: *Effect of Electrical Conductivity Floor on Prediction of Hydrogen Arcjet Performance. (From Butler and King)*

The University of Tennessee Space Institute developed a viscous, equilibrium, axisymmetric arcjet flow solver using global mass, 3 $\times$ momentum, energy, and magnetic field equations [103] [104] [105]. Ohmic dissipation, viscosity, heat conduction, and radiation are included and the equations solved by a semi-implicit procedure. The assumption of equilibrium however caused several problems, most severely in the cooler outer flow where the temperature predicted is too low to provide an adequate number of charge carriers for electrical conduction. Consequently several fixes were used to allow the current to penetrate the cooler layer and attach to the anode. First, if the temperature was less than 10000 K then the electrical conductivity was modified to be many orders of magnitude higher than the equilibrium value. Second, a shape factor was prescribed which specifies the distribution of the current flow, and current attachment was specified to occur evenly over the nozzle wall only. Finally the local input power was multiplied by 0.75 to better match experimental measurements of power. For results of 20-30 kW simulations the specific impulse was overpredicted by 10-15%. With ammonia the voltage was overpredicted by about 35% and with hydrogen the efficiency was was overpredicted by up to 25%.

Miller [85] at M.I.T. was the first to abandon thermal equilibrium and used a separate temperature for the electrons than for the heavier ions, atoms, and molecules. Chemical non-equilibrium (finite rate chemistry), diffusion, heat conduction, viscosity, and ohmic dissipation were also accounted for. Using a two temperature model solved the problem of how the current is conducted across the cool outer flow from the arc core to the anode, when the gas temperature of the outer flow alone is too low to produce enough ionization to carry the current. Instead it was shown that ohmic dissipation from the arc current produces very high electron temperatures in both the inner and outer flows. In the arc core there is nearly thermal equilibrium due to the high degree of ionization ensuring strong collisional coupling. In the outer flow however, the coupling is much weaker and the electron temperature remains high while the gas temperature drops to that of the wall. (See figure 2-9). At the arc attachment region, the electron temperature is elevated above the gas temperature enough that it produces sufficient dissociation and ionization rates to create enough charge carriers for self sustaining conduction of the current across the outer flow.

The only major assumption was that the current was not allowed to attach to the anode in the constrictor. (i.e. the constrictor was modelled as an insulator). This was required or else the arc attachment region would creep upstream well beyond where it was

known to attach experimentally. The model predicted specific impulse to within 5-10% and discharge voltage within 10%. As well as more closely matching bulk properties the electron temperature distribution at the nozzle exit was also seen to be of similar shape and magnitude to experimental results.

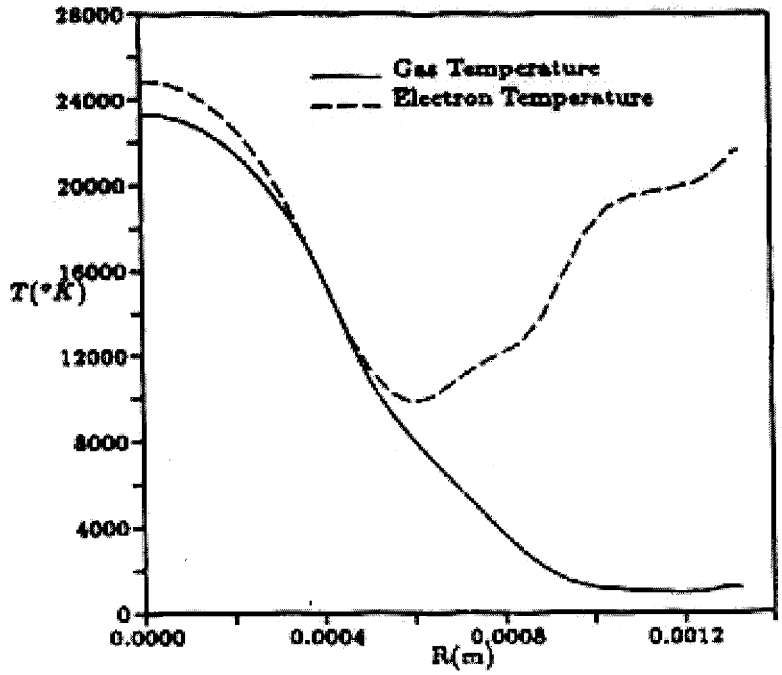

Figure 2-9: *Radial Profile of Gas and Electron Temperature 0.25mm Downstream of the Constrictor Exit. (From Miller)*

The following year (1995) a couple of models very similar to Miller's were published. Megli, Krier, and Burton at the University of Illinois at Urbana Champaign [84] accounted for both N_2 and H_2 allowing simulation of hydrazine as well, and also included a heat balance with the anode. Fujita and Arakawa at the University of Tokyo [31] concentrated on the electrode sheath model and found that neglect of the potential drop at the electrodes not only results in small errors in prediction of the discharge voltage, but has a significant effect on behaviour of the arc close to the electrodes. For argon the current was seen to attach to the upstream part of the constrictor, whereas it was distributed more downstream when using hydrogen. See figures 2-10 and 2-11. The comparatively slow ionization of hydrogen involving first molecular dissociation, and the small ratio of radial ambipolar diffusion to axial flux, suppress the radial extension of the arc. This results in a long arc column and high discharge voltage with hydrogen. This trend is the same as is seen in experiment.

Compared with experiment the voltage was underpredicted by up to 15% and the specific impulse was overestimated by 5-15%.

In 1997 Boyd at Cornell University used a particle based Monte Carlo simulation to examine the nozzle and plume of an arcjet, starting from a continuum solution just downstream of the constrictor [8]. For almost all properties there was a good agreement (to within about 5%) between simulation and experimental measurements. The exception was atomic hydrogen density which underpredicted by a factor of 3, which was believed to be due to insufficiently accurate modelling in the continuum model.

There are still a few issues not addressed in any models to date [81]. The most important is probably whether the arc attachment is diffuse in azimuthal direction or not. If indeed the arc bridge across the cool outer flow is restricted in some places so the current attaches via spokes rather than uniformly in the azimuthal direction, then the arc attachment physics would be very different. The higher current density in the spokes would elevate the gas temperature to approximately the temperature of the electrons as in the models of Maecker [78] and Yamada [135]. This issue can only be resolved by doing a full 3-dimensional numerical simulation.

Another important unresolved issue is the electron energy distribution which to date has only been modelled as a maxwellian, but may in fact be non-maxwellian due to the high level of energy loss from inelastic electron-molecule collisions and non-equilibrium between the molecules' internal energy modes. This may be required to describe the arc attachment more accurately. For example nitrogen molecules can readily absorb collisional energy from free electrons in the 2 to 3 eV range into their vibrational modes. Thus for high electric field to density ratios, in an atomic gas there would be a significant number of electrons above these energy levels, but in a molecular gas there would be very few. Once the electrons are accelerated by the field to the vibrationally active region of the energy spectrum, the energy gained is removed by the molecules and so the distribution dams up against this barrier, and consequently departs greatly from a maxwellian [89]. This is shown in figure 2-12. If the depletion from a maxwellian persists up to the ionizational range (13-16eV) then ionization rate will be greatly affected.

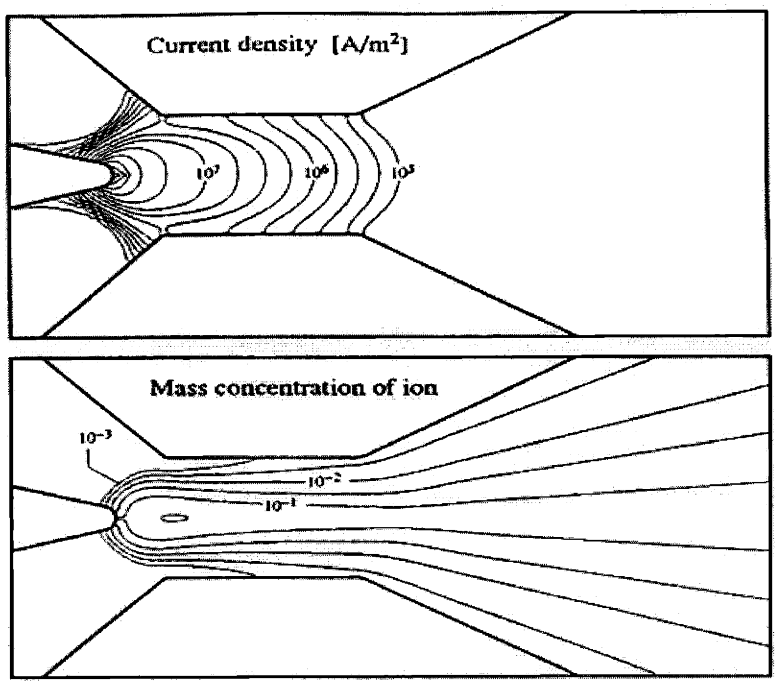

Figure 2-10: *Argon arc behaviour at m=297 mg/s and I=60A. (Logarithmically scaled) From Fujita and Arakawa.*

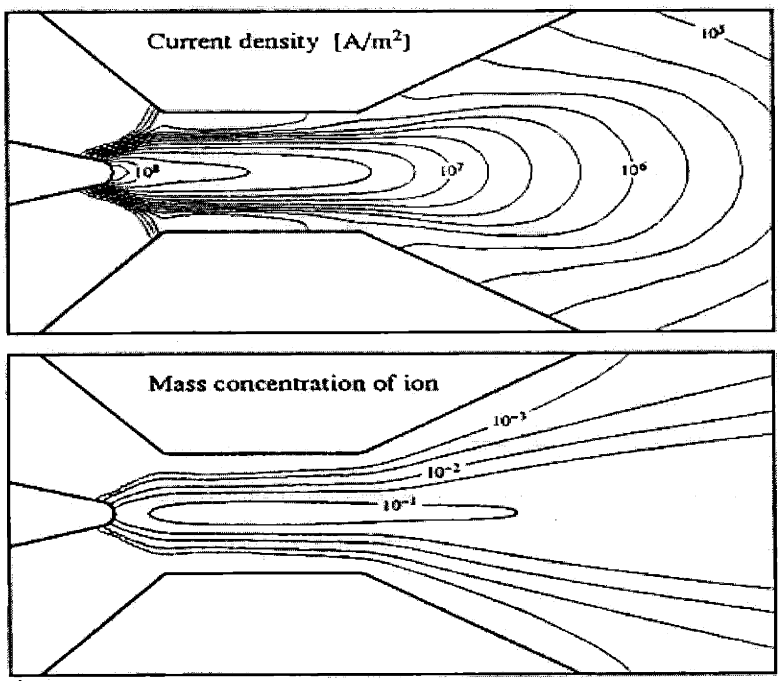

Figure 2-11: *Hydrogen arc behaviour at m=15.0 mg/s and I=60A. (Logarithmically scaled) From Fujita and Arakawa.*

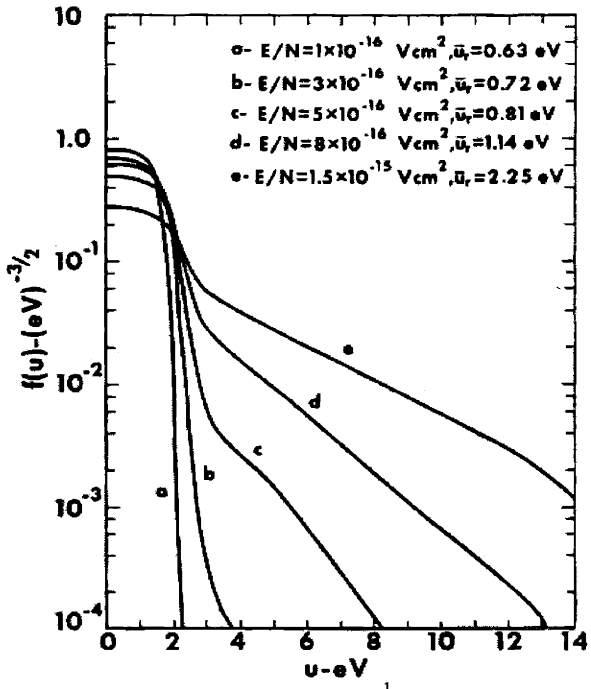

The distribution function is defined such that $\int_0^\infty u^{\frac{1}{2}} f(u)du = 1$, and the reduced average energy such that $\bar{u}_r = \frac{2}{3}\int_0^\infty u^{\frac{3}{2}} f(u)du$.

Figure 2-12: *Electron energy distribution functions in N_2 for various E/N values. (From Nighan)*

2.4 Seeded Arcjets

The frozen losses in an arcjet create the largest loss of efficiency in the system. The idea of seeding is to add a small amount of an easily ionizable material to the flow which produces the electrons required to pass the electric current and is commonly used in magnetohydrodynamic power conversion to obtain good electrical conductivity without ionizing the working gas [112]. More details of this process are explained in section 1.4 and below.

In 1995 Oyerokun at M.I.T. produced a quasi one-dimensional model of an arcjet constrictor seeded with cesium [93] to assess the feasibility of reducing the frozen losses using seeding with 2% cesium by mass. It was found that within reasonable constraints on the constrictor geometry and without allowing the electron temperature to exceed 7000 K, both the ionization and dissociation losses of hydrogen could be essentially eliminated and a specific impulse of 850 s obtained.

The limit on electron temperature was imposed to avoid the instability of hydrogen to ionization, the occurrence of which could lead to a transition back to a conventional hydrogen arc with the associated frozen losses or quenching of the arc. Consequently the

work was extended to do a perturbation analysis [93].

The perturbation analysis suggested there are actually two regimes in which ionization instabilities occur (Figure 2-13). The first, the seed instability was found in regions where the seed is not yet fully ionized, where Coulomb interactions are important, and disappears after the seed is fully ionized. The effect of this would be to drive the electron temperature above its threshold value for near full ionization of the seed. The second mode, is for hydrogen, and was found to depend strongly on the degrees of dissociation and ionization. Therefore operating at higher gas temperatures, hence higher I_{sp}, reduces the maximum allowable electron temperature. The instability was found to occur when the electrons from hydrogen atoms constituted about 2% of the total, so increasing pressure delayed the temperature at which instability occurred. With increasing seed fraction the instability boundaries were found to approach one another, and the ratio where they meet should give an upper bound on the seed fraction, above which the system is always unstable (Figure 2-14).

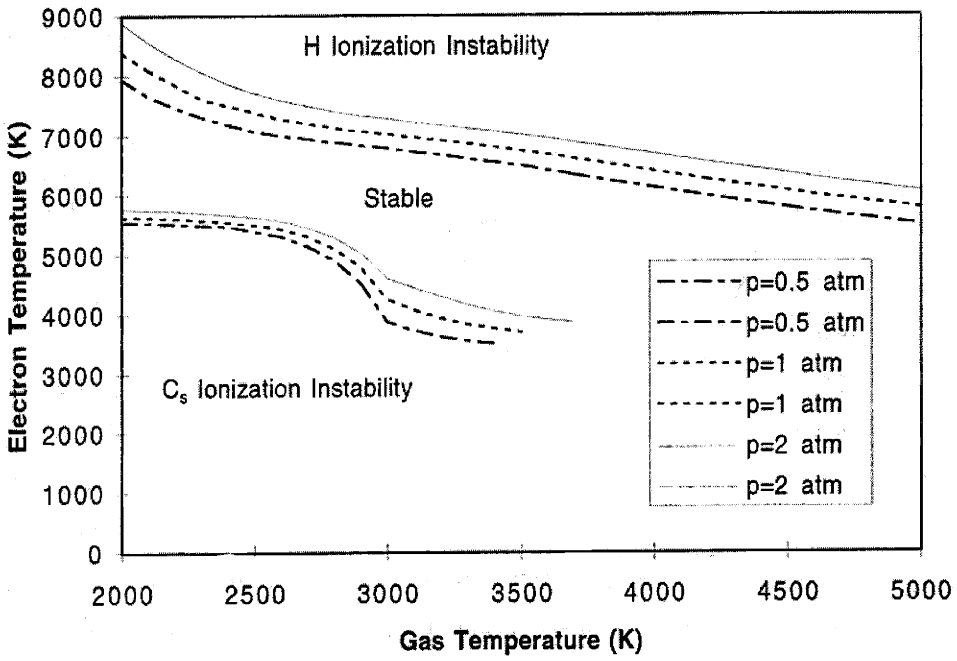

Figure 2-13: *Instability threshold of electron temperature versus gas temperature at different pressures. (Molar seed fraction = $3x10^{-4}$. From Oyerokun)*

In 1997 a two dimensional model of a seeded arcjet was developed by this author to answer several questions [108] [109]. In particular that of instability of the hydrogen to

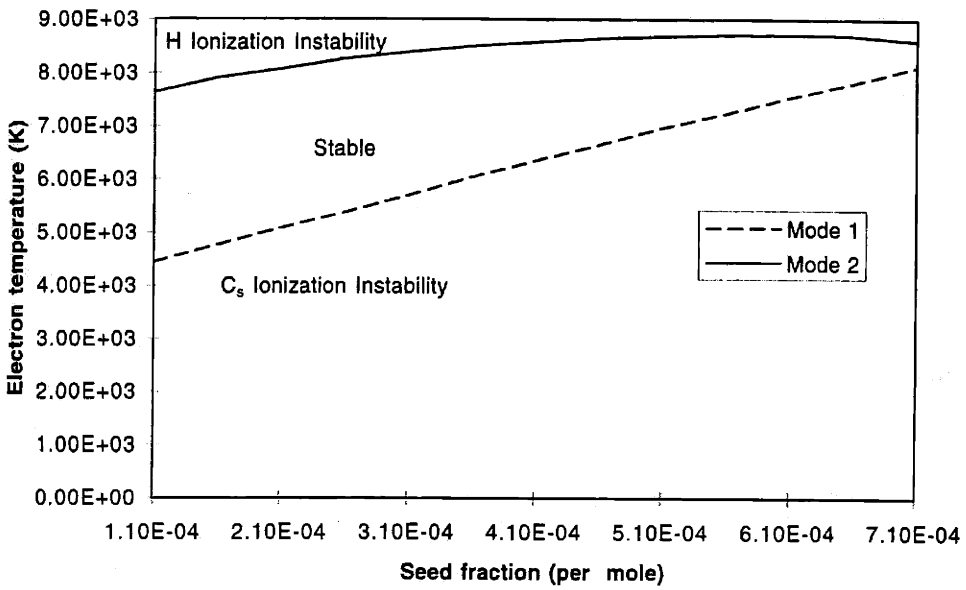

Figure 2-14: *Instability threshold of electron temperature versus cesium seed fraction. (At 1 atm, 2000 K. From Oyerokun)*

ionization. The electric arc has to attach to the anode at some point downstream of the constrictor, where there will be a region of high current density and therefore of strong heating. If the hydrogen ignites when passing through the arc attachment region then the thruster would convert back to conventional operation and all the frozen losses would be back again.

Another issue is the distribution of the current density in the constrictor which was predicted to be uniformly distributed throughout the constrictor and not form the narrow core as seen in conventional arcjets. This is important because it means that the constrictor of a seeded arcjet will have to be made of an insulator or else the arc would not pass down the constrictor and therefore not provide sufficient heating of the propellant.

The 2-D code produced a couple of nominal cases where the hydrogen was fully molecular whilst the cesium was fully ionized, and the current density was indeed uniformly distributed. The 2-D code thus confirmed that there was at least a nominal operating condition where the frozen losses were essentially eliminated.

Chapter 3

Governing Equations

In this chapter the equations governing the flow inside an alkali seeded hydrogen arcjet thruster are derived from moments of Boltzmann's Equation for the flow, and Maxwell's Equations for the electric field. After deriving the equations for conservation of mass, momentum, and energy, the equation of state is modelled as are dissociation and ionization processes, and the molecular transport properties. The derivations draw heavily on the texts by Miller [85], Benson [5], Oyerokun [93], Mitchner and Kruger [86], Hirshfelder, Curtiss, and Bird [48], and Bittencourt [7].

3.1 Maxwell's Equations

Maxwell's equations in a medium would be difficult to implement for the ionized gas due to the complex motion of the charges which make it hard to evaluate the permittivity and permeability of the medium [18]. Since the working substance is a gas there is little error in using Maxwell's equations in a vacuum to describe the behaviour of the electromagnetic field.

$$\nabla \cdot \vec{E} = \frac{\rho_c}{\epsilon_0} \tag{3.1}$$

$$\nabla \times \vec{E} = -\frac{\partial \vec{B}}{\partial t} \tag{3.2}$$

$$\nabla \cdot \vec{B} = 0, \tag{3.3}$$

$$\nabla \times \vec{B} = \mu_0 \left(\vec{J} + \epsilon_0 \frac{\partial \vec{E}}{\partial t} \right) \tag{3.4}$$

where ρ_c is the charge density, ϵ_0 is the permittivity of free space, μ_0 is the permeability of free space, $\vec{J}$ is the current density, and $\vec{E}$ and $\vec{B}$ are the electric and magnetic fields.

3.2 Boltzmann's Equation

In the kinetic theory of gases a distribution function, $f_s(\vec{x}, \vec{v}, t)$, is used to describe the fraction of particles in an ensemble possessing a velocity $\vec{v}$ at a location $\vec{x}$ and time t. The rate of change of this distribution is described by Boltzmann's equation.

$$\frac{\partial f_s}{\partial t} + \vec{v} \cdot \nabla f_s + \frac{\vec{F}_s}{m_s} \cdot \nabla_v f_s = \left(\frac{\partial f_s}{\partial t}\right)_{coll}, \tag{3.5}$$

where $\vec{F}_s$ is the applied body forces, and ∇_v is the gradient operator in velocity space. The term on the right hand side of the equation represents the time rate of change of the distribution function due to collisions, and can be a complicated function of the distribution functions of the various species present, their relative velocities, and collision cross-sections.

The macroscopic conservation equations can be derived by taking the appropriate moments of the Boltzmann equation. We begin by multiplying Equation 3.5 by some quantity $\varphi_s(\vec{x}, \vec{v}, t)$, which may vary with position, velocity, and time. By integrating over all velocity space, the general transport equation is obtained:

$$\frac{\partial}{\partial t}\left(n_s < \varphi_s >\right) - n_s < \frac{\partial \varphi_s}{\partial t} > + \nabla \cdot \left(n_s < \varphi_s \vec{v} >\right) - n_s < \vec{v} \cdot \nabla \varphi_s >$$

$$- n_s < \frac{\vec{F}_s}{m_s} \cdot \nabla_v \varphi_s > = \int \varphi_s \left(\frac{\partial f_s}{\partial t}\right)_{coll} d^3v, \tag{3.6}$$

where $(< >)$ indicates the average value of a quantity in velocity space. The integration reduces the problem from one in six-dimensional phase space and time to one in three-dimensional coordinate space and time. The conservation equations for each species can be obtained by taking φ_s as the correct quantity associated with mass, momentum, and energy. Global equations can then be obtained by summation of species equations. For pressures below about 10^3 atmospheres, binary collisions dominate which simplifies the collisional term.

Using equation 3.6, the species mass conservation equations can be obtained by taking $\varphi_s = m_s$.

$$\frac{\partial \rho_s}{\partial t} + \nabla \cdot (\rho_s \vec{u}_s) = S_s = m_s \int \left(\frac{\partial f_s}{\partial t}\right)_{coll} d^3v, \tag{3.7}$$

where $\vec{u}_s$ is the net bulk velocity of the species, and S_s is a volumetric source term representing the rate of production of mass of species s due to collisions.

The momentum equation comes from taking $\varphi_s = m_s \vec{v}$.

$$\frac{\partial \rho_s \vec{u}_s}{\partial t} + \nabla \cdot (\rho_s \vec{u}_s \vec{u}_s) + \nabla \cdot \bar{\bar{p}}_s - n_s < \vec{F}_s >= \vec{A}_s = m_s \int \vec{v} \left(\frac{\partial f_s}{\partial t}\right)_{coll} d^3v. \tag{3.8}$$

An alternate form of the species momentum equation may be obtained by expanding the momentum flow dyad and substituting Equation 3.7.

$$\rho_s \left[\frac{\partial \vec{u}_s}{\partial t} + (\vec{u}_s \cdot \nabla)\, \vec{u}_s\right] + \nabla \cdot \bar{\bar{p}}_s - n_s < \vec{F}_s >= \vec{A}_s - \vec{u}_s S_s. \tag{3.9}$$

The term $\bar{\bar{p}}_s$ is the kinetic pressure tensor, comprised of the scalar pressure, p_s, and the shear stresses. The quantity $\vec{A}_s$ represents the collisional change of momentum of species s. The body force of interest in arcjets is the Lorentz force:

$$< \vec{F}_s >= q_s \left(\vec{E} + \vec{u}_s \times \vec{B}\right). \tag{3.10}$$

The collisional momentum term can be thought of as the average rate of loss of momentum from particles of species s to the particles of all other species, and can be approximated as

$$\vec{A}_s = \rho_s \sum_s \overline{\nu}_{sr} \frac{m_{sr}}{m_s} \left(\vec{u}_r - \vec{u}_s\right), \tag{3.11}$$

where $\overline{\nu}_{sr}$ is an average collision frequency between species s and species r, and m_{sr} is the reduced mass of species s and species r. Inserting Equations 3.10 and 3.11 into Equations 3.8 and 3.9 yields two forms of the species momentum equation,

$$\frac{\partial \rho_s \vec{u}_s}{\partial t} + \nabla \cdot (\rho_s \vec{u}_s \vec{u}_s) + \nabla \cdot \bar{\bar{p}}_s = n_s q_s \left(\vec{E} + \vec{u}_s \times \vec{B}\right) + \rho_s \sum_s \overline{\nu}_{sr} \left(\vec{u}_r - \vec{u}_s\right), \tag{3.12}$$

which is in conservative form, and

$$\rho_s \left[\frac{\partial \vec{u}_s}{\partial t} + (\vec{u}_s \cdot \nabla) \vec{u}_s \right] + \nabla \cdot \bar{\bar{p}}_s = n_s q_s \left(\vec{E} + \vec{u}_s \times \vec{B} \right) + \rho_s \sum_s \overline{\nu}_{sr} (\vec{u}_r - \vec{u}_s) - \vec{u}_s S_s. \quad (3.13)$$

Finally, the species energy conservation equation can be found by substituting $\varphi_s = m_s v^2$ into the general transport equation.

$$\frac{\partial}{\partial t} \left(\frac{3}{2} p_s + \frac{1}{2} \rho_s u_s^2 \right) + \nabla \cdot \left[\left(\frac{3}{2} p_s + \frac{1}{2} \rho_s u_s^2 \right) \vec{u}_s \right] + \nabla \cdot (\bar{\bar{p}}_s \cdot \vec{u}_s)$$

$$+ \nabla \cdot \vec{q}_s - n_s < \vec{F}_s \cdot \vec{v} >= M_s, \quad (3.14)$$

where

$$M_s = \frac{1}{2} m_s \int v^2 \left(\frac{\partial f_s}{\partial t} \right)_{coll} d^3 v \quad (3.15)$$

represents the rate of energy transfer per unit volume due to collisions and $\vec{q}_s = -\kappa_s \nabla T_s$ is the heat flux vector for species s. M_s can be approximated as

$$M_s = \sum_r \frac{\rho_s \overline{\nu}_{sr}}{m_s + m_r} \left[3k (T_r - T_s) + m_r |\vec{u}_r - \vec{u}_s|^2 \right], \quad (3.16)$$

where k is Boltzmann's constant.

As written, Equation 3.14 only applies to ideal particles with translational energy only, and doesn't apply to particles with additional energy, such as molecules possessing energy in internal vibrational and rotational modes. The rigorous derivation of the energy equation for particles with internal degrees of freedom is discussed in chapter 11 of Chapman and Cowling [16], and results in the following energy equation:

$$\frac{\partial}{\partial t} \left(\frac{3}{2} p_s + \frac{1}{2} \rho_s u_s^2 + \rho_s e_{s,int} \right) + \nabla \cdot \left[\left(\frac{3}{2} p_s + \frac{1}{2} \rho_s u_s^2 + \rho_s e_{s,int} \right) \vec{u}_s \right] + \nabla \cdot (\bar{\bar{p}}_s \cdot \vec{u}_s)$$

$$+ \nabla \cdot \vec{q}_s - n_s < \vec{F}_s \cdot \vec{v} >= \sum_r \frac{\rho_s \overline{\nu}_{sr}}{m_s + m_r} \left[3k (T_r - T_s) + m_r |\vec{u}_r - \vec{u}_s|^2 \right] \quad (3.17)$$

Here $e_{s,int}$ represents the average internal energy per unit mass of species s, including vibrational, rotational, dissociation, and ionization energies where necessary. When the Lorentz force (Equation 3.10) is substituted into Equation 3.17, the terms including the

magnetic field vanish, and the species energy equation becomes:

$$\frac{\partial}{\partial t}\left(\frac{3}{2}p_s + \frac{1}{2}\rho_s u_s^2 + \rho_s e_{s,int}\right) + \nabla\cdot\left[\left(\frac{3}{2}p_s + \frac{1}{2}\rho_s u_s^2 + \rho_s e_{s,int}\right)\vec{u}_s\right] + \nabla\cdot(\overline{\overline{p}}_s\cdot\vec{u}_s)$$

$$+\nabla\cdot\vec{q}_s = \vec{J}_s\cdot\vec{E} + \sum_r \frac{\rho_s\overline{\nu}_{sr}}{m_s+m_r}\left[3k\left(T_r - T_s\right) + m_r\left|\vec{u}_r - \vec{u}_s\right|^2\right], \tag{3.18}$$

where $\vec{J}_s = n_s q_s \vec{u}_s$ is the current density carried by species s.

This equation may be further simplified by defining a total energy per unit mass:

$$E_s = \frac{3}{2}\frac{p_s}{\rho_s} + \frac{1}{2}u_s^2 + e_{s,int}, \tag{3.19}$$

where $\frac{3}{2}\frac{p_s}{\rho_s}$ is the energy per unit mass due to random motion of the particles, $\frac{1}{2}u_s^2$ represents the kinetic energy per unit mass due to directed motion, and $e_{s,int}$ is the internal energy per unit mass. Inserting Equation 3.19 into Equation 3.18 results in:

$$\frac{\partial}{\partial t}\left(\rho_s E_s\right) + \nabla\cdot\left(\rho_s\vec{u}_s E_s\right) + \nabla\cdot(\overline{\overline{p}}_s\cdot\vec{u}_s) - \nabla\cdot\left(\kappa_s\nabla T_s\right) = \vec{j}_s\cdot\vec{E} + M_s. \tag{3.20}$$

3.3 Arcjet Flow Model

The macroscopic conservation equations along with an equation of state form a closed set of coupled nonlinear differential equations which can be tailored to solve the flow within an electrothermal arcjet. In general the equations are a modified form of the Navier-Stokes equations as applied to a multi-species chemically reacting flow. The model as originally derived by Miller takes into account viscous effects, heat conduction, ambipolar diffusion, Ohmic heating, and collisional energy transfer between electrons and heavy species.

3.3.1 Simplifying Assumptions

Although three-dimensional effects probably do occur within arcjets, the set of equations makes the numerical solution in three dimensions very computationally intensive, for any numerical scheme. Fortunately, a great deal of information can be obtained by restricting the physics to a two-dimensional axisymmetric flow. Taking the azimuthal derivatives to be negligible, terms involving $\frac{\partial}{\partial\theta}$ can be eliminated. The terms which are constant in θ but vary in z and r should be retained. In particular, an azimuthal "swirl" velocity component

is retained, since in most experimental arcjets the propellant is injected into the plenum with some swirl velocity. It is believed that this swirl component stabilizes the arc during startup.

When any partially ionized gas is in contact with a solid wall, electrically non-neutral sheaths form on the solid surfaces. As discussed in Section 1.3.1, these sheath regions within an arcjet thruster are typically very small for the range of temperatures and pressures usually found. Due to this fact, the sheath regions are neglected, and the grid boundaries are treated as sheath boundaries. Within the flow, quasi-neutrality ($n_e \approx n_i$) is assumed. The assumption of quasi-neutrality not only makes the calculation of some physical quantities much simpler, but it also reduces the number of necessary mass conservation equations by one.

Another major assumption that is used within this research concerns the temperatures of the various species. Each species within the internal flow of an arcjet can, possibly, have its own translational temperature. In other words, each species can have a different temperature corresponding to its own random thermal motions. In addition, molecules and other complex particles can have temperatures associated with internal degrees of freedom (such as vibrational or rotational modes) which are not in thermal equilibrium with the translational temperature. For simplicity, all the heavy species in this work are assumed to be in translational thermal equilibrium with one another, and the temperatures of the various internal modes are assumed to be in equilibrium with this translational temperature. The exception to this is the electron temperature. An electron temperature which is different from the other temperatures is important in the non-equilibrium production of charge carriers, especially from the buffer gas, and in conventional arcjets. It is also vital for the accurate modelling of the arc attachment to the anode, where the electron temperature may be significantly higher than the heavies temperature.

The final major assumption within this research concerns the self-induced magnetic field, which within an arcjet can be taken to be negligible. This assumption can be quantified by relating the fluid pressure to the magnetic field pressure, defined as

$$p_B = \frac{B_0^2}{2\mu_0}. \tag{3.21}$$

The ratio of the fluid pressure to the magnetic pressure

$$\beta_0 = \frac{\sum_j n_j k T_j}{B_0^2/2\mu_0}, \tag{3.22}$$

provides a measure of the importance of the self-induced magnetic field [18]. Assuming a coaxial current flow through an area of radius R_0, β_0 becomes

$$\beta_0 = \frac{8\pi^2 R_0^2 \sum_j n_j k T_j}{\mu_0 I^2}. \tag{3.23}$$

For arcjets, β_0 is typically large, which means that the induced magnetic field has little effect on the flow. For example, the German TT1 thruster, which operates at $p \approx 1.5$ atmospheres, for a current flow of 100 amperes and $R_0 = 2mm$ (the cathode radius), $\beta_0 = 3.8 \times 10^3$. For comparison, a typical MPD thruster may have a current flow within the arc of $I = 30,000$ A, operating at a pressure of about 10^{-2} atm. If we take $R_0 = 5.2$ cm, as is the case in the MPD thruster of Heimerdinger [44], $\beta_0 = 0.2$.

3.4 Fluid Properties

3.4.1 Equation of State

In this research, each species is assumed to behave as an ideal gas. For the range of temperatures and pressures expected in this research, this is a good approximation.

$$p_s = n_s k T_s = \rho_s R_s T_s, \tag{3.24}$$

where $R_s = \frac{k}{m_s}$ is the gas constant specific to species s in units of $JKg^{-1}K^{-1}$.

3.4.2 Global Properties

Global equations describing the properties of the fluid as a whole are obtained by summing species equations for mass, momentum, and energy. The total density is thus

$$\rho = \sum_s \rho_s \tag{3.25}$$

and the flow velocity is mass averaged as

$$\vec{u} = \frac{1}{\rho} \sum_s \rho_s \vec{u}_s, \tag{3.26}$$

where $\vec{u}_s$ is the species velocity relative to the laboratory reference frame. Using this definition the species velocities can be written as the sum of the global velocity and a slip velocity.

$$\vec{u}_s = \vec{u} + \vec{V}_s, \tag{3.27}$$

where $\vec{V}_s$ is the species slip velocity, relative to the mass averaged velocity. From Equations 3.26 and 3.27, it can be easily shown that the slip velocities obey the relation

$$\sum_s \rho_s \vec{V}_s = 0. \tag{3.28}$$

In this research the slip velocity will be the velocity of mass diffusion.

The global pressure is given by the sum of the partial pressures of the various species,

$$p = \sum_s p_s = \sum_s \rho_s R_s T_s. \tag{3.29}$$

In terms of the species pressure tensor, $\overline{\overline{p}}_s$, the scalar pressure, p_s, is defined as one third of the trace of the pressure tensor, or, in other words, the mean value of the diagonal elements of the pressure tensor:

$$p_s = \frac{1}{3} \left(p_{s11} + p_{s22} + p_{s33} \right). \tag{3.30}$$

Using this definition, the pressure tensor can be separated into two parts:

$$\overline{\overline{p}}_s = p_s \overline{\overline{I}} - \overline{\overline{\tau}}_s \tag{3.31}$$

where $\overline{\overline{I}}$ is an identity matrix, and $\overline{\overline{\tau}}_s$ is the viscous stress tensor for species s. As with the other global quantities, the global pressure tensor can be defined as the sum of the species pressure tensor:

$$\overline{\overline{p}} = \sum_s \overline{\overline{p}}_s = \sum_s \left(p_s \overline{\overline{I}} - \overline{\overline{\tau}}_s \right) = p \overline{\overline{I}} - \overline{\overline{\tau}}. \tag{3.32}$$

Using Equation 3.27, the total current density can be written as

$$\vec{J} = \vec{u}\sum_s n_s q_s + \sum_s n_s q_s \vec{V}_s. \tag{3.33}$$

The first term on the right hand side is the convection current density, which is due to convection of net space charge. The second term is the conduction current density, which occurs because of differing slip velocities. For a quasi-neutral plasma, the first term vanishes, leaving

$$\vec{J} = \sum_s n_s q_s \vec{V}_s. \tag{3.34}$$

Many bulk properties such as the transport properties depend on the fraction of mass or moles of each species present in the mixture. Consequently it is useful to define mass and mole fractions. The mass fractions are given as

$$y_i = \frac{\rho_i}{\rho} = \frac{\rho_i}{\sum_j \rho_j} \tag{3.35}$$

where ρ is the mass density, so for the arcjet model

$$y_{H_2} + y_H + y_{H+} + y_{Cs} + y_{Cs+} + y_e = 1$$

but the mass of electrons is negligible compared to the heavy species so it is more convenient to use

$$y_{H_2} + y_H + y_{H+} + y_{Cs} + y_{Cs+} \approx 1. \tag{3.36}$$

Similarly the mole fractions are given as

$$x_i = \frac{n_i}{n} = \frac{n_i}{\sum_j n_j} \tag{3.37}$$

where n is the number density, so for the arcjet model

$$x_{H_2} + x_H + x_{H+} + x_{Cs} + x_{Cs+} + x_e = 1$$

but due to quasineutrality $n_e = n_{H+} + n_{Cs+}$ so

$$x_{H_2} + x_H + x_{Cs} + 2\left(x_{H+} + x_{Cs+}\right) = 1. \tag{3.38}$$

Conversion between mass and mole fractions can be simply done according to

$$x_i = \frac{y_i/m_i}{\sum_i y_i/m_i} \tag{3.39}$$

$$y_i = \frac{x_i m_i}{\sum_i x_i m_i} \tag{3.40}$$

where m_i is the mass of species i.

3.4.3 Specific Heats

The ratio of specific heats for the plasma as a whole, γ, is required in the calculation of the Mach number and in obtaining the stability criteria used in calculating the time step for integrating the fluid equations. According to thermodynamics, a particle has $\frac{1}{2}kT$ of internal energy per degree of freedom [115] so the total internal energy is $U = \frac{1}{2}fNkT = \frac{1}{2}fnRT$. The molar specific heat at constant volume is the change in energy per change in temperature per mole at constant volume, $C_V = \frac{\partial u}{\partial T} = \frac{\partial}{\partial T}\left(\frac{1}{2}fRT\right) = \frac{f}{2}R$ .The molar specific heat at constant pressure is given by $C_P = C_V + R = \frac{f+2}{2}R$ hence the ratio of specific heats $\gamma = \frac{C_P}{C_V} = \frac{f+2}{f}$. For a gas composed of monatomic particles, the particles only have three degrees of freedom corresponding to the three possible mutually perpendicular directions of motion in space. Diatomic particles on the other hand have fully 14 degrees of freedom. However most of the degrees of freedom are frozen out at low temperatures, so do not contribute to the specific heat. As the temperature is increased more modes of storing energy come into effect as can be seen in figure 3-1 for hydrogen taken from Sears and Salinger [115].

The characteristic temperature for rotation of H_2 perpendicular to the bond axis is $\Theta_r = 85.5\ K$ and the temperature for vibration is $\Theta_v = 6140\ K$. The temperatures associated with the other modes are high enough such that in most circumstances H_2 will dissociate into its component H atoms before they are excited. Consequently in an arcjet the two rotational modes can be considered fully excited and the vibrational mode must be accounted for as a function of temperature. Kestin and Dorfman [63] give the specific heat associated with vibration as

$$\left(\frac{C_V}{R}\right)_{vib} = \zeta = \frac{\left(\frac{\Theta_v}{T}\right)^2 e^{\frac{\Theta_v}{T}}}{\left(e^{\frac{\Theta_v}{T}} - 1\right)^2} = \left(\frac{\frac{\Theta_v}{2T}}{\sinh\frac{\Theta_v}{2T}}\right)^2. \tag{3.41}$$

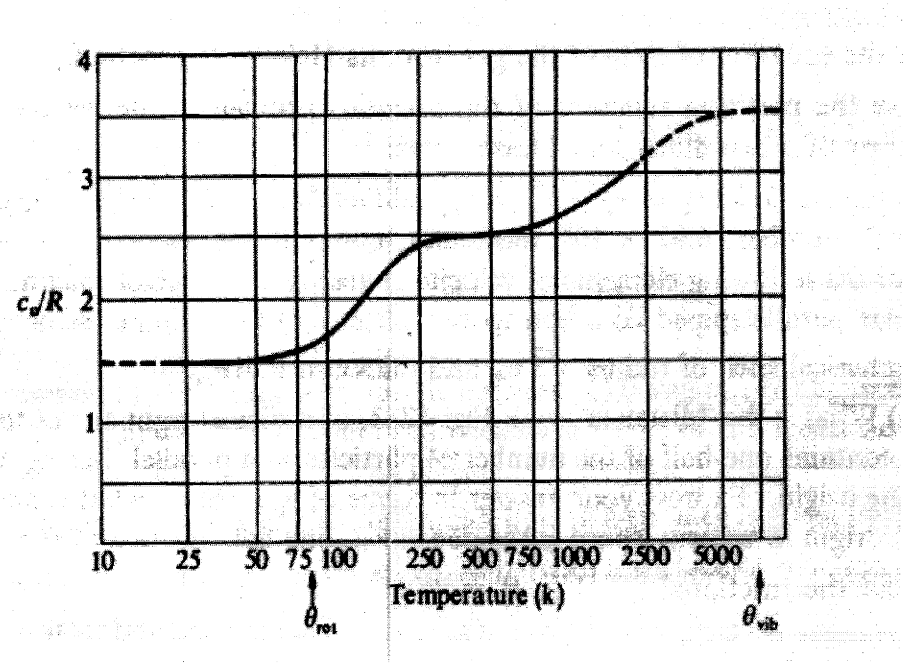

Figure 3-1: *Experimental Values of Cv/R for Hydrogen as a Function of Temperature.*

The specific heats associated with each mode of energy add so $\gamma = 1 + \frac{R}{C_V} = 1 + \frac{R}{C_{V_{translation}} + C_{V_{rotation}} + C_{V_{vibration}}}$ so for H_2 the ratio of specific heats will be

$$\gamma_{H_2} = 1 + \frac{1}{\left(\frac{5}{2} + \frac{\theta^2 e^\theta}{(e^\theta - 1)^2}\right)}, \tag{3.42}$$

where $\theta = \frac{\Theta_v}{T}$. For mixtures the specific heat averages by the number of moles of each species present so that

$$\bar{c}_v = \sum_s x_s \hat{c}_{v,s} \quad \left[\text{J mol}^{-1}\,\text{K}^{-1}\right]. \tag{3.43}$$

Thus for a mixture of monatomic species with H_2 the ratio of specific heats is

$$\gamma = \frac{x_{H_2}\left(\frac{7}{2} + \zeta\right) + \frac{5}{2}\left(1 - x_{H_2}\right)}{x_{H_2}\left(\frac{5}{2} + \zeta\right) + \frac{3}{2}\left(1 - x_{H_2}\right)}, \tag{3.44}$$

where x_{H_2} is the mole fraction of H_2 and ζ is the vibrational specific heat of H_2 as given in equation 3.41.

3.5 Electric Potential Equation

The electric potential equation can be derived utilizing the species momentum equation (Equation 3.13) and Maxwell's equations. By summing over all species and using the definition of current density (Equation 3.34) and electrical conductivity (cf. Section 3.10.5), the generalized Ohm's law for a partially ionized, collision-dominated gas may be obtained [86]:

$$\sigma\left(\vec{E}+\vec{u}\times\vec{B}+\frac{\nabla p_e}{en_e}\right)=\vec{J}+\beta_e\vec{J}\times\vec{b}+s\vec{b}\times\left(\vec{J}\times\vec{b}\right), \tag{3.45}$$

where $\vec{b}=\frac{\vec{B}}{B}$ and ∇p_e is the electron pressure gradient. In this equation, the definitions of electron Hall parameter,

$$\beta_e=\frac{eB}{m_e\sum_r\overline{\nu}_{er}}, \tag{3.46}$$

ion Hall parameter,

$$\beta_i=\frac{q_iB}{m_{in}\sum_r\overline{\nu}_{ir}}, \tag{3.47}$$

and ion slip factor,

$$s=\left(\frac{\rho_n}{\rho}\right)^2\beta_e\beta_i, \tag{3.48}$$

have been used; where q_i is the ion charge magnitude, $m_{in}=\frac{m_im_n}{m_i+m_n}$ is the reduced mass of an ion and a neutral, and ρ_n is the total density of the neutral species. Assuming that only electrons carry the current is a good assumption in collision-dominated plasmas, and neglecting the magnetic field the generalized Ohm's law simplifies to

$$\vec{J}=\sigma\vec{E}+\psi\nabla p_e, \tag{3.49}$$

where

$$\psi=\frac{\sigma}{en_e}=\frac{e}{m_e\sum_r\overline{\nu}_{er}} \tag{3.50}$$

is the electron mobility.

Since the plasma is macroscopically neutral and the self-induced magnetic field is negligible, Maxwell's equations reduce to $\nabla\cdot\vec{E}=0$ and $\nabla\times\vec{E}=0$. Therefore, the electric field vector may be written as the gradient of a scalar potential:

$$\vec{E}=-\nabla\phi. \tag{3.51}$$

In addition, $\nabla \cdot \vec{J} = 0$ due to charge conservation. Inserting Equation 3.51 into Equation 3.49, and noting that the divergence of the current density is zero, we obtain the electric potential equation:

$$\nabla \cdot (\sigma \nabla \phi - \psi \nabla p_e) = 0. \tag{3.52}$$

Written in a cylindrical coordinate system, and neglecting azimuthal gradients, the potential equation is found to be

$$\frac{1}{r}\frac{\partial}{\partial r}\left(r\sigma\frac{\partial \phi}{\partial r}\right) + \frac{\partial}{\partial z}\left(\sigma\frac{\partial \phi}{\partial z}\right) = \frac{1}{r}\frac{\partial}{\partial r}\left(r\psi\frac{\partial p_e}{\partial r}\right) + \frac{\partial}{\partial z}\left(\psi\frac{\partial p_e}{\partial z}\right). \tag{3.53}$$

3.6 Mass Conservation Equations

Using Equation 3.7, the species mass conservation equation can be written as

$$\frac{\partial \rho_s}{\partial t} + \nabla \cdot (\rho_s \vec{u}_s) = m_s \dot{n}_s \tag{3.54}$$

where $\dot{n}_s$ represents the net rate of production of species s per unit volume. In axisymmetric coordinates, the species mass conservation equation becomes

$$\frac{\partial \rho_s}{\partial t} + \frac{\partial \rho_s u_{sr}}{\partial r} + \frac{\rho_s u_{sr}}{r} + \frac{\partial \rho_s u_{sz}}{\partial z} = m_s \dot{n}_s, \tag{3.55}$$

where $u_{sr} = u_r + V_{sr}$ and $u_{sz} = u_z + V_{sz}$. The diffusion velocities are calculated as in Section 3.10.2.

In the seeded arcjet modelling hydrogen was chosen as the buffer gas due to its low weight hence high specific impulse, and cesium was chosen as the seed due to its low ionization potential and good electrical conductivity at low temperatures. The code should be reasonably easy to alter to model other diatomic buffer and atomic seed combinations such as nitrogen with potassium. In the three fluid model the cesium was initially predicted to be all but fully ionized within the thruster so only cesium ions were modelled, although cesium atoms were later included in the two fluid model. For hydrogen the species H_2, H, and H^+ were to be accounted for, with H^-, H_2^+ and more exotic species ignored. Electrons, of course, were also modelled.

The species mass conservation equations which characterize the flow are then

$$\frac{\partial \rho_{H_2}}{\partial t} + \nabla \cdot (\rho_{H_2} \vec{u}_{H_2}) = -m_H \left(\dot{n}_H + k_d^e n_e n_{H_2}\right) \tag{3.56}$$

$$\frac{\partial \rho_H}{\partial t} + \nabla \cdot (\rho_H \vec{u}_H) = m_H \left(\dot{n}_H + k_d^e n_e n_{H_2} - \dot{n}_{H^+}\right) \tag{3.57}$$

$$\frac{\partial \rho_{H^+}}{\partial t} + \nabla \cdot (\rho_{H^+} \vec{u}_{H_+}) = m_H \dot{n}_{H^+} \tag{3.58}$$

$$\frac{\partial \rho_{Cs}}{\partial t} + \nabla \cdot (\rho_{Cs} \vec{u}_{Cs}) = -m_{Cs} \dot{n}_{Cs^+} \tag{3.59}$$

$$\frac{\partial \rho_{Cs^+}}{\partial t} + \nabla \cdot (\rho_{Cs^+} \vec{u}_{Cs_+}) = m_{Cs} \dot{n}_{Cs^+} \tag{3.60}$$

$$\frac{\partial \rho_e}{\partial t} + \nabla \cdot (\rho_e \vec{u}_e) = m_e \left(\dot{n}_{H^+} + \dot{n}_{Cs^+}\right). \tag{3.61}$$

The current density does not appear in the electron equation, since $\nabla \cdot \vec{J} = 0$. In the above equations, $\dot{n}_H$ represents the net rate of production of monatomic neutrals per unit volume by heavy species dissociating collisions, and $k_d^e n_e n_{S_2}$ represents the rate of production of atomic species per unit volume by electron impact dissociation. $\dot{n}_{H^+}$ and $\dot{n}_{Cs^+}$ represent the production of hydrogen ions and cesium ions per unit volume through inelastic collisions. Whilst the dissociation process is modelled by including electron impact dissociation of the molecules in addition to dissociation and recombination due to collisions between the heavy species, the probability of an electron colliding with a molecule, dissociating it, and at the same time ionizing one or both of the resulting atoms is assumed to be much smaller than the probability of two separate collisions causing dissociation then ionization.

Summing over all species to obtain a global fluid, the source terms of the species equations cancel giving the global mass conservation equation,

$$\frac{\partial \rho}{\partial t} + \nabla \cdot (\rho \vec{u}) = 0, \tag{3.62}$$

which in axisymmetric coordinates is,

$$\frac{\partial \rho}{\partial t} + \frac{\partial \rho u_r}{\partial r} + \frac{\rho u_r}{r} + \frac{\partial \rho u_z}{\partial z} = 0. \tag{3.63}$$

Since quasi-neutrality is assumed, this can take the place of one equation and the global

equation can also be used in place of one of the species equations. To fully determine the composition of the flow quasineutrality, the global equation, two hydrogen species and both cesium species equation were used.

3.7 Momentum Conservation Equations

With a two fluid model the momentum equations for the heavy species and the electrons could either be modelled completely separately or a global equation could replace one. Since the electron velocities will be determined largely by the applied electric field and thus the electric potential equation, to remove as many sources of interaction as possible a global momentum equation was used in place of just a heavy species equation. Summing equation 3.12 over all species and utilizing the definitions of the global density, mass averaged velocity, and pressure, the global momentum conservation equation results. The collision terms on the right hand side all cancel, and due to quasineutrality the electric field source terms also cancel.

$$\frac{\partial}{\partial t}\left(\rho\vec{u}\right) + \nabla\cdot\left(\rho\vec{u}\vec{u}\right) + \nabla\cdot\bar{\bar{p}} = 0 \tag{3.64}$$

Separating out the viscous stress tensor (cf. Equation 3.32) and expanding the vectors the global momentum conservation equations can be written as

$$\frac{\partial}{\partial t}\left(\rho u_r\right) + \frac{\partial}{\partial r}\left(\rho u_r^2 + p - \tau_{rr}\right) + \frac{\partial}{\partial z}\left(\rho u_r u_z - \tau_{rz}\right) + \frac{1}{r}\left(\rho u_r^2 - \rho u_\theta^2 - \tau_{rr} + \tau_{\theta\theta}\right) = 0 \tag{3.65}$$

$$\frac{\partial}{\partial t}\left(\rho u_\theta\right) + \frac{\partial}{\partial r}\left(\rho u_r u_\theta - \tau_{r\theta}\right) + \frac{\partial}{\partial z}\left(\rho u_\theta u_z - \tau_{\theta z}\right) + \frac{2}{r}\left(\rho u_r u_\theta - \tau_{r\theta}\right) = 0 \tag{3.66}$$

$$\frac{\partial}{\partial t}\left(\rho u_z\right) + \frac{\partial}{\partial r}\left(\rho u_r u_z - \tau_{rz}\right) + \frac{\partial}{\partial z}\left(\rho u_z^2 + p - \tau_{zz}\right) + \frac{1}{r}\left(\rho u_r u_z - \tau_{rz}\right) = 0, \tag{3.67}$$

where the viscous stress terms in cylindrical coordinates are given by Thompson [127], and the azimuthal gradient terms have been neglected for the axisymmetric formulation.

$$\tau_{rr} = \frac{2}{3}\mu_g\left(2\frac{\partial u_r}{\partial r} - \frac{\partial u_z}{\partial z} - \frac{u_r}{r}\right) \tag{3.68}$$

$$\tau_{\theta\theta} = \frac{2}{3}\mu_g\left(2\frac{u_r}{r} - \frac{\partial u_r}{\partial r} - \frac{\partial u_z}{\partial z}\right) \tag{3.69}$$

$$\tau_{zz} = \frac{2}{3}\mu_g\left(2\frac{\partial u_z}{\partial z} - \frac{\partial u_r}{\partial r} - \frac{u_r}{r}\right) \tag{3.70}$$

$$\tau_{r\theta} = \mu_g \left(\frac{\partial u_\theta}{\partial r} - \frac{u_\theta}{r} \right) \tag{3.71}$$

$$\tau_{rz} = \mu_g \left(\frac{\partial u_r}{\partial z} + \frac{\partial u_z}{\partial r} \right) \tag{3.72}$$

$$\tau_{\theta z} = \mu_g \frac{\partial u_\theta}{\partial z}. \tag{3.73}$$

In calculating the viscosity the electron viscosity is assumed to be negligible [27, 86] and the heavy species viscosity coefficient, μ_g, will be derived later in Section 3.10.3.

3.8 Energy Conservation Equations

Since the gas within an arcjet is collision dominated, it is assumed that all of the heavy species (molecules, atoms, ions) have a common translational temperature, and that the molecular vibrational and rotational temperatures are in thermal equilibrium with this translational temperature. Consequently the heavy species can be modelled by a single energy equation. The electrons are known to have a temperature that may be significantly larger than the heavy species temperature [85] in certain regions of an arcjet such as where the arc attaches to an electrode. To accurately model arcjet physics the electrons must be modelled with their own temperature hence they require their own energy equation.

Heavy Species

The conservation equations for the heavy species are found by summing Equation 3.20 over all the heavy species. Separating out the viscous stress tensor, the species energy conservation equations can be written as

$$\frac{\partial}{\partial t}(\rho_{H_2} E_{H_2}) + \nabla \cdot (\rho_{H_2} H_{H_2} \vec{u}_{H_2}) + \nabla \cdot (\overline{\overline{\tau}}_{H_2} \cdot \vec{u}_{H_2}) - \nabla \cdot (\kappa_{H_2} \nabla T_g) = M_{H_2} \tag{3.74}$$

$$\frac{\partial}{\partial t}(\rho_H E_H) + \nabla \cdot (\rho_H H_H \vec{u}_H) + \nabla \cdot (\overline{\overline{\tau}}_H \cdot \vec{u}_H) - \nabla \cdot (\kappa_H \nabla T_g) = M_H \tag{3.75}$$

$$\frac{\partial}{\partial t}(\rho_{H+} E_{H+}) + \nabla \cdot (\rho_{H+} H_{H+} \vec{u}_{H+}) + \nabla \cdot (\overline{\overline{\tau}}_{H+} \cdot \vec{u}_{H+}) - \nabla \cdot (\kappa_{H+} \nabla T_g) = \vec{J}_{H+} \cdot \vec{E} + M_{H+} \tag{3.76}$$

$$\frac{\partial}{\partial t}(\rho_{Cs} E_{Cs}) + \nabla \cdot (\rho_{Cs} H_{Cs} \vec{u}_{Cs}) + \nabla \cdot (\overline{\overline{\tau}}_{Cs} \cdot \vec{u}_{Cs}) - \nabla \cdot (\kappa_{Cs} \nabla T_g) = M_{Cs} \tag{3.77}$$

$$\frac{\partial}{\partial t}(\rho_{Cs+} E_{Cs+}) + \nabla \cdot (\rho_{Cs+} H_{Cs+} \vec{u}_{Cs+}) + \nabla \cdot (\overline{\overline{\tau}}_{Cs+} \cdot \vec{u}_{Cs+}) - \nabla \cdot (\kappa_{Cs+} \nabla T_g) = \vec{J}_{Cs+} \cdot \vec{E} + M_{Cs+} \tag{3.78}$$

where T_g is the temperature common to all heavy species, and H_s is the total enthalpy per unit mass of species s given by $H_s = E_s + \frac{p_s}{\rho_s}$.

The total enthalpy H_s, of each species, and hence the total energy, is determined by the number of degrees of freedom that the species possesses. For an ideal gas with only translational energy, it will have three degrees of freedom corresponding to the three possible mutually perpendicular directions of motion in space. For molecules energy is also present in internal modes such as vibration and rotation, which may or may not be frozen out. [63] Finally, the energies of dissociation and ionization must also be taken into account. For this model, the energy of dissociation is arbitrarily assigned to the neutral atoms and the ionization energy is arbitrarily bound to the electrons.

The enthalpy per particle for the different species is found to be

$$h_{H_2} = \frac{7}{2}kT_g - e_d + \frac{e_v}{e^{\frac{e_v}{kT_g}} - 1} + \Delta \tag{3.79}$$

for molecules, and

$$h_H = h_{H+} = \frac{5}{2}kT_g + \frac{\Delta}{2} \tag{3.80}$$

for the hydrogen atoms and ions, and

$$h_{Cs} = h_{Cs+} = \frac{5}{2}kT_g \tag{3.81}$$

for the cesium atoms and ions. where e_d and e_v are energies of dissociation and vibration, respectively, and Δ is a constant chosen to make the enthalpy of the H_2 molecule zero at the common reference temperature, $T_f = 298.15$ K. The $\frac{7}{2}$ fraction for the diatomic species accounts for translation ($\frac{3}{2}kT$), rotation (kT), and pressure work (kT). There is no rotational energy associated with the atomic species and the ions, hence the $\frac{5}{2}$ coefficient (translation and pressure work only) in equations 3.80 and 3.81. For gases such as H_2 or N_2 the vibrational energy is negligible at the reference temperature, so $\Delta = e_d - \frac{7}{2}kT_f$. Therefore

$$h_{H_2} = \frac{7}{2}k\left(T_g - T_f\right) + \frac{e_v}{e^{\frac{e_v}{kT_g}} - 1} \tag{3.82}$$

for molecules, and

$$h_H = h_{H+} = \frac{5}{2}kT_g + \frac{1}{2}e_d - \frac{7}{4}kT_f \tag{3.83}$$

for the hydrogen atoms and ions, and

$$h_{Cs} = h_{Cs+} = \frac{5}{2}kT_g \tag{3.84}$$

for the cesium atoms and ions. The energy per particle is given as $e_s = h_s - kT_g$.

The total enthalpy and energy per unit volume can then be defined as

$$\rho H = \sum_s n_s h_s + \sum_s \frac{1}{2}\rho_s u_s^2 \tag{3.85}$$

so

$$\begin{aligned}\rho H = &\frac{5}{2}\left(\rho_H + \rho_{H+}\right) R_H T_g + \frac{5}{2}\left(\rho_{Cs} + \rho_{Cs+}\right) R_{Cs} T_g + \frac{7}{2}\rho_{H_2} R_{H_2} T_g + \frac{1}{2}\left(\rho_H + \rho_{H+}\right) R_H \theta_d \\ &+ \frac{\rho_{H_2} R_{H_2} \theta_v}{e^{\frac{\theta_v}{T_g}} - 1} - \frac{7}{2}\rho_{H_2} R_{H_2} T_f - \frac{7}{4}\left(\rho_H + \rho_{H+}\right) R_H T_f - \frac{7}{4}\left(\rho_{Cs} + \rho_{Cs+}\right) R_{Cs} T_f \\ &+ \frac{1}{2}\rho_{H_2} u_{H_2}^2 + \frac{1}{2}\rho_H u_H^2 + \frac{1}{2}\rho_{H+} u_{H+}^2 + \frac{1}{2}\rho_{Cs} u_{Cs}^2 + \frac{1}{2}\rho_{Cs+} u_{Cs+}^2\end{aligned} \tag{3.86}$$

where it should also be noted that

$$\rho E = \rho H - \rho_{H_2} R_{H_2} T_g - \left(\rho_H + \rho_{H+}\right) R_H T_g - \left(\rho_{Cs} + \rho_{HCs+}\right) R_{Cs} T_g, \tag{3.87}$$

where $\theta_d = \frac{e_d}{k}$ and $\theta_v = \frac{e_v}{k}$ are the characteristic temperatures of dissociation and vibration, respectively.

Summing the heavy species energy equations 3.74-3.78 the total heavy species energy equation will be given as

$$\begin{aligned}\frac{\partial}{\partial t}\left(\sum_s \rho_s E_s\right) + \nabla \cdot \left(\sum_s \rho_s \vec{u}_s E_s\right) + \nabla \cdot \left(\sum_s \overline{\overline{P}}_s \cdot \vec{u}_s\right) - \nabla \cdot \left(\kappa_g \nabla T_g\right) \\ = \vec{J}_{H+} + \vec{J}_{Cs+} + \sum_s M_s\end{aligned} \tag{3.88}$$

where κ_g is an overall heavy species conductivity, to be derived in Section 3.10.4.

Since the sum of the collision over all species including electrons is zero, $M_{H_2} + M_H + M_{H+} + M_{Cs} + M_{Cs+} + M_e = 0$ the sum over the heavy species must be equal to minus the electron collisional energy transfer rate per unit volume.

Electrons are much lighter and more mobile than ions so most of the current is conducted

by the electrons, and consequently the ion current density $\vec{J}$ is small compared to the other terms and can be neglected.

Defining the total energy as $\rho E = \sum_s \rho_s E_s$ and using the definition of slip velocity (Equation 3.27), and also expanding the pressure tensor as $\overline{\overline{p}}_s = p_s \overline{\overline{I}} - \overline{\overline{\tau}}_s$ (Equation 3.31) we obtain the **Strong Conservative Form** of the energy equation.

$$\frac{\partial}{\partial t}(\rho E) + \nabla \cdot (\rho E \vec{u}) + \nabla \cdot \left(\sum_s \rho_s E_s \vec{V}_s \right) + \nabla \cdot (P\vec{u}) - \nabla \cdot (\overline{\overline{\tau}} \cdot \vec{u})$$

$$+\nabla \cdot \left(\sum_s P_s \vec{V}_s \right) - \nabla \cdot \left(\sum_s \overline{\overline{\tau}}_s \cdot \vec{V}_s \right) - \nabla \cdot (\kappa_g \nabla T_g) = -M_e \tag{3.89}$$

where E_s, the total energy of the species, is the sum of the thermal and internal energies with the kinetic energy: $E = e + \frac{u^2}{2}$.

It should be noted that the dissipation due to species diffusive slip ($\nabla \cdot (\overline{\overline{\tau}}_s \cdot \vec{V}_s)$) will be negligible compared to the dissipation due to the bulk motion. As found by Miller [85], the strong conservative form of the energy equation, Equation 3.89, is not appropriate for the arcjet simulation. In certain regions of the flow the dissociation energy dominates the total energy whilst in other regions the kinetic energy dominates. The combined effect leads to a situation where the gas temperature is indeterminate or becomes negative in certain regions of the flow. To overcome this difficulty, Miller uses the internal energy form of the energy equation. In this form, the kinetic energy terms are eliminated by utilizing the species mass and momentum conservation equations. The terms which include the dissociation energy can be moved to the right hand side of the equation as a single source term. This modified heavy species energy equation is not strongly conservative, but is accurate as long as the flow is free of shocks and other discontinuities.

Separating out the dissociation and kinetic energy terms, define a new internal energy e from the total energy E as

$$\rho E = \rho e + \frac{1}{2}(\rho_H + \rho_{H+}) R_H \Theta_d + \sum_s \frac{1}{2} \rho_s u_s^2 \tag{3.90}$$

and *REDEFINE* the species energies as

$$e_{H_2} = \frac{5}{2} R_{H_2} T_g - \frac{7}{2} R_{H_2} T_f + \frac{R_{H_2} \theta_v}{e^{\frac{\theta_v}{T_g}} - 1} \tag{3.91}$$

$$e_H = e_{H+} = \frac{3}{2} R_H T_g - \frac{7}{4} R_H T_f \tag{3.92}$$

$$e_{Cs} = e_{Cs+} = \frac{3}{2} R_{Cs} T_g. \tag{3.93}$$

Note the absence of a dissociation term in the hydrogen atom and ion energies.

The strong conservative energy equation can now be expanded as

$$\begin{aligned}
&\frac{\partial}{\partial t}\left(\rho e + \frac{1}{2}\left(\rho_H + \rho_{H+}\right) R_H \Theta_d + \sum_s \frac{1}{2}\rho_s u_s^2\right) \\
&+\nabla\cdot\left(\left(\rho e + \frac{1}{2}\left(\rho_H + \rho_{H+}\right) R_H \Theta_d + \sum_s \frac{1}{2}\rho_s u_s^2\right)\vec{u}\right) \\
&+\nabla\cdot\left(\left(\rho_{H_2} e_{H_2} + \frac{1}{2}\rho_{H_2} u_{H_2}^2\right)\vec{V}_{H_2}\right) \\
&+\nabla\cdot\left(\left(\rho_H e_H + \frac{1}{2}\rho_H u_H^2 + \frac{1}{2}\rho_H R_H \Theta_d\right)\vec{V}_H\right) \\
&+\nabla\cdot\left(\left(\rho_{H+} e_{H+} + \frac{1}{2}\rho_{H+} u_{H+}^2 + \frac{1}{2}\rho_{H+} R_{H+} \Theta_d\right)\vec{V}_{H+}\right) \\
&+\nabla\cdot\left(\left(\rho_{Cs} e_{Cs} + \frac{1}{2}\rho_{Cs} u_{Cs}^2\right)\vec{V}_{Cs} + \left(\rho_{Cs+} e_{Cs+} + \frac{1}{2}\rho_{Cs+} u_{Cs+}^2\right)\vec{V}_{Cs+}\right) \\
&+\nabla\cdot\left(P\vec{u}\right) - \nabla\cdot\left(\overline{\overline{\tau}}\cdot\vec{u}\right) + \nabla\cdot\left(\sum_s P_s \vec{V}_s\right) \\
&-\nabla\cdot\left(\kappa_g \nabla T_g\right) = -M_e.
\end{aligned} \tag{3.94}$$

First consider the terms involving the dissociation energy which sum to

$$\frac{1}{2} R_H \Theta_d \left(\frac{\partial}{\partial t}\left(\rho_H + \rho_{H+}\right) + \nabla\cdot\left(\rho_H \vec{u}_H + \rho_{H+}\vec{u}_{H+}\right)\right).$$

From continuity this is

$$\frac{1}{2} R_H \Theta_d m_H \left(\dot{n}_H + k_d^e n_e n_{H_2}\right)$$

which can be moved to the right hand side of the conservation equation.

Now consider the kinetic energy terms which sum to

$$\sum_s \left(\frac{\partial}{\partial t}\left(\frac{1}{2}\rho_s u_s^2\right) + \nabla\cdot\left(\frac{1}{2}\rho_s u_s^2 \vec{u}_s\right)\right)$$

which is the equation for the rate of change of kinetic energy. This can be derived by

multiplying the species momentum equations 3.12 by $\vec{u}$:

$$\vec{u}_s \cdot \frac{\partial}{\partial t}\left(\rho_s \vec{u}_s\right) + \vec{u}_s \cdot \nabla\left(\rho_s \vec{u}_s \vec{u}_s\right) + \vec{u}_s \cdot \left(\nabla \cdot \overline{\overline{P}}_s\right) = \vec{u}_s \rho_s \sum_s \overline{\nu}_{sr}\left(\vec{u}_r - \vec{u}_s\right) \tag{3.95}$$

which can be rewritten as

$$\frac{\partial}{\partial t}\left(\frac{1}{2}\rho_s u_s^2\right) + \nabla\left(\frac{1}{2}\rho_s u_s^2 \vec{u}_s\right)$$

$$= \vec{u}_s \cdot \rho_s \sum_s \overline{\nu}_{sr}\left(\vec{u}_r - \vec{u}_s\right) - \vec{u}_s \cdot \left(\nabla \cdot \overline{\overline{P}}_s\right) - \frac{1}{2}u_s^2\left(\frac{\partial \rho_s}{\partial t} + \nabla \cdot \left(\rho_s \vec{u}_s\right)\right). \tag{3.96}$$

To obtain the total kinetic energy the species kinetic energies need to be summed. Neglecting the kinetic energy transfer by collisions with electrons the remaining collisional transfer terms will sum to zero thereby eliminating that term. Summing the final term and neglecting the slip velocities and the electron mass this results in $\frac{1}{2}u^2\left(\frac{\partial \rho}{\partial t} + \nabla \cdot \left(\rho \vec{u}\right)\right)$ which by continuity is zero. Thus the desired equation for kinetic energy conservation is

$$\sum_s \left(\frac{\partial}{\partial t}\left(\frac{1}{2}\rho_s u_s^2\right) + \nabla\left(\frac{1}{2}\rho_s u_s^2 \vec{u}_s\right)\right) = -\sum_s \vec{u_s} \cdot \left(\nabla \cdot \overline{\overline{P}}_s\right) \tag{3.97}$$

so with the new definitions of energy for each species, the energy conservation equation becomes

$$\frac{\partial}{\partial t}\left(\rho e\right) + \nabla \cdot \left(\rho e \vec{u}\right) + \nabla \cdot \left(\sum_s \rho_s e_s \vec{V}_s\right) + \nabla \cdot \left(P\vec{u}\right) - \nabla \cdot \left(\overline{\overline{\tau}} \cdot \vec{u}\right) + \nabla \cdot \left(\sum_s P_s \vec{V}_s\right) - \sum_s \vec{u}_s \cdot \left(\nabla \cdot \overline{\overline{P}}_s\right)$$

$$-\nabla \cdot \left(\kappa_g \nabla T_g\right) = -M_e - \frac{1}{2}R_H \Theta_d m_H\left(\dot{n}_H + k_d^e n_e n_{H_2}\right). \tag{3.98}$$

Expanding $\overline{\overline{P}}_s$ and making use of the definition of enthalpy this can be simplified to

$$\frac{\partial}{\partial t}\left(\rho e\right) + \nabla \cdot \left(\rho h \vec{u}\right) + \nabla \cdot \left(\sum_s \rho_s h_s \vec{V}_s\right) - \vec{u} \cdot \nabla P - \sum_s \vec{V}_s \cdot \nabla P_s - \nabla \cdot \left(\overline{\overline{\tau}} \cdot \vec{u}\right) + \vec{u} \cdot \left(\nabla \cdot \overline{\overline{\tau}}\right)$$

$$-\nabla \cdot \left(\kappa_g \nabla T_g\right) = -M_e - \frac{1}{2}R_H \Theta_d m_H\left(\dot{n}_H + k_d^e n_e n_{H_2}\right). \tag{3.99}$$

Finally, the viscous dissipation terms can be combined as $-\left(\overline{\overline{\tau}} \cdot \nabla\right) \cdot \vec{u}$ giving the

Internal Energy Form of the energy equation.

$$\frac{\partial}{\partial t}(\rho e) + \nabla \cdot (\rho h \vec{u}) + \nabla \cdot \left(\sum_s \rho_s h_s \vec{V}_s \right) - \vec{u} \cdot \nabla P - \sum_s \vec{V}_s \cdot \nabla P_s - (\overline{\overline{\tau}} \cdot \nabla) \cdot \vec{u}$$

$$-\nabla \cdot (\kappa_g \nabla T_g) = -M_e - \frac{1}{2} R_H \Theta_d m_H \left(\dot{n}_H + k_d^e n_e n_{H_2} \right) \tag{3.100}$$

Expanding this with axisymmetric cylindrical coordinates, letting $\vec{q} = -\kappa_g \nabla T_g$, and also expanding the stress tensor gives the equation to be discretised.

$$\frac{\partial}{\partial t}(\rho e_g) + \frac{\partial}{\partial r}(\rho h_g u_r + q_{gr}) + \frac{1}{r}(\rho h_g u_r + q_{gr}) + \frac{\partial}{\partial z}(\rho h_g u_z + q_{gz}) - u_r \frac{\partial p_g}{\partial r} - u_z \frac{\partial p_g}{\partial z}$$

$$+\frac{\partial}{\partial r}(\rho_{H_2} h_{H_2} V_{H_2 r} + \rho_H h_H V_{Hr} + \rho_{H+} h_{H+} V_{H+r} + \rho_{Cs} h_{Cs} V_{Csr} + \rho_{Cs+} h_{Cs+} V_{Cs+r})$$

$$+\frac{1}{r}(\rho_{H_2} h_{H_2} V_{H_2 r} + \rho_H h_H V_{Hr} + \rho_{H+} h_{H+} V_{H+r} + \rho_{Cs} h_{Cs} V_{Csr} + \rho_{Cs+} h_{Cs+} V_{Cs+r})$$

$$+\frac{\partial}{\partial z}(\rho_{H_2} h_{H_2} V_{H_2 z} + \rho_H h_H V_{Hz} + \rho_{H+} h_{H+} V_{H+z} + \rho_{Cs} h_{Cs} V_{Csz} + \rho_{Cs+} h_{Cs+} V_{Cs+z})$$

$$-V_{H_2 r} \frac{\partial p_{H_2}}{\partial r} - V_{Hr} \frac{\partial p_H}{\partial r} - V_{H+r} \frac{\partial p_{H+}}{\partial r} - V_{Csr} \frac{\partial p_{Cs}}{\partial r} - V_{Cs+r} \frac{\partial p_{Cs+}}{\partial r}$$

$$-V_{H_2 z} \frac{\partial p_{H_2}}{\partial z} - V_{Hz} \frac{\partial p_H}{\partial z} - V_{H+z} \frac{\partial p_{H+}}{\partial z} - V_{Csz} \frac{\partial p_{Cs}}{\partial z} - V_{Cs+z} \frac{\partial p_{Cs+}}{\partial z}$$

$$= \Phi - M_e - \frac{1}{2} e_d \left(\dot{n}_H + k_d^e n_e n_{H_2} \right), \tag{3.101}$$

where

$$\Phi = \mu_g \left[2 \left(\frac{\partial u_r}{\partial r} \right)^2 + 2 \left(\frac{\partial u_z}{\partial z} \right)^2 + 2 \left(\frac{u_r}{r} \right)^2 + \left(\frac{\partial u_r}{\partial z} + \frac{\partial u_z}{\partial r} \right)^2 \right.$$

$$\left. + \left(\frac{\partial u_\theta}{\partial r} - \frac{u_\theta}{r} \right)^2 + \left(\frac{\partial u_\theta}{\partial z} \right)^2 - \frac{2}{3} \left(\frac{\partial u_r}{\partial r} + \frac{\partial u_z}{\partial z} + \frac{u_r}{r} \right)^2 \right] \tag{3.102}$$

is the viscous dissipation term. In summary the enthalpies and energies are

$$\rho e_g = \frac{3}{2}(\rho_H + \rho_{H+}) R_H T_g + \frac{3}{2}(\rho_{Cs} + \rho_{Cs+}) R_{Cs} T_g + \frac{5}{2} \rho_{H_2} R_{H_2} T_g$$

$$+\frac{\rho_{H_2} R_{H_2} \theta_v}{e^{\frac{\theta_v}{T_g}} - 1} - \frac{7}{4}(\rho_H + \rho_{H+} + \rho_{H_2}) R_H T_g \tag{3.103}$$

$$e_{H_2} = \frac{5}{2} R_{H_2} T_g - \frac{7}{2} R_{H_2} T_f + \frac{R_{H_2} \theta_v}{e^{\frac{\theta_v}{T_g}} - 1} \tag{3.104}$$

$$e_H = e_{H+} = \frac{3}{2} R_H T_g - \frac{7}{4} R_H T_f \tag{3.105}$$

$$e_{Cs} = e_{Cs+} = \frac{3}{2} R_{Cs} T_g \tag{3.106}$$

$$\rho h_g = \rho e_g + \rho_{H_2} R_{H_2} T_g + (\rho_H + \rho_{H+}) R_H T_g + (\rho_{Cs} + \rho_{Cs+}) R_{Cs} T_g \tag{3.107}$$

$$h_s = e_s + R_s T_g = e_s + \frac{P_s}{\rho_s}. \tag{3.108}$$

As a final note on the heavy energy equation the electron collision term should be expanded from equation 3.31. The term due to temperature differences is of order $\frac{1}{m_H}$ whereas the term due to kinetic energy differences is of order 1 and since $m_H \ll 1$ the kinetic energy differences may be neglected. The theory behind the collisional energy transfer rate assumes elastic collisions which is very good for collisions between electrons or atoms, but needs correcting when molecules are involved since energy may be transfered to internal modes such as vibration or rotation. The correction is easily accomplished with an inelastic correction factor δ so

$$\begin{aligned} M_e &= 3k\left(T_g - T_e\right) \frac{\rho_e}{m_H} \left(\overline{\nu}_{eH+} + \overline{\nu}_{eH} + \frac{1}{2} \delta_{H_2} \overline{\nu}_{eH_2} \right) + 3k\left(T_g - T_e\right) \frac{\rho_e}{m_{Cs}} \left(\overline{\nu}_{eCs+} + \overline{\nu}_{eCs} \right) \\ &= \frac{m_e}{m_H} 3k\left(T_g - T_e\right) n_e \left(n_{H_2} \overline{c}_e Q_{eH_2} \frac{\delta_{H_2}}{2} + n_H \overline{c}_e Q_{eH} + n_{H+} \overline{c}_e Q_{eH+} \right) \\ &\quad + \frac{m_e}{m_{Cs}} 3k\left(T_g - T_e\right) n_e \left(n_{Cs} \overline{c}_e Q_{eCs} + n_{Cs+} \overline{c}_e Q_{eCs+} \right) \end{aligned} \tag{3.109}$$

where the collision frequency has been expanded and taking into account that electron random thermal velocities are much higher than heavy species thermal velocities, and that Q is the cross section

The inelastic collision correction factor δ_{H_2} is well known for a variety of molecules and is shown in Figure 3-2 for hydrogen and nitrogen where the data was taken from Sutton and Sherman [123]).

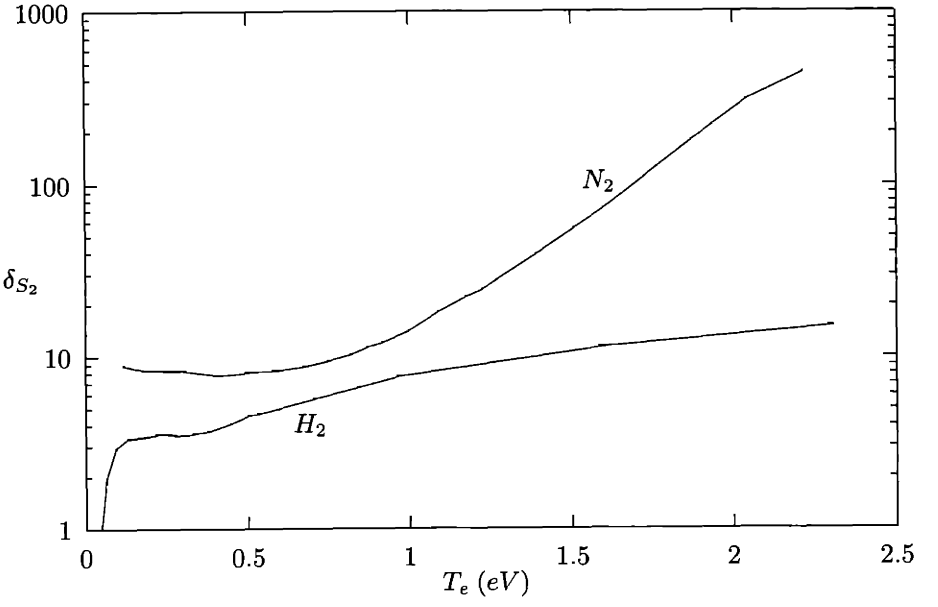

Figure 3-2: *Inelastic Correction Factor for Energy Transfer Between Electrons and Hydrogen and Nitrogen Molecules*

Electrons

Equation 3.20 written for the electrons is

$$\frac{\partial}{\partial t}\left(\rho_e E_e\right) + \nabla\cdot\left(\rho_e E_e \vec{u}_e\right) + \nabla\cdot\left(\overline{\overline{p}}_e\cdot\vec{u}_e\right) - \nabla\cdot\left(\kappa_e\nabla T_e\right) = \vec{J}_e\cdot\vec{E} + M_e. \tag{3.110}$$

Expanding the energy terms and including the ionization energy per particle, the electron energy conservation equation becomes

$$\frac{\partial}{\partial t}\left(\frac{3}{2}p_e + \frac{1}{2}\rho_e u_e^2 + \rho_e\frac{e_i}{m_e}\right) + \nabla\cdot\left(\frac{5}{2}p_e\vec{u}_e + \frac{1}{2}\rho_e u_e^2\vec{u}_e + \rho_e\frac{e_i}{m_e}\vec{u}_e\right) - \nabla\cdot\left(\kappa_e\nabla T_e\right)$$

$$= \frac{J^2}{\sigma} + M_e - e_d\, k_d^e\, n_e n_{S_2} - \dot{R}, \tag{3.111}$$

where viscous shear stress terms have been neglected. As in the heavy species energy equation, M_e represents the collisional energy transfer to the electrons from the heavy species. The energy lost per unit volume due to dissociation by electron impact is denoted by $e_d\, k_d^e\, n_e n_{S_2}$, and $\dot{R}$ represents energy lost per unit volume due to radiation. As with the heavy species energy conservation equation, it is advantageous to relegate the ionization energy term to the right hand side as a source term. Using the species mass conservation

equation applied to the electrons and the definitions of total species energy and enthalpy, Equation 3.111 becomes

$$\frac{\partial}{\partial t}\left(\rho_e E_e\right) + \frac{\partial}{\partial r}\left(\rho_e H_e u_{er} + q_{er}\right) + \frac{1}{r}\left(\rho_e u_{er} H_e + q_{er}\right) + \frac{\partial}{\partial z}\left(\rho_e H_e u_{ez} + q_{ez}\right)$$

$$= \frac{J^2}{\sigma} + M_e - e_d\, k_d^e\, n_e n_{S_2} - e_i \dot{n}_e - \dot{R}, \tag{3.112}$$

where

$$E_e = \frac{3}{2} R_e T_e + \frac{1}{2} u_e^2, \tag{3.113}$$

$$H_e = E_e + R_e T_e, \tag{3.114}$$

$$q_{er} = -\kappa_e \frac{\partial T_e}{\partial r} \quad \text{and} \quad q_{ez} = -\kappa_e \frac{\partial T_e}{\partial z}. \tag{3.115}$$

3.9 Dissociation and Ionization Processes

3.9.1 Overview

The equation for a general chemical reaction i with N_s species has the form

$$\sum_{j=1}^{N_s} \nu'_{ij} s_j \rightleftharpoons \sum_{j=1}^{N_s} \nu''_{ij} s_j, \tag{3.116}$$

where s_j is the j^{th} species, and ν'_{ij} and ν''_{ij} are the stoichiometric coefficients of species s_j of reaction i. The arrows ($\rightleftharpoons$) denote the ability of a reaction to proceed in the forward ($\rightharpoonup$) or backward ($\leftharpoondown$) direction. In general, the forward and backward reactions need not occur at the same rate, resulting in a net production or depletion of a species.

Experimental studies of chemical reactions [130] and simple kinetic theory assuming one step reactions (neglecting intermediate steps) imply that the rate of production of a species C is proportional to the product of the concentrations of the species from which C is produced. In other words, if a reaction is given by $aA + bB \rightarrow C$, then the production of C is governed by

$$\frac{d[C]}{dt} = k\,[A]^a\,[B]^b\,. \tag{3.117}$$

This form will be assumed for the reactions modelled in this thesis. In terms of molar concentrations, the net rate of production of species s_j for the *forward* reaction i is

$$\left(\frac{d\hat{n}_j}{dt}\right)_{f,i} = k_{f,i}\left(\nu''_{ij} - \nu'_{ij}\right)\prod_{j=1}^{N_s}\left(\hat{n}_j\right)^{\nu'_{ij}}, \tag{3.118}$$

while the net rate of production of species s_j for the *backward* reaction i is found to be

$$\left(\frac{d\hat{n}_j}{dt}\right)_{b,i} = k_{b,i}\left(\nu'_{ij} - \nu''_{ij}\right)\prod_{j=1}^{N_s}\left(\hat{n}_j\right)^{\nu''_{ij}}. \tag{3.119}$$

Adding Equations 3.118 and 3.119 and summing over all reactions N_r results in the total net rate of production of species s_j:

$$\frac{d\hat{n}_j}{dt} = \sum_{i=1}^{N_r}\left(\nu''_{ij} - \nu'_{ij}\right)\left[k_{f,i}\prod_{j=1}^{N_s}\left(\hat{n}_j\right)^{\nu'_{ij}} - k_{b,i}\prod_{j=1}^{N_s}\left(\hat{n}_j\right)^{\nu''_{ij}}\right]. \tag{3.120}$$

This equation can also be applied to partial pressures, p_j, and number densities, n_j, with

corresponding changes in the units of $k_{f,i}$ and $k_{b,i}$. Forward rate constants are usually of the form

$$k_{f,i} = A_i T^{n_{f,i}} \exp\left(-\frac{B_i}{\hat{R}T}\right), \tag{3.121}$$

where A_i, B_i and $n_{f,i}$ are constants obtained from curve fitting experimental data. This equation is known as the Arrhenius formula. The rate constants for the corresponding backward reaction sometimes have a simpler form,

$$k_{b,i} = C_i T^{n_{b,i}}. \tag{3.122}$$

In equilibrium, the net rate of production of all species over all reactions is zero, so each individual reaction has a net zero production rate, and Equation 3.120 yields

$$k_{f,i} \prod_{j=1}^{N_s} \left(\hat{n}_j^*\right)^{\nu'_{ij}} - k_{b,i} \prod_{j=1}^{N_s} \left(\hat{n}_j^*\right)^{\nu''_{ij}} = 0, \tag{3.123}$$

or

$$K_{c,i} \equiv \frac{k_{f,i}}{k_{b,i}} = \frac{\prod_{j=1}^{N_s} \left(\hat{n}_j^*\right)^{\nu''_{ij}}}{\prod_{j=1}^{N_s} \left(\hat{n}_j^*\right)^{\nu'_{ij}}}, \tag{3.124}$$

where $K_{c,i}$ is defined as the equilibrium constant of reaction i, and the asterisks (*) denote equilibrium quantities. From Equations 3.121 and 3.122 it can be seen that the equilibrium constant is a function of temperature only. Substituting Equation 3.124 into Equation 3.120 yields another form of the net production rate:

$$\frac{d\hat{n}_j}{dt} = \sum_{i=1}^{N_r} \left(\nu''_{ij} - \nu'_{ij}\right) k_{f,i} \left[\prod_{j=1}^{N_s} \left(\hat{n}_j\right)^{\nu'_{ij}} - \frac{1}{K_{c,i}} \prod_{j=1}^{N_s} \left(\hat{n}_j\right)^{\nu''_{ij}}\right]. \tag{3.125}$$

By using different versions of the ideal gas law, the equilibrium constant may be obtained in terms of partial pressures or number densities. With $p_j^* = \hat{n}_j^* \hat{R}T$ the equilibrium constant can be written as

$$K_{p,i} = \frac{\prod_{j=1}^{N_s} \left(p_j^*\right)^{\nu''_{ij}}}{\prod_{j=1}^{N_s} \left(p_j^*\right)^{\nu'_{ij}}} \tag{3.126}$$

with

$$K_{p,i} = \left(K_{c,i} \left(\hat{R}T\right)\right)^{\sum_{j=1}^{N_s} \left(\nu''_{ij} - \nu'_{ij}\right)}. \tag{3.127}$$

Alternatively, with $\hat{n}_j^* = n_j^*/N_A$, the equilibrium constant becomes

$$K_{n,i} = \frac{\prod_{j=1}^{N_s} \left(n_j^*\right)^{\nu_{ij}''}}{\prod_{j=1}^{N_s} \left(n_j^*\right)^{\nu_{ij}'}} \tag{3.128}$$

with

$$K_{n,i} = \left(K_{c,i}\left(N_A\right)\right)^{\sum_{j=1}^{N_s}\left(\nu_{ij}''-\nu_{ij}'\right)} = \left(K_{p,i}\left(kT\right)\right)^{\sum_{j=1}^{N_s}\left(\nu_{ij}'-\nu_{ij}''\right)} \tag{3.129}$$

where N_A is Avogadro's number and $\hat{R}$ is the universal gas constant.

The equilibrium constant may be found in tabulated data or from more theoretical arguments through the methods of statistical mechanics. Specifically, the equilibrium constant can be written in terms of partition functions, which indicate how the total energy of a population of particles may be partitioned over the various possible energy levels in which a particle can exist. For example, the number of particles of species a existing in an energy level l with energy ϵ_l is

$$\bar{N}_a^l = g_l \exp\left(-\frac{\epsilon_l + \mu_a}{kT}\right), \tag{3.130}$$

where μ_a is the chemical potential of species a and g_l is the degeneracy of level l, or the number of particles of type a populating level l at one time. The total number of particles of species a is simply

$$\bar{N}_a = \sum_l g_l \exp\left(-\frac{\epsilon_l + \mu_a}{kT}\right). \tag{3.131}$$

The sum on the right hand side of Equation 3.131 is known as the partition function of species a, denoted by Q_a.

The total partition function is expressible as the product of individual partition functions for each independent mode in which energy can be stored. For example, the partition function of a species a with translational, rotational, vibrational, and electronic excitation energies can be written as

$$Q_a = Q_{a,tr} Q_{a,rot} Q_{a,vib} Q_{a,el}. \tag{3.132}$$

For diatomic molecules, these partition functions are given as

$$Q_{a,tr} = V\left(\frac{2\pi m_a kT}{h^2}\right)^{\frac{3}{2}} \tag{3.133}$$

$$Q_{a,rot} = \frac{1}{\sigma}\left(\frac{T}{\theta_r}\right) \tag{3.134}$$

$$Q_{a,vib} = \frac{1}{1 - e^{\theta_v/T}} \tag{3.135}$$

$$Q_{a,el} = \sum_m g_m e^{-\epsilon_m/kT} \tag{3.136}$$

for translation, rotation, vibration, end electronic excitation, respectively; where V is the volume, $h = 6.6261 \times 10^{-34}\ J\ s^{-1}$ is Planck's constant, σ is a molecular symmetry factor (1 for heteronuclear diatomic molecules, 2 for homonuclear diatomic molecules), θ_r and θ_v are characteristic rotational and vibrational temperatures, and m denotes only the electron energy levels.

It is often easier to deal with partition functions per unit volume. Since only the translational partition function is proportional to volume, the total partition function per unit volume is given simply as

$$q_a = \frac{Q_a}{V} = \frac{Q_{a,tr}Q_{a,rot}Q_{a,vib}Q_{a,el}}{V} = q_{a,tr}q_{a,rot}q_{a,vib}q_{a,el}. \tag{3.137}$$

Since $n_a = \frac{\tilde{N}_a}{V} = \frac{Q_a}{V} = q_a$, an explicit form of the equilibrium constant can be obtained by inserting Equation 3.137 into Equation 3.128:

$$K_{n,i} = \frac{\prod_{j=1}^{N_s}\left(n_j^*\right)^{\nu''_{ij}}}{\prod_{j=1}^{N_s}\left(n_j^*\right)^{\nu'_{ij}}} = \frac{\prod_{j=1}^{N_s}\left(q_j\right)^{\nu''_{ij}}}{\prod_{j=1}^{N_s}\left(q_j\right)^{\nu'_{ij}}}. \tag{3.138}$$

Typically, the energy levels of the various species are measured relative to a reference energy level. In hydrogen, for example, the reference state is the ground state of the hydrogen molecule, and the exponential of Equation 3.130 must be modified to take into account the difference between the ground state of the hydrogen molecule and the ground state of, say, the hydrogen atom. After this modification, the equilibrium constant becomes

$$K_{n,i} = \frac{\prod_{j=1}^{N_s}\left(q_j\right)^{\nu''_{ij}}}{\prod_{j=1}^{N_s}\left(q_j\right)^{\nu'_{ij}}}\exp\left[\frac{1}{kT}\sum_{j=1}^{N_s}\left(\nu'_{ij} - \nu''_{ij}\right)\epsilon_j^0\right], \tag{3.139}$$

where ϵ_j^0 is the energy of the ground state of species j relative to the ground state of the reference species. The equilibrium pressure and concentration constants can easily be found by appropriate substitution of Equation 3.139 into Equation 3.129.

3.9.2 Dissociation Processes

The chemical equation for dissociation of a diatomic gas is given by

$$M + S_2 \rightleftharpoons 2S + M. \tag{3.140}$$

The third body, M, is necessary to provide the energy necessary to dissociate the molecule and to carry away energy liberated by the atomic recombination. Over the range of temperatures where dissociation occurs (typically 1000 - 12000 K), data is readily available, and the equilibrium constants and forward rate constants of the Arrhenius form are easily found. The dissociation energy of the hydrogen molecule is 4.516 eV ($7.236 \times 10^{-19}\,J$), while the dissociation energy of the nitrogen molecule is 9.800 eV ($1.570 \times 10^{-18}\,J$).

Equilibrium Dissociation

For a diatomic gas, the equilibrium constant in terms of partial pressures is

$$\frac{p_S^2}{p_{S_2}} = K_{p,dis}, \tag{3.141}$$

while in terms of number densities the constant is

$$K_{n,dis} = \frac{K_p}{kT} = \frac{n_S^2}{n_{S_2}} = \frac{q_S^2}{q_{S_2}} e^{-\theta_d/T}. \tag{3.142}$$

The equilibrium constant written in terms of partition functions (neglecting electron excitation) for hydrogen is

$$K_{n,dis} = \frac{2\theta_r}{T}\left(\frac{\pi m_H kT}{h^2}\right)^{\frac{3}{2}}\left(1 - e^{-\theta_v/T}\right)e^{-\theta_d/T}, \tag{3.143}$$

or

$$K_{p,dis} = 2k\theta_r\left(\frac{\pi m_H kT}{h^2}\right)^{\frac{3}{2}}\left(1 - e^{-\theta_v/T}\right)e^{-\theta_d/T}, \tag{3.144}$$

where m_H is the mass of the hydrogen atom and the characteristic temperatures are appropriate to the hydrogen dissociation reaction.

As can be seen, the equilibrium constant is a function of temperature only for a given reaction. The equilibrium constant K_p can easily be found or calculated from the literature.

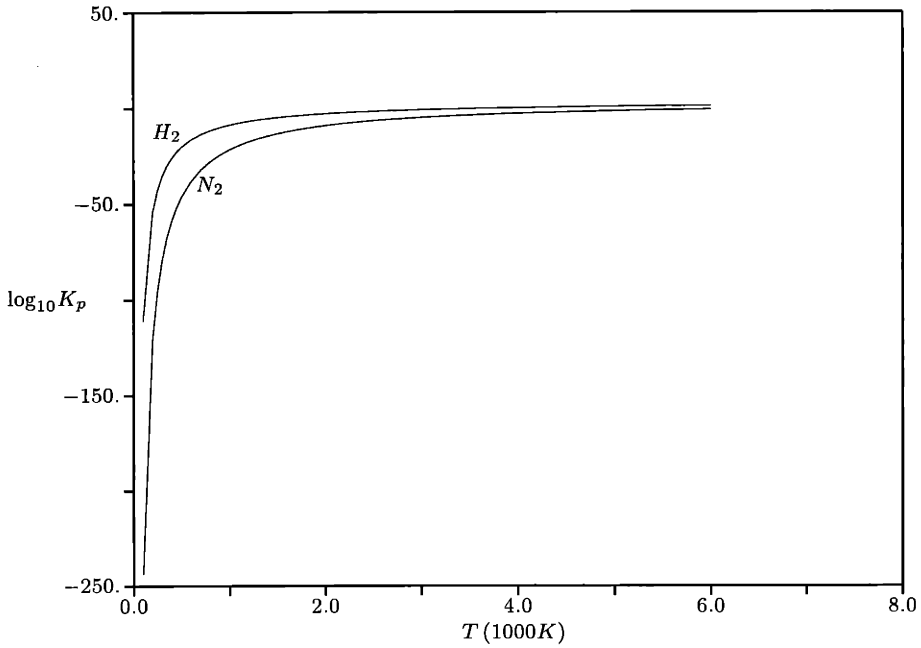

Figure 3-3: *Equilibrium Constant Versus Temperature for the Hydrogen and Nitrogen Dissociation Reactions*

It is often easier to use these tabulated values, as it becomes more difficult to evaluate the constant for more complex compounds and reactions. Figure 3-3 shows $\log_{10} K_{p,dis}$ versus temperature for both the hydrogen and nitrogen dissociation reactions, from the JANAF Thermochemical Tables [17]. These values are tabulated in Appendix B up to 6000 K. As listed, these values are for the dissociation of one half mole of H_2 into one mole of H, so must be multiplied by a factor of 2 to be used in Equation 3.141. The effect of the higher dissociation energy of the nitrogen molecule is to lower the curve, as shown.

For chemical equilibrium the partial pressures of the diatomic and monatomic species can then be easily calculated using Equation 3.141. For chemical non-equilibrium the equilibrium constant $K_{p,dis}$ can be used to determine the production rate of the species involved, to be discussed in the next section.

When only diatomic and monatomic neutrals are of concern, the equilibrium quantities can be calculated through the solution of a simple quadratic equation. Figures 3-4 and 3-5 show the equilibrium mole fraction of atomic hydrogen and nitrogen, respectively, for a range of temperatures and pressures. When ionization becomes a factor, simultaneous solution of this quadratic equation and another quadratic equation derived from the Saha equation is necessary.

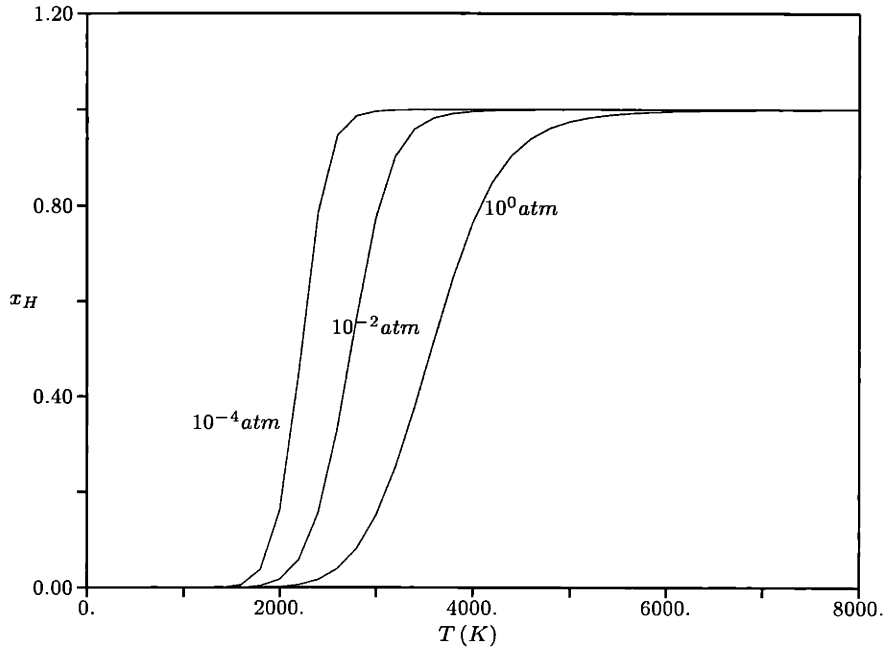

Figure 3-4: *Equilibrium Dissociation of Hydrogen versus Temperature and Pressure*

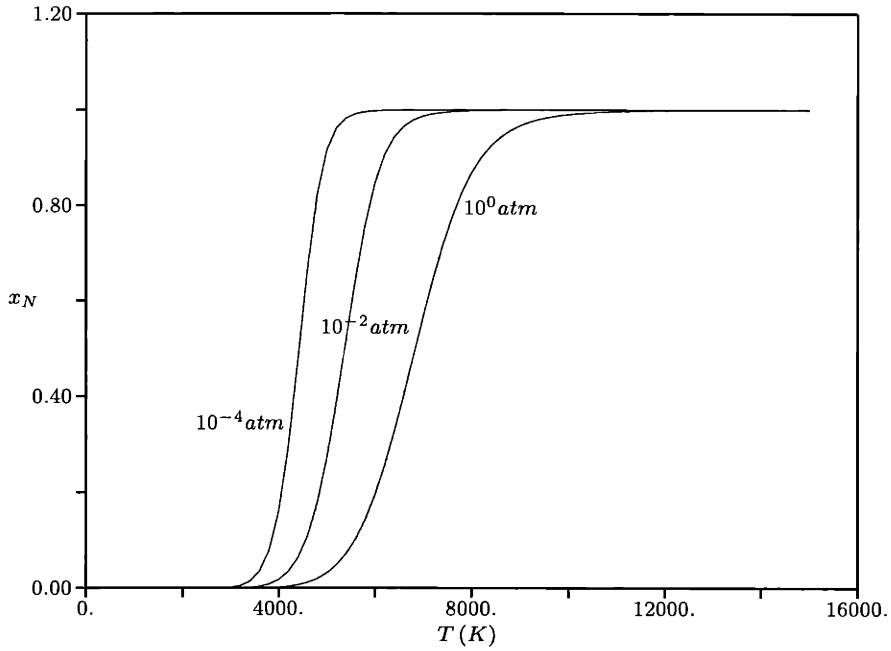

Figure 3-5: *Equilibrium Dissociation of Nitrogen versus Temperature and Pressure*

	Hydrogen	Nitrogen
$A\ (m^3/mol-s)$	5.5×10^{12}	2.1×10^{15}
$B\ (J/mol)$	435,600	943,800
n_f	-1.0	-1.5
$\hat{m}_S$	5.0	3.0
$\hat{m}_{S_2}$	2.0	5.0

Table 3.1: *Arrhenius Constants for the Hydrogen and Nitrogen Dissociation Rate Equations*

Non-equilibrium Dissociation

If the species are not in chemical equilibrium then a net rate of production (or depletion) of each species will result. Equation 3.125, when applied to the dissociation-recombination process, becomes

$$\frac{d\hat{n}_S}{dt} = k_f \hat{n}_M \left(\hat{n}_{S_2} - \frac{1}{K_{c,dis}} \hat{n}_S^2 \right). \tag{3.145}$$

The third body molar concentration for reaction i is given as

$$\hat{n}_{M,i} = \sum_{j=1}^{N_s} \hat{m}_{ij} \hat{n}_j. \tag{3.146}$$

where the $\hat{m}_{ij}$ are known as the third body efficiencies. With the forward rate constant, k_f, given by Equation 3.121, and using Equation 3.145, the net production rate of atomic species can be written as

$$\dot{n}_S = A N_A T^{n_f} \exp\left(-\frac{B}{\hat{R}T} \right) \left(\hat{m}_S \hat{n}_S + \hat{m}_{S_2} \hat{n}_{S_2} \right) \left(\hat{n}_{S_2} - \frac{\hat{R}T}{K_{p,dis}} \hat{n}_S^2 \right). \tag{3.147}$$

The constants required by Equation 3.147 for hydrogen and nitrogen are listed in Table 3.1, and were taken from Rogers and Schexnayder [110] for hydrogen and Langan et al. [71] for nitrogen.

As it stands, Equation 3.147 does not take dissociation due to direct electron impact into account. To do so, a term of the form

$$\dot{n}_{S,e} = k_d^e n_e n_{S_2} \tag{3.148}$$

is required, where k_d^e is just the reaction rate coefficient of the $S_2 + e \rightarrow 2S + e$ reaction.

For the dissociation of diatomic hydrogen, the reaction rate coefficient[1] is taken from Janev et al. [57], and is shown in Figure 3-6.

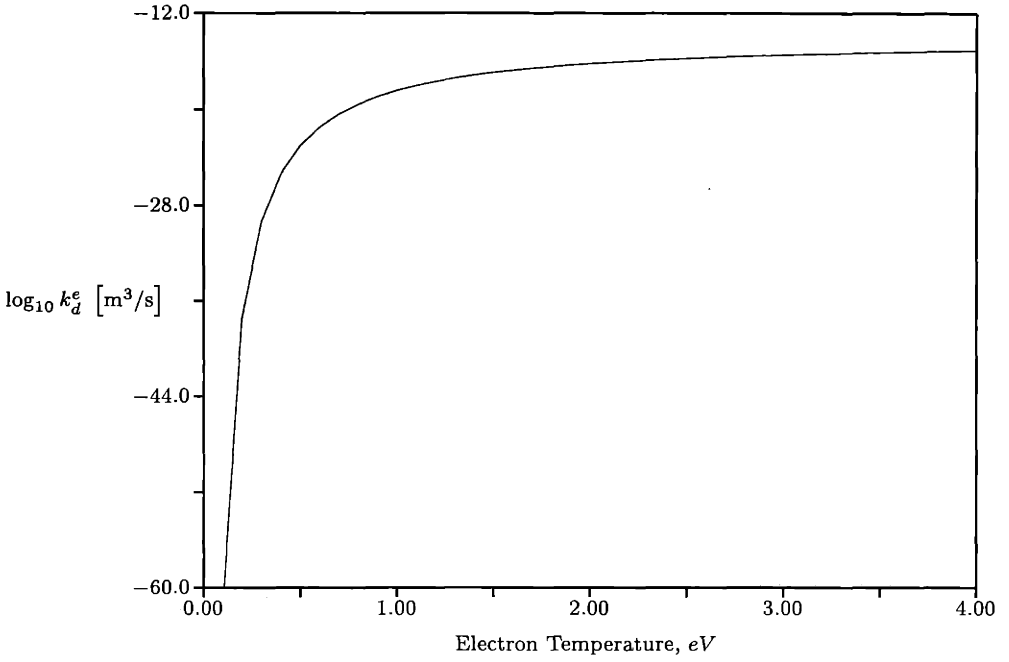

Figure 3-6: *Reaction Rate Coefficient k_d^e for the Electron Impact Dissociation of Hydrogen*

Accounting for this and the reverse reaction ($S + S + e \rightarrow S_2 + e$) equation 3.145 then becomes

$$\frac{d\hat{n}_S}{dt} = (k_f \hat{n}_M + k_d^e n_e)\left(\hat{n}_{S_2} - \frac{1}{K_{c,dis}}\hat{n}_S^2\right). \tag{3.149}$$

The total net rate of production of atomic species is then given by

$$\dot{n}_{S,total} = \dot{n}_{S,heavy} + \dot{n}_{S,e}$$

$$= \left(AN_A T^{n_f} e^{-B/\hat{R}T}\left(\hat{m}_S \hat{n}_S + \hat{m}_{S_2}\hat{n}_{S_2}\right) + k_d^e\, n_e\right)\left(\hat{n}_{S_2} - \frac{\hat{R}T}{K_{p,dis}}\hat{n}_S^2\right). \tag{3.150}$$

3.9.3 Ionization Processes

The chemical equation for ionization of a monatomic gas is given by

$$e + S \rightleftharpoons e + e + S^+. \tag{3.151}$$

[1]Note: For hydrogen, the reaction rate coefficient k_d^e is identical to the reaction rate coefficient $< \sigma v >$ of Janev et al. [57] and Miller [85].

where S is either hydrogen or cesium in this research. Only electrons were considered as third bodies for this research since in the regions of the flow where significant amounts of molecules exist, a collision between an atom and a molecule would be more likely to dissociate the molecule, because of the lower molecular bond energy in comparison with the ionization energy. Also, in atom-atom collisions it is highly improbable that the collision would ionize one of the atoms since in arcjets the high collision rate prevents the ions from attaining the necessary translational energy. Thus only electrons are capable of acquiring enough energy to cause ionization. The ionization energy of the hydrogen atom is 13.598 eV ($2.179 \times 10^{-18} J$), while the nitrogen atom has an ionization energy of 14.534 eV ($2.329 \times 10^{-18} J$).

Equilibrium Ionization

The equilibrium level of ionization can be calculated easily from the application of equation 3.139 to the ionization reaction, which is called the Saha equation.

$$K_{n,ion} = \frac{n_e n_{S+}}{n_S} = \frac{2g_{S+}}{g_S} \left(\frac{2\pi m_e \kappa T_e}{h^2} \right)^{\frac{3}{2}} e^{-\epsilon_{i,S}/kT_e}, \tag{3.152}$$

where the g_s are the corresponding degeneracy functions ($g_e = 2$) and $\epsilon_{i,S}$ is the ionization energy of the atom considered. Note that since the electrons have a much higher thermal velocity than the heavy species it is the electron temperature which is relevant to the ionization reaction.

For the range of temperatures encountered within an arcjet, the degeneracies of the ground states of neutral and singly ionized atomic hydrogen can be approximated as $g_H \approx 2$, $g_{H+} \approx 1$, $g_{Cs} \approx 1$, $g_{Cs+} \approx 1$. [29]

Non-equilibrium Ionization

The net rate of production of ions is given by Equation 3.125 applied to the ionization reaction, and is given as

$$\dot{n}_{S+} = k_f n_e \left(n_S - \frac{1}{K_{n,ion}} n_e n_{S+} \right). \tag{3.153}$$

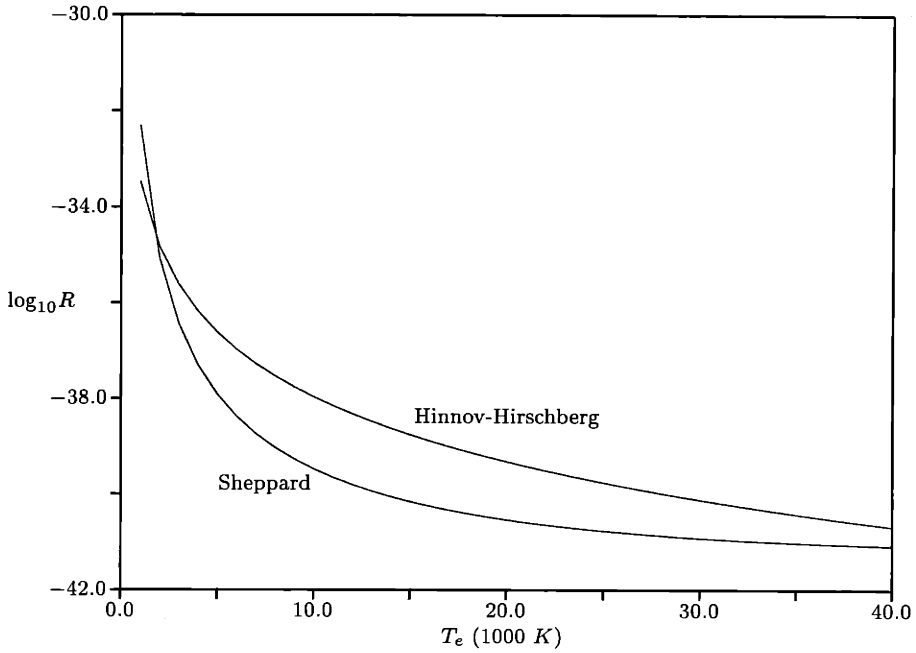

Figure 3-7: *Comparison of Hinnov-Hirschberg and Sheppard Reaction Rate Coefficients for the Recombination of Ionized Hydrogen*

This equation can be written in a generalized form after Mitchner and Kruger [86] as

$$\dot{n}_{S+} = R n_e \left(S_S n_S - n_e n_{S+} \right), \tag{3.154}$$

where R is the recombination rate coefficient and $S = K_{n,ion}$. A commonly quoted recombination rate coefficient is that of Hinnov and Hirschberg [46]:

$$R_{HH} = 1.09 \times 10^{-20} \, T_e^{-\frac{9}{2}} \quad \mathrm{m}^3 \, \mathrm{s}^{-1}. \tag{3.155}$$

Hinnov and Hirschberg derived their recombination coefficient based on the structure of the hydrogen atom, and upon assumptions which break down above 3000 K. This coefficient does, indeed, give good results below this temperature, but can dramatically overestimate recombination at higher temperatures [86] [118]. Sheppard [118] found a recombination rate coefficient for hydrogen based upon a three level collisional-radiative model valid for electron temperatures up to 60000 K:

$$R_{Sh} = 6.985 \times 10^{-42} \exp \left[\frac{\left(\ln \frac{T_e}{1000.0} - 4.0833 \right)^2}{0.8179} \right] \quad \mathrm{m}^3 \mathrm{s}^{-1}. \tag{3.156}$$

The Sheppard recombination rate coefficient is used in this research for hydrogen. Figure 3-7 shows a comparison of the Hinnov-Hirschberg and Sheppard recombination rate coefficients over a range of electron temperatures.

3.9.4 Dissociation and Ionization with Thermal Non-equilibrium

As mentioned in Section 3.3.1, an electron temperature different from the heavy species temperature is necessary in the non-equilibrium production of ions and electrons which are required for a self-consistent arc attachment at the anode. In the regions of arc attachment on the anode, Miller showed that in conventional arcjets the electron temperature can be on the order of 20,000 K, while the heavy species temperature is just 1000 K. To demonstrate the effect of an electron temperature higher than the heavy species temperature Benson [5] calculated the composition of hydrogen and nitrogen over a range of temperatures for two situations: the first assuming the electrons in thermal equilibrium with the heavy species and the second assuming an electron temperature at twice that of the heavy species temperature, over a temperature range of 0 - 24000 K. Figures 3-8 and 3-10 show the composition of hydrogen and nitrogen, respectively, with the electron temperature in equilibrium with the heavy species temperature, at a pressure of one atmosphere. As can be seen, there are well defined regions of dominance for molecular, atomic, and ionic species. In comparison, Figures 3-9 and 3-11 show the composition of hydrogen and nitrogen, respectively, with the electron temperature fixed at $T_e = 2\,T_g$. At intermediate temperatures there is much less of a distinct zone where atomic species dominate, but rather the hotter electrons cause more ionization, which is especially seen in the case of nitrogen.

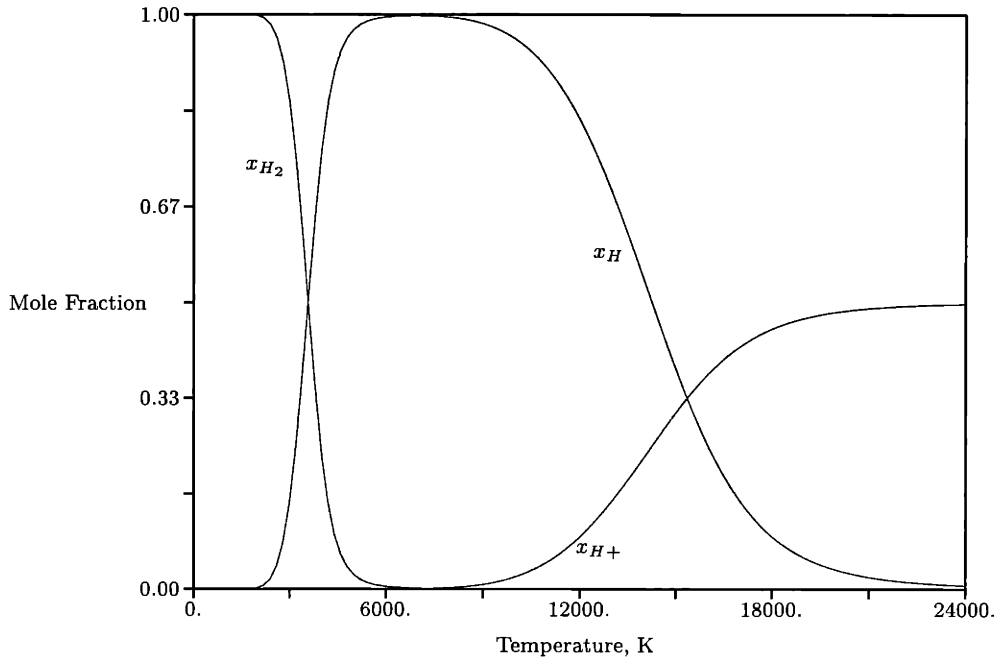

Figure 3-8: *Composition of Hydrogen in Chemical and Thermal Equilibrium, $p = 1\,atm$*

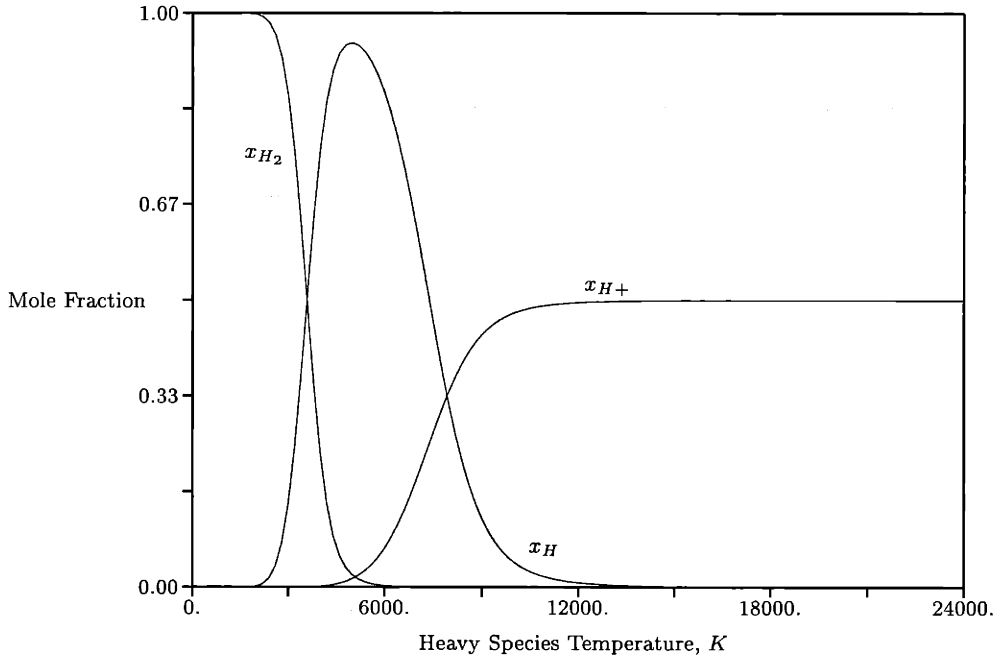

Figure 3-9: *Composition of Hydrogen, $p = 1\,atm$, $T_e = 2\,T_g$*

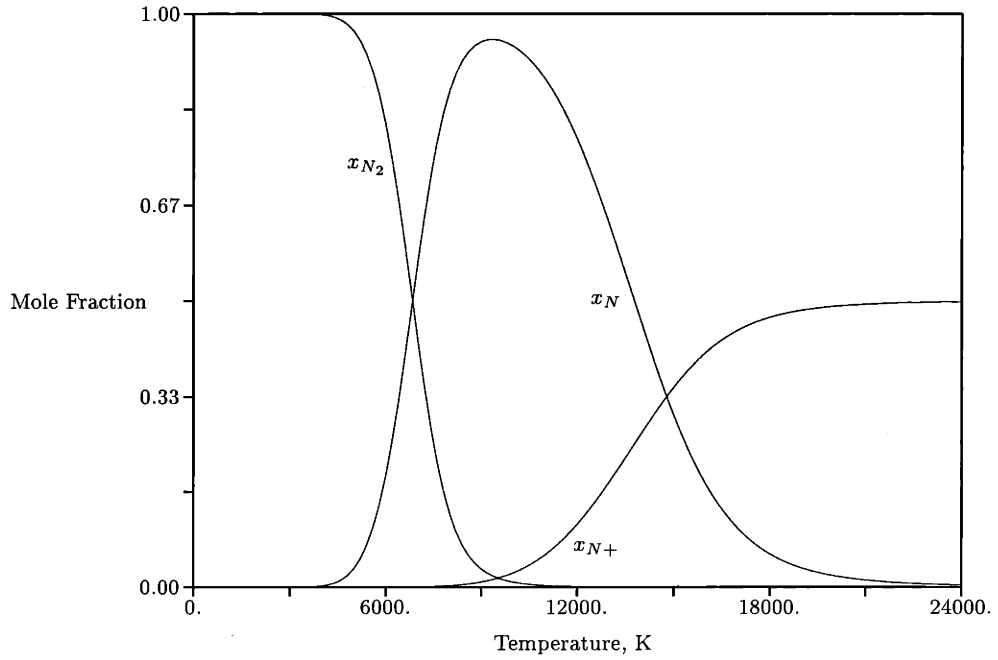

Figure 3-10: *Composition of Nitrogen in Chemical and Thermal Equilibrium, $p = 1\,atm$*

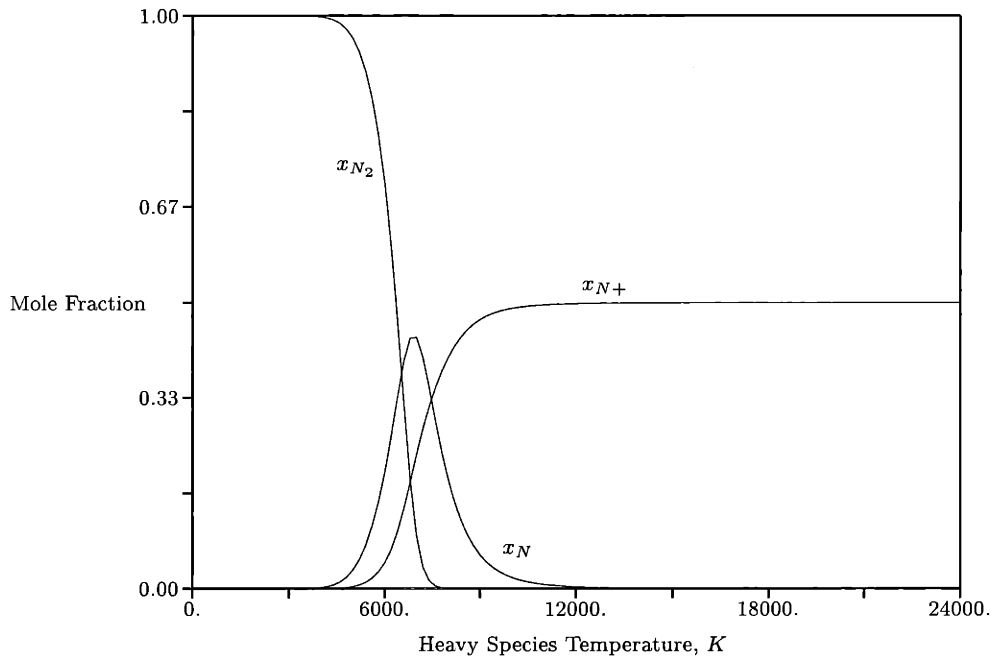

Figure 3-11: *Composition of Nitrogen, $p = 1\,atm$, $T_e = 2\,T_g$*

3.10 Transport Properties

Gradients in concentration, velocity, and temperature, cause a net transport of mass, momentum, and thermal energy, respectively. The general form of a flux of a property in terms of a gradient can be approximated by

$$\vec{J} = -c\nabla\varphi, \tag{3.157}$$

where $\vec{J}$ is the flux appropriate to quantity φ, and c is a proportionality constant known as the transport coefficient. The negative sign applies because the quantity is transported from regions of high concentration to regions of low concentration. The transport coefficient for mass transport is the diffusion coefficient, D $(m^2\,s^{-1})$, with the flux vector being represented as $\rho\vec{V}$, where $\vec{V}$ is the diffusion velocity. For momentum transport, the transport coefficient is the viscosity, μ $(kg\,m^{-1}\,s^{-1})$. This momentum flux has nine components, since both velocity and the gradient vector have three components each, and is typically called the viscous stress tensor, $\overline{\overline{\tau}}$. Finally, the transport coefficient applicable to the transport of thermal energy is the thermal conductivity, κ $(J\,m^{-1}\,s^{-1}\,K^{-1})$, with the flux vector being that of heat flux, $\vec{q}$. These flux vectors and their associated quantities and proportionality constants are summarized in Table 3.2.

Quantity	φ	c	$\vec{J}$
Mass	ρ	D	$\rho\vec{V}$
Momentum	$\vec{u}$	μ	$\overline{\overline{\tau}}$
Temperature	T	κ	$\vec{q}$

Table 3.2: *Flux Vectors and Associated Quantities Due to Gradients*

From mean free path arguments, the transport coefficients can only be found to an accuracy of the order of two or three [86]. To obtain a reliable estimate of arcjet performance a more accurate method of determining the transport coefficients was deemed necessary. The Chapman-Enskog solution to the Boltzmann equation can provide much greater accuracy even though it is technically only valid in regions of thermal equilibrium and for distribution functions that are only slightly perturbed from a Maxwellian distribution. However, due to the highly collisional flow within an arcjet, it still gives a better approximation to the

transport coefficients than do mean free path arguments.

3.10.1 Overview: Chapman-Enskog Solution to the Boltzmann Equation

The Chapman-Enskog solution is derived mathematically in texts by Chapman and Cowling [16] and Hirschfelder, Curtiss, and Bird [48]. This argument follows the methods of Hirschfelder et al. To obtain the Chapman-Enskog solution, it is first assumed that the distribution function of species s is slightly perturbed from equilibrium:

$$f_s^1(\vec{r},\vec{v},t) = f_s^0(\vec{r},\vec{v},t)\left[1+\zeta_s(\vec{r},\vec{v},t)\right], \tag{3.158}$$

where

$$f_s^0 = n_s\left(\frac{m_s}{2\pi kT}\right)^{\frac{3}{2}}\exp\left(\frac{-m_s\left|\vec{v}_s(\vec{r},t)-\vec{u}(\vec{r},t)\right|^2}{2kT}\right) \tag{3.159}$$

is the Maxwellian distribution function in three dimensions and the perturbation function is found to be

$$\zeta_s = -\left(\vec{A}_s\cdot\nabla\ln T\right) - \left(\overline{\overline{B}}_s:\nabla\vec{u}\right) + n\sum_r\left(\vec{C}_s^{(r)}\cdot\vec{d}_r\right), \tag{3.160}$$

where $\vec{A}_s$, $\overline{\overline{B}}_s$, and $\vec{C}_s^{(r)}$ are functions of velocity, concentration, and temperature; and $\vec{d}_r$ is the generalized driving force:

$$\vec{d}_r = \nabla x_r + (x_r - y_r)\frac{\nabla p}{p} - \left(\frac{n_r m_r}{p\rho}\right)\left[\frac{\rho}{m_r}\vec{F}_r - \sum_t n_t\vec{F}_t\right], \tag{3.161}$$

where x_r and y_r are the mole and mass fractions of species r, respectively; and $\vec{F}_r$ and $\vec{F}_t$ are the body forces affecting species r and t, respectively.

By substituting Equation 3.158 into the Boltzmann equation (Equation 3.5) and taking the moments as in Section 3.2, a set of integral equations results. These equations are solved by the methods of variational calculus, using Sonine polynomials as test functions. The transport coefficients can then be represented as finite expansions of these polynomials. Chapman and Cowling assumed an infinite series of polynomials, while Hirschfelder et al. use a finite series of polynomials. The reason for this is that a very good approximation can be obtained with only a few terms of the Sonine polynomial expansion.

Chapman and Cowling show that these Sonine polynomial expansions can be written

as a linear combination of *collision integrals*[2] which are effectively energy averaged cross sections times velocity to give collision frequencies per unit number densities.

$$\Omega_{ij}^{(l,s)}(T) = \sqrt{\frac{kT}{2\pi m_{ij}}} \int_0^\infty e^{-\gamma^2} \gamma^{2s+3} Q_{ij}^{(l)}(g)\, d\gamma, \tag{3.162}$$

where $\gamma^2 = \frac{1}{2} m_{ij} g^2 / kT$, m_{ij} is the reduced mass of the colliding particles, g is the relative velocity of the colliding particles, and $Q_{ij}^{(l)}(g)$ is the integral cross section:

$$Q_{ij}^{(l)}(g) = 2\pi \int_0^\infty \left(1 - \cos^l \chi\right) b\, db \tag{3.163}$$

in which the deflection angle, χ, is given by the equation

$$\chi(g,b) = \pi - 2b \int_{r_m}^\infty \frac{dr/r^2}{\left(1 - b^2/r^2 - V(r)/\frac{1}{2} m_{ij}\, g^2\right)^{\frac{1}{2}}}, \tag{3.164}$$

where b is the impact parameter and $V(r)$ is the interaction potential of the two colliding particles. The lower bound on the integral, r_m, occurs at the point where the denominator in Equation 3.164 vanishes.

The interaction potential can have a variety of forms. A common potential used in the calculation of collision integrals is the shielded Coulomb potential for charged particle interactions,

$$V(r) = Z_1 Z_2 \frac{e^2 \exp(-r/\lambda)}{r}, \tag{3.165}$$

where λ is a screening length, typically the Debye length:

$$\lambda_D = \sqrt{\frac{\epsilon_0 kT}{e^2 \sum_j Z_j^2 n_j}}. \tag{3.166}$$

This potential has an advantage in that the collision cross section of two colliding charged particles is not infinite, as is the case with the unscreened Coulomb potential. For neutral particle collisions, a potential which fits data very accurately is the Lennard-Jones potential

$$V(r) = 4\epsilon \left[\left(\frac{\sigma}{r}\right)^{12} - \left(\frac{\sigma}{r}\right)^{6} \right], \tag{3.167}$$

[2]The notation of the collision integrals here is actually that of Hirschfelder et al. The $\Omega_{ij}^{(l,s)}$ integrals of Hirschfelder are identical to the $\Omega_{ij}^{(l)}(s)$ integrals of Chapman and Cowling.

where ϵ and σ are parameters specific to the collision. For the simplest interaction potential, rigid hard spheres, the integral cross section and the collision integral have simple closed-form analytical solutions:

$$Q^l_{RS} = \left[1 - \frac{1}{2}\frac{1+(-1)^l}{1+l}\right]\pi\sigma_{ij}^2, \tag{3.168}$$

where σ_{ij} in this case is the effective radius of the colliding particles, and

$$\Omega^{(l,s)}_{RS} = \sqrt{\frac{kT}{2\pi m_{ij}}}\frac{(s+1)!}{2}\,Q^l_{RS}. \tag{3.169}$$

Rather than represent the transport coefficients in terms of pure collision integrals, the collision integrals are typically non-dimensionalised according to their rigid sphere values. These non-dimensional values can then be thought of as coefficients which correct for deviations from the rigid sphere model:

$$\Omega^{(l,s)*}_{ij} = \frac{\sqrt{\frac{2\pi m_{ij}}{kT}}\,\Omega^{(l,s)}_{ij}}{\frac{(s+1)!}{2}\left[1 - \frac{1}{2}\frac{1+(-1)^l}{1+l}\right]\pi\sigma_{ij}^2}. \tag{3.170}$$

The transport coefficients can be calculated using these non-dimensional values. In the equations representing the various transport coefficients, the effective collision radius (σ_{ij}) appears explicitly. Knowing this, the more frequent form of the collision integrals is that of an energy averaged cross section:

$$\langle\Omega^{(l,s)}_{ij}\rangle = \sigma_{ij}^2\Omega^{(l,s)*}_{ij} = \left[\frac{\pi}{2}(s+1)!\left(1 - \frac{1}{2}\frac{1+(-1)^l}{1+l}\right)\right]^{-1}\int_0^\infty e^{-\gamma^2}\gamma^{2s+3}Q^l_{ij}(g)\,d\gamma. \tag{3.171}$$

It is this form of the collision integrals which is typically found in the literature.

3.10.2 Diffusion

Diffusion coefficient

The first approximation to the diffusion coefficient of a pure substance (coefficient of *self diffusion*) [48] is

$$D = 2.628\times10^{-7}\sqrt{\frac{T^3}{M}}\frac{1}{P\,\langle\Omega^{(1,1)}\rangle} \qquad \left[\mathrm{m^2\,s^{-1}}\right], \tag{3.172}$$

where M is the molecular weight of the species in g mol^{-1}, P is the pressure in atmospheres, T is in Kelvins, and $\langle\Omega^{(1,1)}\rangle$ is in units of angstroms squared, Å^2. The first approximation for the coefficient of *binary* diffusion (i.e. two species) is

$$D_{12} = 2.628 \times 10^{-7} \sqrt{\frac{T^3\,(M_1 + M_2)}{2M_1M_2}}\,\frac{1}{P\langle\Omega_{12}^{(1,1)}\rangle}. \tag{3.173}$$

For flows where there are more than two species, the *multicomponent* diffusion coefficients $\overline{D}_{ij}$ are given in terms of binary diffusion coefficients by Hirschfelder as:

$$\overline{D}_{ij} = \frac{1}{M_j}\left(\sum_k x_k M_k\right)\frac{K^{ji} - K^{ii}}{|K|}, \tag{3.174}$$

where the summation is taken to be over all species, x_k is the mole fraction of species k,

$$K_{ij} = \frac{x_i}{D_{ij}} + \frac{M_j}{M_i}\sum_{k\neq i}\frac{x_k}{D_{ik}}, \quad i \neq j \tag{3.175}$$

$K_{ii} = 0$, $|K|$ is the determinant of the K_{ij} and the K^{ji} are the minor determinants

$$K^{ji} = (-1)^{i+j}\begin{vmatrix} 0 & \cdots & K_{1,i-1} & K_{1,i+1} & \cdots & K_{1,\nu} \\ \vdots & & \vdots & \vdots & & \vdots \\ K_{j-1,1} & \cdots & K_{j-1,i-1} & K_{j-1,i+1} & \cdots & K_{j-1,\nu} \\ K_{j+1,1} & \cdots & K_{j+1,i-1} & K_{j+1,i+1} & \cdots & K_{j+1,\nu} \\ \vdots & & \vdots & \vdots & & \vdots \\ K_{\nu,1} & \cdots & K_{\nu,i-1} & K_{\nu,i+1} & \cdots & K_{\nu,\nu} \end{vmatrix}, \tag{3.176}$$

where ν is the total number of species present.

As can be seen, the multicomponent diffusion coefficients are ratios of determinants. For a ternary mixture, the mathematics is relatively straight forward. However, as the number of species increases, Equations 3.174 - 3.176 become increasingly cumbersome and computationally intensive. Therefore the simpler formulation of Krier et al. [68] is used. In this formulation, the multicomponent diffusion coefficients are replaced by *effective* diffusion coefficients D_i. For species i,

$$D_i = \frac{1 - x_i}{\sum_{j\neq i}\frac{x_j}{D_{ij}}}, \tag{3.177}$$

where the D_{ij} are the binary diffusion coefficients defined above. Benson [5] showed that this approximation of the diffusion coefficients is crude, and doesn't always yield desirable results. However, it does take into account a flow's multicomponent nature, and is easy to calculate.

The diffusion coefficients so far discussed assume that different species are free to diffuse, independent of the other species. However when the fluid in question is a plasma, the charged particles interact to try and drive the system to quasineutrality. Concentration gradients cause a diffusion of electrons and ions. The electrons being much lighter than the ions tend to diffuse at a much higher speed than the ions. This causes a local separation of charge, which in turn creates a local electric field. This local field tends to retard the electrons and speed up the ions, so that both ions and electrons tend to diffuse at the same common speed. For charged species the net flux due to diffusion is the sum of the diffusion flux and the space charge flux which can be combined as an ambipolar flux [111].

$$n_i V_i = -D_i \nabla n_i + q_i n_i \mu_i E_{spacecharge} = -D_{ai} \nabla n_i \tag{3.178}$$

where n_i is the number density, q_i the charge, $\mu_i = \frac{D_i}{kT_i}$ the mobility, and D_{ai} the ambipolar diffusion coefficient. The ambipolar condition is that the net flux of charge due to diffusion is zero.

$$\sum_i q_i n_i V_i = 0 \tag{3.179}$$

from which the space charge can be calculated as

$$E_{spacecharge} = \frac{\sum_i q_i D_i \nabla n_i}{\sum_i q_i^2 n_i \mu_i}. \tag{3.180}$$

Thus the ambipolar diffusivity is

$$D_{ai} = \frac{\sum_{k \neq i} \left(q_k^2 \mu_k D_i n_k / n_i - q_i q_k \mu_i D_k \nabla n_k / \nabla n_i \right)}{\sum_k q_k^2 \mu_k n_k / n_i}. \tag{3.181}$$

If quasineutrality is assumed to hold then $\sum_i q_i n_i = 0$, which simplifies matters, but the equation still requires the evaluation of density gradients which is time consuming computationally, so proportionality is often assumed to hold as well: $\frac{\nabla n_k}{\nabla n_i} \approx \frac{n_k}{n_i}$. This only need hold for the charged species, and whilst probably a very good assumption for conventional

arcjets where all the charged species are present near the core, may well be a very poor assumption for seeded arcjets which were expected to run with the cesium fully ionized and well spread across the constrictor, and with any hydrogen ions formed being present only at the cathode tip and maybe the anode attachment point. Nevertheless this assumption was used on the basis that the slip velocities of the charged species would probably be dominated by the applied electric field rather than the ambipolar diffusion.

$$D_{ai} = \frac{\sum_{k \neq i} \left(n_k \left(q_k^2 \mu_k D_i - q_i q_k \mu_i D_k \right) \right)}{\sum_k q_k^2 \mu_k n_k} \tag{3.182}$$

Evaluating this for electrons, Cs^+, and H^+ and making use of $\mu_i = \frac{D_i}{kT_i}$ yields

$$D_{ae} = \frac{n_{Cs+} D_{Cs+} D_e \left(\frac{1}{T_e} + \frac{1}{T_g} \right) + n_{H+} D_{H+} D_e \left(\frac{1}{T_e} + \frac{1}{T_g} \right)}{n_{Cs+} \frac{D_{Cs+}}{T_g} + n_{H+} \frac{D_{H+}}{T_g} + n_e \frac{D_e}{T_e}} \tag{3.183}$$

$$D_{aCs+} = \frac{n_e D_e D_{Cs+} \left(\frac{1}{T_e} + \frac{1}{T_g} \right)}{n_{Cs+} \frac{D_{Cs+}}{T_g} + n_{H+} \frac{D_{H+}}{T_g} + n_e \frac{D_e}{T_e}} \tag{3.184}$$

$$D_{aH+} = \frac{n_e D_e D_{H+} \left(\frac{1}{T_e} + \frac{1}{T_g} \right)}{n_{Cs+} \frac{D_{Cs+}}{T_g} + n_{H+} \frac{D_{H+}}{T_g} + n_e \frac{D_e}{T_e}} \tag{3.185}$$

Slip Velocities

With charged species the concentration gradient is not the sole source of the slip velocity when there is an externally applied electric field present. The slip velocities of the charged species are what defines the current conducted. This is especially important in the constrictor where the density decreases downstream, but the electric field, whilst accelerating the electrons downstream, is accelerating the positively charged ions upstream, i.e. slowing the ions relative to the bulk motion, so they will have a slip velocity upstream.

$$n_i V_i = -D_i \nabla n_i + q_i n_i \mu_i E_{external} = -D_i \nabla n_i - \frac{q_i n_i D_i}{kT_i} \nabla \phi \tag{3.186}$$

In this research, six species are modeled, hydrogen molecules, atoms, and ions, cesium atoms and ions, and electrons. Equations 3.28 and 3.34 become

$$\rho_{H_2} \vec{V}_{H_2} + \rho_H \vec{V}_H + \rho_{H+} \vec{V}_{H+} + \rho_{Cs} \vec{V}_{Cs} + \rho_{Cs+} \vec{V}_{Cs+} + \rho_e \vec{V}_e = 0 \tag{3.187}$$

and

$$\vec{J} = e\left(n_{H+}\vec{V}_{H+} + n_{Cs+}\vec{V}_{Cs+} - n_e\vec{V}_e\right). \tag{3.188}$$

Rearranging for the electron flux this is

$$\rho_e\vec{V}_e = \frac{m_e}{m_H}\vec{V}_{H+} + \frac{m_e}{m_{Cs}}\vec{V}_{Cs+} - \frac{m_e}{e}\vec{J}. \tag{3.189}$$

Eliminating $\vec{V}_e$ in equation 3.187 and neglecting terms of order $\frac{m_e}{m_H}$ gives

$$\rho_{H_2}\vec{V}_{H_2} + \rho_H\vec{V}_H + \rho_{H+}\vec{V}_{H+} + \rho_{Cs}\vec{V}_{Cs} + \rho_{Cs+}\vec{V}_{Cs+} - \frac{m_e}{e}\vec{J} = 0. \tag{3.190}$$

Since the current density, $\vec{J}$, is determined from the electric potential calculation, only four gradients and their corresponding effective diffusion coefficients are necessary to determine the diffusion velocities uniquely. This leaves one slip velocity which is required to take up the slack so that equation 3.190 is obeyed, rather than being calculated from the density gradient. Benson [5] did a lot of work to find out which species was best relegated to this position, since the effective diffusion coefficients were only crudely calculated, and concluded that this should be the atomic species. However in a seeded arcjet it was found that since the hydrogen was mostly molecular with only a minimum of atomic hydrogen that this formulation caused numerical problems. Similar numerical problems were found with all the species except for molecular hydrogen, which is present in large mass fractions throughout the seeded arcjet. Consequently H_2 was relegated to taking up the slack for purely numerical reasons rather than physical ones. Thus the formulation settled on was:

$$\vec{V}_H = -\frac{D_H}{\rho_H}\nabla\rho_H \tag{3.191}$$

$$\vec{V}_{Cs} = -\frac{D_{Cs}}{\rho_{Cs}}\nabla\rho_{Cs} \tag{3.192}$$

$$\vec{V}_{H+} = -\frac{D_{H+}}{\rho_{H+}}\nabla\rho_{H+} - \frac{eD_{H+}}{kT_g}\nabla\phi \tag{3.193}$$

$$\vec{V}_{Cs+} = -\frac{D_{Cs+}}{\rho_{Cs+}}\nabla\rho_{Cs+} - \frac{eD_{H+}}{kT_g}\nabla\phi \tag{3.194}$$

$$\rho_{H_2}\vec{V}_{H_2} = \frac{m_e}{e}\vec{J} - \rho_H\vec{V}_H - \rho_{H+}\vec{V}_{H+} - \rho_{Cs}\vec{V}_{Cs} - \rho_{Cs+}\vec{V}_{Cs+}. \tag{3.195}$$

3.10.3 Viscosity

The first approximation to the viscosity coefficient in a single species fluid [48] is

$$\mu = 2.6693 \times 10^{-6} \frac{\sqrt{MT}}{\langle \Omega^{(2,2)} \rangle} \quad \left[\mathrm{kg\,m^{-1}\,s^{-1}}\right], \tag{3.196}$$

and the first approximation of a binary mixture is

$$\mu_{12} = 2.6693 \times 10^{-6} \sqrt{\frac{2M_1M_2T}{M_1+M_2}} \frac{1}{\langle \Omega_{12}^{(2,2)} \rangle}, \tag{3.197}$$

with $\langle \Omega_{12}^{(2,2)} \rangle$ in $\mathring{A}^2$. As with the diffusion coefficient, the first approximation for the viscosity of a multicomponent mixture can be represented as a ratio of determinants:

$$\mu_{mix} = -\frac{\begin{vmatrix} H_{11} & H_{12} & H_{13} & \cdots & H_{1\nu} & x_1 \\ H_{12} & H_{22} & H_{23} & \cdots & H_{2\nu} & x_2 \\ H_{13} & H_{23} & H_{33} & \cdots & H_{3\nu} & x_3 \\ \vdots & \vdots & \vdots & & \vdots & \vdots \\ H_{1\nu} & H_{2\nu} & H_{3\nu} & \cdots & H_{\nu\nu} & x_\nu \\ x_1 & x_2 & x_3 & \cdots & x_\nu & 0 \end{vmatrix}}{\begin{vmatrix} H_{11} & H_{12} & H_{13} & \cdots & H_{1\nu} \\ H_{12} & H_{22} & H_{23} & \cdots & H_{2\nu} \\ H_{13} & H_{23} & H_{33} & \cdots & H_{3\nu} \\ \vdots & \vdots & \vdots & & \vdots \\ H_{1\nu} & H_{2\nu} & H_{3\nu} & \cdots & H_{\nu\nu} \end{vmatrix}}, \tag{3.198}$$

where

$$H_{ii} = \frac{x_i^2}{\mu_i} + \sum_{k \neq i} \frac{2x_ix_k}{M_i+M_k} \frac{\hat{R}T}{pD_{ik}} \left(1 + \frac{3}{5}\frac{M_k}{M_i}\frac{\langle \Omega_{ik}^{(2,2)} \rangle}{\langle \Omega_{ik}^{(1,1)} \rangle}\right) \tag{3.199}$$

for the diagonal terms and

$$H_{ij} = -\frac{2x_ix_j}{M_i+M_j} \frac{\hat{R}T}{pD_{ij}} \left(1 - \frac{3}{5}\frac{\langle \Omega_{ij}^{(2,2)} \rangle}{\langle \Omega_{ij}^{(1,1)} \rangle}\right) \tag{3.200}$$

for the off diagonal terms, and where $\hat{R}$ is the universal gas constant.

As with the diffusion coefficient, the matrix form for the multicomponent viscosity coefficient is much too cumbersome to use in a fluid dynamic code, so instead the mixture rule given by Mitchner and Kruger [86] was applied to the pure viscosity coefficients calculated by equation 3.196.

$$\mu_{mix} \approx \sum_{i=1}^{\nu} \frac{n_i \mu_i}{\sum_{j=1}^{\nu} n_j \chi_{ij}}, \tag{3.201}$$

where

$$\chi_{ij} = \sqrt{\frac{2m_{ij}}{m_i}} \frac{\langle \Omega_{ij}^{(2,2)} \rangle}{\langle \Omega_{ii}^{(2,2)} \rangle}$$

Using this equation, but with mole fractions rather than number densities, the heavy species viscosity coefficient is approximated as

$$\begin{aligned}
\mu_g \approx & \frac{x_{H_2}\mu_{H_2}\langle \Omega_{H_2H_2}^{(2,2)} \rangle}{x_{H_2}\langle \Omega_{H_2H_2}^{(2,2)} \rangle + x_H\sqrt{\frac{2}{3}}\langle \Omega_{H_2H}^{(2,2)} \rangle + x_{H^+}\sqrt{\frac{2}{3}}\langle \Omega_{H_2H^+}^{(2,2)} \rangle + x_{Cs}\sqrt{\frac{266}{135}}\langle \Omega_{H_2Cs}^{(2,2)} \rangle + x_{Cs^+}\sqrt{\frac{266}{135}}\langle \Omega_{H_2Cs^+}^{(2,2)} \rangle} \\
& + \frac{x_H\mu_H\langle \Omega_{HH}^{(2,2)} \rangle}{x_{H_2}\sqrt{\frac{4}{3}}\langle \Omega_{H_2H}^{(2,2)} \rangle + x_H\langle \Omega_{HH}^{(2,2)} \rangle + x_{H^+}\langle \Omega_{HH^+}^{(2,2)} \rangle + x_{Cs}\sqrt{\frac{266}{134}}\langle \Omega_{HCs}^{(2,2)} \rangle + x_{Cs^+}\sqrt{\frac{266}{134}}\langle \Omega_{HCs^+}^{(2,2)} \rangle} \\
& + \frac{x_{H^+}\mu_{H^+}\langle \Omega_{H^+H^+}^{(2,2)} \rangle}{x_{H_2}\sqrt{\frac{4}{3}}\langle \Omega_{H_2H^+}^{(2,2)} \rangle + x_H\langle \Omega_{HH^+}^{(2,2)} \rangle + x_{H^+}\langle \Omega_{H^+H^+}^{(2,2)} \rangle + x_{Cs}\sqrt{\frac{266}{134}}\langle \Omega_{H^+Cs}^{(2,2)} \rangle + x_{Cs^+}\sqrt{\frac{266}{134}}\langle \Omega_{H^+Cs^+}^{(2,2)} \rangle} \\
& + \frac{x_{Cs}\mu_{Cs}\langle \Omega_{CsCs}^{(2,2)} \rangle}{x_{H_2}\sqrt{\frac{4}{135}}\langle \Omega_{H_2Cs}^{(2,2)} \rangle + x_H\sqrt{\frac{2}{134}}\langle \Omega_{HCs}^{(2,2)} \rangle + x_{H^+}\sqrt{\frac{2}{134}}\langle \Omega_{H^+Cs}^{(2,2)} \rangle + x_{Cs}\langle \Omega_{CsCs}^{(2,2)} \rangle + x_{Cs^+}\langle \Omega_{CsCs^+}^{(2,2)} \rangle} \\
& + \frac{x_{Cs^+}\mu_{Cs^+}\langle \Omega_{Cs^+Cs^+}^{(2,2)} \rangle}{x_{H_2}\sqrt{\frac{4}{135}}\langle \Omega_{H_2Cs^+}^{(2,2)} \rangle + x_H\sqrt{\frac{2}{134}}\langle \Omega_{HCs^+}^{(2,2)} \rangle + x_{H^+}\sqrt{\frac{2}{134}}\langle \Omega_{H^+Cs^+}^{(2,2)} \rangle + x_{Cs}\langle \Omega_{CsCs^+}^{(2,2)} \rangle + x_{Cs^+}\langle \Omega_{Cs^+Cs^+}^{(2,2)} \rangle}.
\end{aligned} \tag{3.202}$$

3.10.4 Thermal Conductivity

The first approximation of the coefficient of thermal conductivity in a pure fluid [48] is

$$\kappa = 8.3227 \times 10^{-5} \frac{\sqrt{T/M}}{\langle \Omega^{(2,2)} \rangle} = \frac{15}{4} \frac{\hat{R}}{M} \mu \quad \left[\mathrm{J\,m^{-1}\,s^{-1}\,K^{-1}} \right]. \tag{3.203}$$

However, this equation only applies to particles without internal degrees of freedom. To account for internal degrees of freedom, the Eucken correction is applied to Equation 3.203:

$$\kappa_{polyatomic} = \frac{15}{4}\frac{\hat{R}}{M}\mu\left(\frac{4}{15}\frac{\hat{c}_v}{\hat{R}} + \frac{3}{5}\right), \tag{3.204}$$

where $\hat{c}_v$ is the specific heat of the molecule at constant volume. For monatomic species, the thermal conductivity simplifies to Equation 3.203. For diatomic molecules such as H_2 at moderate temperatures $\hat{c}_v \approx \frac{5}{2}\hat{R}$, and the thermal conductivity becomes

$$\kappa_{diatomic} \approx \frac{19}{4}\frac{\hat{R}}{M}\mu. \tag{3.205}$$

As with the previous transport coefficients, the multicomponent thermal conductivity can be represented as a ratio of matrices, but a simpler mixture rule of Mitchner and Kruger is employed instead, resulting in the heavy species thermal conductivity as

$$\begin{aligned}
\kappa_g \approx & \frac{x_{H_2}\kappa_{H_2}\langle\Omega^{(2,2)}_{H_2H_2}\rangle}{x_{H_2}\langle\Omega^{(2,2)}_{H_2H_2}\rangle + x_H\sqrt{\frac{2}{3}}\langle\Omega^{(2,2)}_{H_2H}\rangle + x_{H^+}\sqrt{\frac{2}{3}}\langle\Omega^{(2,2)}_{H_2H^+}\rangle + x_{Cs}\sqrt{\frac{266}{135}}\langle\Omega^{(2,2)}_{H_2Cs}\rangle + x_{Cs^+}\sqrt{\frac{266}{135}}\langle\Omega^{(2,2)}_{H_2Cs^+}\rangle} \\
& + \frac{x_H\kappa_H\langle\Omega^{(2,2)}_{HH}\rangle}{x_{H_2}\sqrt{\frac{4}{3}}\langle\Omega^{(2,2)}_{H_2H}\rangle + x_H\langle\Omega^{(2,2)}_{HH}\rangle + x_{H^+}\langle\Omega^{(2,2)}_{HH^+}\rangle + x_{Cs}\sqrt{\frac{266}{134}}\langle\Omega^{(2,2)}_{HCs}\rangle + x_{Cs^+}\sqrt{\frac{266}{134}}\langle\Omega^{(2,2)}_{HCs^+}\rangle} \\
& + \frac{x_{H^+}\kappa_{H^+}\langle\Omega^{(2,2)}_{H^+H^+}\rangle}{x_{H_2}\sqrt{\frac{4}{3}}\langle\Omega^{(2,2)}_{H_2H^+}\rangle + x_H\langle\Omega^{(2,2)}_{HH^+}\rangle + x_{H^+}\langle\Omega^{(2,2)}_{H^+H^+}\rangle + x_{Cs}\sqrt{\frac{266}{134}}\langle\Omega^{(2,2)}_{H^+Cs}\rangle + x_{Cs^+}\sqrt{\frac{266}{134}}\langle\Omega^{(2,2)}_{H^+Cs^+}\rangle} \\
& + \frac{x_{Cs}\kappa_{Cs}\langle\Omega^{(2,2)}_{CsCs}\rangle}{x_{H_2}\sqrt{\frac{4}{135}}\langle\Omega^{(2,2)}_{H_2Cs}\rangle + x_H\sqrt{\frac{2}{134}}\langle\Omega^{(2,2)}_{HCs}\rangle + x_{H^+}\sqrt{\frac{2}{134}}\langle\Omega^{(2,2)}_{H^+Cs}\rangle + x_{Cs}\langle\Omega^{(2,2)}_{CsCs}\rangle + x_{Cs^+}\langle\Omega^{(2,2)}_{CsCs^+}\rangle} \\
& + \frac{x_{Cs^+}\kappa_{Cs^+}\langle\Omega^{(2,2)}_{Cs^+Cs^+}\rangle}{x_{H_2}\sqrt{\frac{4}{135}}\langle\Omega^{(2,2)}_{H_2Cs^+}\rangle + x_H\sqrt{\frac{2}{134}}\langle\Omega^{(2,2)}_{HCs^+}\rangle + x_{H^+}\sqrt{\frac{2}{134}}\langle\Omega^{(2,2)}_{H^+Cs^+}\rangle + x_{Cs}\langle\Omega^{(2,2)}_{CsCs^+}\rangle + x_{Cs^+}\langle\Omega^{(2,2)}_{Cs^+Cs^+}\rangle}.
\end{aligned} \tag{3.206}$$

Since the electrons are treated as a separate fluid, the electron thermal conductivity is needed in the electron energy equation. Applying Mitchner and Kruger's mixing rule (Equation 3.201) to the electrons only when immersed in the plasma results in

$$\kappa_e \approx \frac{(x_{H^+} + x_{Cs^+})\,\kappa_e^{pure}\langle\Omega^{(2,2)}_{ee}\rangle}{(x_{H^+} + x_{Cs^+}) + x_{H_2}\sqrt{2}\langle\Omega^{(2,2)}_{eH_2}\rangle + x_H\sqrt{2}\langle\Omega^{(2,2)}_{eH}\rangle + x_{H^+}\sqrt{2}\langle\Omega^{(2,2)}_{eH^+}\rangle + x_{Cs}\sqrt{2}\langle\Omega^{(2,2)}_{eCs}\rangle + x_{Cs^+}\sqrt{2}\langle\Omega^{(2,2)}_{eCs^+}\rangle}. \tag{3.207}$$

3.10.5 Electrical Conductivity

For an ionized gas in the presence of electrical and magnetic fields, all of the transport coefficients are functions of the direction of these fields as well as pressure and concentration gradients. For example, if the magnetic field is taken to be in the $\hat{z}$ direction, and ion currents and pressure gradients are neglected (although Pressure gradients can be included by replacing $\vec{E}$ with $\vec{E} + \frac{\nabla P_e}{en_e}$), Ohm's Law can be represented in matrix notation as

$$\begin{bmatrix} J_{ex} \\ J_{ey} \\ J_{ez} \end{bmatrix} = \begin{bmatrix} \sigma_\perp & -\sigma_H & 0 \\ \sigma_H & \sigma_\perp & 0 \\ 0 & 0 & \sigma_{||} \end{bmatrix} \begin{bmatrix} E'_x \\ E'_y \\ E'_z \end{bmatrix}, \tag{3.208}$$

where

$$\sigma_{||} = \frac{e^2 n_e}{m_e \sum_r \overline{\nu}_{er}} \qquad \sigma_\perp = \frac{\sigma_{||}}{1+\beta^2} \qquad \sigma_H = \frac{\beta \sigma_{||}}{1+\beta^2}, \tag{3.209}$$

where β is the Hall parameter. The subscripts denote the conductivity in the directions parallel to $\vec{B}$, perpendicular to $\vec{B}$ and parallel to $\vec{E} \times \vec{B}$, respectively. In the absence of magnetic fields, $\sigma_\perp = \sigma_{||}$ and $\sigma_H = 0$, and Ohm's Law reduces to $\vec{J} = \sigma \vec{E}$.

The electrical conductivity of an ionized gas is given approximately as

$$\sigma = \sigma_e + \sigma_i \tag{3.210}$$

where

$$\sigma_e = \frac{e^2 n_e}{m_e \sum_g \overline{\nu}_{eg}} \quad \text{and} \quad \sigma_i = \frac{e^2 n_i}{m_i \sum_g \overline{\nu}_{eg}} \left[1 + \frac{\rho_n}{\rho_i} \frac{\overline{\nu}_{en}}{\overline{\nu}_{in}}\right] \tag{3.211}$$

where $\overline{\nu}_{eg}$ is the average collision frequency of electrons with all heavy species, $\overline{\nu}_{en}$ is the average electron-neutral collision frequency, and $\overline{\nu}_{in}$ is the ion-neutral collision frequency. Since quasineutrality holds and $\frac{m_e}{m_i} \ll 1$, the contribution due to ions can be neglected so $\sigma \approx \sigma_e$.

As with the other transport properties, mean free path arguments are only accurate to within a factor of two or three. Miller [85] and Benson [5] discuss a variety of more accurate models for the conductivity but they tend to be unsuitable due to either being in the limits of weakly or strongly ionized plasmas, or from being computationally expensive. In the end

Miller used the formulation developed by Grier [39] for hydrogen, and modified by Pipkin [96] with a correction factor, although this is still fairly cumbersome so Benson rejected it in favour of the similar although simpler formulation of Krier et al. [68], which I shall use;

$$\sigma = \frac{3}{16}\sqrt{\frac{2e^4}{\pi m_e k T_e}}\frac{x_{H+} + x_{Cs+}}{\sum_{s\neq e} x_s \langle \Omega_{es}^{(1,1)} \rangle}. \tag{3.212}$$

3.10.6 Collision Frequencies

Collision frequencies determine the rate of energy and momentum transfer between species and electrons. In general, the average collision frequency of a particle of species s with all particles of species r is

$$\overline{\nu}_{sr} = n_r \overline{g}_{sr} \overline{Q}_{sr}, \tag{3.213}$$

where $\overline{Q}_{sr}$ is the average collision cross section of the colliding particles and $\overline{g}_{sr}$ is the average relative speed of the colliding particles. For electron collisions with the heavy species, as will be used in determining the energy transfer, the relative speed can be approximated as the thermal speed of the electrons, because they travel much faster due to the mass of the electron being so much smaller than that of the other species. Thus

$$\overline{g}_{er} \approx \overline{c}_e = \sqrt{\frac{8kT_e}{\pi m_e}},$$

which makes the collision frequencies of the electrons with the heavy species

$$\begin{aligned}
\overline{\nu}_{eH_2} &= n_{H_2} \overline{c}_e \overline{Q}_{eH_2} \\
\overline{\nu}_{eH} &= n_H \overline{c}_e \overline{Q}_{eH} \\
\overline{\nu}_{eH+} &= n_{H+} \overline{c}_e \overline{Q}_{eH+} \\
\overline{\nu}_{eCs} &= n_{Cs} \overline{c}_e \overline{Q}_{eCs} \\
\overline{\nu}_{eCs+} &= n_{Cs+} \overline{c}_e \overline{Q}_{eCs+}
\end{aligned} \tag{3.214}$$

The hydrogen atom collision cross-section, $\overline{Q}_H$, is taken from Devoto [28], and the molecular cross-sections, $\overline{Q}_{H_2}$ is taken from Itikawa [54]. The cesium atom collision cross-section, $\overline{Q}_{Cs}$, is from Brode [9]. These cross-sections are listed in tabular form in Table C of

Appendix C. For electron-ion collisions, the collision cross section used was the approximate Coulomb cross section:

$$\overline{Q}_{ei} = 6\pi \bar{b}_0^2 \ln\Lambda,$$

$$\bar{b}_0 = \frac{Ze^2}{12\pi\epsilon_0 kT_e}$$

$$\Lambda = \frac{\lambda_D}{\bar{b}_0} = \frac{12\pi\left(\epsilon_0 kT_e\right)^{\frac{3}{2}}}{e^3\sqrt{n_e}} = 1.238 \times 10^7 \sqrt{\frac{T_e^3}{n_e}} \tag{3.215}$$

where λ_D is the Debye length and $\bar{b}_0$ is the impact parameter for 90^o scattering. In this equation, it has been assumed that $\ln\Lambda \gg 1$. This assumption is valid in a majority of physical situations, but breaks down at lower temperatures and higher electron densities. If this situation were to occur, the collision cross section would become negative. In the rare occasions where this would occur, a more accurate form of the Coulomb cross section for electron-ion collisions is [86]

$$\overline{Q}_{ei} = 4\pi b_0^2 \ln\left[1 + \left(\frac{\lambda_D}{b_0}\right)^2\right]^{1/2},$$

$$b_0 = \frac{Ze^2}{32\epsilon_0 kT_e}. \tag{3.216}$$

(note the lack of the over-bar)

3.10.7 Collision Integrals

In the first order approximation to the transport coefficients only the $\langle\Omega_{ij}^{(1,1)}\rangle$ and $\langle\Omega_{ij}^{(2,2)}\rangle$ collision integrals are required. Collision integrals have been calculated by a number of authors, and are easily found for interactions involving hydrogen plasmas. Collision integrals for interactions involving cesium however were not found, so instead were calculate based on cross sections when available or on simple collision theory when not. The $\langle\Omega_{ij}^{(1,1)}\rangle$ integrals are listed in Table D.1 and the $\langle\Omega_{ij}^{(2,2)}\rangle$ integrals are listed in Table D.3 all of which are in Appendix D. For the hydrogen interactions, the data were taken from Vanderslice et al. [129] for the $\langle\Omega_{H_2H_2}^{(2,2)}\rangle$, $\langle\Omega_{H_2H}^{(2,2)}\rangle$, $\langle\Omega_{HH}^{(2,2)}\rangle$, $\langle\Omega_{H_2H_2}^{(1,1)}\rangle$, and $\langle\Omega_{HH}^{(1,1)}\rangle$ for temperatures up to 15,000 K; from Belov [4] for $\langle\Omega_{HH}^{(2,2)}\rangle$ and from Grier [39] for $\langle\Omega_{HH+}^{(2,2)}\rangle$, $\langle\Omega_{eH}^{(2,2)}\rangle$, $\langle\Omega_{eH}^{(1,1)}\rangle$ for the temperature range 5,000-35,000 K. The $\langle\Omega_{H_2e}^{(1,1)}\rangle$ and $\langle\Omega_{H_2e}^{(2,2)}\rangle$ integrals were taken from Benson [5] who calculated them using Equation 3.171 and the total elastic cross-section of

Itikawa [54].

If in future it was wished to change the code to model nitrogen instead of hydrogen as the buffer gas the nitrogen collision integrals have been included. Cubley and Mason [21] have calculated the $\langle\Omega^{(1,1)}_{N_2N_2}\rangle$ and $\langle\Omega^{(2,2)}_{N_2N_2}\rangle$ collision integrals using the exponential repulsive potential, and have curve-fitted their results to the form

$$\langle\Omega^{(l,s)}_{ij}\rangle = AT^{-n}, \tag{3.217}$$

A and n being constants. For the $N_2 - N_2$ interaction, these curve fits are

$$\langle\Omega^{(1,1)}_{N_2N_2}\rangle = 60.6\,T^{-0.274}, \tag{3.218}$$

and

$$\langle\Omega^{(2,2)}_{N_2N_2}\rangle = 51.3\,T^{-0.231}, \tag{3.219}$$

which are valid for a temperature range of 300 - 15,000 K. The $\langle\Omega^{(1,1)}_{N_2N}\rangle$ and $\langle\Omega^{(2,2)}_{N_2N}\rangle$ integrals are taken from Yun and Mason [138] for 1,000 - 15,000 K, the $\langle\Omega^{(1,1)}_{NN}\rangle$ and $\langle\Omega^{(2,2)}_{NN}\rangle$ integrals are taken from Rainwater et al. [102] for 1,000 - 20,000 K, and the $\langle\Omega^{(1,1)}_{NN+}\rangle$ and $\langle\Omega^{(2,2)}_{NN+}\rangle$ integrals are from Stallcop, Partridge, and Levin [121] for 1,000 - 35,000 K.

For the collision integrals for which even cross sections were unavailable, a potential based on a central force was assumed, so $F = -\frac{C}{r^s}$ and $V = -\frac{C}{(s-1)r^{s-1}}$ from which the cross section can be calculated from binary collision theory [130] as

$$Q = 0.844\pi b_o^2 \tag{3.220}$$

where

$$b_o = \left(\frac{\alpha}{\mu g^2}\right)^{\frac{1}{s-1}} \tag{3.221}$$

and converted to a function of temperature using $\frac{1}{2}\mu g^2 = \frac{3}{2}kT$. For collisions between a charged particle and a neutral particle the Maxwellian polarized force was used.

$$F = \left(\frac{2e^2\varrho}{(4\pi\varepsilon_o^2)^2}\right)\frac{1}{r^5}. \tag{3.222}$$

For collisions between neutral particles the London dispersion forces as the attractive $\frac{1}{r^6}$

potential of the Van der Waals force were used.

$$V_{London} = -\frac{3}{2}\left(\frac{E_1 E_2}{E_1 + E_2}\right)\frac{\varrho_1 \varrho_2}{r^6} \tag{3.223}$$

where ϱ is the polarisability and E is the ionization potential. $E_H = E_{H_2} = 13.6\ eV$, $E_{Cs} = 3.87\ eV$. The polarisabilities for H and H_2 are from Hirschfelder, Curtiss, and Bird [48], and the polarisability of Cs was calculated from the cross section between electrons and cesium by Bullis [12]: $\varrho_{H_2} = 0.790\ \mathring{A}^3$, $\varrho_H = 4.5a_o^3 = 0.667\ \mathring{A}^3$, where a_o is the Bohr radius, and $\varrho_{Cs} = 1195\ \mathring{A}^3$.

Once the total cross section $Q^{(1)}$ is known the momentum transfer cross section can be approximated as $Q^{(2)} = \frac{2}{3}Q^{(1)}$ and the required collision integrals calculated from equation 3.171

Whilst collision integrals involving neutral particles are independent of pressure, the Coulombic collision integrals are functions of both pressure and temperature, as shown by equation 3.215. For the $S^+ - S^+$ and $e - e$ interactions the collision integrals are accurately modelled by the methods of Paquette et al. [94] using a repulsive static screened Coulomb potential (SSCP) (see Equation 3.165). For the $e - S^+$ interaction Paquette's methods as modified by MacDonald [77] using the attractive SSCP were used. In both methods, the collision integrals are non-dimensionalised and expressed as a function of a dimensionless variable ψ_{ij}, defined as

$$\psi_{ij} = \ln\left[\ln\left(1 + \gamma_{ij}^2\right)\right], \tag{3.224}$$

where γ_{ij} is another dimensionless variable defined as

$$\gamma_{ij} = \frac{16\pi\epsilon_0 kT\lambda}{Z_i Z_j e^2}, \tag{3.225}$$

where the length scale λ is in meters. In terms of the $\langle\Omega^{(i,j)}\rangle$ collision integrals defined previously, the collision integrals for the repulsive SSCP are

$$\langle\Omega^{(1,1)}\rangle_{rep} = \frac{1}{4}\left(\frac{Z_i Z_j e^2}{4\pi\epsilon_0 kT}\right)^2 F_{Paq}^{(1,1)} \tag{3.226}$$

and

$$\langle\Omega^{(2,2)}\rangle_{rep} = \frac{1}{8}\left(\frac{Z_i Z_j e^2}{4\pi\epsilon_0 kT}\right)^2 F_{Paq}^{(2,2)}, \tag{3.227}$$

while the integrals for the attractive SSCP are

$$\langle \Omega^{(1,1)} \rangle_{att} = \frac{1}{8} \left(\frac{Z_i Z_j e^2}{4\pi\epsilon_0 kT} \right)^2 F_{Mac}^{(1,1)} \tag{3.228}$$

and

$$\langle \Omega^{(2,2)} \rangle_{att} = \frac{1}{16} \left(\frac{Z_i Z_j e^2}{4\pi\epsilon_0 kT} \right)^2 F_{Mac}^{(2,2)}, \tag{3.229}$$

where the $F_{Paq}^{(i,j)}$ and $F_{Mac}^{(i,j)}$ are the dimensionless collision integrals as defined by Paquette et al. and MacDonald, respectively. The factor of $\frac{1}{2}$ difference occurs because of a difference in the way the quantities are defined between the two methods. The resulting expressions for the Coulomb collision integrals are very close in form to Equation 3.10.6 and are in fact a refinement. The advantage of these methods is that both temperature and pressure (concentration) are accounted for implicitly in the γ_{ij}. Table D.5 of Appendix D lists the $F^{(i,j)}$ for both Paquette and MacDonald. At or above $\psi_{ij} = 3.0$, both methods provide simple expressions for the dimensionless collision integrals:

$$F_{Paq}^{(1,1)} = 1.00141\, e^{\psi_{i,j}} - 3.18209 \tag{3.230}$$

$$F_{Paq}^{(2,2)} = 1.99016\, e^{\psi_{i,j}} - 4.56958 \tag{3.231}$$

$$\ln F_{Mac}^{(1,1)} = \psi_{i,j} - 3.30447\, e^{-\psi_{i,j}} - 6.00170\, e^{-2\psi_{i,j}} \tag{3.232}$$

$$\ln F_{Mac}^{(2,2)} = \psi_{i,j} - 2.30571\, e^{-\psi_{i,j}} - 2.92018\, e^{-2\psi_{i,j}} + 0.69315\,. \tag{3.233}$$

For the range of values within an arcjet, however, $\psi_{st} < 3$.

3.11 Summary of Equations

Conservation of Mass

$$\frac{\partial \rho_s}{\partial t} + \frac{1}{r}\left(\frac{\partial \rho_s u_{sr} r}{\partial r} + \frac{\partial \rho_s u_{sz} r}{\partial z}\right) = m_s \dot{n}_s \quad \text{(species)} \tag{3.234}$$

$$\frac{\partial \rho}{\partial t} + \frac{1}{r}\left(\frac{\partial \rho u_r r}{\partial r} + \frac{\partial \rho u_z r}{\partial z}\right) = 0 \quad \text{(global)} \tag{3.235}$$

$$\dot{n}_{S+} = R n_e \left(S_S n_S - n_e n_{S+}\right) \tag{3.236}$$

$$\dot{n}_H = \left(A N_A T^{n_f} e^{-B/\hat{R}T}\left(\hat{m}_H \hat{n}_H + \hat{m}_{H_2}\hat{n}_{H_2}\right) + k_d^e n_e\right)\left(\hat{n}_{H_2} - \frac{\hat{R}T}{K_{p,dis}}\hat{n}_H^2\right) \tag{3.237}$$

Conservation of Momentum

$$\frac{\partial}{\partial t}\left(\rho u_r r\right) + \frac{\partial}{\partial r}\left(\rho u_r^2 r + pr - \tau_{rr} r\right) + \frac{\partial}{\partial z}\left(\rho u_r u_z r - \tau_{rz} r\right) = \rho u_\theta^2 - \tau_{\theta\theta} + p \tag{3.238}$$

$$\frac{\partial}{\partial t}\left(\rho u_\theta r\right) + \frac{\partial}{\partial r}\left(\rho u_r u_\theta r - \tau_{r\theta} r\right) + \frac{\partial}{\partial z}\left(\rho u_\theta u_z r - \tau_{\theta z} r\right) = \tau_{r\theta} - \rho u_r u_\theta \tag{3.239}$$

$$\frac{\partial}{\partial t}\left(\rho u_z r\right) + \frac{\partial}{\partial r}\left(\rho u_r u_z r - \tau_{rz} r\right) + \frac{\partial}{\partial z}\left(\rho u_z^2 r + pr - \tau_{zz} r\right) = 0 \tag{3.240}$$

$$\tau_{rr} = \frac{2}{3}\mu_g\left(2\frac{\partial u_r}{\partial r} - \frac{\partial u_z}{\partial z} - \frac{u_r}{r}\right) \tag{3.241}$$

$$\tau_{\theta\theta} = \frac{2}{3}\mu_g\left(2\frac{u_r}{r} - \frac{\partial u_r}{\partial r} - \frac{\partial u_z}{\partial z}\right) \tag{3.242}$$

$$\tau_{zz} = \frac{2}{3}\mu_g\left(2\frac{\partial u_z}{\partial z} - \frac{\partial u_r}{\partial r} - \frac{u_r}{r}\right) \tag{3.243}$$

$$\tau_{r\theta} = \mu_g\left(\frac{\partial u_\theta}{\partial r} - \frac{u_\theta}{r}\right) \tag{3.244}$$

$$\tau_{rz} = \mu_g\left(\frac{\partial u_r}{\partial z} + \frac{\partial u_z}{\partial r}\right) \tag{3.245}$$

$$\tau_{\theta z} = \mu_g \frac{\partial u_\theta}{\partial z} \tag{3.246}$$

Conservation of Energy

Heavy Species Energy Equation:

$$\frac{\partial}{\partial t}\left(\rho e_g\right)+\frac{\partial}{\partial r}\left(\rho h_g u_r+q_{gr}\right)+\frac{1}{r}\left(\rho h_g u_r+q_{gr}\right)+\frac{\partial}{\partial z}\left(\rho h_g u_z+q_{gz}\right)-u_r\frac{\partial p_g}{\partial r}-u_z\frac{\partial p_g}{\partial z}$$

$$+\frac{\partial}{\partial r}\left(\rho_{H_2}h_{H_2}V_{H_2r}+\rho_H h_H V_{Hr}+\rho_{H+}h_{H+}V_{H+r}+\rho_{Cs}h_{Cs}V_{Csr}+\rho_{Cs+}h_{Cs+}V_{Cs+r}\right)$$

$$+\frac{1}{r}\left(\rho_{H_2}h_{H_2}V_{H_2r}+\rho_H h_H V_{Hr}+\rho_{H+}h_{H+}V_{H+r}+\rho_{Cs}h_{Cs}V_{Csr}+\rho_{Cs+}h_{Cs+}V_{Cs+r}\right)$$

$$+\frac{\partial}{\partial z}\left(\rho_{H_2}h_{H_2}V_{H_2z}+\rho_H h_H V_{Hz}+\rho_{H+}h_{H+}V_{H+z}+\rho_{Cs}h_{Cs}V_{Csz}+\rho_{Cs+}h_{Cs+}V_{Cs+z}\right)$$

$$-V_{H_2r}\frac{\partial p_{H_2}}{\partial r}-V_{Hr}\frac{\partial p_H}{\partial r}-V_{H+r}\frac{\partial p_{H+}}{\partial r}-V_{Csr}\frac{\partial p_{Cs}}{\partial r}-V_{Cs+r}\frac{\partial p_{Cs+}}{\partial r}$$

$$-V_{H_2z}\frac{\partial p_{H_2}}{\partial z}-V_{Hz}\frac{\partial p_H}{\partial z}-V_{H+z}\frac{\partial p_{H+}}{\partial z}-V_{Csz}\frac{\partial p_{Cs}}{\partial z}-V_{Cs+z}\frac{\partial p_{Cs+}}{\partial z}$$

$$=\Phi-M_e-\frac{1}{2}e_d\left(\dot{n}_H+k_d^e n_e n_{H_2}\right) \tag{3.247}$$

$$\Phi=\mu_g\left[2\left(\frac{\partial u_r}{\partial r}\right)^2+2\left(\frac{\partial u_z}{\partial z}\right)^2+2\left(\frac{u_r}{r}\right)^2+\left(\frac{\partial u_r}{\partial z}+\frac{\partial u_z}{\partial r}\right)^2\right.$$

$$\left.+\left(\frac{\partial u_\theta}{\partial r}-\frac{u_\theta}{r}\right)^2+\left(\frac{\partial u_\theta}{\partial z}\right)^2-\frac{2}{3}\left(\frac{\partial u_r}{\partial r}+\frac{\partial u_z}{\partial z}+\frac{u_r}{r}\right)^2\right] \tag{3.248}$$

$$M_e=3k\left(T_g-T_e\right)\frac{\rho_e}{m_H}\left(\overline{\nu}_{eH+}+\overline{\nu}_{eH}+\frac{1}{2}\delta_{H_2}\overline{\nu}_{eH_2}\right)+3k\left(T_g-T_e\right)\frac{\rho_e}{m_{Cs}}\left(\overline{\nu}_{eCs+}+\overline{\nu}_{eCs}\right)$$

$$=\frac{m_e}{m_H}3k\left(T_g-T_e\right)n_e\left(n_{H_2}\overline{c}_e Q_{eH_2}\frac{\delta_{H_2}}{2}+n_H\overline{c}_e Q_{eH}+n_{H+}\overline{c}_e Q_{eH+}\right)$$

$$+\frac{m_e}{m_{Cs}}3k\left(T_g-T_e\right)n_e\left(n_{Cs}\overline{c}_e Q_{eCs}+n_{Cs+}\overline{c}_e Q_{eCs+}\right) \tag{3.249}$$

$$\rho e_g=\frac{3}{2}\left(\rho_H+\rho_{H+}\right)R_H T_g+\frac{3}{2}\left(\rho_{Cs}+\rho_{Cs+}\right)R_{Cs}T_g+\frac{5}{2}\rho_{H_2}R_{H_2}T_g$$

$$+\frac{\rho_{H_2}R_{H_2}\theta_v}{e^{\frac{\theta_v}{T_g}}-1}-\frac{7}{4}\left(\rho_H+\rho_{H+}+\rho_{H_2}\right)R_H T_g \tag{3.250}$$

$$e_{H_2} = \frac{5}{2} R_{H_2} T_g - \frac{7}{2} R_{H_2} T_f + \frac{R_{H_2} \theta_v}{e^{\frac{\theta_v}{T_g}} - 1} \tag{3.251}$$

$$e_H = e_{H+} = \frac{3}{2} R_H T_g - \frac{7}{4} R_H T_f \tag{3.252}$$

$$e_{Cs} = e_{Cs+} = \frac{3}{2} R_{Cs} T_g \tag{3.253}$$

$$\rho h_g = \rho e_g + \rho_{H_2} R_{H_2} T_g + (\rho_H + \rho_{H+}) R_H T_g + (\rho_{Cs} + \rho_{Cs+}) R_{Cs} T_g \tag{3.254}$$

$$h_s = e_s + R_s T_g = e_s + \frac{P_s}{\rho_s} \tag{3.255}$$

Electron Energy Equation

$$\frac{\partial}{\partial t}(\rho_e E_e r) + \frac{\partial}{\partial r}(\rho_e H_e u_{er} r + q_{er} r) + \frac{\partial}{\partial z}(\rho_e H_e u_{ez} r + q_{ez} r)$$

$$= \left(\frac{j^2}{\sigma} + M_e - e_d \, k_d^e \, n_e n_{S_2} - e_i \dot{n}_e - \dot{R} \right) r \tag{3.256}$$

$$E_e = \frac{3}{2} R_e T_e + \frac{1}{2} u_e^2 \tag{3.257}$$

$$H_e = E_e + R_e T_e \tag{3.258}$$

Electrical Potential

$$\frac{\partial}{\partial r}\left(r\sigma \frac{\partial \phi}{\partial r} \right) + \frac{\partial}{\partial z}\left(r\sigma \frac{\partial \phi}{\partial z} \right) = \frac{\partial}{\partial r}\left(r\psi \frac{\partial p_e}{\partial r} \right) + \frac{\partial}{\partial z}\left(r\psi \frac{\partial p_e}{\partial z} \right) \tag{3.259}$$

Equation of State

$$p_g = \rho_{H_2} R_{H_2} T_g + \rho_H R_H T_g + \rho_{H+} R_H T_g + \rho_{Cs} R_{Cs} T_g + \rho_{Cs+} R_{Cs} T_g \tag{3.260}$$

$$p_e = \rho_e R_e T_e \tag{3.261}$$

Miscellaneous Equations

Current Density:

$$j_z = \psi \frac{\partial p_e}{\partial z} - \sigma \frac{\partial \phi}{\partial z} \qquad j_r = \psi \frac{\partial p_e}{\partial r} - \sigma \frac{\partial \phi}{\partial r} \tag{3.262}$$

Heat Flux:

$$q_{gz} = -\kappa_g \frac{\partial T_g}{\partial z} \qquad q_{gr} = -\kappa_g \frac{\partial T_g}{\partial r} \tag{3.263}$$

$$q_{ez} = -\kappa_e \frac{\partial T_e}{\partial z} \qquad q_{er} = -\kappa_e \frac{\partial T_e}{\partial r} \tag{3.264}$$

Slip Velocity:

$$u_{sz} = u_z + V_{sz} \qquad u_{sr} = u_r + V_{sr} \tag{3.265}$$

$$V_{Hz} = -\frac{D_H}{\rho_H}\frac{\partial \rho_H}{\partial z} \qquad V_{Hr} = -\frac{D_H}{\rho_H}\frac{\partial \rho_H}{\partial r} \tag{3.266}$$

$$V_{Csz} = -\frac{D_{Cs}}{\rho_{Cs}}\frac{\partial \rho_{Cs}}{\partial z} \qquad V_{Csr} = -\frac{D_{Cs}}{\rho_{Cs}}\frac{\partial \rho_{Cs}}{\partial r} \tag{3.267}$$

$$V_{H+z} = -\frac{D_{H+}}{\rho_{H+}}\frac{\partial \rho_{H+}}{\partial z} - \frac{eD_{H+}}{kT_g}\frac{\partial \phi}{\partial z} \qquad V_{H+r} = -\frac{D_{H+}}{\rho_{H+}}\frac{\partial \rho_{H+}}{\partial r} - \frac{eD_{H+}}{kT_g}\frac{\partial \phi}{\partial r} \tag{3.268}$$

$$V_{Cs+z} = -\frac{D_{Cs+}}{\rho_{Cs+}}\frac{\partial \rho_{Cs+}}{\partial z} - \frac{eD_{Cs+}}{kT_g}\frac{\partial \phi}{\partial z} \qquad V_{Cs+r} = -\frac{D_{Cs+}}{\rho_{Cs+}}\frac{\partial \rho_{Cs+}}{\partial r} - \frac{eD_{Cs+}}{kT_g}\frac{\partial \phi}{\partial r} \tag{3.269}$$

$$\rho_{H_2}\vec{V}_{H_2} = \frac{m_e}{e}\vec{J} - \rho_H\vec{V}_H - \rho_{H+}\vec{V}_{H+} - \rho_{Cs}\vec{V}_{Cs} - \rho_{Cs+}\vec{V}_{Cs+} \tag{3.270}$$

Chapter 4

Numerical Method

Once the equations governing the physics have been derived, it is then necessary to discretize the equations for numerical calculations. Typically, the conservation equations are put in strong conservative form, in anticipation of shocks or other discontinuities within the flow. The reason for this is that the fluxes as defined in the conservative formulation are conserved across discontinuities such as shocks. Although no shocks are anticipated within the flow to be modeled, the conservative form was used.

The governing equations are, basically, a modified form of the compressible Navier-Stokes equations, with terms added to account for non-equilibrium chemistry and thermodynamics. In axisymmetric coordinates, the governing equations can be represented as

$$\frac{\partial \mathbf{U}}{\partial t} + \frac{1}{r}\left(\frac{\partial \mathbf{F}}{\partial z} + \frac{\partial \mathbf{G}}{\partial r}\right) = \mathbf{S}, \tag{4.1}$$

where $\mathbf{U}$ is the state vector, $\mathbf{F}$ and $\mathbf{G}$ are flux vectors in the z and r directions, respectively, and $\mathbf{S}$ is a vector of source terms. Putting the previously derived equations in vector form, these vector quantities are:

$$\mathbf{U} = \begin{bmatrix} \rho \\ \rho u_z \\ \rho u_r \\ \rho u_\theta \\ \rho e_g \\ \\ \rho_e E_e \\ \\ \rho_H \\ \rho_{H+} \\ \rho_{Cs} \\ \rho_{Cs+} \end{bmatrix},$$

$$\mathbf{F} = \begin{bmatrix} \rho u_z r \\ \left(\rho u_z^2 + P - \tau_{zz}\right) r \\ \left(\rho u_r u_z - \tau_{rz}\right) r \\ \left(\rho u_\theta u_z - \tau_{\theta z}\right) r \\ \left(\rho h_g u_z + q_{gz} + \sum_s \rho_s h_s V_{sz}\right) r \\ \\ \left(\rho_e H_e u_{ez} + q_{ez}\right) r \\ \\ \rho_H \left(u_z + V_{Hz}\right) r \\ \rho_{H+} \left(u_z + V_{H+z}\right) r \\ \rho_{Cs} \left(u_z + V_{Csz}\right) r \\ \rho_{Cs+} \left(u_z + V_{Cs+z}\right) r \end{bmatrix},$$

$$\mathbf{G} = \begin{bmatrix} \rho u_r r \\ (\rho u_r u_z - \tau_{rz})\, r \\ (\rho u_r^2 + P - \tau_{rr})\, r \\ (\rho u_r u_\theta - \tau_{r\theta})\, r \\ (\rho h_g u_r + q_{gr} + \sum_s \rho_s h_s V_{sr})\, r \\ \\ (\rho_e H_e u_{er} + q_{er})\, r \\ \\ \rho_H\,(u_r + V_{Hr})\, r \\ \rho_{H+}\,(u_r + V_{H+r})\, r \\ \rho_{Cs}\,(u_r + V_{Csr})\, r \\ \rho_{Cs+}\,(u_r + V_{Cs+r})\, r \end{bmatrix},$$

$$\mathbf{S} = \begin{bmatrix} 0 \\ 0 \\ (\rho u_\theta^2 - \tau_{\theta\theta} + P)\,/r \\ (\tau_{r\theta} - \rho u_r u_\theta)\,/r \\ u_r \frac{\partial p_g}{\partial r} + u_z \frac{\partial p_g}{\partial z} + \sum_s \vec{v}_s \cdot \nabla P_s - M_e + \Phi - \frac{1}{2} e_d \dot{n}_{H,total} \\ \\ \left(\frac{J^2}{\sigma} + M_e - e_d k_d^e n_e n_{H_2} - e_{iH}\dot{n}_{H+} - e_{iCs}\dot{n}_{Cs+} - \dot{R}\right) r \\ \\ m_H\,(\dot{n}_{H,total} - \dot{n}_{H+}) \;=\; m_H\,(\dot{n}_{H,heavy} + k_d^e\, n_e n_{H_2} - \dot{n}_{H+}) \\ m_H \dot{n}_{H+} \\ -m_{Cs}\dot{n}_{Cs+} \\ m_{Cs}\dot{n}_{Cs+} \end{bmatrix}. \tag{4.2}$$

Because of the complexity of the equations and the boundary conditions, initially an explicit numerical scheme was chosen to integrate the fluid equations, since it is simpler to implement. Startup behaviour and transient phenomena may be of interest so the scheme should be accurate in time, and was originally implemented with a global timestep, although this led to the inlet area (where the flow is very slow) taking an extremely long time to

converge, so was changed to local timestepping. MacCormack's Method was originally chosen as the scheme because in its explicit form, it was simpler to code than an implicit scheme, and also because this scheme is second order accurate in both space and time. Later many different integrations schemes were tried, settling on a particular Total Variation Diminishing (TVD) Scheme that seemed to perform well. Due to its elliptic nature, the potential equation (Equation 3.53) is solved using Successive Over-Relaxation (SOR) since if it was solved by MacCormack's Method this would result in prohibitively small timesteps in order to ensure stability.

4.1 Coordinate Transformation

Both the fluid integration schemes and Successive Over-Relaxation use finite differences to approximate the derivatives. Since the computational grid used is curvilinear and not Cartesian, the governing equations first have to be transformed into the coordinate system of the grid, also known as the natural coordinate system.

Using the chain rule of calculus, the radial and axial derivatives can be converted into derivatives in the natural coordinates ξ and η

$$\frac{\partial}{\partial r} = \frac{\partial \xi}{\partial r}\frac{\partial}{\partial \xi} + \frac{\partial \eta}{\partial r}\frac{\partial}{\partial \eta} = \xi_r \frac{\partial}{\partial \xi} + \eta_r \frac{\partial}{\partial \eta}, \tag{4.3}$$

$$\frac{\partial}{\partial z} = \frac{\partial \xi}{\partial z}\frac{\partial}{\partial \xi} + \frac{\partial \eta}{\partial z}\frac{\partial}{\partial \eta} = \xi_z \frac{\partial}{\partial \xi} + \eta_z \frac{\partial}{\partial \eta}, \tag{4.4}$$

where ξ_r, ξ_z, η_r, and η_z are known as the metrics of the transformation. From the definition of a total derivative, it can be shown [1] that:

$$\begin{bmatrix} \xi_z & \xi_r \\ \eta_z & \eta_r \end{bmatrix} = \begin{bmatrix} z_\xi & z_\eta \\ r_\xi & r_\eta \end{bmatrix}^{-1} = \frac{1}{J}\begin{bmatrix} r_\eta & -z_\eta \\ -r_\xi & z_\xi \end{bmatrix}, \tag{4.5}$$

where $J = z_\xi r_\eta - z_\eta r_\xi$ is the Jacobian of the transformation. Similarly, the second derivatives in r and z may be written as

$$\begin{aligned} \frac{\partial^2}{\partial r^2} &= \left(\xi_r \frac{\partial}{\partial \xi} + \eta_r \frac{\partial}{\partial \eta}\right)\left(\xi_r \frac{\partial}{\partial \xi} + \eta_r \frac{\partial}{\partial \eta}\right) \\ &= {\xi_r}^2 \frac{\partial^2}{\partial \xi^2} + 2\xi_r \eta_r \frac{\partial^2}{\partial \xi \partial \eta} + {\eta_r}^2 \frac{\partial^2}{\partial \eta^2} + \xi_{rr}\frac{\partial}{\partial \xi} + \eta_{rr}\frac{\partial}{\partial \eta} \end{aligned} \tag{4.6}$$

$$\begin{aligned}\frac{\partial^2}{\partial z^2} &= \left(\xi_z\frac{\partial}{\partial\xi}+\eta_z\frac{\partial}{\partial\eta}\right)\left(\xi_z\frac{\partial}{\partial\xi}+\eta_z\frac{\partial}{\partial\eta}\right)\\ &= {\xi_z}^2\frac{\partial^2}{\partial\xi^2}+2\xi_z\eta_z\frac{\partial^2}{\partial\xi\partial\eta}+{\eta_z}^2\frac{\partial^2}{\partial\eta^2}+\xi_{zz}\frac{\partial}{\partial\xi}+\eta_{zz}\frac{\partial}{\partial\eta},\end{aligned} \tag{4.7}$$

where

$$\xi_{rr}=\xi_r\left(\xi_r\right)_\xi+\eta_r\left(\xi_r\right)_\eta=\left[z_\eta\left(z_{\xi\eta}J-z_\eta J_\xi\right)-z_\xi\left(z_{\eta\eta}J-z_\eta J_\eta\right)\right]/J^3 \tag{4.8}$$

$$\xi_{zz}=\xi_z\left(\xi_z\right)_\xi+\eta_z\left(\xi_z\right)_\eta=\left[r_\eta\left(r_{\xi\eta}J-r_\eta J_\xi\right)-r_\xi\left(r_{\eta\eta}J-r_\eta J_\eta\right)\right]/J^3 \tag{4.9}$$

$$\eta_{rr}=\xi_r\left(\eta_r\right)_\xi+\eta_r\left(\eta_r\right)_\eta=\left[z_\xi\left(z_{\xi\eta}J-z_\xi J_\eta\right)-z_\eta\left(z_{\xi\xi}J-z_\xi J_\xi\right)\right]/J^3 \tag{4.10}$$

$$\eta_{zz}=\xi_z\left(\eta_z\right)_\xi+\eta_z\left(\eta_z\right)_\eta=\left[r_\xi\left(r_{\xi\eta}J-r_\xi J_\eta\right)-r_\eta\left(r_{\xi\xi}J-r_\xi J_\xi\right)\right]/J^3. \tag{4.11}$$

4.1.1 Numerical Grid

To discretize the domain within an arcjet initially two grids were used. The first mesh was used for the fluid flow field, and approximates the geometry of the German TT1 arcjet. The fluid grid is clustered near the walls in order to resolve the viscous boundary layer, and also near the cathode tip and arc attachment point at the constrictor exit, in order to resolve sharp gradients at those locations.

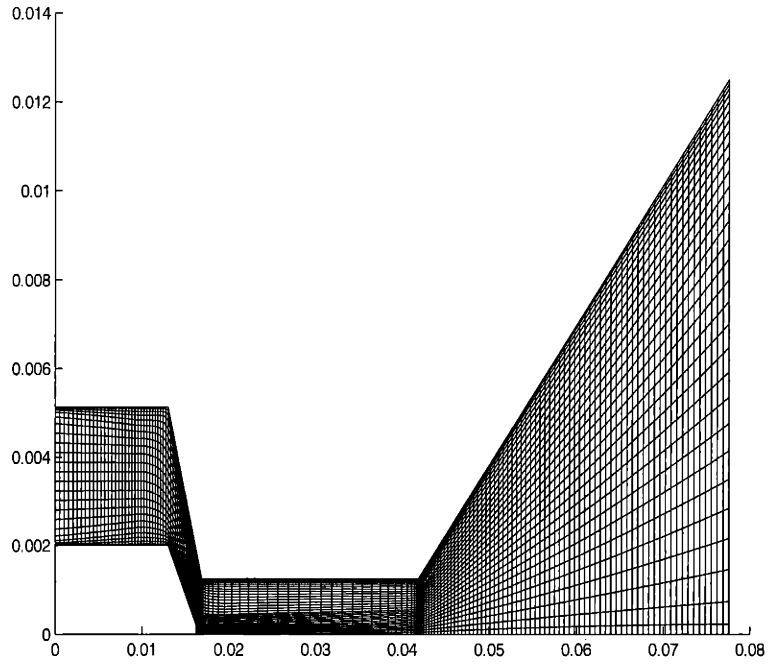

Figure 4-1: *Original Grid on which Flow was Modelled*

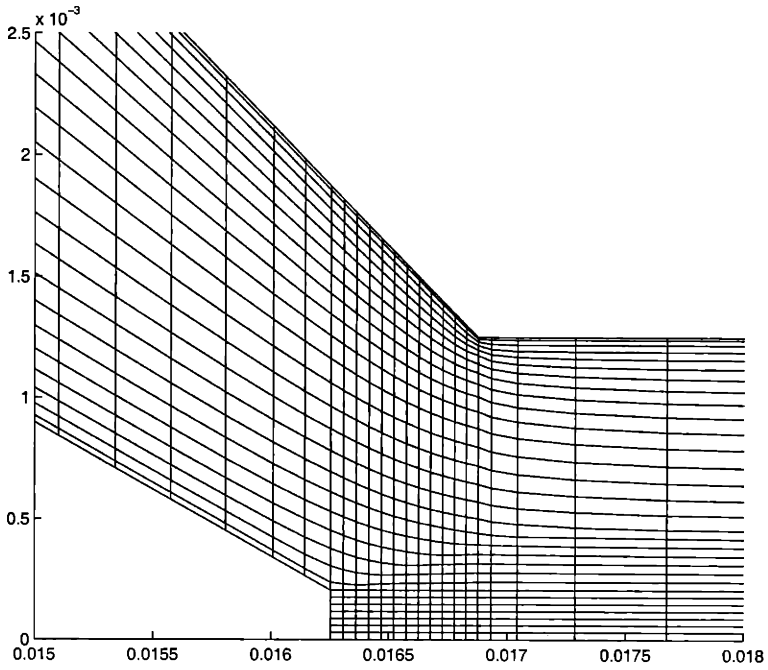

Figure 4-2: *The Original Flow Grid near the Cathode Tip*

The original fluid grid is 162 by 30, and only half the thruster is modelled since it is axisymmetric about the centreline. The cathode tip is modelled as a blunt vertical plane to make modelling the boundary conditions there simpler, which is not unreasonable since physically during startup of an arcjet the arc ablates the cathode tip until the tip is blunted. The grid was stretched from the original TT1 design used by Miller, to a length over diameter ratio of ten. This is because for a seeded arcjet which is to be run at much lower temperatures than a conventional arcjet the electrical conductivity is much lower which leads to less power deposited per unit volume. Thus to deposit a comparable amount of energy the seeded arcjet needs a much longer constrictor for the propellant to flow through and be heated. Oyerokun [93] in his research found that for a cesium seed fraction of two percent by mass in hydrogen, the required L/D ratio was about 10. Grid lines of constant ξ were taken to be of constant z as well, although lines of constant η were allowed to float in the r direction to obtain a smoothly distributed grid. Generally it is better to keep grid lines orthogonal to each other and to the boundaries especially, whereas the grids used meet at an angle, but the advantage with this formulation is that $\frac{\partial \xi}{\partial r} = 0$ so

$$\frac{\partial}{\partial r} = \eta_r \frac{\partial}{\partial \eta} \qquad \frac{\partial}{\partial z} = \eta_z \frac{\partial}{\partial \eta} + \xi_z \frac{\partial}{\partial \xi} \tag{4.12}$$

which means that less calculations have to be done within the code, hence it is faster. Later grids allowed lines of constant ξ to vary in the z direction, and the $\xi_r \frac{\partial}{\partial \xi}$ term was reinstated.

The second mesh is for the electric potential calculation. All the current was confined to attaching on the cathode tip and also not allowed to flow upstream. This means that if calculations were done on the fluid grid a lot of time could be wasted in calculating the potential upstream of the entrance to the constrictor. Secondly, although the fluid grid is concentrated at the cathode tip, it is not concentrated enough to obtain smooth and accurate values for the potential. Consequently a separate grid was used for the potential near the cathode tip, which was then patched to the fluid grid for calculations within the constrictor and nozzle. Potentials calculated on the finer potential grid are then interpolated onto the fluid grid for fluid flow calculations.

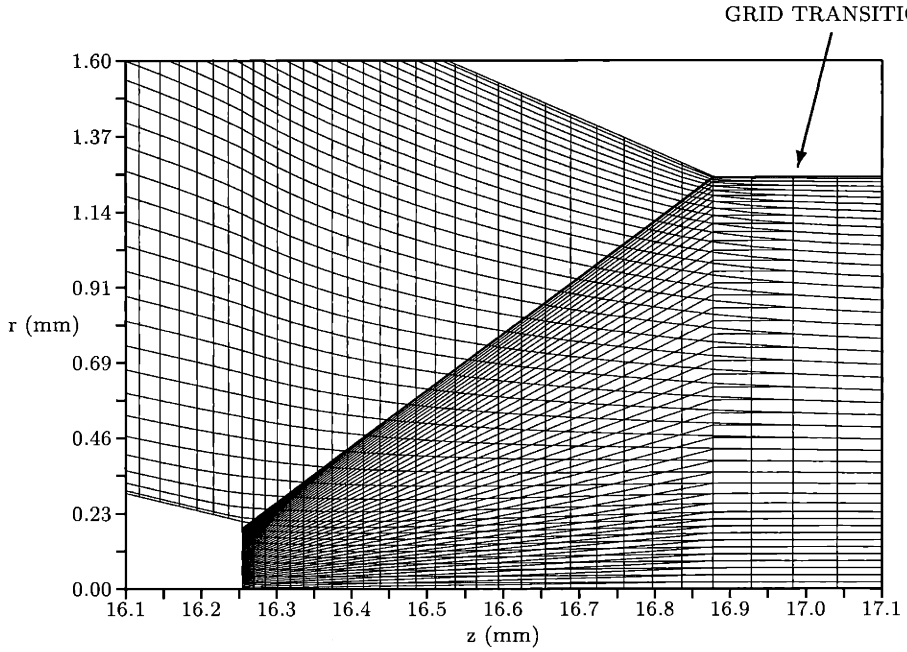

Figure 4-3: *Electric Potential Grid shown overlapping the Flow Grid*

Later grids included grids containing more points, especially near the boundary layers, and also curvilinear grids where a line of constant ξ connected the cathode tip to the constrictor entrance. For these grids a separate potential grid was not always used.

4.1.2 Fluid Flow Equations

Using Equations 4.3,4.4 and 4.5, the vector form of the governing fluid equations becomes

$$\frac{\partial \mathbf{U}}{\partial t} + \frac{1}{r}\left(\frac{r_\eta}{J}\frac{\partial \mathbf{F}}{\partial \xi} - \frac{r_\xi}{J}\frac{\partial \mathbf{F}}{\partial \eta} - \frac{z_\eta}{J}\frac{\partial \mathbf{G}}{\partial \xi} + \frac{z_\xi}{J}\frac{\partial \mathbf{G}}{\partial \eta}\right) = S. \tag{4.13}$$

Multiplying both sides by J and noting that

$$r_\eta \frac{\partial \mathbf{F}}{\partial \xi} = \frac{\partial}{\partial \xi}(\mathbf{F} r_\eta) - \mathbf{F} r_{\xi\eta} \tag{4.14}$$

$$r_\xi \frac{\partial \mathbf{F}}{\partial \eta} = \frac{\partial}{\partial \eta}(\mathbf{F} r_\xi) - \mathbf{F} r_{\xi\eta} \tag{4.15}$$

$$z_\eta \frac{\partial \mathbf{G}}{\partial \xi} = \frac{\partial}{\partial \xi}(\mathbf{G} z_\eta) - \mathbf{G} z_{\xi\eta} \tag{4.16}$$

$$z_\xi \frac{\partial \mathbf{G}}{\partial \eta} = \frac{\partial}{\partial \eta}(\mathbf{G} z_\xi) - \mathbf{G} z_{\xi\eta}, \tag{4.17}$$

the conservative form of the governing equations in natural coordinates can be written as

$$J\frac{\partial \mathbf{U}}{\partial t} + \frac{1}{r}\left(\frac{\partial \tilde{\mathbf{F}}}{\partial \xi} + \frac{\partial \tilde{\mathbf{G}}}{\partial \eta}\right) = J\mathbf{S}, \tag{4.18}$$

where

$$\tilde{\mathbf{F}} = \mathbf{F} r_\eta - \mathbf{G} z_\eta \tag{4.19}$$

$$\tilde{\mathbf{G}} = \mathbf{G} z_\xi - \mathbf{F} r_\xi. \tag{4.20}$$

Since the grid is not changing with time, the Jacobian of the transformation can be lumped with the state vector inside the $\frac{\partial}{\partial t}$ term or left outside with equal accuracy. Computationally, the latter formulation is performed, since the state vector can then be found directly from the integration.

As with all numerical methods, some sort of numerical smoothing is necessary so that the discretized set of equations does not diverge. Applying this numerical smoothing to the right hand side of Equation 4.18, the resulting form can be written as

$$J\frac{\partial \mathbf{U}}{\partial t} + \frac{1}{r}\left(+\frac{\partial \tilde{\mathbf{F}}}{\partial \xi} + \frac{\partial \tilde{\mathbf{G}}}{\partial \eta}\right) = J\mathbf{S} + \nu_2\left(\frac{\partial^2 \mathbf{U}}{\partial \xi^2} + \frac{\partial^2 \mathbf{U}}{\partial \eta^2}\right) + \nu_4\left(\frac{\partial^4 \mathbf{U}}{\partial \xi^4} + \frac{\partial^4 \mathbf{U}}{\partial \eta^4}\right), \tag{4.21}$$

where ν_2 and ν_4 are artificial viscosity coefficients, and are adjusted depending on the

amount of smoothing necessary. It is this form of the governing equations which was originally integrated. The second order terms are needed in regions of steep gradients such as capturing shocks, while the fourth order terms are needed to damp out sawtooth oscillations that are a solution to the discretized equation, but not the continuous differential one.

4.1.3 Potential Equation

Transforming the electrical potential equation is rather long winded, due to the second derivative terms and the elliptical nature of the potential equation. The electrical potential equation in axisymmetric coordinates is given by Equation 3.259 and restated here:

$$\frac{\partial}{\partial r}\left(r\sigma\frac{\partial\phi}{\partial r}\right)+\frac{\partial}{\partial z}\left(r\sigma\frac{\partial\phi}{\partial z}\right)=\frac{\partial}{\partial r}\left(r\psi\frac{\partial p_e}{\partial r}\right)+\frac{\partial}{\partial z}\left(r\psi\frac{\partial p_e}{\partial z}\right), \tag{4.22}$$

which becomes, after expanding the derivative terms,

$$\sigma\frac{\partial^2\phi}{\partial z^2}+\sigma\frac{\partial^2\phi}{\partial r^2}+\frac{\partial\sigma}{\partial z}\frac{\partial\phi}{\partial z}+\left(\frac{\partial\sigma}{\partial r}+\frac{\sigma}{r}\right)\frac{\partial\phi}{\partial r}=\psi\frac{\partial^2 p_e}{\partial z^2}+\psi\frac{\partial^2 p_e}{\partial r^2}+\frac{\partial\psi}{\partial z}\frac{\partial p_e}{\partial z}+\left(\frac{\partial\psi}{\partial r}+\frac{\psi}{r}\right)\frac{\partial p_e}{\partial r}. \tag{4.23}$$

Using Equations 4.3-4.11 the potential equation is transformed into

$$a\frac{\partial^2\phi}{\partial\xi^2}+b\frac{\partial^2\phi}{\partial\eta^2}+c\frac{\partial^2\phi}{\partial\xi\partial\eta}+d\frac{\partial\phi}{\partial\xi}+e\frac{\partial\phi}{\partial\eta}=f\left(p_e,\sigma,\psi,r\right), \tag{4.24}$$

where

$$a=\sigma\left(\xi_r^2+\xi_z^2\right) \tag{4.25}$$

$$b=\sigma\left(\eta_r^2+\eta_z^2\right) \tag{4.26}$$

$$c=2\sigma\left(\xi_r\eta_r+\xi_z\eta_z\right) \tag{4.27}$$

$$d=\sigma\left(\xi_{rr}+\xi_{zz}+\frac{\xi_r}{r}\right)+\frac{a}{\sigma}\frac{\partial\sigma}{\partial\xi}+\frac{c}{2\sigma}\frac{\partial\sigma}{\partial\eta} \tag{4.28}$$

$$e=\sigma\left(\eta_{rr}+\eta_{zz}+\frac{\eta_r}{r}\right)+\frac{c}{2\sigma}\frac{\partial\sigma}{\partial\xi}+\frac{b}{\sigma}\frac{\partial\sigma}{\partial\eta} \tag{4.29}$$

and

$$f\left(p_e,\sigma,\psi,r\right)=\frac{\psi}{\sigma}\left(a\frac{\partial^2 p_e}{\partial\xi^2}+b\frac{\partial^2 p_e}{\partial\eta^2}+c\frac{\partial^2 p_e}{\partial\xi\partial\eta}\right)+d'\frac{\partial p_e}{\partial\xi}+e'\frac{\partial p_e}{\partial\eta}, \tag{4.30}$$

where

$$d' = \psi\left(\xi_{rr} + \xi_{zz} + \frac{\xi_r}{r}\right) + \frac{a}{\sigma}\frac{\partial\psi}{\partial\xi} + \frac{c}{2\sigma}\frac{\partial\psi}{\partial\eta} \tag{4.31}$$

$$e' = \psi\left(\eta_{rr} + \eta_{zz} + \frac{\eta_r}{r}\right) + \frac{c}{2\sigma}\frac{\partial\psi}{\partial\xi} + \frac{b}{\sigma}\frac{\partial\psi}{\partial\eta}. \tag{4.32}$$

4.2 MacCormack's Method

4.2.1 Description

MacCormack's method [74], developed in 1969, is a two step predictor-corrector scheme based on the Lax-Wendroff method. The overall scheme is accurate to order $(\Delta t)^2, (\Delta x)^2$, where Δt is the timestep and Δx is the grid spacing, which allows accurate prediction of transient phenomena if necessary. In terms of the transformed fluid equations, MacCormack's method is written as

Predictor

$$\mathbf{U}^P_{i,j} = \mathbf{U}^n_{i,j} - \frac{\Delta t}{\Delta\xi}\left(\tilde{\mathbf{F}}^n_{i+1,j} - \tilde{\mathbf{F}}^n_{i,j}\right) - \frac{\Delta t}{\Delta\eta}\left(\tilde{\mathbf{G}}^n_{i,j+1} - \tilde{\mathbf{G}}^n_{i,j}\right) + \Delta t\mathbf{S}^n_{i,j} \tag{4.33}$$

Corrector

$$\mathbf{U}^{n+1}_{i,j} = \frac{1}{2}\left[\mathbf{U}^P_{i,j} + \mathbf{U}^n_{i,j} - \frac{\Delta t}{\Delta\xi}\left(\tilde{\mathbf{F}}^P_{i,j} - \tilde{\mathbf{F}}^P_{i-1,j}\right) - \frac{\Delta t}{\Delta\eta}\left(\tilde{\mathbf{G}}^P_{i,j} - \tilde{\mathbf{G}}^P_{i,j-1}\right) + \Delta t\mathbf{S}^P_{i,j}\right] \tag{4.34}$$

where the superscript n denotes the iteration step, and the subscripts i,j denote the discrete grid points, and because of the coordinate transformation, $\Delta\xi = \Delta\eta = 1$.

In addition to the flux differencing, finite differences are needed for the gradients in the transport equations. It is important to difference the gradients properly to ensure second order accuracy. This is accomplished as follows, where fluxes in the $z-r$ coordinate system are used for simplicity. In the $\mathbf{F}$ flux vectors, the derivatives with respect to z are differenced opposite to the way $\mathbf{F}$ is differenced, while the r derivatives are differenced centrally. In the $\mathbf{G}$ flux vectors, the derivatives with respect to r are differenced opposite to the way $\mathbf{G}$ is differenced, while the z derivatives are differenced centrally. For example, take the z-momentum term in the radial momentum equation:

$$F = \left(\rho u_r u_z - \mu\frac{\partial u_r}{\partial z} - \mu\frac{\partial u_z}{\partial r}\right) r. \tag{4.35}$$

When used in the corrector step above, the $\frac{\partial u_r}{\partial z}$ term is differenced in the forward direction, since the flux vector itself is differenced in the backward direction. The $\frac{\partial u_z}{\partial r}$ is differenced centrally. Therefore, a correctly differenced z-momentum term in the corrector step would appear as

$$\frac{F^n_{i,j} - F^n_{i-1,j}}{\Delta z} = \frac{1}{\Delta z}\left[(\rho u_r u_z r)_{i,j} - \mu_{i,j}\frac{u_{r\,i+1,j} - u_{r\,i,j}}{\Delta z} r_{i,j} - \mu_{i,j}\frac{u_{z\,i,j+1} - u_{z\,i,j-1}}{2\Delta r} r_{i,j}\right.$$

$$\left. - (\rho u_r u_z r)_{i-1,j} + \mu_{i-1,j}\frac{u_{r\,i,j} - u_{r\,i-1,j}}{\Delta z} r_{i-1,j} + \mu_{i-1,j}\frac{u_{z\,i-1,j+1} - u_{z\,i-1,j-1}}{2\Delta r} r_{i-1,j}\right]. \quad (4.36)$$

4.2.2 Consistency, Stability and Convergence

A numerical scheme is consistent if the discretized equations are identical to the differential equation in the limit of infinitesimal length and time steps, [1], but more than that is necessary for the discrete equation to yield a correct solution. According to the Lax Equivalence Theorem (see Richtmyer and Morton [107]), stability is the necessary and sufficient condition for a finite difference scheme to converge to the solution of the differential equation. Implicit numerical schemes, by their very nature, are unconditionally stable. Explicit methods are only conditionally stable, which means there is a limit on the timestep that can be used in the numerical integration. For most non-linear equations the maximum allowable timestep cannot be determined exactly, only estimated. Anderson, Tannehill, and Pletcher [1] give an approximate time step criterion for MacCormack's method

$$\Delta t \leq \frac{\alpha\,(\Delta t)_{CFL}}{1 + \frac{2}{Re_\Delta}}, \quad (4.37)$$

where α is a safety factor and $(\Delta t)_{CFL}$ is the inviscid Courant-Friedrichs-Lewy criterion [75]

$$(\Delta t)_{CFL} \leq \left(\frac{|u|}{\Delta\xi} + \frac{|v|}{\Delta\eta} + c\sqrt{\frac{1}{(\Delta\xi)^2} + \frac{1}{(\Delta\eta)^2}}\right)^{-1}, \quad (4.38)$$

where

$$Re_\Delta = \min\left(Re_{\Delta\xi}, Re_{\Delta\eta}\right), \quad (4.39)$$

$$Re_{\Delta\xi} = \frac{\rho|u|\Delta\xi}{\mu}, \quad (4.40)$$

$$Re_{\Delta\eta} = \frac{\rho|v|\Delta\eta}{\mu}, \quad (4.41)$$

and where $c = \sqrt{\frac{\gamma p}{\rho}}$ is the local speed of sound. The time step is calculated over the entire mesh by this method. When doing time accurate transient calculations, the smallest time step is used globally. When steady state solutions are desired, the equations are integrated according to the local time steps at each grid point, to decrease the number of iterations necessary for convergence. One further step would be to use time split calculations using separate maximum timesteps in the r and z directions as discussed by MacCormack and Baldwin [76], although this was not done.

4.2.3 Numerical Smoothing

Due to numerical oscillations, the discretized Navier-Stokes equations can diverge, so the oscillations need to be damped. Numerical oscillations arise in areas where the computational grid is not refined adequately to resolve any large gradients which occur. To overcome this problem, numerical smoothing terms, sometimes called artificial viscosity terms, are added to the equations to reduce the effect of these oscillations. Typically, the smoothing terms are made up of components which are proportional to the second derivative and fourth derivative of the state vector. The second order numerical smoothing is used in regions of shocks, so as to prevent Gibbs phenomena from appearing around the discontinuity. The fourth order smoothing is needed to dampen sawtooth modes, which are actually solutions of the discrete equation, but not the partial differential equation.

For MacCormack's method, MacCormack and Baldwin [76] devised product type fourth order smoothing terms of the form

$$D_\xi = \nu_{4\xi} (\Delta\xi)^4 \frac{\partial}{\partial\xi} \left[\frac{|u| + c}{4p} \left| \frac{\partial^2 p}{\partial \xi^2} \right| \frac{\partial \mathbf{U}}{\partial \xi} \right] \tag{4.42}$$

$$D_\eta = \nu_{4\eta} (\Delta\eta)^4 \frac{\partial}{\partial\eta} \left[\frac{|u| + c}{4p} \left| \frac{\partial^2 p}{\partial \eta^2} \right| \frac{\partial \mathbf{U}}{\partial \eta} \right], \tag{4.43}$$

where $\nu_{4\xi}$ and $\nu_{4\eta}$ are fourth order artificial viscosity coefficients, and for stability, $0 \leq \nu_4 \leq 0.5$. Miller [85] found that this form of the numerical smoothing terms was inadequate to dampen the oscillations, because of the ambiguity in the calculation of the pressure switch terms due to the fluid consisting of several different species, so changed to using a simple

one step smoothing term based on the method of Kutler, Sakell, and Aiello [70]:

$$D^n_{i,j} = \nu_{2\xi}\left(\mathbf{U}^n_{i+1,j} - 2\mathbf{U}^n_{i,j} + \mathbf{U}^n_{i-1,j}\right) + \nu_{2\eta}\left(\mathbf{U}^n_{i,j+1} - 2\mathbf{U}^n_{i,j} + \mathbf{U}^n_{i,j-1}\right)$$
$$-\nu_{4\xi}\left(\mathbf{U}^n_{i+2,j} - 4\mathbf{U}^n_{i+1,j} + 6\mathbf{U}^n_{i,j} - 4\mathbf{U}^n_{i-1,j} + \mathbf{U}^n_{i-2,j}\right)$$
$$-\nu_{4\eta}\left(\mathbf{U}^n_{i,j+2} - 4\mathbf{U}^n_{i,j+1} + 6\mathbf{U}^n_{i,j} - 4\mathbf{U}^n_{i,j-1} + \mathbf{U}^n_{i,j-2}\right) \tag{4.44}$$

which was added to the corrector step only.

$$\mathbf{U}^{n+1}_{i,j} = \frac{1}{2}\left[\mathbf{U}^P_{i,j} + \mathbf{U}^n_{i,j} - \frac{\Delta t}{\Delta\xi}\left(\tilde{\mathbf{F}}^P_{i,j} - \tilde{\mathbf{F}}^P_{i-1,j}\right) - \frac{\Delta t}{\Delta\eta}\left(\tilde{\mathbf{G}}^P_{i,j} - \tilde{\mathbf{G}}^P_{i,j-1}\right) + \Delta t\mathbf{S}^P_{i,j} + \mathbf{D}^n_{i,j}\right] \tag{4.45}$$

Miller then spent some time adjusting the ν coefficients by hand in different regions of the flow to set them to the minimum possible and still maintain stability. Benson tried a different, more autonomous formulation but still had serious problems with the stability. Here the smoothing term of Kutler, Sakell, and Aiello were used, and similar problems with the stability were found. After some experimentation on sine functions with sawtoothing added, the optimum choice which eliminated most sawtoothing without overshooting was found to be $\nu_{4\xi} = \nu_{4\eta} = \frac{1}{11}$ for interior points and $\nu_{4\xi} = \nu_{4\eta} = \frac{1}{16}$ for the boundary points and the points one grid line inside them. These values were used as constants and not varied with location nor the property being damped. For the second order damping they had to be large enough to prevent unphysical situations from arising that could be caused by the fourth order damping. The problem with the fourth order damping is that it does not exist in nature and when faced with steep gradients such as a square wave it will not decrease the gradient but will rather round the square wave by overshooting the peaks and troughs. (See figure 4-4). This means that if there is a steep gradient in a property such as the density the fourth order damping can cause the density to become negative. Simply putting an absolute limit on the density whilst superficially fixing the problem, could in some regions of the arcjet flow, interact to cause equally unphysical solutions. One way to solve the problem is to increase the second order damping to compensate, since second order damping rounds a square wave by lowering the peaks rather than overshooting. This led to the selection of $\nu_{2\xi} = \nu_{2\eta} = 0.3$ and also the discovery that the second order damping had to be applied in two sweeps. As the damping algorithm sweeps across the grid, using

updated earlier points in the calculation of the damping term, it will not uniformly round off a square wave unless the sweep is then applied in the other direction as shown in figure 4-5. For some less well behaved properties such as the electron velocities, which can acquire very large gradients $\nu_2 = 0.4$ was used.

Another problem with damping involved the temperature distribution. Due to the density decreasing strongly through the arcjet the energy $\rho_e E_e$ similarly has strong variations, which with the damping led to the temperature behaving in an unphysical manner. This was simply solved by damping $\frac{\rho_e E_e}{\rho_e}$ instead.

One considered solution to the fourth order damping problem would be to damp the variables in log space rather than linear space. Thus no matter how negative the logarithms of density or energy become, they will never take on unphysical negative values themselves.

The damping described above was found to be useful in obtaining a first estimate of the flow within the arcjet, but was also found to not conserve flux very well, as the damping terms were so dominant in some regions they smoothed out the flow too much. This led me back to the problem that Miller [85] had encountered and required a lot of hands on decreasing of the second and fourth order coefficients, until an instability was met. In this way, slowly the amount of damping could be reduced to the minimum amount required by the flow and the scheme, and flux was conserved to within acceptable limits. Unfortunately this hands-on approach, combined with the complex nature of the governing equations meant that the amount of time required to obtain a converged solution was a few weeks at best. Consequently MacCormack's Method was abandoned in favour of a more modern Total Variation Diminishing scheme.

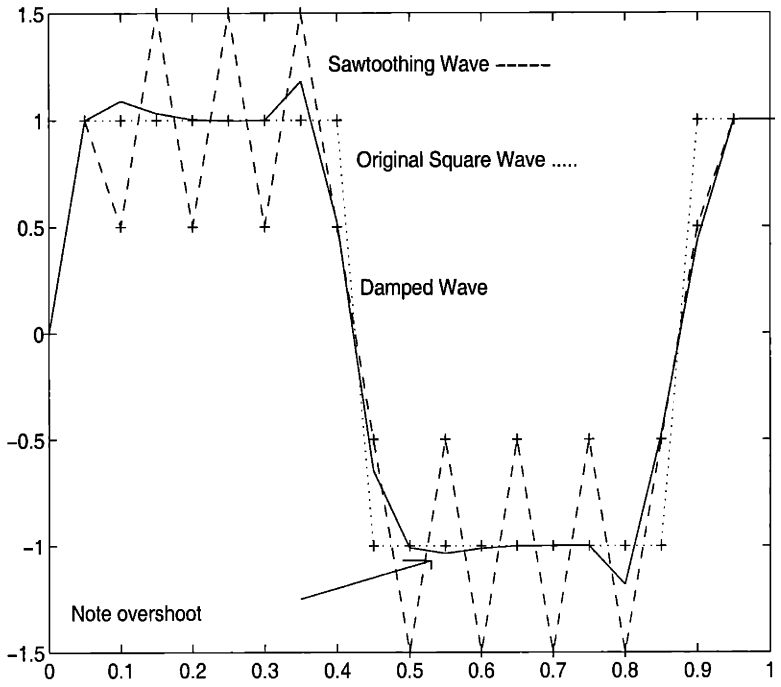

Figure 4-4: *Overshoot of Fourth Order Damping*

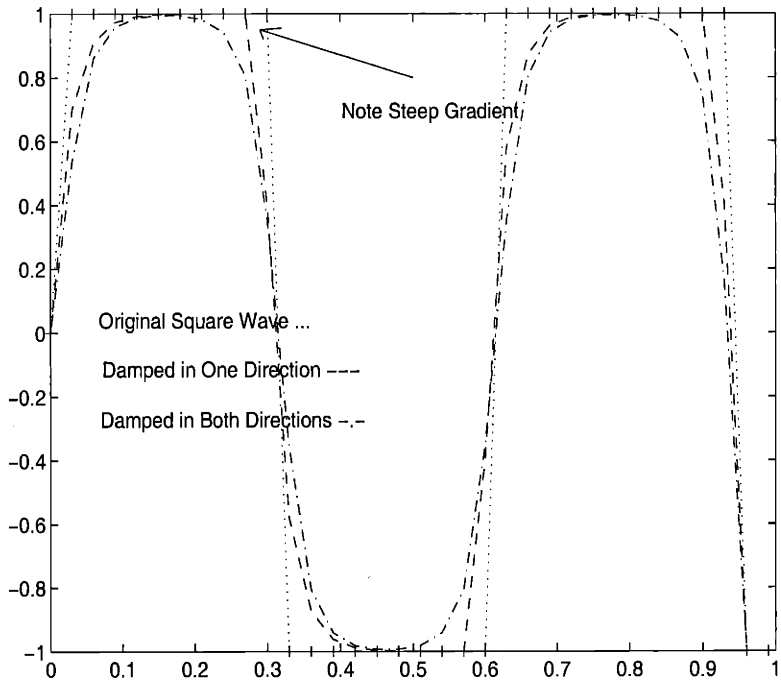

Figure 4-5: *Smoothing with Second Order Damping*

4.3 Total Variation Diminishing Schemes

First order schemes give poor resolution but can be made to produce non-oscillatory solutions. Higher order schemes produce oscillatory solutions at discontinuities which can cause instability. Total Variation Diminishing (TVD) schemes, are a class of second order accurate integration schemes, where the fluxes are limited in a non-linear fashion to give an oscillation free scheme. Also to improve the accuracy of the simulation an upwind scheme was used.

The theory in this section draws heavily upon "Numerical Computation of Internal and External Flows, Volume 2" by Hirsch [47], and "A Class of High-Resolution Explicit and Implicit Shock-Capturing Methods" by Yee [136].

4.3.1 Upwind Schemes

Centrally discretized schemes do not distinguish upstream from downstream, and hence do not consider the physical propagation of perturbations along characteristic lines as exist for hyperbolic equations. The physical properties can be taken into account in the discretization process at a number of different levels.

Flux Split Schemes

At the first level, the sign of the eigenvalues of the system (propagation speeds) is used to determine the direction of the discretization and leads to what are called flux split methods.

For the linear convection equation

$$\frac{du}{dt} + a\frac{du}{dx} = 0, \tag{4.46}$$

when integrated by a first order forward difference in time $u^{n+1} - u^n$, a spatially central difference $\frac{1}{2}(u_{i+1} - u_{i-1})$ leads to an unstable scheme. With a one sided difference, the scheme

$$u_i^{n+1} = u_i^n - a\frac{\Delta t}{\Delta x}(u_i - u_{i-1}) \qquad \text{is stable for} \quad 0 \leq a\frac{\Delta t}{\Delta x} \leq 1, \tag{4.47}$$

but the scheme

$$u_i^{n+1} = u_i^n - a\frac{\Delta t}{\Delta x}(u_{i+1} - u_i) \qquad \text{is stable for} \quad -1 \leq a\frac{\Delta t}{\Delta x} \leq 0. \tag{4.48}$$

Each of these schemes is stable when the discretization is in the upwind direction, so that at the new timestep the node is updated using information from its domain of dependence. They can however be combined into a scheme which is stable whatever the sign of the convection speed. Defining positive and negative projections,

$$a^+ = \max(a,0) = \frac{1}{2}(a+|a|) \qquad a^- = \min(a,0) = \frac{1}{2}(a-|a|) \tag{4.49}$$

an upwind scheme can be written as

$$u_i^{n+1} - u_i^n = -\frac{\Delta t}{\Delta x}\left(a^+(u_i - u_{i-1}) + a^-(u_{i+1} - u_i)\right) \quad \text{which is stable for } |a|\frac{\Delta t}{\Delta x} \leq 1. \tag{4.50}$$

A system of equations,

$$\frac{\partial U}{\partial t} + \vec{\nabla}\cdot\vec{F} = S, \tag{4.51}$$

can be linearized as

$$\frac{\partial U}{\partial t} + \vec{A}\cdot\nabla\vec{U} = S, \qquad \text{where } \vec{A} = \frac{\partial \vec{F}}{\partial U} \tag{4.52}$$

or explicitly

$$\frac{\partial U}{\partial t} + A\frac{\partial U}{\partial x} + B\frac{\partial U}{\partial y} + C\frac{\partial U}{\partial z} = S,$$
$$\text{where } A = \frac{\partial F}{\partial U} \quad B = \frac{\partial G}{\partial U} \quad C = \frac{\partial H}{\partial U}. \tag{4.53}$$

For a 1-D scalar equation A is simply the propagation speed, whereas for a system A, B, and C are matrices, which will each possess a set of eigenvalues λ_i, which can be arranged in a diagonal matrix $\Lambda = \begin{pmatrix} \lambda_1 & & & \\ & \lambda_2 & & \\ & & \ddots & \\ & & & \lambda_n \end{pmatrix}$, and a set of left and right eigenvectors which can be arranged in matrices such that $AL = \Lambda L$ and $L^{-1}A = \Lambda L^{-1}$ where the left eigenvectors are the rows of L^{-1} and the right eigenvectors are the columns of L. The eigenvalues of the matrix

$$K = \vec{A}\cdot\vec{k} = A\cdot k_x + B\cdot k_y + C\cdot k_z \tag{4.54}$$

associated with an arbitrary direction of propagation $\vec{k}$ determine the behaviour of the

solution to the Euler equations. Wave-like solutions exist if the eigenvalues of K are real with linear dependence of the corresponding left eigenvectors. For a multidimensional system the eigenvalues are obtained from

$$\det|\lambda\overline{\overline{I}} - \overline{\overline{K}}| = 0. \tag{4.55}$$

The eigenvectors obtained from the eigenvalues will diagonalize the matrix K by

$$\Lambda = L^{-1}KL \tag{4.56}$$

and will be functions of $\vec{k}$. It is important to note that while one can diagonalize any linear combination $A \cdot k_x + B \cdot k_y + C \cdot k_z$, using the appropriate $L(\vec{k})$, it is *not possible* to simultaneously diagonalize all three jacobians, A, B, C. Selecting ($k_x = 1,\ k_y = 0,\ k_z = 0$), will give a matrix L_1 which will diagonalize A, and ($k_x = 0,\ k_y = 1,\ k_z = 0$) will give a matrix L_2 which will diagonalize B:

$$L_1^{-1}AL_1 = \Lambda_1 \qquad L_2^{-1}BL_2 = \Lambda_2. \tag{4.57}$$

For the 2-D Euler equations for example these are

$$\Lambda_1 = \begin{pmatrix} u & & & \\ & u & & \\ & & u+c & \\ & & & u-c \end{pmatrix} \qquad \Lambda_2 = \begin{pmatrix} v & & & \\ & v & & \\ & & v+c & \\ & & & v-c \end{pmatrix}. \tag{4.58}$$

Flux vector splitting separates each eigenvalue matrix into its positive and negative components so

$$\Lambda_1^+ = \max(\Lambda_1, 0), \qquad \Lambda_1^- = \min(\Lambda_1, 0) \qquad \text{and} \quad \Lambda_1 = \Lambda_1^+ + \Lambda_1^-. \tag{4.59}$$

Using the split eigenvalue matrices the jacobians are then reconstituted as

$$A^+ = L_1\Lambda_1^+L_1^{-1} \qquad B^+ = L_2\Lambda_2^+L_2^{-1}$$

$$A^- = L_1\Lambda_1^-L_1^{-1} \qquad B^- = L_2\Lambda_2^-L_2^{-1}. \tag{4.60}$$

Finally the split fluxes are calculated as

$$f^{\pm} = A^{\pm}U \qquad g^{\pm} = B^{\pm}U, \tag{4.61}$$

which can be applied as

$$\frac{\partial U}{\partial t} + \frac{\partial f^{+}}{\partial x} + \frac{\partial f^{-}}{\partial x} + \frac{\partial g^{+}}{\partial y} + \frac{\partial g^{-}}{\partial y} = S \tag{4.62}$$

or

$$\frac{\partial U}{\partial t} + A^{+}\frac{\partial U}{\partial x} + A^{-}\frac{\partial U}{\partial x} + B^{+}\frac{\partial U}{\partial y} + B^{-}\frac{\partial U}{\partial y} = S. \tag{4.63}$$

Provided such a scheme is run within the CFL limit of $\tau|\lambda|_{max} \leq 1$, with a first order accurate discretization it should always be stable.

Godunov Schemes

The Godunov-type schemes go a step further. In the basic scheme, as shown in figure 4-6, the solution is considered as piecewise constant over each mesh cell. The evolution of the flow to the next timestep comes from the interaction of waves originating at the boundaries between adjacent cells. The Euler solution to this problem is known as the Shock-Tube or Riemann problem, which can be solved exactly or approximately, based on the conditions at each side of the discontinuity. Finally the new state is given as the average of the state variables after the specified timestep.

In two dimensions for Godunov-type methods the numerical fluxes are obtained from the solution (exact or approximate) of the Riemann problem in the directions normal to the cell interfaces. For each cell two Riemann problems have to be solved, one in the x direction based on the Jacobian A of the flux component f and one in the y direction associated with the flux component g and Jacobian B. In curvilinear coordinates though, this becomes one in the xi (ξ) direction and one in the eta (η) direction.

This scheme is limited to first order accuracy only by the assumption of piecewise constant variation across each cell, which is completely decoupled from the physical stage where the Riemann problems are solved at the cell interfaces. Consequently higher order schemes can be created by extrapolation of the variables to a higher order. Thus a linear approximation of the solution in each cell leads to a second-order spatial discretization (fig. 4-7), and a quadratic representation yields a third-order discretization.

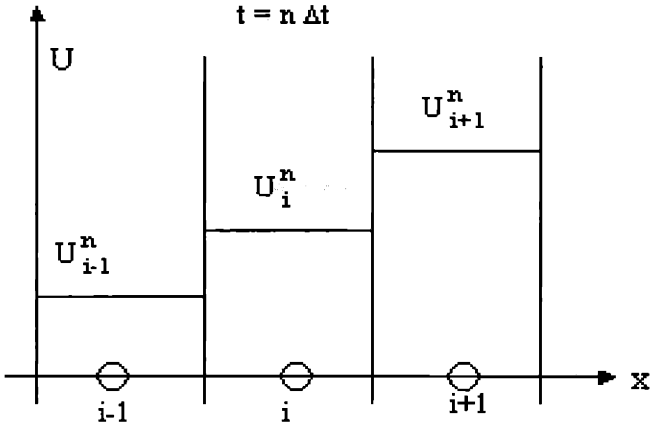

Step 1: Piecewise constant distribution at t=nΔt.

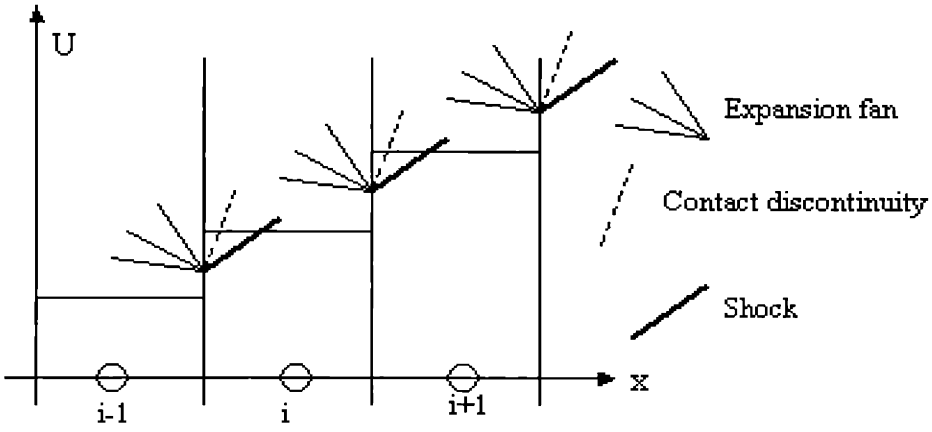

Step 2: Resolution of Riemann problem at interfaces.

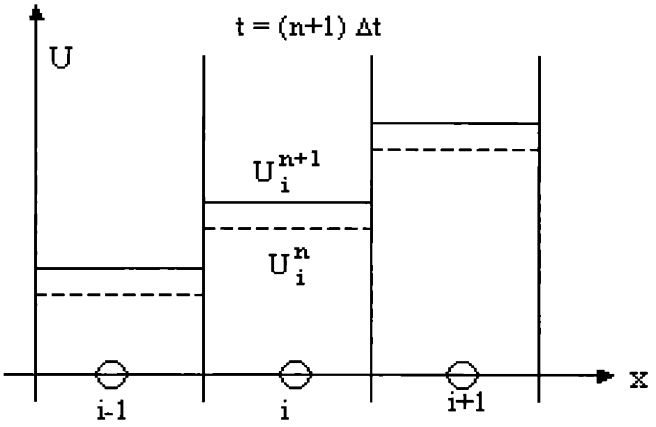

Step 3: Averaging of perturbed state after time interval Δt.

Figure 4-6: *Basic Godunov's Method*

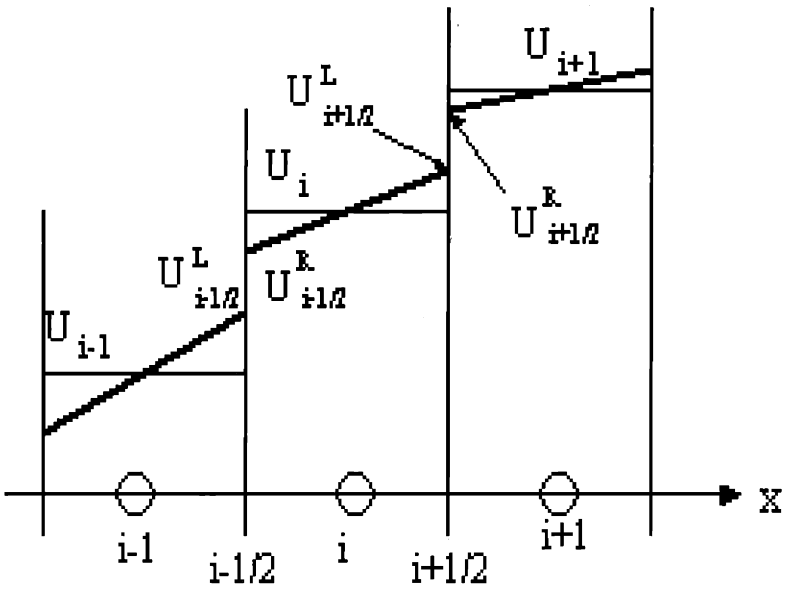

Piecewise linear variation within cells.

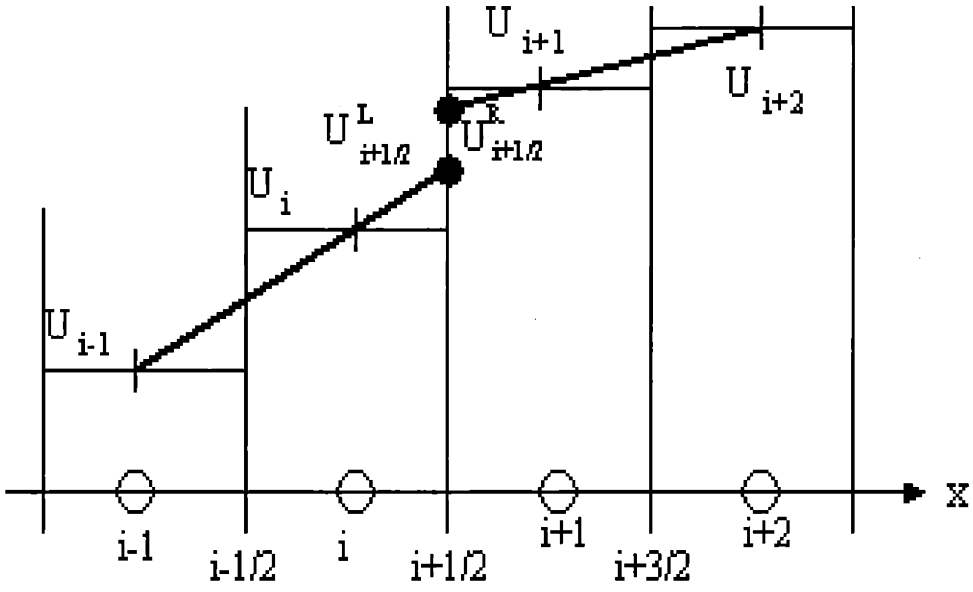

Linear one-sided extrapolation for k = -1.

Figure 4-7: *Variable Extrapolation.*

Within a cell the state U can be represented as

$$U(x) = U_i + \frac{1}{\Delta x}(x - x_i)\delta_i U + \frac{3k}{2\Delta x^2}\left((x - x_i)^2 - \frac{\Delta x^2}{12}\right)\delta_i^2 U \tag{4.64}$$

$$x_{i-1/2} < x < x_{i+1/2}$$

where U_i is the average value and $\delta_i U$ and $\delta_i^2 U$ are the first and second derivatives, which can be written as

$$\delta_i U = \frac{U_{i+1} - U_{i-1}}{2} \tag{4.65}$$

$$\delta_i^2 U = U_{i+1} - 2U_i + U_{i-1}. \tag{4.66}$$

For $k = \frac{1}{3}$ this gives the correct Taylor expansion to third order, whereas other values of k give a linear representations with truncation terms that correspond to a certain amount of upwinding.

The interface values are then given by

$$U^L_{i+1/2} = U_i + \epsilon\left(\frac{1}{2}\delta_i U + \frac{k}{4}\delta_i^2 U\right) \tag{4.67}$$

$$U^R_{i-1/2} = U_i + \epsilon\left(-\frac{1}{2}\delta_i U + \frac{k}{4}\delta_i^2 U\right), \tag{4.68}$$

where ϵ is the order switch: $\epsilon = 0$ for a first order scheme, and $\epsilon = 1$ for a second order scheme. k is the wind switch and can reasonably take any value between -1 and +1.

$k = -1$, corresponds to fully upwind extrapolation as in the lower part of figure 4-7.

$k = 0$, gives centred interpolation as shown in the upper portion.

$k = 0.5$, gives B.P. Leonard's QUICK scheme.

$k = 1$, should not be used as this corresponds to a central not an upstream scheme where there are no discontinuities at the cell interfaces.

The first order explicit upwind schemes can be summarized as

$$U_i^{n+1} - U_i^n = -\frac{\Delta t}{\Delta x}\left(f^*_{i+1/2} - f^*_{i-1/2}\right) \tag{4.69}$$

where $f^*_{i+1/2} = f^*(U_i, U_{i+1})$, which can take the following forms:

Flux vector splitting:	$f^{*(FS)}_{i+1/2} = f^-(U_{i+1}) + f^+(U_i)$
Exact Godunov scheme:	$f^{*(G)}_{i+1/2} = f(U^{(Riemann)}_{i+1/2}(0, U_i, U_{i+1/2}))$
Osher's approximate Riemann solver:	$f^{*(O)}_{i+1/2} = \frac{1}{2}(f_i + f_{i+1}) - \frac{1}{2}\sum_j \int_{\Gamma(j)} \lvert\lambda_{(j)}\rvert r^{(j)} dw$
Roe's approximate Riemann solver:	$f^{*(R)}_{i+1/2} = \frac{1}{2}(f_i + f_{i+1}) - \frac{1}{2}\sum_j \lvert\bar{\bar{\lambda}}_{(j)}\rvert \partial w_j \bar{\bar{r}}^{(j)}$

(4.70)

Any of the above schemes can be made second order space accurate by replacing U_i with $U^L_{i+1/2}$, and U_{i+1} with $U^R_{i+1/2}$, so $f^*_{i+1/2} = f^*(U_i, U_{i+1})$ becomes

$$f^{*(2nd)}_{i+1/2} = f^*(U^L_{i+1/2}, U^R_{i+1/2}). \tag{4.71}$$

With variable extrapolation described above the variables are extrapolated to the cell interfaces, and the fluxes calculated based on these values. An alternative option is flux extrapolation where the fluxes are calculated in the cells and then extrapolated to the boundaries. A general backward extrapolation of the forward going flux is defined as

$$f^{+b}_{i+1/2} = f^+_i + \frac{\epsilon}{4}\left((1-k)(f^+_i - f^+_{i-1}) + (1+k)(f^+_{i+1} - f^+_i)\right), \tag{4.72}$$

and the forward extrapolation of the backward going flux as

$$f^{-f}_{i+1/2} = f^-_{i+1} - \frac{\epsilon}{4}\left((1+k)(f^-_{i+1} - f^-_i) + (1-k)(f^-_{i+2} - f^-_{i+1})\right), \tag{4.73}$$

and

$$f^{*(2nd)}_{i+1/2} = f^{+b}_{i+1/2} + f^{-f}_{i+1/2}. \tag{4.74}$$

4.3.2 Total Variation Diminishing Schemes

An upwind algorithm by itself is not sufficient to avoid the appearance of oscillations around discontinuities. Figure 4-8 shows how such oscillations are generated. When the gradient in a cell exceeds the gradient between adjacent mean values, the solution to linear convection after one timestep leads to an undershoot where $U^{n+1}_i < U^{n+1}_{i-1}$ whereas before $U^n_i > U^n_{i-1}$.

Total Variation is defined as

$$TV(U^n) = \sum_i |U^n_{i+1} - U^n_i|. \tag{4.75}$$

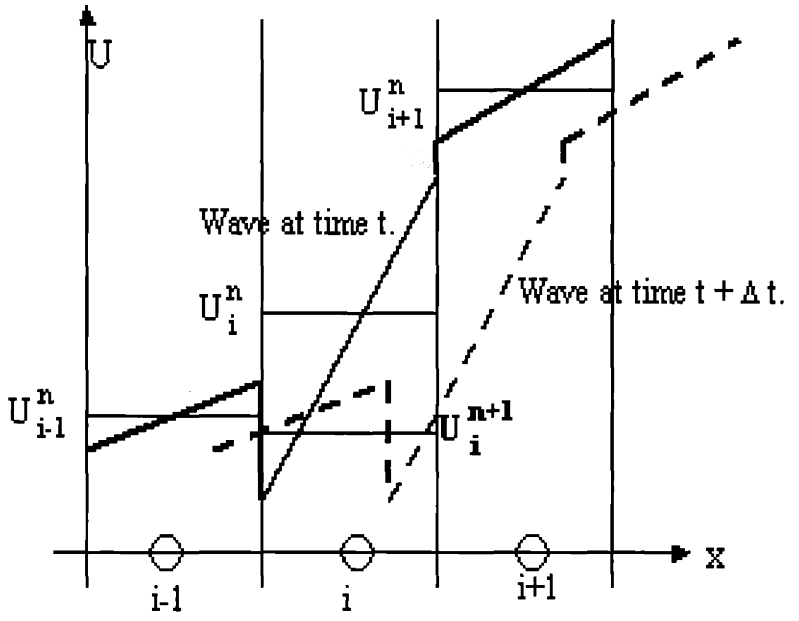

Generation of oscillations in numerical solutions.

Figure 4-8: *Mechanism of Generation of Oscillations.*

If $TV(U^{n+1}) < TV(U^n)$ then the scheme is said to be total variation diminishing, which implies that no new extrema can be created, the value of a local minimum is non-decreasing, and the value of a local maximum is non-increasing. If a scheme is written in the form

$$U_i^{n+1} = U_i^n + D_{i+\frac{1}{2}} \Delta U^n_{i+\frac{1}{2}} - C_{i-\frac{1}{2}} \Delta U^n_{i-\frac{1}{2}}, \tag{4.76}$$

where $\Delta U^n_{i+\frac{1}{2}} = U_{i+1} - U_i$, it can be shown [47] that it is TVD if and only if for all i,

$$C_{i+\frac{1}{2}} \geq 0$$

$$D_{i+\frac{1}{2}} \geq 0$$

$$C_{i+\frac{1}{2}} + D_{i+\frac{1}{2}} \leq 1. \tag{4.77}$$

Godunov's Theorem states that no second or higher order accurate **constant coefficient** scheme can be TVD. Thus all higher order TVD schemes must be non-linear.

TVD schemes work by applying non-linear limiters to restrict the gradients, and thus prevent overshoots. For a given scheme the coefficients C and D can be written in terms of

consecutive variations or fluxes, so flux limiters Ψ are defined as functions of these ratios:

$$\Psi_{i+1/2} = \Psi(r_{i+1/2}) \qquad r_{i+1/2} = \frac{\Delta U_{i-1/2}}{\Delta U_{i+1/2}}. \tag{4.78}$$

$r \leq 0$ implies an extrema is present at that location and $r \geq 0$ implies the function is smooth there. For second order schemes to be TVD the flux limiters are confined to the region shown in figure 4-9 (See reference [47] for derivation).

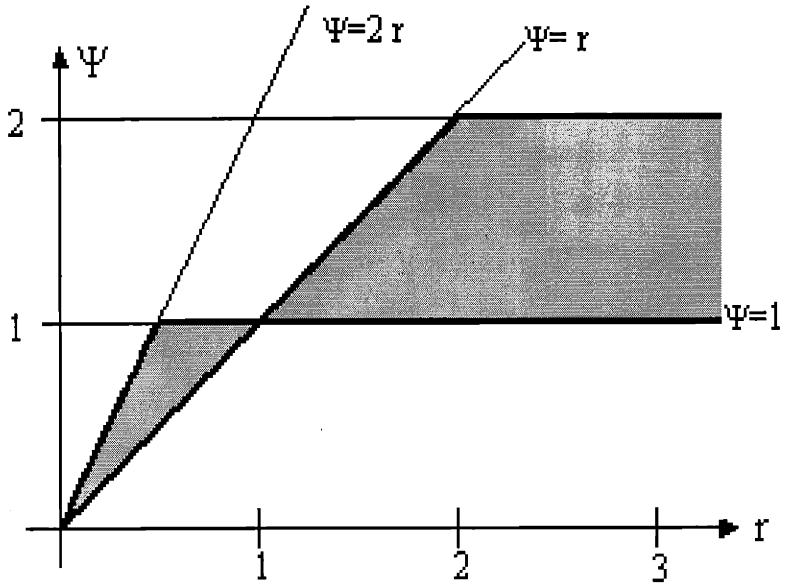

Figure 4-9: *Limiter Region for Second Order TVD Schemes.*

Popular choices for limiter functions are:

Minmod (The lowest bound)	$\Psi(r) = max(0, min(1, r))$
Superbee (The highest bound)	$\Psi(r) = max(0, min(1, 2r), min(2, r))$
Van Leer	$\Psi(r) = \frac{r+\|r\|}{1+r}$
Van Albada	$\Psi(r) = \frac{r^2+r}{1+r^2}$

(4.79)

The Van Leer limiter passes through the middle of the TVD region but tends to 2 at high flux ratios. This is overcompressive and slowly converts sine waves into square waves. The Van Albada limiter has a smoother behaviour as it tends to 1 at high flux ratios. They

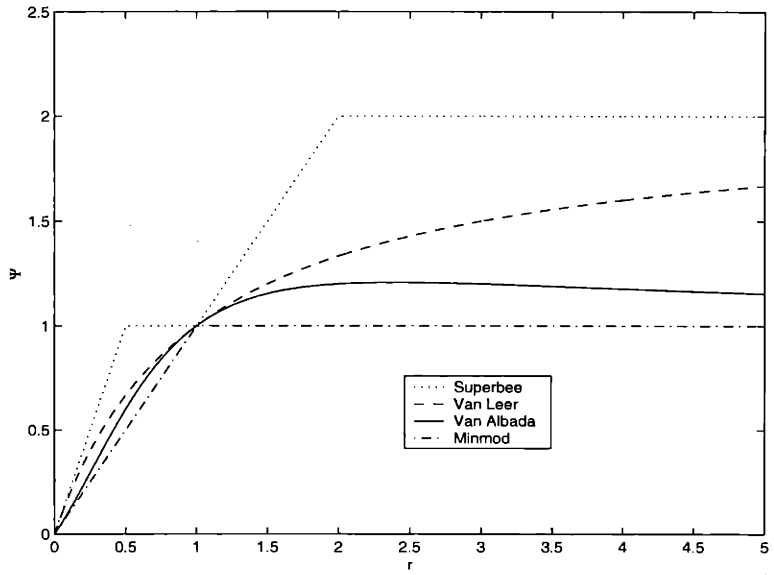

Figure 4-10: *Popular Flux Limiters.*

all produce a second order scheme when the solution is smooth and reduce to upwind at discontinuities. They also possess a symmetry such that

$$\frac{\Psi(r)}{r} = \Psi\left(\frac{1}{r}\right). \tag{4.80}$$

For $r \leq 0$, $\Psi = 0$ is the most common choice, and gives a first order upwind scheme at the discontinuities as shown in figure 4-11.

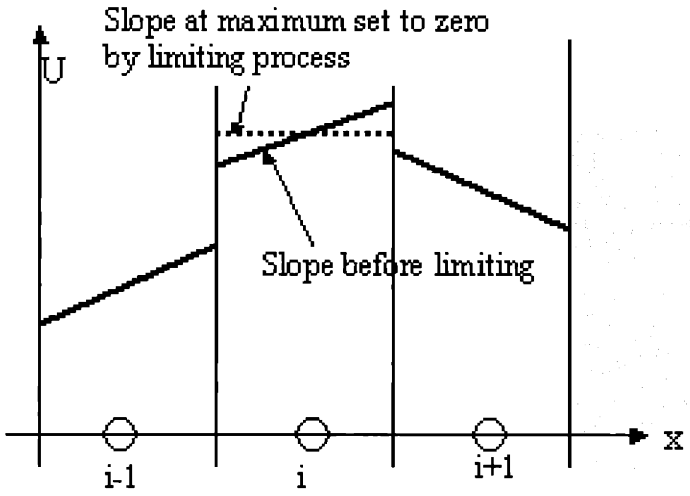

Figure 4-11: *Slope Limiting at Extrema.*

With variable extrapolation the limiters are applied to the variables when calculating the interface values U^L and U^R from equations 4.67 and 4.68. The fluxes are then calculated as before using the limited interface values instead. Thus the TVD extrapolated variables are

$$U^L_{i+1/2} = U_i + \frac{\epsilon}{4}\left((1-k)\Psi^+_{i-1/2}\left(U_i - U_{i-1}\right) + (1+k)\Psi^-_{i+1/2}\left(U_{i+1} - U_i\right)\right), \tag{4.81}$$

$$U^R_{i+1/2} = U_{i+1} - \frac{\epsilon}{4}\left((1-k)\Psi^-_{i+3/2}\left(U_{i+2} - U_{i+1}\right) + (1+k)\Psi^+_{i+1/2}\left(U_{i+1} - U_i\right)\right), \tag{4.82}$$

where $\Psi^{\pm}$ are defined as functions of the variable ratios

$$r^+_{i+1/2} = \frac{u_{i+2} - u_{i+1}}{u_{i+1} - u_i}, \qquad r^-_{i+1/2} = \frac{u_i - u_{i-1}}{u_{i+1} - u_i}. \tag{4.83}$$

With flux extrapolation the limiters are applied to the calculated fluxes in the integration step itself: The TVD form of the semi-discretized equation can be written as

$$\frac{du_i}{dt} = -\frac{1}{\Delta x}\delta^-[f^*_{i+1/2} + \frac{1}{2}\Psi^+_{i-1/2}(f_i - f^*_{i-1/2}) + \frac{1}{2}\Psi^-_{i+3/2}(f_{i+1} - f^*_{i+3/2})], \tag{4.84}$$

where f is the plain flux at the node, and f^* is the second order upwind flux from equation 4.74. The limiter functions $\Psi^{\pm}$ are defined as functions of the flux difference ratios

$$r^+_{i+1/2} = \frac{f_{i+2} - f^*_{i+3/2}}{f_{i+1} - f^*_{i+1/2}}, \qquad r^-_{i+1/2} = \frac{f_{i-1} - f^*_{i-1/2}}{f_i - f^*_{i+1/2}}. \tag{4.85}$$

Using the symmetry property of flux limiters the semi discretized equation can then be written as

$$\frac{du_i}{dt} = -\frac{1}{\Delta x}\left(1 + \frac{1}{2}\Psi(r^+_{i-1/2}) - \frac{1}{2}\frac{\Psi(r^+_{i-3/2})}{r^+_{i-3/2}}\right)\left(f_i - f^*_{i-1/2}\right)$$

$$-\frac{1}{\Delta x}\left(1 + \frac{1}{2}\Psi(r^-_{i+1/2}) - \frac{1}{2}\frac{\Psi(r^-_{i+3/2})}{r^-_{i+3/2}}\right)\left(f^*_{i+1/2} - f_i\right). \tag{4.86}$$

It should be noted that the term "total variation diminishing" only applies to the flux terms in the scheme. Maxima and minima can still be introduced through the boundary conditions, such viscous no-slip conditions on the walls, or a pressure gradient at the inlet and outlet. Extrema can also be introduced from source terms in the equations which is of specific relevance to the arcjet model with chemical reactions changing the amounts of

each chemical species present, and the separate electron and heavy species energy equations transferring energy between each other.

4.3.3 Implicit Schemes

Writing a scheme in its most basic form

$$\frac{dU}{dt} = H(U,t), \tag{4.87}$$

any generic 2-step method can be written as

$$(1+\xi)U^{n+1} - (1+2\xi)U^n + \xi U^{n-1} =$$

$$\Delta t\left(\theta H^{n+2} + (1-\theta-\phi)H^{n+1} - \phi H^n\right), \tag{4.88}$$

and a 1-step method as

$$U^{n+1} - U^n = \Delta t\left(\theta H^{n+1} + (1-\theta)H^n\right). \tag{4.89}$$

Using the incremental form $\Delta U^n = U^{n+1} - U^n$, for $\phi = 0$

$$(1+\xi)\Delta U^n - \xi U^{n-1} = \Delta t\left(\theta H^{n+1} + (1-\theta)H^n\right). \tag{4.90}$$

These schemes are stable for any timestep (A-stable) if and only if

$$\theta \geq \phi + \frac{1}{2}, \qquad \xi \geq -\frac{1}{2}, \qquad \xi \leq \theta + \phi - \frac{1}{2},$$

as illustrated in figure 4-12

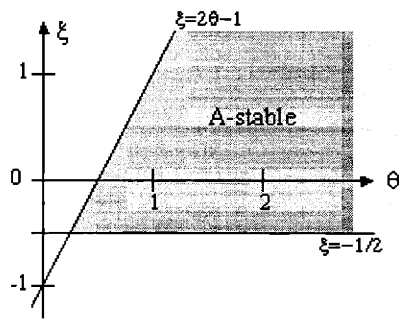

Figure 4-12: *A-Stable Regime for Generic 2-Step Method.*

These schemes still need $H^{n+1} = H(U^{n+1})$ but U^{n+1} is unknown at the current timestep, so H can be linearized and predicted as

$$H^{n+1} = H^n + \left(\frac{\partial H}{\partial U}\right) \Delta U^n + O(\Delta t^2) \tag{4.91}$$

so

$$\left((1+\xi) - \theta \Delta t \frac{\partial H}{\partial U}\right) \Delta U^n = \Delta t H^n + \xi \Delta U^{n-1}. \tag{4.92}$$

For $H = \frac{\partial f}{\partial x}$ and $A = \frac{\partial f}{\partial U}$ this becomes

$$\left((1+\xi) - \theta \Delta t \frac{\partial}{\partial x} A\right) \Delta U^n = -\Delta t \frac{\partial f^n}{\partial x} + \xi \Delta U^{n-1}. \tag{4.93}$$

4.3.4 Resultant Scheme

Many different schemes were tried, with different limiters, upwind switches, implicit or explicit schemes etc, with varying degrees of success. The final scheme can briefly be described as an explicit flux split upwind method using TVD variable extrapolation, which is spatially second order accurate with a first order accurate Euler time integration method.

The Euler terms require TVD treatment as they contain the potentially unstable convection components so are split off from the full Navier-Stokes Equations. The remaining viscous terms do not require a TVD treatment as they should always be dissipative, and seek to damp out the solution rather than to potentially create shocks or otherwise steep gradients.

In curvilinear coordinates the equation to be solved as from equation 4.18 is

$$\frac{\partial U}{\partial t} + \frac{1}{Jr}\left(\frac{\partial \tilde{F}}{\partial \xi} + \frac{\partial \tilde{G}}{\partial \eta}\right) = S. \tag{4.94}$$

Linearizing in U

$$\frac{\partial U}{\partial t} + \frac{1}{Jr}\frac{\partial}{\partial \xi}\left(\frac{\partial \tilde{F}}{\partial U} U\right) + \frac{1}{Jr}\frac{\partial}{\partial \eta}\left(\frac{\partial \tilde{G}}{\partial U} U\right) = S. \tag{4.95}$$

Now let

$$\begin{aligned} K &= \frac{1}{r}\frac{\partial F}{\partial U} k_z + \frac{1}{r}\frac{\partial G}{\partial U} k_r \\ &= \frac{1}{r}\frac{\partial}{\partial U}(F k_z + G k_r). \end{aligned} \tag{4.96}$$

But $Fk_z + Gk_r = \frac{1}{J}(\tilde{F}k_\xi + \tilde{G}k_\eta)$ so

$$K = \frac{1}{Jr}\frac{\partial}{\partial U}(\tilde{F}k_\xi + \tilde{G}k_\eta). \tag{4.97}$$

Thus

$$\frac{\partial \tilde{F}}{\partial U} = \frac{Jr}{k_\xi}K(\xi) \qquad \frac{\partial \tilde{G}}{\partial U} = \frac{Jr}{k_\eta}K(\eta) \tag{4.98}$$

where $K(\xi)$ is K evaluated with $\vec{k} = (k_z, k_r)$ in the ξ direction. Defining $A = K(\xi)$ and $B = K(\eta)$ and splitting these jacobians into their upwind components, the equation to be solved becomes

$$\frac{\partial U}{\partial t} + \frac{1}{Jr}\frac{\partial}{\partial \xi}\left(\frac{Jr}{k_\xi}A^{\pm}U\right) + \frac{1}{Jr}\frac{\partial}{\partial \eta}\left(\frac{Jr}{k_\eta}B^{\pm}U\right) = S \tag{4.99}$$

where there is an implied sum over the terms involving A^+, A^- and B^+, B^-.

For the seeded arcjet as in equation 4.2, with state vector U written as

$U = (\rho, m, n, l, \varepsilon_g, \varepsilon_e, \rho_H, \rho_{H+}, \rho_{Cs}, \rho_{Cs+})$, with the viscous terms separated off from the flux terms,

$$K = \begin{pmatrix}
0 & k_z & k_r & 0 & 0 & 0 & 0 & 0 & 0 & 0 \\
\frac{-m}{\rho}u_k & \frac{2m}{\rho}k_z + \frac{n}{\rho}k_r & \frac{m}{\rho}k_r & 0 & (\gamma-1)k_z & \frac{2}{3}k_z & 0 & 0 & 0 & 0 \\
\frac{-n}{\rho}u_k & \frac{n}{\rho}k_z & \frac{m}{\rho}k_z + \frac{2n}{\rho}k_r & 0 & (\gamma-1)k_r & \frac{2}{3}k_r & 0 & 0 & 0 & 0 \\
\frac{-l}{\rho}u_k & \frac{l}{\rho}k_z & \frac{l}{\rho}k_r & u_k & 0 & 0 & 0 & 0 & 0 & 0 \\
\frac{-(\varepsilon_g+P_g)}{\rho}u_k & \frac{\varepsilon_g+P_g}{\rho}k_z & \frac{\varepsilon_g+P_g}{\rho}k_r & 0 & \gamma u_k & 0 & 0 & 0 & 0 & 0 \\
0 & 0 & 0 & 0 & 0 & \frac{5}{3}u_{ek} & 0 & 0 & 0 & 0 \\
\frac{-\rho_H}{\rho}u_k & \frac{\rho_H}{\rho}k_z & \frac{\rho_H}{\rho}k_r & 0 & 0 & 0 & u_k & 0 & 0 & 0 \\
\frac{-\rho_{H+}}{\rho}u_k & \frac{\rho_{H+}}{\rho}k_z & \frac{\rho_{H+}}{\rho}k_r & 0 & 0 & 0 & 0 & u_k & 0 & 0 \\
\frac{-\rho_{Cs}}{\rho}u_k & \frac{\rho_{Cs}}{\rho}k_z & \frac{\rho_{Cs}}{\rho}k_r & 0 & 0 & 0 & 0 & 0 & u_k & 0 \\
\frac{-\rho_{Cs+}}{\rho}u_k & \frac{\rho_{Cs+}}{\rho}k_z & \frac{\rho_{Cs+}}{\rho}k_r & 0 & 0 & 0 & 0 & 0 & 0 & u_k
\end{pmatrix} \tag{4.100}$$

where

$$u_k = \frac{m}{\rho}k_z + \frac{n}{\rho}k_r \qquad u_{ek} = u_{ez}k_z + u_{er}k_r.$$

The eigenvalues are

$$\lambda_{1-7} = u_k \qquad \lambda_8 = \frac{1}{2}(\gamma+1)u_k + c \qquad \lambda_9 = \frac{1}{2}(\gamma+1)u_k - c \qquad \lambda_{10} = \frac{5}{3}u_{ek}. \tag{4.101}$$

and the right and left eigenvector matrices are

$$L = \begin{pmatrix} 0 & 1 & 0 & 0 & 0 & 0 & 0 & 1 & 1 & 1 \\ 1 & 0 & 0 & 0 & 0 & 0 & 0 & k_r v_k + \lambda_8 k_z & k_r v_k + \lambda_9 k_z & \frac{5}{3}u_{ek}k_z - u_k k_r \\ -\frac{k_z}{k_r} & -\frac{u_k}{k_r} & 0 & 0 & 0 & 0 & 0 & -k_z v_k + \lambda_8 k_r & -k_z v_k + \lambda_9 k_r & \frac{5}{3}u_{ek}k_r - u_k k_z \\ 0 & 0 & 1 & 0 & 0 & 0 & 0 & w & w & w \\ 0 & 0 & 0 & 0 & 0 & 0 & 0 & (\lambda_8 - u_k)u_k + h & (\lambda_9 - u_k)u_k + h & h\frac{g_1}{g_2} \\ 0 & 0 & 0 & 0 & 0 & 0 & 0 & 0 & 0 & \\ 0 & 0 & 0 & 1 & 0 & 0 & 0 & y_H & y_H & y_H \\ 0 & 0 & 0 & 0 & 1 & 0 & 0 & y_H+ & y_H+ & y_H+ \\ 0 & 0 & 0 & 0 & 0 & 1 & 0 & y_{Cs} & y_{Cs} & y_{Cs} \\ 0 & 0 & 0 & 0 & 0 & 0 & 1 & y_{Cs+} & y_{Cs+} & y_{Cs+} \end{pmatrix} \tag{4.102}$$

$$L^{-1} = \begin{pmatrix} u_k\left(k_z - \frac{u_k u}{h}\right) & k_r^2 + k_z\frac{u_k u}{h} & k_r\left(\frac{u_k u}{h} - k_z\right) & 0 & -\frac{u}{h} & -\frac{u_k u}{\frac{3}{2}hg_1} & 0 & 0 & 0 & 0 \\ 1 - \frac{u_k^2}{h} & k_z\frac{u_k}{h} & k_r\frac{u_k}{h} & 0 & -\frac{1}{h} & -\frac{u_k}{\frac{3}{2}hg_1} & 0 & 0 & 0 & 0 \\ -w\frac{u_k^2}{h} & k_z\frac{wu_k}{h} & k_r\frac{wu_k}{h} & 1 & -\frac{w}{h} & -\frac{wu_k}{\frac{3}{2}hg_1} & 0 & 0 & 0 & 0 \\ -y_H\frac{u_k^2}{h} & k_z\frac{y_H u_k}{h} & k_r\frac{y_H u_k}{h} & 1 & -\frac{y_H}{h} & -\frac{y_H u_k}{\frac{3}{2}hg_1} & 1 & 0 & 0 & 0 \\ -y_{H+}\frac{u_k^2}{h} & k_z\frac{y_{H+}u_k}{h} & k_r\frac{y_{H+}u_k}{h} & 1 & -\frac{y_{H+}}{h} & -\frac{y_{H+}u_k}{\frac{3}{2}hg_1} & 0 & 1 & 0 & 0 \\ -y_{Cs}\frac{u_k^2}{h} & k_z\frac{y_{Cs}u_k}{h} & k_r\frac{y_{Cs}u_k}{h} & 1 & -\frac{y_{Cs}}{h} & -\frac{y_{Cs}u_k}{\frac{3}{2}hg_1} & 0 & 0 & 1 & 0 \\ -y_{Cs+}\frac{u_k^2}{h} & k_z\frac{y_{Cs+}u_k}{h} & k_r\frac{y_{Cs+}u_k}{h} & 1 & -\frac{y_{Cs+}}{h} & -\frac{y_{Cs+}u_k}{\frac{3}{2}hg_1} & 0 & 0 & 0 & 1 \\ -\frac{u_k}{2c\left(1+\mu_1\frac{u_k}{h}\right)} & \frac{k_z}{2c\left(1+\mu_1\frac{u_k}{h}\right)} & \frac{k_r}{2c\left(1+\mu_1\frac{u_k}{h}\right)} & 0 & -\frac{\mu_1}{2ch} & \frac{h(\mu_1-g_1)-\mu_1 u_k g_2}{3ch(g_1 g_2 - h(\gamma-1))} & 0 & 0 & 0 & 0 \\ \frac{u_k}{2c\left(1+\mu_2\frac{u_k}{h}\right)} & -\frac{k_z}{2c\left(1+\mu_2\frac{u_k}{h}\right)} & -\frac{k_r}{2c\left(1+\mu_2\frac{u_k}{h}\right)} & 0 & \frac{\mu_2}{2ch} & -\frac{h(\mu_2-g_1)-\mu_2 u_k g_2}{3ch(g_1 g_2 - h(\gamma-1))} & 0 & 0 & 0 & 0 \\ 0 & 0 & 0 & 0 & 0 & \frac{g_2}{\frac{3}{2}g_1(g_1 g_2 - h(\gamma-1))} & 0 & 0 & 0 & 0 \end{pmatrix} \tag{4.103}$$

where

$$u = u_z \qquad v = u_r \qquad w = u_\theta \qquad h = e_g + \frac{P_g}{\rho} \qquad u_{ek} = u_{ez}k_z + u_{er}k_r$$

$$u_k = uk_z + vk_r \qquad v_k = uk_r - vk_z \qquad c = \sqrt{(\gamma-1)\left(h + \tfrac{1}{4}(\gamma-1)u_k^2\right)}$$

$$g_1 = \tfrac{5}{3}u_{ek} - u_k \qquad g_2 = \tfrac{5}{3}u_{ek} - \gamma u_k$$

$$\mu_1 = \tfrac{1}{2}(\gamma-1)u_k - c \qquad \mu_2 = \tfrac{1}{2}(\gamma-1)u_k + c.$$

The first step in the scheme is extrapolation of the state variables, U from equation 4.2, to the interfaces between the nodes. This is done using equations 4.81 and 4.82 in the i direction to obtain the left and right interface values, U^L and U^R and similarly in the j direction to obtain the up and down values, U^U and U^D. The TVD flux limiter used was the Van Albada limiter from equation 4.79, with full upwinding specified by $k = -1$.

Next the diagonalizing matrices L and L^{-1} are evaluated in the ξ and η directions to obtain L_1, L_1^{-1}, L_2, L_2^{-1}. The eigenvalues of K are also evaluated in the ξ and η directions and split into their positive and negative components, Λ_1^+, Λ_1^-, Λ_2^+, Λ_2^-. The flux split jacobians $A^{\pm}$, $B^{\pm}$ are then calculated as in equation 4.60.

The next step is the calculation of the split fluxes,

$$F^+ = A^+U \qquad F^- = A^-U \qquad G^+ = B^+U \qquad G^- = B^-U. \tag{4.104}$$

For example the forward flux gradient $\mathcal{F}^+ = \frac{1}{Jr}\frac{\partial}{\partial\xi}\left(\frac{Jr}{k_\xi}A^+U\right)$ is given by

$$\mathcal{F}^+_{i,j} = \frac{1}{J_{i,j}r_{i,j}}\left(\frac{J_{i+1/2,j}r_{i+1/2,j}}{k_{\xi\ i+1/2,j}}A^+_{i+1/2,j}U^L_{i+1/2,j} - \frac{J_{i-1/2,j}r_{i-1/2,j}}{k_{\xi\ i-1/2,j}}A^+_{i-1/2,j}U^L_{i-1/2,j}\right) \tag{4.105}$$

and the backward flux gradient $\mathcal{F}^- = \frac{1}{Jr}\frac{\partial}{\partial\xi}\left(\frac{Jr}{k_\xi}A^-U\right)$ is given by

$$\mathcal{F}^-_{i,j} = \frac{1}{J_{i,j}r_{i,j}}\left(\frac{J_{i+1/2,j}r_{i+1/2,j}}{k_{\xi\ i+1/2,j}}A^-_{i+1/2,j}U^R_{i+1/2,j} - \frac{J_{i-1/2,j}r_{i-1/2,j}}{k_{\xi\ i-1/2,j}}A^-_{i-1/2,j}U^R_{i-1/2,j}\right) \tag{4.106}$$

Finally the viscous and other terms not included in $\mathcal{F}^+$ and $\mathcal{F}^-$ were calculated using central differences, converted into curvilinear coordinates and added back to the flux terms,

$$\mathcal{F} = \mathcal{F}^+ + \mathcal{F}^- + \mathcal{F}_{viscous} \tag{4.107}$$

and

$$U^{n+1} = U^n - \Delta t(\mathcal{F} + \mathcal{G} - S). \tag{4.108}$$

I chose to use a simple explicit first order time integration, as the complexity of the source terms made it difficult to calculate the source term jacobian required for an implicit

scheme. The rapid rate of chemical reactions resulted in the implicit scheme being unstable unless the source term jacobian was calculated to allow a linearized prediction of the source term.

Earlier runs using a global timestep with the MacCormack scheme had shown the resulting solution to be fairly constant with time, and since we were more interested in the converged solution than start-up behaviour, local timestepping was used. This made the need for second order accuracy in time less important so first order time integration was used, thereby requiring much less coding than would be required for a predictor-corrector step. This can be summarized as using equation 4.69, with the split fluxes of 4.70, made second order using variable extrapolation as in equation 4.71, and total variation diminishing using equations 4.81 and 4.82.

4.4 Successive Over-Relaxation

Relaxation schemes start with an initial guess and iterate a system of linear equations. How the iteration is performed depends upon the relaxation scheme used. The general form of a system of linear equations is

$$\overline{\overline{A}} \cdot \vec{x} = \vec{b}, \tag{4.109}$$

where $\overline{\overline{A}}$ is a coefficient matrix, $\vec{x}$ is a vector of unknowns, and $\vec{b}$ is a vector of constants. The matrix $\overline{\overline{A}}$ can be decomposed into parts

$$\overline{\overline{A}} = \overline{\overline{L}} + \overline{\overline{D}} + \overline{\overline{U}}, \tag{4.110}$$

where $\overline{\overline{D}}$ is the diagonal part of $\overline{\overline{A}}$, $\overline{\overline{L}}$ is the lower triangular portion of $\overline{\overline{A}}$ with zeros along the diagonal, and $\overline{\overline{U}}$ is the upper triangular portion of $\overline{\overline{A}}$, also with zeros along the diagonal. Relaxation schemes require diagonal dominance to work correctly. In other words, the magnitude of the coefficients along the diagonal is larger than the other coefficients. For the sparse matrix generated by finite differencing, diagonal dominance is nearly guaranteed.

The starting point for understanding relaxation methods is Jacobi's method. In matrix notation, Jacobi's method appears as

$$\overline{\overline{D}} \cdot \vec{x}^{\,n} = \vec{b} - \left(\overline{\overline{L}} + \overline{\overline{U}}\right) \cdot \vec{x}^{\,n-1}, \tag{4.111}$$

where the superscripts indicate the iteration level. From this equation one can see that all of the values at time level $n-1$ are used to update the new values at time level n at each point. It terms of computer resources, this requires more memory, since there must be an array to hold the old values plus an array in which the new values are stored. In addition, Jacobi's method converges rather slowly. To reduce the overall error by a factor of 10^{-p} for an $m \times m$ grid, the approximate number of iterations needed for large m is [100]

$$n \approx \frac{1}{2} p m^2, \tag{4.112}$$

which is hopelessly large for many problems. For a 100×100 grid, an error of 10^{-4} requires about 20,000 iterations.

An improvement to Jacobi's method is the Gauss-Seidel method. In matrix notation,

the Gauss-Seidel method is

$$\left(\overline{\overline{L}} + \overline{\overline{D}}\right) \cdot \vec{x}^{\,n} = \vec{b} - \overline{\overline{U}} \cdot \vec{x}^{\,n-1}. \tag{4.113}$$

If one were to write out Equation 4.113 in components, it would easily be seen that the updated values of $\vec{x}$ are used as they are acquired. This reduces the amount of necessary memory, as the old values of $\vec{x}$ are overwritten as the new values of $\vec{x}$ are found. The convergence characteristics are a bit better. For large m, the number of iterations needed to reduce the overall error by a factor of 10^{-p} is

$$n \approx \frac{1}{4} p m^2, \tag{4.114}$$

which is better, but still not very good.

With Jacobi's method and the Gauss-Seidel method the initial estimate moves monotonically towards the correct solution, never quite reaching it, so a method of increasing the speed of convergence is to jump a little bit further than the scheme predicts for each updating, anticipating future corrections. The Successive Over-Relaxation (SOR) method does just this. In the Successive Over-Relaxation scheme, the answer from the Gauss-Seidel method is over-corrected through an overcorrection factor, ω. In matrix notation, Successive Over-Relaxation is written as

$$\overline{\overline{D}} \cdot \vec{x}^{\,n} = (1-\omega)\,\overline{\overline{D}} \cdot \vec{x}^{\,n-1} + \omega\left(\vec{b} - \overline{\overline{L}} \cdot \vec{x}^{\,n} - \overline{\overline{U}} \cdot \vec{x}^{\,n-1}\right). \tag{4.115}$$

The convergence characteristics of SOR are entirely determined by the overcorrection factor. The optimal value of ω is

$$\omega = \frac{2}{1 + \sqrt{1 - \rho_{Jacobi}^2}}, \tag{4.116}$$

where ρ_{Jacobi} is known as the spectral radius of Jacobi's method, which is given by Press et al. [100] as

$$\rho_{Jacobi} = \frac{\cos\frac{\pi}{m} + \left(\frac{\Delta\xi}{\Delta\eta}\right)^2 \cos\frac{\pi}{n}}{1 + \left(\frac{\Delta\xi}{\Delta\eta}\right)^2}, \tag{4.117}$$

where m and n are the grid dimensions. For this optimal value of ω, the number of iterations

to reduce the error by a factor of 10^{-p} on a square grid with large m is

$$n \approx \frac{1}{3} pm, \tag{4.118}$$

which is a dramatic improvement over both the Jacobi and Gauss-Seidel methods. For a 100×100 grid, the number of iterations needed to reduce the error by a factor of 10^{-4} is about 134 iterations, which is less than 1% of the iterations needed for Jacobi's method.

Using central differences for second order accuracy, the discretized electrical potential equation (Equation 4.24) becomes

$$\begin{aligned} & a_{i,j}\left(\phi_{i+1,j} - 2\phi_{i,j} + \phi_{i-1,j}\right) + b_{i,j}\left(\phi_{i,j+1} - 2\phi_{i,j} + \phi_{i,j-1}\right) \\ & + \frac{c_{i,j}}{4}\left(\phi_{i+1,j+1} - \phi_{i+1,j-1} - \phi_{i-1,j+1} + \phi_{i-1,j-1}\right) \\ & + \frac{d_{i,j}}{2}\left(\phi_{i+1,j} - \phi_{i-1,j}\right) + \frac{e_{i,j}}{2}\left(\phi_{i,j+1} - \phi_{i,j-1}\right) = f_{i,j}, \end{aligned} \tag{4.119}$$

where iteration levels have been left off to avoid confusion. When used with SOR just described, the solution to the electrical potential at each point of the grid is iterated according to

$$\begin{aligned} \phi_{i,j}^{n+1} = (1-\omega)\,\phi_{i,j}^{n} + \frac{\omega}{2\left(a_{i,j} + b_{i,j}\right)} \Bigg[& \left(a_{i,j} + \frac{d_{i,j}}{2}\right)\phi_{i+1,j}^{n} + \left(a_{i.j} - \frac{d_{i,j}}{2}\right)\phi_{i-1,j}^{n+1} \\ & + \left(b_{i,j} + \frac{e_{i,j}}{2}\right)\phi_{i,j+1}^{n} + \left(b_{i,j} - \frac{e_{i,j}}{2}\right)\phi_{i,j-1}^{n+1} \\ & + \frac{c_{i,j}}{4}\left(\phi_{i+1,j+1}^{n} - \phi_{i+1,j-1}^{n} - \phi_{i-1,j+1}^{n} + \phi_{i-1,j-1}^{n+1}\right) - f_{i,j} \Bigg], \end{aligned} \tag{4.120}$$

where the $2\left(a_{i,j} + b_{i,j}\right)$ factor in the denominator corresponds to the elements of $\overline{\overline{D}}$, while the other constants correspond to the off-diagonal elements in $\overline{\overline{L}}$ and $\overline{\overline{U}}$.

Within the numerical scheme even a hundred iterations took too long and greatly slowed the code, but a simple way to speed up the convergence of the potential calculation was found. Provided that the constrictor is an insulator so that no current is allowed to attach within the constrictor. Since the current supplied to the arcjet is prescribed rather than the voltage this means that the prescribed current must pass through the constrictor. An iteration of the potential calculation as it sweeps through the array updates the potentials

at a given axial location. Within the constrictor it is then possible to calculate the current across that plane in the constrictor predicted by this potential, and then on bulk adjust the potential to match the specified current that will be the converged solution. If the planes chosen are at constant axial distances along the thruster this leaves the potential to sort out just the radial distribution. The current passed at a given constant z plane is given discretely as

$$I = \sum_{j=0}^{n_j-1} \frac{\pi}{2} \left(J_{zj+1} + J_{zj}\right) \left(r_{j+1}^2 - r_j^2\right). \tag{4.121}$$

Expanding the current density in terms of the electric potential and electron pressure this is

$$I = \frac{\pi}{2} \sum_{j=0}^{n_j-1} \left(r_{j+1}^2 - r_j^2\right) \left(\psi \frac{\partial P_e}{\partial z}\right) - \frac{\pi}{2} \sum_{j=0}^{n_j-1} \left(r_{j+1}^2 - r_j^2\right) \sigma \frac{\partial \xi}{\partial z} \left(\phi_{i+1,j} - \phi_{i,j}\right). \tag{4.122}$$

At a given timestep the electron pressure term will be a constant, C. Comparing this current to the specified current, and setting the difference to zero by adding a constant amount Δ to each current $\phi_{i,j}$ we have

$$I - I_{spec} = 0 = C - I_{spec} - \frac{\pi}{2} \sum_{j=0}^{n_j-1} \left(r_{j+1}^2 - r_j^2\right) \sigma \frac{\partial \xi}{\partial z} \left(\phi_{i+1,j} - \left(\phi_{i,j} - \Delta\right)\right), \tag{4.123}$$

so

$$\frac{d\left(I - I_{spec}\right)}{d\Delta} = -\frac{\pi}{2} \sum_{j=0}^{n_j-1} \left(r_{j+1}^2 - r_j^2\right) \sigma. \tag{4.124}$$

Thus to pass the specified current the correction Δ is simply

$$\Delta = \frac{\left(I - I_{spec}\right)}{\frac{d\left(I - I_{spec}\right)}{d\Delta}} \tag{4.125}$$

and

$$\phi_{i,j}^{new} = \phi_{i,j} - \Delta. \tag{4.126}$$

4.5 Boundary Conditions

In any numerical integration scheme, the correct boundary conditions are essential in getting a correct solution. There are two types of boundary conditions; firstly Dirichlet conditions where the absolute value at the boundary is known, and secondly Neumann conditions where the gradient at the boundary is known. An example of a Neumann condition is if the gradient of the quantity φ at the boundary is specified according to

$$\left.\frac{\partial \varphi}{\partial \hat{n}}\right|_{boundary} = \Theta, \tag{4.127}$$

where $\hat{n}$ is the unit outward normal and Θ is often zero, then this can be rewritten as

$$(\nabla \varphi \cdot \hat{n})_{bndy} = \left[\left(\frac{\partial \varphi}{\partial z}\,\hat{z} + \frac{\partial \varphi}{\partial r}\,\hat{r}\right) \cdot \hat{n}\right]_{bndy} = \Theta, \tag{4.128}$$

where $\nabla\varphi$ is the gradient in the $z-r$ coordinate system. The unit outward normal vector is defined as shown in Figure 4-13, where $\hat{z}$ and $\hat{r}$ are unit vectors in the z and r directions, respectively, and $\hat{n}$ and $\hat{s}$ are the outward unit surface normal and counterclockwise unit surface tangent vectors, respectively, and β is the angle between $\hat{z}$ and $\hat{n}$.

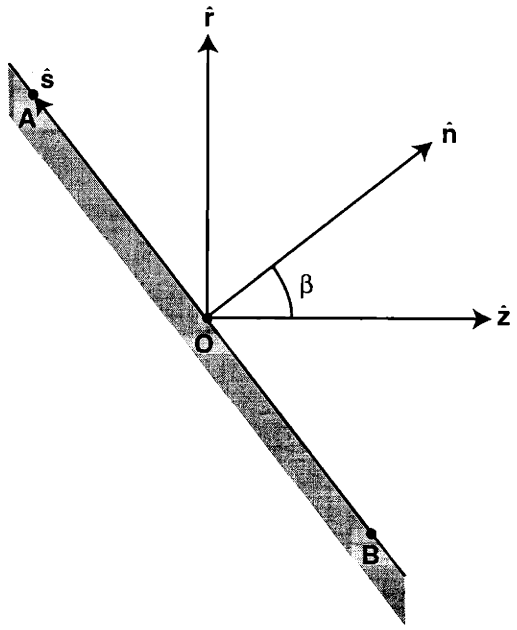

Figure 4-13: *Coordinate Axes Used for the Calculation of Boundary Conditions*

In terms of β, $\hat{z}$, and $\hat{r}$, the unit normal and tangent vectors can be written as

$$\hat{n} = \cos\beta\,\hat{z} + \sin\beta\,\hat{r} \tag{4.129}$$

and

$$\hat{s} = -\sin\beta\,\hat{z} + \cos\beta\,\hat{r}. \tag{4.130}$$

Since the z and r values are known at the boundary, the unit tangent vector can be written as

$$\hat{s} = \frac{z_A - z_B}{\Delta s}\,\hat{z} + \frac{r_A - r_B}{\Delta s}\,\hat{r}, \tag{4.131}$$

where

$$\Delta s = \sqrt{(z_A - z_B)^2 + (r_A - r_B)^2}\,, \tag{4.132}$$

and it has been assumed that $\overline{OB}$ and $\overline{OA}$ are collinear. From the above equations it is easily seen that

$$\cos\beta = \frac{r_A - r_B}{\Delta s} \tag{4.133}$$

and

$$\sin\beta = -\frac{z_A - z_B}{\Delta s}\,, \tag{4.134}$$

so that the unit normal vector can be written as

$$\hat{n} = \frac{r_A - r_B}{\Delta s}\,\hat{z} - \frac{z_A - z_B}{\Delta s}\,\hat{r}. \tag{4.135}$$

The differences $r_A - r_B$ and $z_A - z_B$ can be put in terms of the grid metrics at the boundaries. For example, at the exit boundary, if O is at the grid point (i, j), then A is located at $(i, j+1)$ and B is at $(i, j-1)$. The unit normal vector can then be calculated as

$$\hat{n} = \frac{r_{i,j+1} - r_{i,j-1}}{\Delta s}\,\hat{z} - \frac{z_{i,j+1} - z_{i,j-1}}{\Delta s}\,\hat{r}, \tag{4.136}$$

with

$$\Delta s = \sqrt{(r_{i,j+1} - r_{i,j-1})^2 + (z_{i,j+1} - z_{i,j-1})^2}, \tag{4.137}$$

which can conveniently be written as

$$\hat{n} = \left.\frac{r_\eta}{\Delta s}\right|_{i,j} \hat{z} - \left.\frac{z_\eta}{\Delta s}\right|_{i,j} \hat{r}, \tag{4.138}$$

with

$$\Delta s = \sqrt{r_\eta^2 + z_\eta^2}, \tag{4.139}$$

where r_η and z_η are the same grid metrics which need to be calculated anyway in the transformation of the governing equations from real to natural coordinates. This form of the unit tangent vector makes boundary value calculations much easier, as the values of the grid metrics would already be stored in memory from the grid transformation calculations.

4.5.1 Fluid Boundary Conditions

Inlet Boundary

The inlet and outlet boundary conditions proved to be most difficult to specify in order to obtain realistic behaviour of the internal flow, many different approaches were tried including Riemann invariants, specification of total pressure or temperature, and simple extrapolation methods. The simplest methods behaved most predictably and caused the least problems, so finally the inlet pressure or mass flow rate was specified, and the other extrapolated upstream.

At the inlet a distinction is made between the the *inlet flow* and the *inlet boundary*. The inlet flow denotes the flow upstream of the grid and is assumed to behave as a free stream flow, and cannot "see" the grid. The inlet boundary contains the first boundary nodes of the computational grid to be affected by the inlet flow. The inlet flow is assumed to be uniform and subsonic. The flow variables at an inlet boundary node are specified according to the assumed inlet flow and information about the first point inside the inlet boundary. In most experimental arcjets, either the total mass flow rate or the plenum pressure is specified, so either can be specified in the code. Since for subsonic inlet flow another gas property has to be specified, this was chosen to be the temperature. It was assumed that the inflowing propellant was heated by conduction through the thruster or even regenerative cooling to a temperature of five hundred Kelvin.

The inlet gas composition at 500 K was taken to contain only a minimum amount of

dissociated hydrogen and ionized hydrogen and cesium. These minimum values were not zero due to numerical problems if they were allowed below certain limits. The remaining bulk of the mixture was taken to be molecular hydrogen with a seed mass fraction of two percent atomic cesium.

Given that the composition was specified and so were the pressure and temperature this means the gas constant, ratio of specific heats, and density were also known at the inlet.

For the velocities, the inlet flow is assumed to be uniform and parallel to the thruster walls, so there is no radial velocity. The axial velocity was obtained by extrapolating the mass flux ρu_z from the first two interior grid points. The inlet azimuthal velocity was specified to be a certain fraction of the inlet axial velocity, although to date this fraction has only been set to zero.

No current is allowed to exist at the inlet so the slip velocities were set to zero, so the electron velocity was just the gas velocity. The electron thermal conductivity is much higher than the heavy species thermal conductivity if the electron number density is significant, so it is arguable that the electron temperature should be extrapolated upstream from the interior. However there are virtually no electrons at the inlet and in the limit that $n_e \to 0$ the electrons would be in equilibrium with the heavy species, so the electron temperature was specified to be the inlet gas temperature of 500 K. Since the electron density is known because of quasineutrality with the specified density of ions at the inlet, the electron pressure is therefore also known at the inlet.

Outlet Boundary

The values at the outlet boundary typically vary according to whether the flow is subsonic or supersonic.

In the supersonic regions of the exit plane, the flow variables can simply be extrapolated, since no information propagates upstream. Therefore, the variables at boundary node (i, j) are specified according to

$$\varphi_{i,j} = 2\varphi_{i-1,j} - \varphi_{i-2,j}. \tag{4.140}$$

The pressure, temperature, mass fractions, and velocities are all extrapolated at the exit plane. The density is then calculated based on these values.

The subsonic regions at the outlet boundary are near the nozzle walls, in the viscous

boundary layer, and may also occur during startup from a subsonic flow. First Riemann Invariants were tried, although in the non-equilibrium boundary layer the validity of using the Riemann invariants to find the flow variables is questionable at best, especially in the presence of electric and magnetic fields. However, the subsonic region at the nozzle exit is typically very small, and since the current is forced to attach upstream of the exit, the current effects are minimal. Nevertheless numerous problems with that formulation were encountered so instead to the exit pressure was specified, and the gas temperature, mass fractions and velocities were then extrapolated. If the entire exit flow was subsonic the exit pressure was set to a nominal low exit pressure simulating the background vacuum, but which was not low enough to cause numerical problems. The low exit pressure then causes the gas in the nozzle to accelerate to supersonic speeds. For the subsonic boundary layer in an otherwise supersonic flow, the pressure is approximately constant across the boundary layer, so the exit pressure was set that of the first exit node where the flow was supersonic.

For the electron temperature due to the electrons' high mobility the electron temperature gradient was taken to be zero and simply set the exit electron temperature to be equal to that of the last interior grid point $T_{e\,i,j} = T_{e\,i-1,j}$. This is not strictly accurate if the grid is not orthogonal at the exit, but the more accurate formulation

$$T_{e\,i,j} = T_{e\,i-1,j} + \left.\frac{z_\xi z_\eta + r_\xi r_\eta}{z_\eta^2 + r_\eta^2}\right|_{i,j} \frac{T_{e\,i,j+1} - T_{e\,i,j-1}}{2} \tag{4.141}$$

when coupled with the electrical potential calculation proved to be unstable.

Centreline Boundary

The centreline boundary of the arcjet is a symmetry boundary along the axis of the thruster, so the radial and swirl velocities are set to zero, and a zero gradient condition is imposed on all of the other flow variables. Since the centreline boundary is one of constant η the variables at the centreline boundary are calculated using forward differences in η and central in ξ. In terms of the grid metrics, the flow variables at the centreline are calculated according to

$$\varphi_{i,j} = \varphi_{i,j+1} - \left.\frac{z_\xi z_\eta + r_\xi r_\eta}{z_\xi^2 + r_\xi^2}\right|_{i,j} \frac{\varphi_{i+1,j} - \varphi_{i-1,j}}{2}. \tag{4.142}$$

Wall Boundaries

The boundary wall conditions only caused problems when modelled as plasma sheaths rather than as solid walls or internal flow before the plasma presheath is encountered. The problems basically arose because of large gradients in the mass fractions of the species which occur because charged species are neutralized at walls in a real plasma.

Any solid surface immersed in a partially ionized gas develops a non-neutral sheath adjacent to it due to the higher mobility of the electrons. The thickness of this sheath depends on temperature and pressure and is of the order of the Debye length. For the range of temperatures and pressures within arcjets, the Debye length is of the order of $10^{-8} - 10^{-6}$ meters. For this reason, the sheath region is neglected in the actual calculations, and the wall boundaries should be treated as sheath boundaries.

At the wall boundaries, it can be assumed that the ion velocity at the edge of the plasma sheath is limited by an electrostatically choked flow beyond which the ions free fall collisionlessly through the sheath to the wall. The flow equations at the wall are simplified for electrons to

$$kT_e \frac{dn_e}{dx} = -en_e E \tag{4.143}$$

neglecting inertia, and for ions,

$$\frac{d}{dx}\left(m_i n_i V_i^2 + n_i k T_i\right) = en_e E - \mu_{in}\nu_{in} n_i V_i. \tag{4.144}$$

Adding these together and substituting the flux $\Gamma = nV$, which is approximately constant across the sheath, gives

$$\frac{d}{dx}\left(m_i \frac{\Gamma_i^2}{n_i} + n_i k T_i + n_e k T_e\right) = eE\left(n_i - n_e\right) - \mu_{in}\nu_{in}\Gamma_i. \tag{4.145}$$

Noting that $eE\left(n_i - n_e\right) = \varepsilon_o E \frac{dE}{dx}$. and whilst quasineutrality is not held well enough to shield any electric fields, $n_e \approx n_i$ so integrating with respect to x yields

$$m_i \frac{\Gamma_i^2}{n_i} + n_i k(T_e + T_i) = \frac{1}{2}\varepsilon_o E^2 - \mu_{in}\nu_{in}\Gamma_i(x - x_o). \tag{4.146}$$

The left hand term contains a minimum with respect to n_i, beyond which quasineutrality can no longer hold and free fall to the wall occurs. The edge of the sheath occurs at this

last point where quasineutrality holds and in the pre-sheath electric pressure is still small so can be neglected, so at the minimum with respect to n_i,

$$-\frac{m_i\Gamma_i^2}{n_i^2} + k(T_e + T_i) = 0, \tag{4.147}$$

therefore

$$V_i = \sqrt{\frac{k(T_e + T_i)}{m_i}} = V_{Bohm}. \tag{4.148}$$

This is the velocity at which ions enter the sheath from the pre-sheath [45], and is known as the Bohm velocity. It is the isothermal isentropic speed of sound in the plasma, which is acquired by having choking at the entrance to the sheath. It is analogous to reaching the speed of sound at the end of a pipe which opens into a vacuum.

Rewriting equation 4.143 as

$$kT_e\frac{dn_e}{dx} = -en_e\frac{d\phi}{dx} \tag{4.149}$$

and integrating yields

$$n_e = n_{e\infty}\exp\left(\frac{e\phi}{kT_e}\right). \tag{4.150}$$

For ions in the sheath the electrostatic attraction is dominant so

$$\frac{1}{2}m_i n_i V_i^2 = -en_i\phi. \tag{4.151}$$

Extrapolating this to the sheath edge where v_i is the Bohm velocity gives

$$\phi_{sheath\ edge} = -\frac{k(T_e + T_i)}{2e}, \tag{4.152}$$

so

$$\left.\frac{n_e}{n_{e\infty}}\right|_{sheath\ edge} = \exp\left(-\frac{T_e + T_i}{2T_e}\right). \tag{4.153}$$

Thus the flux of ions falling into the sheath is

$$\Gamma_i = n_{e\infty}\sqrt{\frac{k(T_e + T_i)}{m_i}}\exp\left(-\frac{T_e + T_i}{2T_e}\right). \tag{4.154}$$

For $T_e \gg T_i$ the exponential term is 0.61 as used by Miller [85], or for $T_e = T_i$ it is 0.37 as used by Benson [5].

To calculate the densities of the ionic species it is assumed that the diffusion flux arriving at the sheath boundary is the same as the flux of ions reaching the wall at the Bohm velocity [43] [131], so

$$\rho_i \alpha_i \sqrt{\frac{k(T_e + T_i)}{m_i}} = D_i \frac{\partial \rho_i}{\partial \hat{n}}, \tag{4.155}$$

where $\alpha_i = \exp\left(-\frac{T_e+T_i}{2T_e}\right)$, and can either be evaluated at the grid node or reasonably assumed to take any value between 0.37 and 0.61. Thus the boundary conditions for ions becomes

$$\frac{\partial \rho_i}{\partial \hat{n}} = \frac{0.37\rho_i}{D_{ai}} \sqrt{\frac{k\left(T_e + T_i\right)}{m_i}}, \tag{4.156}$$

where D_{ai} is the ambipolar diffusion coefficient. Summing over the ionic species the boundary condition for electrons is

$$\frac{\partial \rho_e}{\partial \hat{n}} = \sum_{ions} \frac{0.37\rho_i}{D_{ai}} \sqrt{\frac{k\left(T_e + T_i\right)}{m_i}}. \tag{4.157}$$

For molecules which are assumed to be reflected unchanged from the wall For molecules:

$$\frac{\partial \rho_m}{\partial \hat{n}} = 0. \tag{4.158}$$

Due to catalytic ion-electron recombination at the wall, the flux of neutral atoms away from the wall, must equal the flux of ions to the wall,

$$\rho_a V_a + \rho_i V_i = 0 \qquad \text{so} \qquad V_a = -\frac{\rho_i}{\rho_a} \sqrt{\frac{k(T_e + T_i)}{m_i}}. \tag{4.159}$$

From equation 4.135 the unit vectors normal to the surface are given as:
On the upper surface:

$$\hat{n} = \left(\frac{r_\xi}{\Delta s}\hat{z} \ , \ -\frac{z_\xi}{\Delta s}\hat{r}\right). \tag{4.160}$$

On the lower surface:

$$\hat{n} = \left(-\frac{r_\xi}{\Delta s}\hat{z} \ , \ \frac{z_\xi}{\Delta s}\hat{r}\right). \tag{4.161}$$

On the cathode tip:

$$\hat{n} = \left(-\frac{r_\eta}{\Delta s_\eta}\hat{z} \ , \ 0\right), \tag{4.162}$$

where $\Delta s_\eta = \sqrt{r_\eta^2 + z_\eta^2}$.

Now for the upper surface we have

$$\Theta = \frac{\varphi_z r_\xi}{\Delta s} - \frac{\varphi_r z_\xi}{\Delta s} \tag{4.163}$$

which in terms of derivatives in ξ and η is

$$\begin{aligned}\Delta s\,\Theta &= r_\xi\left(\xi_z\varphi_\xi + \eta_z\varphi_\eta\right) - z_\xi\left(\xi_r\varphi_\xi + \eta_r\varphi_\eta\right)\\ &= \left(r_\xi\xi_z - z_\xi\xi_r\right)\varphi_\xi + \left(r_\xi\eta_z - z_\xi\eta_r\right)\varphi_\eta\\ &= \frac{\left(r_\xi r_\eta + z_\xi z_\eta\right)}{J}\varphi_\xi + \frac{\left(-r_\xi^2 - z_\xi^2\right)}{J}\varphi_\eta. \end{aligned}\tag{4.164}$$

But $\Delta s^2 = r_\xi^2 + z_\xi^2$ therefore

$$-\frac{J\Theta}{\Delta s} = \varphi_\eta - \frac{r_\xi r_\eta + z_\xi z_\eta}{\Delta s^2}\varphi_\xi \tag{4.165}$$

where $\varphi_\eta = \varphi_{n_j} - \varphi_{n_j-1}$ and centred differencing should be used in ξ.

Similarly for the lower surface

$$\Theta = \frac{-\varphi_z r_\xi}{\Delta s} + \frac{\varphi_r z_\xi}{\Delta s} \tag{4.166}$$

which leads to

$$+\frac{J\Theta}{\Delta s} = \varphi_\eta - \frac{r_\xi r_\eta + z_\xi z_\eta}{\Delta s^2}\varphi_\xi \tag{4.167}$$

where $\varphi_\eta = \varphi_{j+1} - \varphi_j$ and centred differencing should be used in ξ.

On the cathode tip the gradient equation becomes

$$+\frac{J\Theta}{\Delta s} = \varphi_\xi - \frac{r_\xi r_\eta + z_\xi z_\eta}{\Delta s_\eta^2}\varphi_\eta \tag{4.168}$$

where $\varphi_\xi = \varphi_{i+1} - \varphi_i$ and centred differencing should be used in η.

Thus for the ion density where, for example, the boundary condition on the upper and lower walls is given by

$$\frac{\partial \rho_i}{\partial \hat{n}} = \frac{0.37\rho_i}{D_{ai}}\sqrt{\frac{k\left(T_e + T_i\right)}{m_i}} = C\rho_i \tag{4.169}$$

which when discretized becomes

$$\rho_{e\,i,j} = \left(\frac{1}{1+\frac{JC}{\Delta s}}\right)\left(\rho_{e\,i,j\mp1} \pm \left.\frac{z_\xi z_\eta + r_\xi r_\eta}{z_\xi^2 + r_\xi^2}\right|_{i,j} \frac{\rho_{e\,i+1,j} - \rho_{e\,i-1,j}}{2}\right), \tag{4.170}$$

where the upper sign is for the upper wall boundary and the lower sign is for the lower wall boundary. On the cathode tip, ξ = constant and

$$\rho_{e\,i,j} = \left(\frac{1}{1+\frac{JC}{\Delta s_\eta}}\right)\left(\rho_{e\,i+1,j} - \left.\frac{z_\xi z_\eta + r_\xi r_\eta}{z_\eta^2 + r_\eta^2}\right|_{i,j} \frac{\rho_{e\,i,j+1} - \rho_{e\,i,j-1}}{2}\right). \tag{4.171}$$

Using these boundary conditions the resulting sharp changes in species densities could cause instabilities under certain circumstances. Consequently they were abandoned in favour of the simpler condition of zero gradient as will be found at the internal flow to presheath boundary rather than the presheath to sheath boundary. Ignoring wall recombination however will slightly exaggerate performance.

For the heavy species temperature it should ideally be modelled by including a heat transfer model in the anode block. However Miller [85] found that whether this was done or the boundary temperature merely imposed caused no significant change in the flow behaviour. Thus to save computational effort the heat balance with the anode was neglected. This left the choice of either specifying the wall temperature or applying a zero gradient condition. Without any experimental seeded arcjets yet in existence, following Oyerokun [93] zero gradient was specified. The effect of doing this is that the walls will be hotter than would be tolerable by most materials. If cooling were then put in place to cool the walls to tolerable temperatures a region near the walls of cooler and thus denser gas would result. This needs to be investigated further as it may have a substantial effect on seeded arcjet performance.

For the electron temperature due to the electrons' high mobility a zero gradient condition was also applied, so on the η = constant boundaries,

$$T_{e\,i,j} = T_{e\,i,j\mp1} \pm \left.\frac{z_\xi z_\eta + r_\xi r_\eta}{z_\xi^2 + r_\xi^2}\right|_{i,j} \frac{T_{e\,i+1,j} - T_{e\,i-1,j}}{2}, \tag{4.172}$$

and on the cathode tip,

$$T_{e\,i,j} = T_{e\,i+1,j} - \left.\frac{z_\xi z_\eta + r_\xi r_\eta}{z_\eta^2 + r_\eta^2}\right|_{i,j} \frac{T_{e\,i,j+1} - T_{e\,i,j-1}}{2}. \tag{4.173}$$

Once the electron temperature is determined, the electron pressure is calculated. The zero gradient condition is then applied to the total static pressure ($p_g + p_e$), using equations of the form of 4.172 and 4.173. The heavy species pressure is then found by subtracting the electron pressure from the total static pressure. Once the heavy species pressure is found, the global density is then determined.

At the wall boundaries, the no-slip velocity condition is enforced. Therefore, the mass-averaged velocities at the walls are set to zero. In other words, $u_z = u_r = u_\theta = 0$. This does not apply for the diffusion velocities normal to the wall boundaries, and indeed cannot apply if equation 4.155 is to be enforced. Therefore, the different species do have a nonzero normal velocity at the walls equal to the diffusion velocity. It is only on aggregate that the velocity is zero.

4.5.2 Electrical Potential Boundary Conditions

Cathode Tip

The boundary condition on the cathode tip is of the Dirichlet type, but only in a convoluted sense. Since prediction of the potential drop in the sheath region is sketchy, at best, the best way to assure the correct current flow throughout the core of the thruster during numerical simulation is to specify the current on the cathode tip. As mentioned previously, the cathode tip is made to be a flat surface for simplicity. Therefore, since this flat area of the cathode tip is known, specifying the current on the cathode tip amounts to specifying the current density at the boundary nodes themselves. This is achieved by the method described at the end of section 4.4 where the specified current is enforced throughout the constrictor and not just on the cathode tip.

Outlet Boundary

At the outlet, the current density is forced to be zero so that no current can leave the thruster, i.e.

$$\vec{j} \cdot \hat{n} = (\sigma \nabla \phi - \psi \nabla p_e) \cdot \hat{n} = 0 \tag{4.174}$$

at all of the boundary nodes. Transforming to natural coordinates and using backward differences for the derivatives in ξ and central differences for derivatives in η yields the

difference equation used to calculate the potential at the outlet

$$\phi_{i,j} = \phi_{i-1,j} + \frac{p_{ei,j} - p_{ei-1,j}}{en_{ei,j}} + \frac{1}{2}\frac{z_\xi z_\eta + r_\xi r_\eta}{z_\eta^2 + r_\eta^2}\bigg|_{i,j}\left(\phi_{i,j+1} - \phi_{i,j-1} - \frac{p_{ei.j+1} - p_{ei,j-1}}{en_{ei,j}}\right), \tag{4.175}$$

where the relation $\sigma = en_e\psi$ has been used in simplifying. As mentioned above, the electron temperature can interact in a negative way with the above equation. Because of this, the following simplified equation was used to calculate the potential at the outlet boundary:

$$\phi_{i,j} = \phi_{i-1,j} + \frac{p_{ei,j} - p_{ei-1,j}}{en_{ei,j}}. \tag{4.176}$$

Centreline Boundary

The centreline is a symmetry boundary, so therefore, $\vec{j}\cdot\hat{n} = 0$. In transformed natural coordinates and using the necessary grid metrics, the potential along the centreline is calculated according to

$$\phi_{i,j} = \phi_{i,j+1} - \frac{p_{ei,j+1} - p_{ei,j}}{en_{ei,j}} - \frac{1}{2}\frac{z_\xi z_\eta + r_\xi r_\eta}{z_\xi^2 + r_\xi^2}\bigg|_{i,j}\left(\phi_{i+1,j} - \phi_{i-1,j} - \frac{p_{ei+1,j} - p_{ei-1,j}}{en_{ei,j}}\right). \tag{4.177}$$

Upper Wall Boundary

As mentioned in Section 4.1.1, the grid used for potential calculations only coincides with the flow grid in the region downstream of the constrictor entrance. As Figure 4-3 shows, the "upper wall" of a portion of the potential grid does not coincide with a wall at all, but lies within a region of the flow field. Since the current is not allowed to creep upstream, the portion of the potential grid within the flow field is treated as an insulator. At all points of the fluid upstream of this grid, the current density is set to zero, and no electrical potential calculation is performed. Along the insulating portions of the upper wall, the potential is calculated from

$$\phi_{i,j} = \phi_{i,j-1} + \frac{p_{ei,j} - p_{ei,j-1}}{en_{ei,j}} + \frac{1}{2}\frac{z_\xi z_\eta + r_\xi r_\eta}{z_\xi^2 + r_\xi^2}\bigg|_{i,j}\left(\phi_{i+1,j} - \phi_{i-1,j} - \frac{p_{ei+1,j} - p_{ei-1,j}}{en_{ei,j}}\right). \tag{4.178}$$

This insulated portion extends to the constrictor exit. In modelling conventional arcjets this can be done for numerical reasons [85] even though the constrictor in conventional arcjets

is usually conducting. For the case of seeded arcjets the constrictor was specifically chosen as an insulator. This is because in conventional arcjets there is only strong ionization and hence a conducting path in the core of the constrictor and a narrow arc is formed, but when a readily ionizable seed is added it was expected that there would be charged particles spread throughout the constrictor and so the current would also be uniformly spread throughout the constrictor. With the current behaving in this manner and focused into a narrow region in the core there is a conducting path straight to the constrictor walls, so if the constrictor was made of an insulator it is believed that the current would attach itself immediately without passing all the way through the constrictor, which would mean a very short high power arc through which the propellant would pass too quickly to be substantially heated, as is required for the arcjet to work as conceptualized.

Along the anode wall from the constrictor exit to the nozzle exit, the wall is treated as a conductor, and the potential is set to be at a reference potential of 1000 V.

4.6 Initial Conditions

The initial conditions should be chosen as to most closely approximate the steady state solution. For the very first few runs when the general behaviour was not known a variety of initial conditions were tried from a simple subsonic isentropic flow that can be calculated straightforwardly, to converged solutions of Miller [85] of a conventional arcjet to which cesium was added. The numerical transients experienced however were in some cases so wild that they caused the code to crash. This was eventually dealt with by placing limits on the rate of change of all the properties, so that the finite timestep estimated could actually be used, without going to unusefully small timesteps. This should not be a problem in a real thruster, as for the most part the transients were merely an artifact of the finite timestep used. Once the simulation settled down, the restrictions were removed as the timestep was then short enough. The first few runs showed that when run near the nominal operating point the flow is very uniform which then lead to simple 1-D heat addition to flow in a pipe being used as the initial condition. This was found to be very successful and gave minimal transients.

Chapter 5

Fluid Model Results

5.1 Nominal Run

The grid used to calculate the seeded arcjet performance on, as shown in 4.1.1, was essentially that of the the German TT1 thruster but with the constrictor stretched to give a length to diameter ratio of ten. The prescribed variables such as the inlet pressure and temperature, and the applied current, were chosen to be similar to those used by Oyerokun [93], although in the course of obtaining a converged run these values were altered slightly.

Seed Mass Fraction	2%
Inlet Pressure	8×10^5 Pa
Inlet Temperature	500 K
Applied Current	17 V

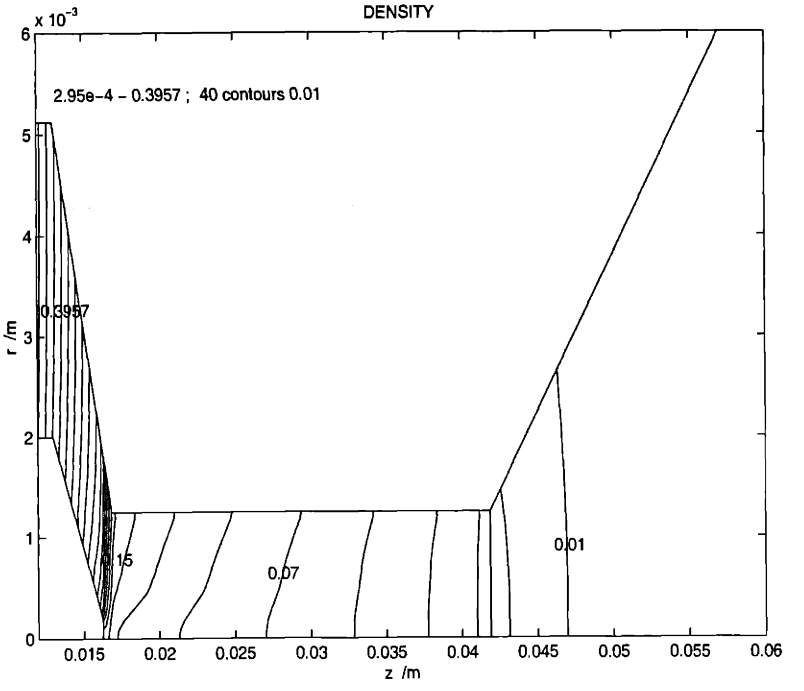

Figure 5-1: *Density in a Seeded Arcjet*

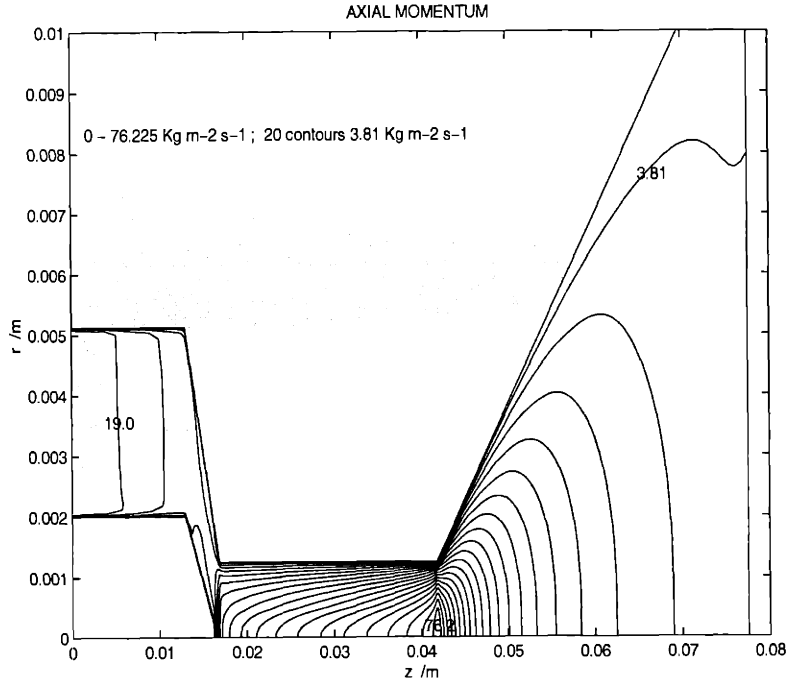

Figure 5-2: *Axial Momentum in a Seeded Arcjet*

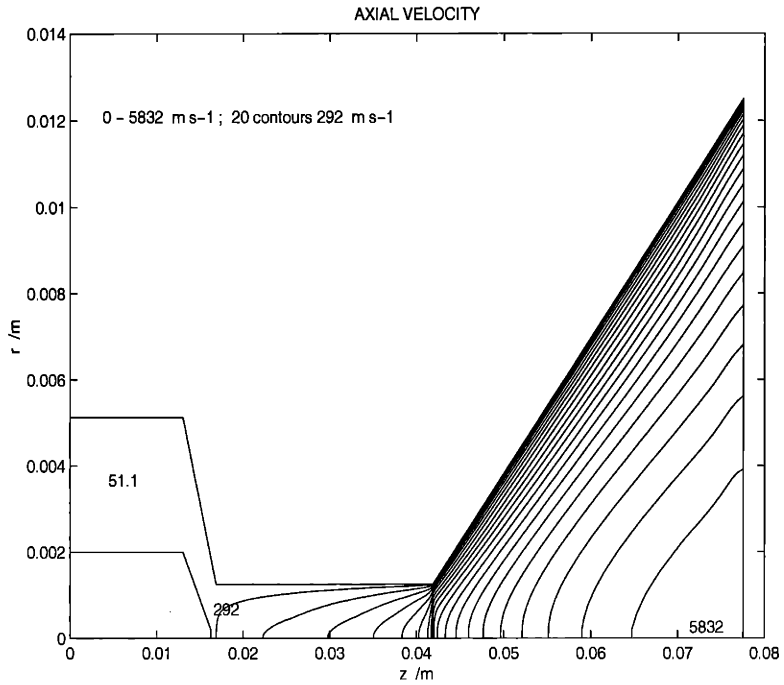

Figure 5-3: *Axial Velocity in a Seeded Arcjet*

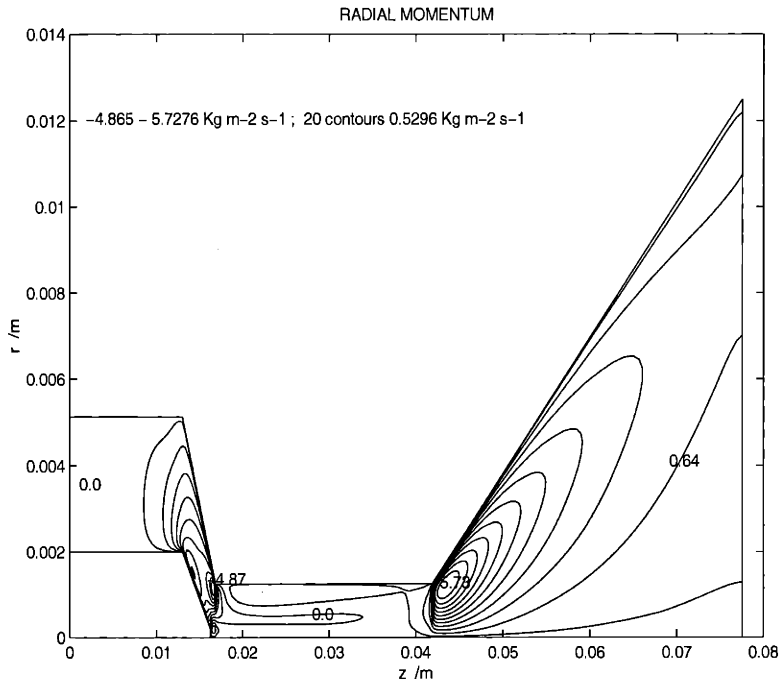

Figure 5-4: *Radial Momentum in a Seeded Arcjet*

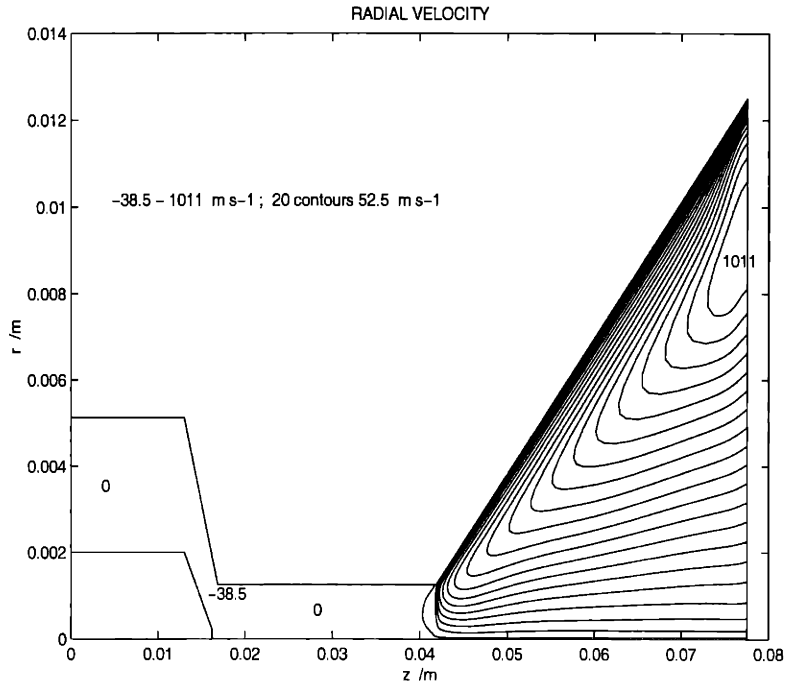

Figure 5-5: *Radial Velocity in a Seeded Arcjet*

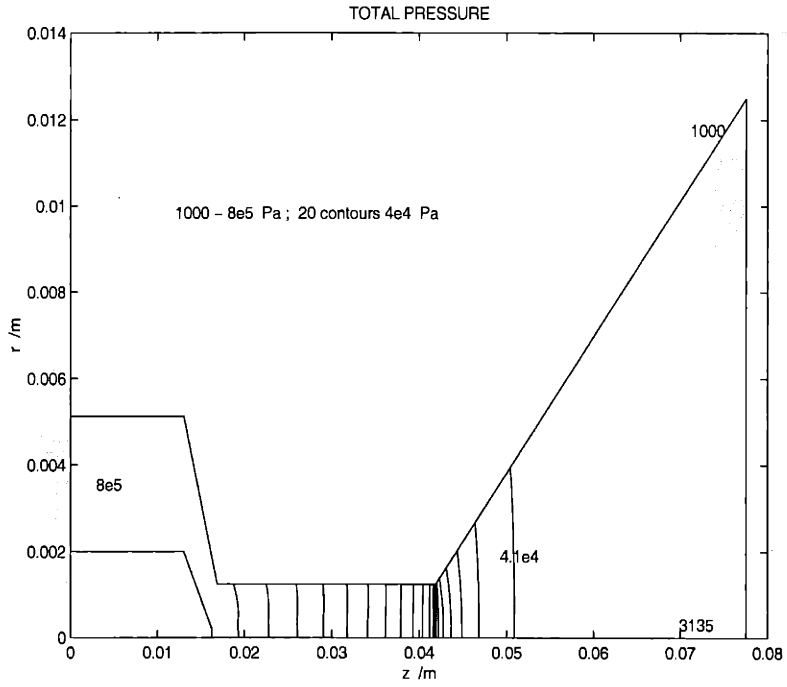

Figure 5-6: *Pressure in a Seeded Arcjet*

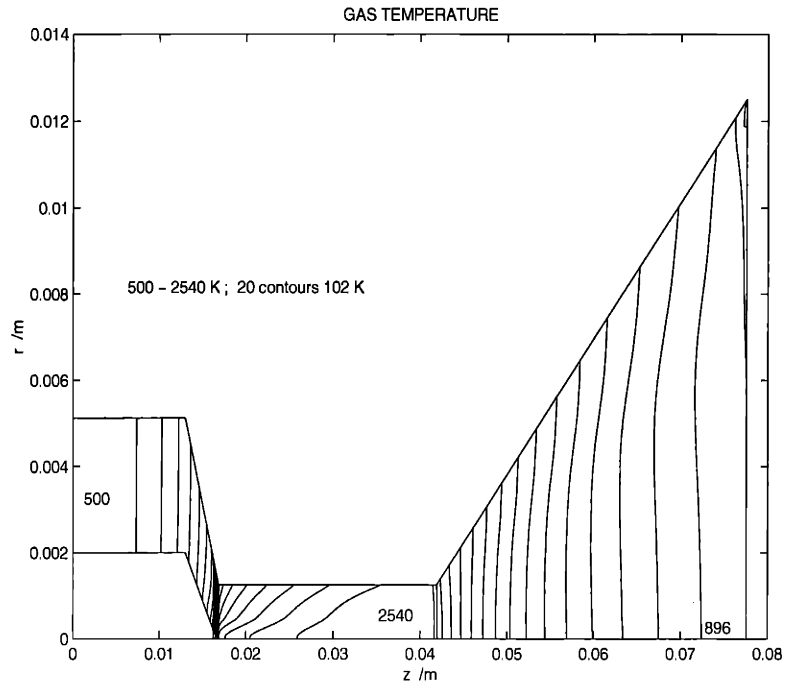

Figure 5-7: *Gas Temperature in a Seeded Arcjet*

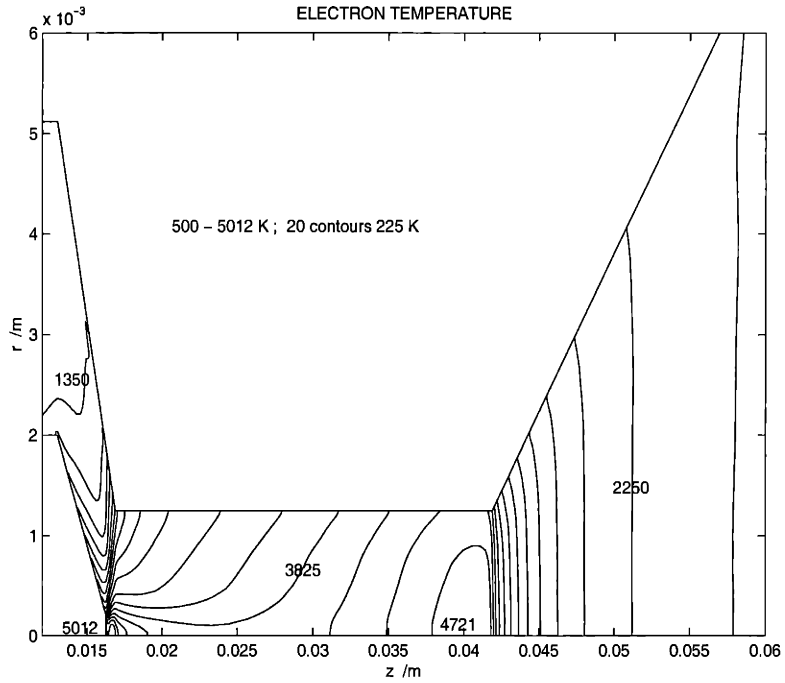

Figure 5-8: *Electron Temperature in a Seeded Arcjet*

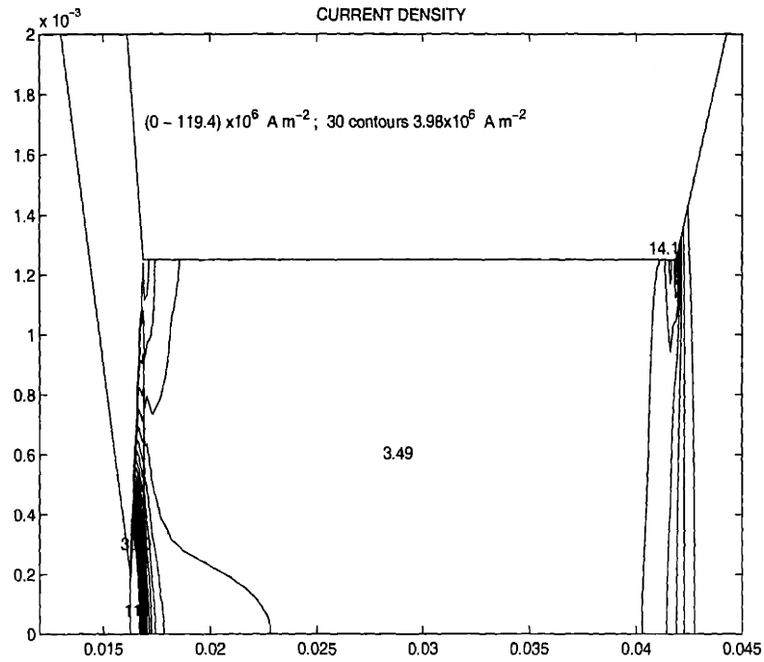

Figure 5-9: *Current Density in a Seeded Arcjet*

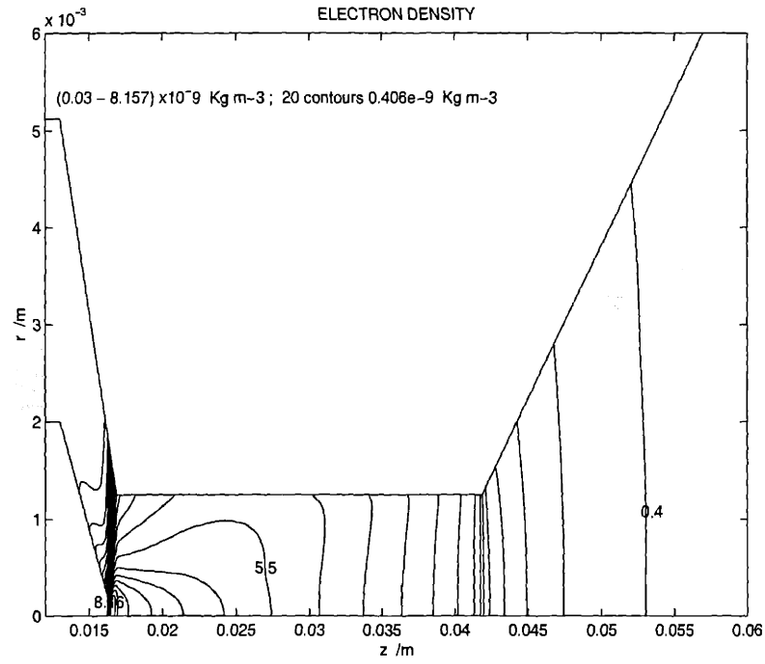

Figure 5-10: *Electron Density in a Seeded Arcjet*

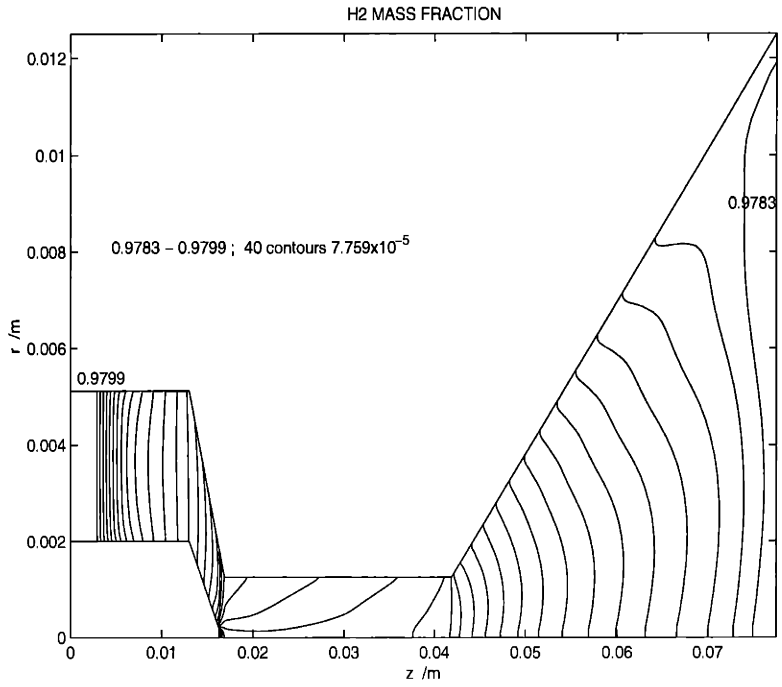

Figure 5-11: *H_2 Mass Fraction in a Seeded Arcjet*

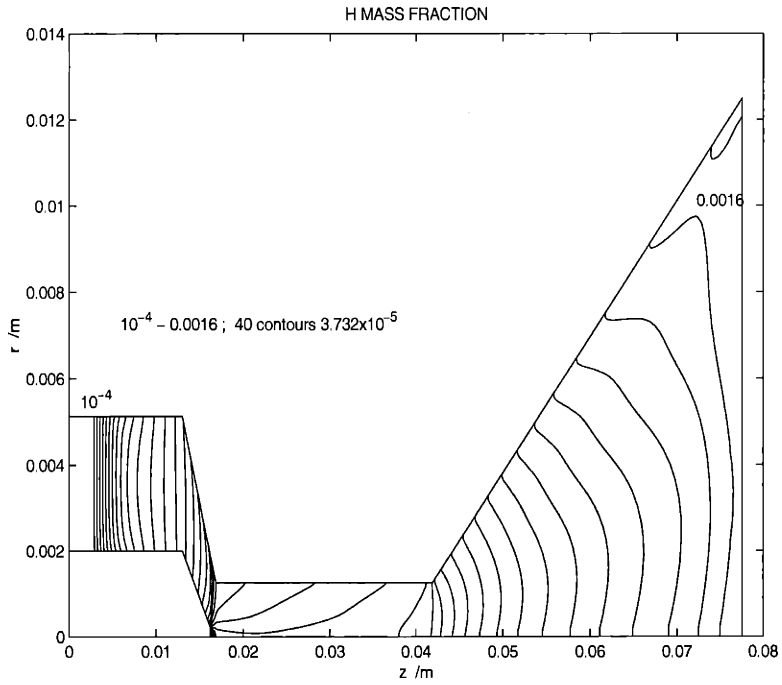

Figure 5-12: *H Mass Fraction in a Seeded Arcjet*

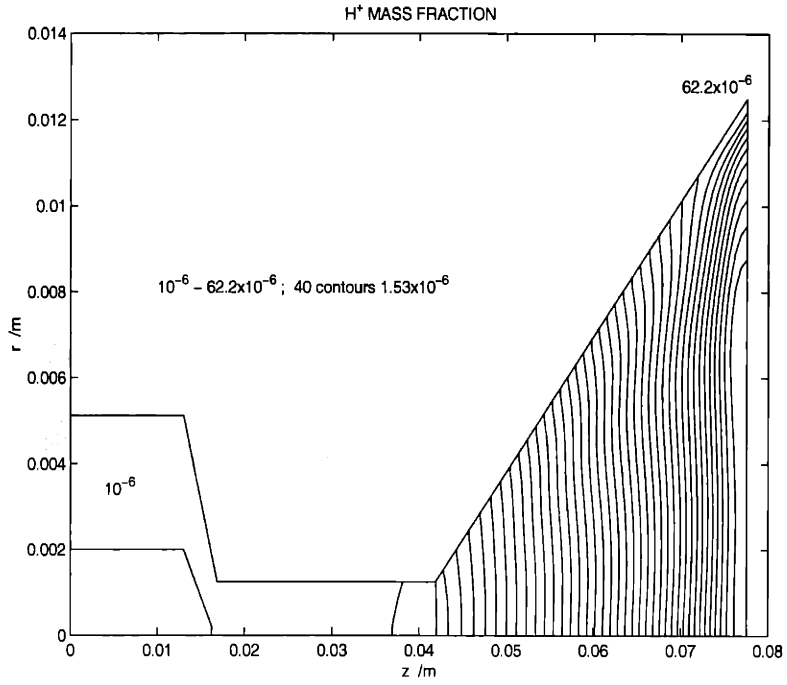

Figure 5-13: H^+ *Mass Fraction in a Seeded Arcjet*

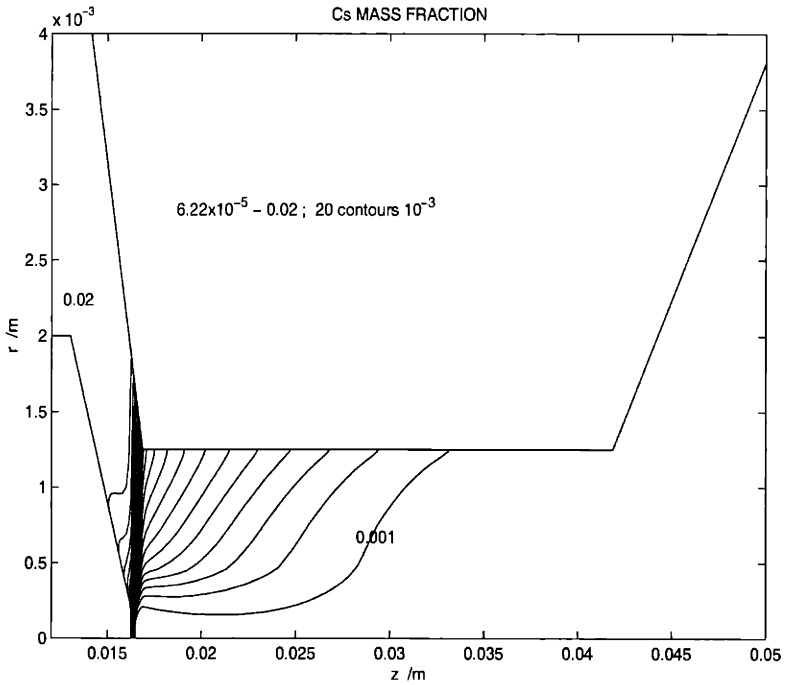

Figure 5-14: *Cs Mass Fraction in a Seeded Arcjet*

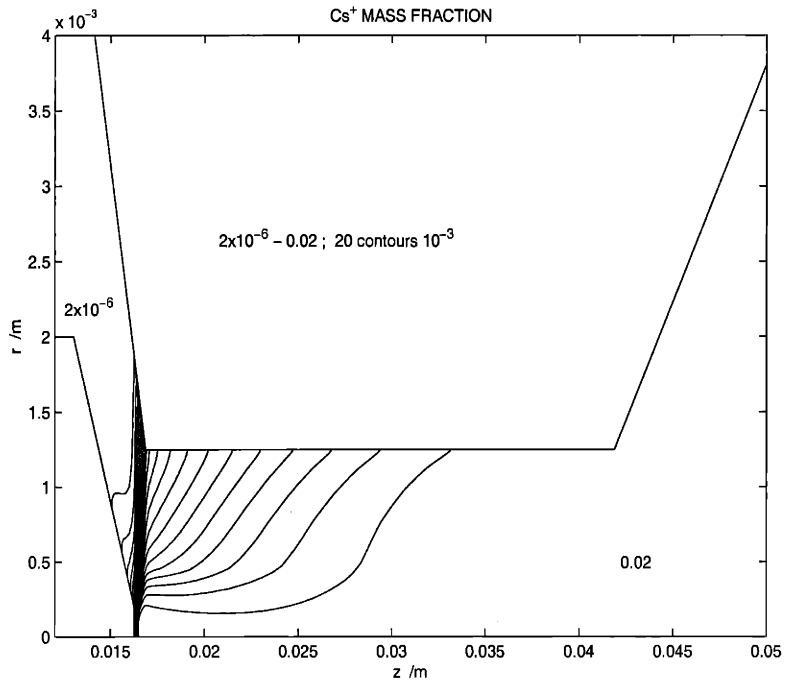

Figure 5-15: *Cs^+ Mass Fraction in a Seeded Arcjet*

It should be noted that the total pressure in figure 5-6 is the sum of the electron and heavy species pressures, and does not include the dynamic pressure.

Figures 5-14 and 5-15 show as was predicted that the cesium is very rapidly ionized as it enters the constrictor region, and the resulting ions are well spread throughout, and not concentrated in a core.

With the operating parameters as in table 5.1, it can also be seen that the electron temperature (figure 5-8) and gas temperature (figure 5-7) do not get high enough to cause any significant dissociation or ionization above the artificial minimum level, which was set for numerical reasons. This can be seen in figure 5-11 for the H_2 mass fraction, figure 5-12 for the H mass fraction, and figure 5-13 for the H^+ mass fraction.

Since the hydrogen is not dissociated or ionized, but the cesium is nearly fully ionized throughout most of the constrictor, the current density (figure 5-9 follows the profile of the cesium ions, and as such is also almost uniformly spread across the constrictor. When passing through the arc attachment region on the anode, there is no noticeable dissociation or ionization, and no ionizational instabilities were observed, that could cause the hydrogen to ignite and revert to conventional operation.

Looking again at the gas and electron temperatures, significant non-equilibrium can

be seen to exist with the electron temperature a couple of thousand Kelvin hotter in the constrictor. It should also be noted that these temperatures are similar in both value and profile as those obtained by Oyerokun [93].

Figure 5-2 of the axial momentum, shows that as the working fluid is heated it accelerates through the constrictor. The specific impulse obtained is only 550 s as seen in figure 5-3 which is low since the gas is not very hot when it leaves the constrictor and is accelerated in the nozzle, so does not have much thermal energy to convert to kinetic energy. Also the presence of cesium being much heavier than hydrogen slows the overall exhaust velocity since it requires more energy to accelerate it to a given speed than hydrogen does.

5.2 Comparison to Conventional Arcjets

For comparison of the seeded arcjet to a conventional arcjet, included here are figures made from Miller's data. [85]

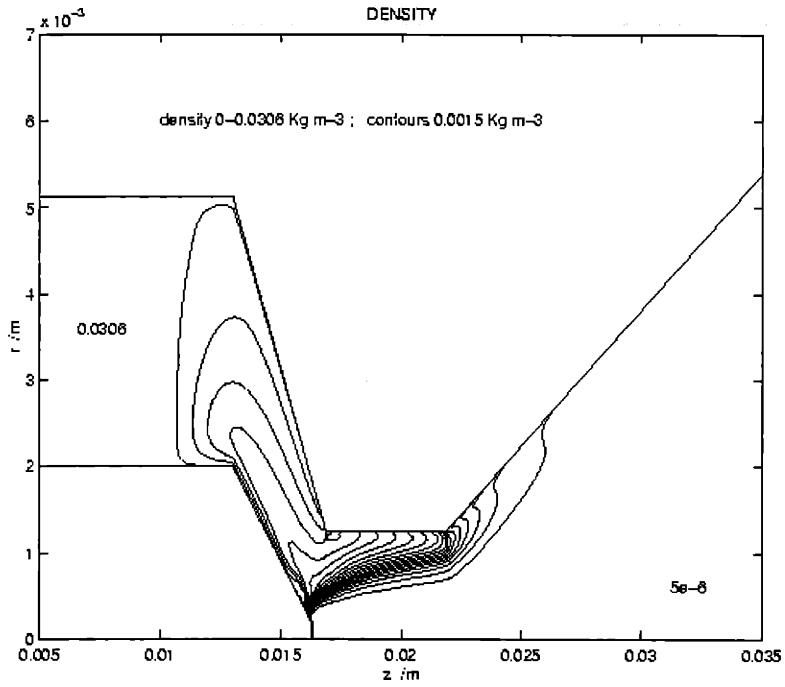

Figure 5-16: *Density in a Conventional Arcjet*

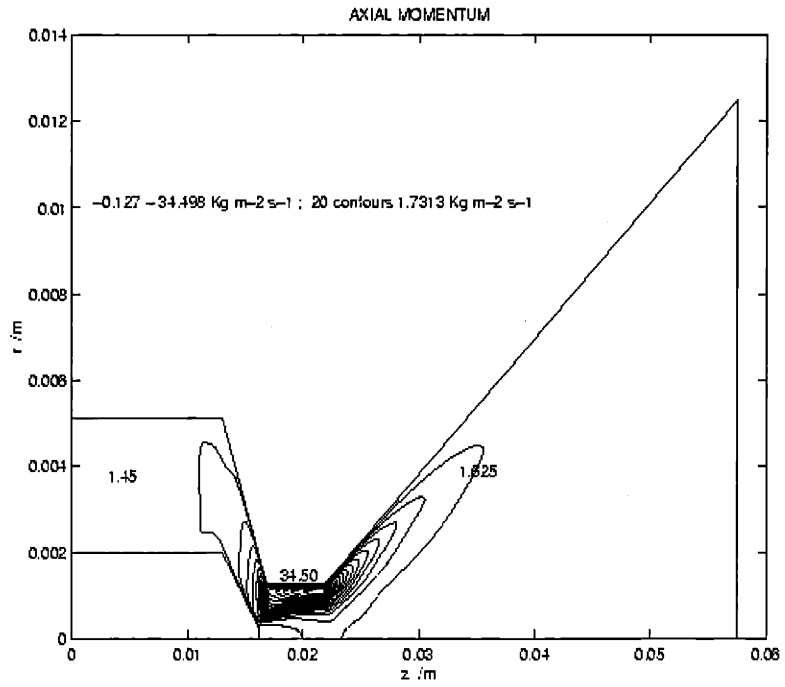

Figure 5-17: *Axial Momentum in a Conventional Arcjet*

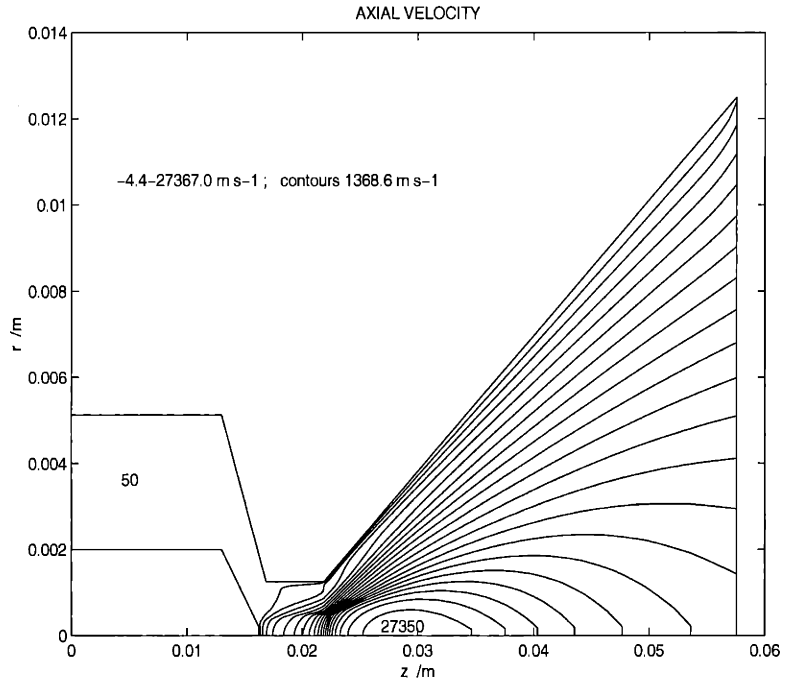

Figure 5-18: *Axial Velocity in a Conventional Arcjet*

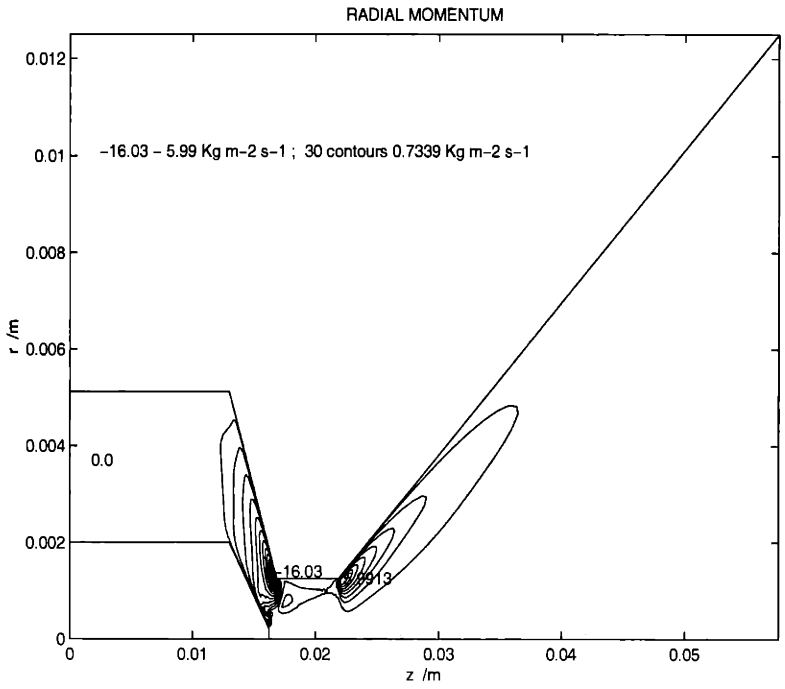

Figure 5-19: *Radial Momentum in a Conventional Arcjet*

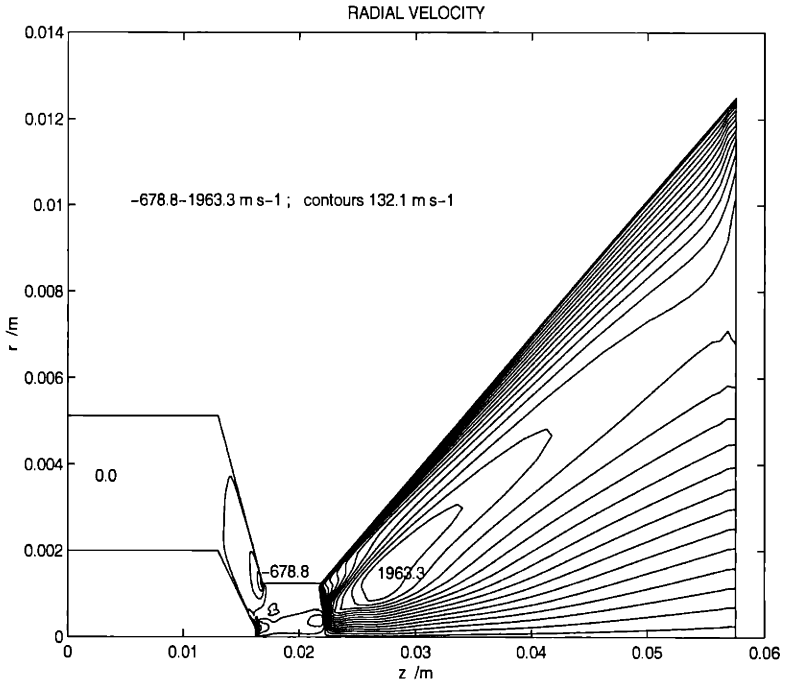

Figure 5-20: *Radial Velocity in a Conventional Arcjet*

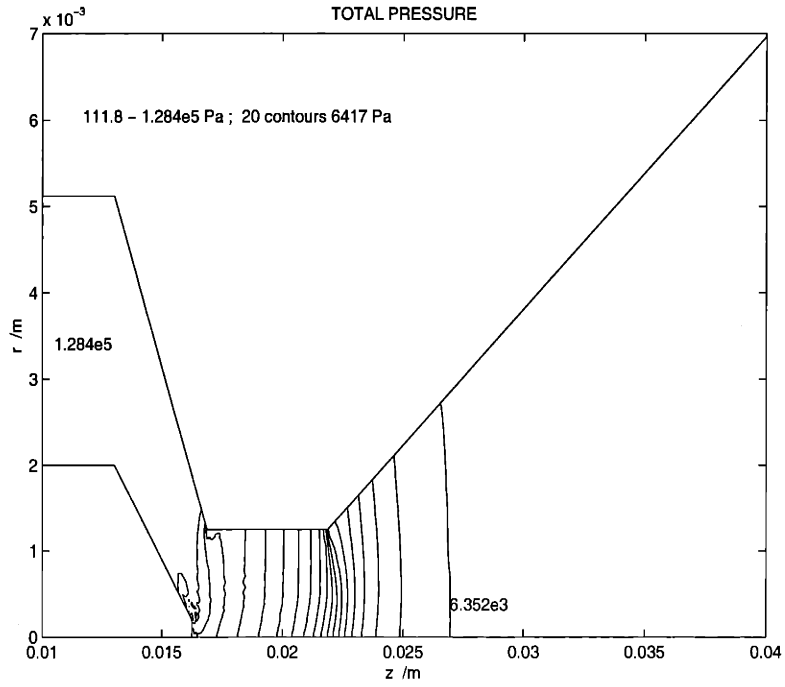

Figure 5-21: *Pressure in a Conventional Arcjet*

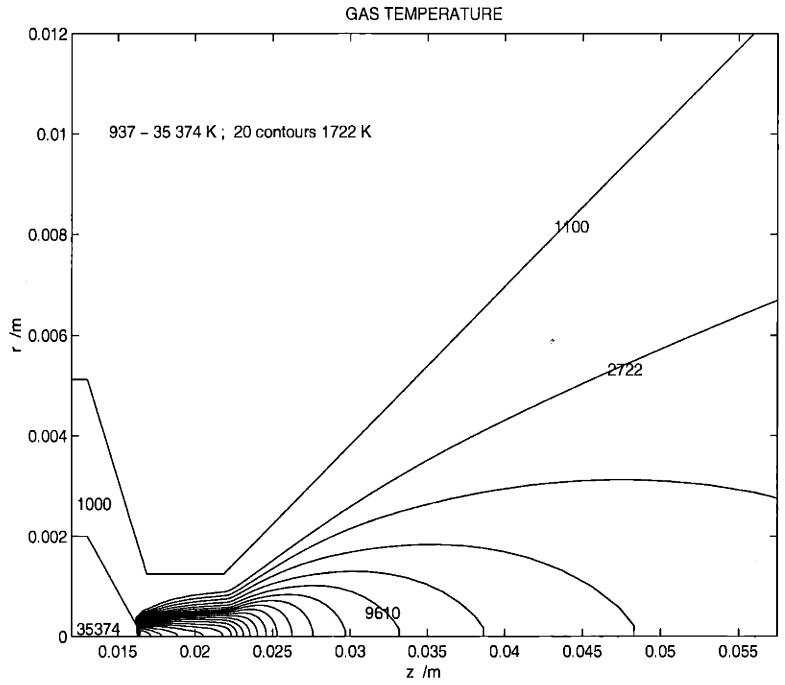

Figure 5-22: *Gas Temperature in a Conventional Arcjet*

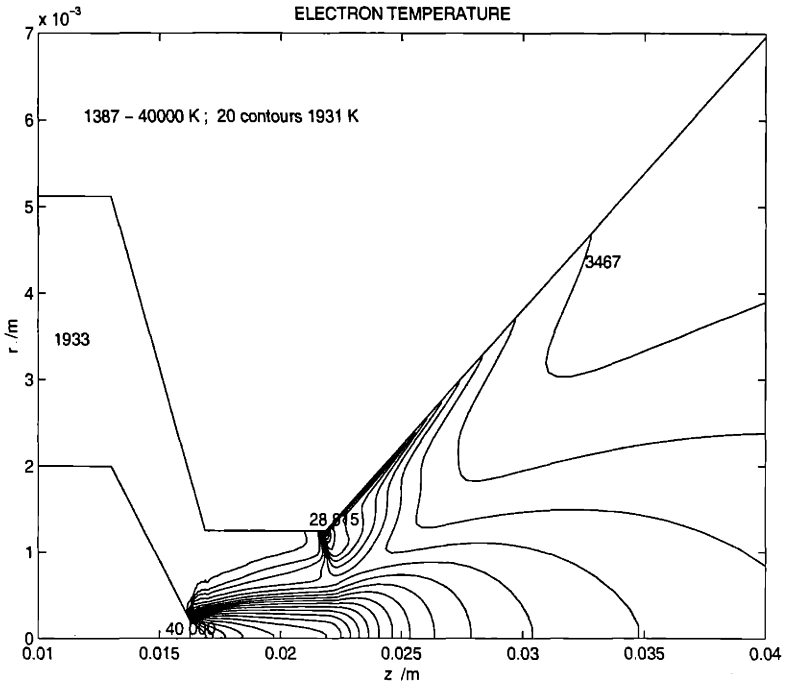

Figure 5-23: *Electron Temperature in a Conventional Arcjet*

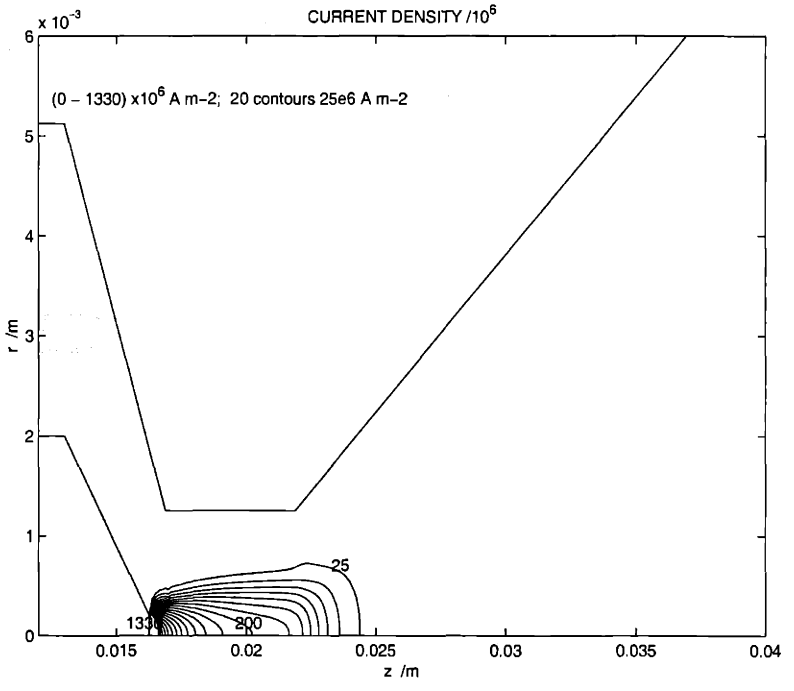

Figure 5-24: *Current Density in a Conventional Arcjet*

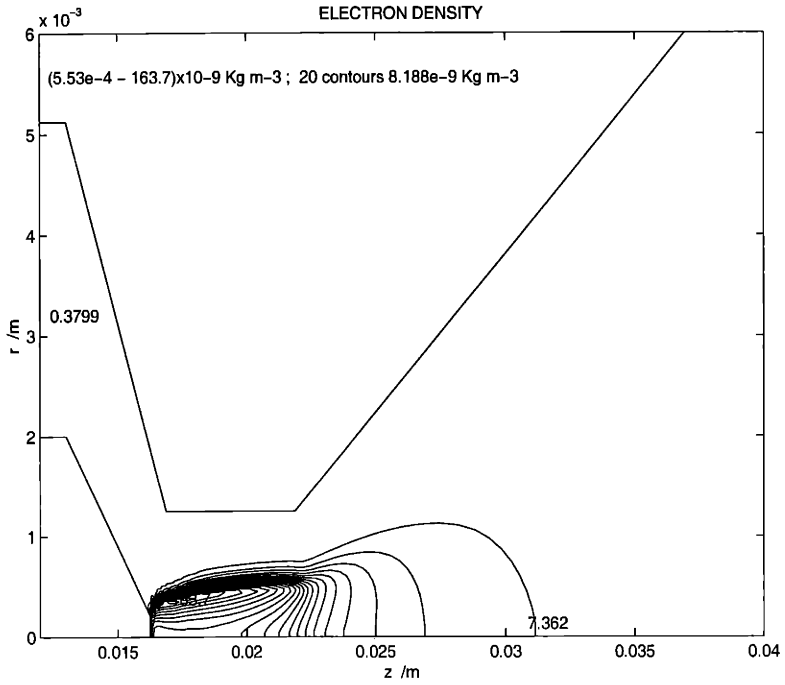

Figure 5-25: *Electron Density in a Conventional Arcjet*

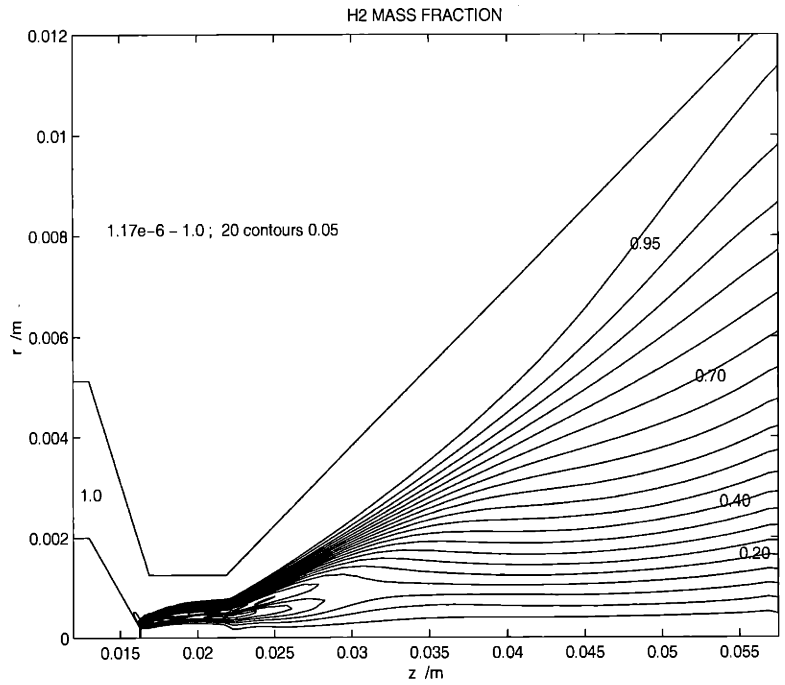

Figure 5-26: *H_2 Mass Fraction in a Conventional Arcjet*

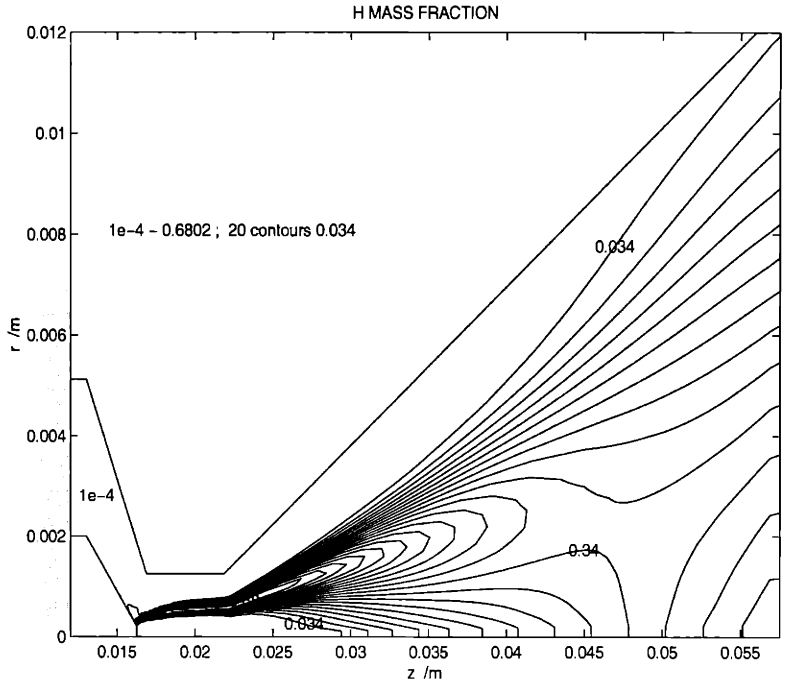

Figure 5-27: *H Mass Fraction in a Conventional Arcjet*

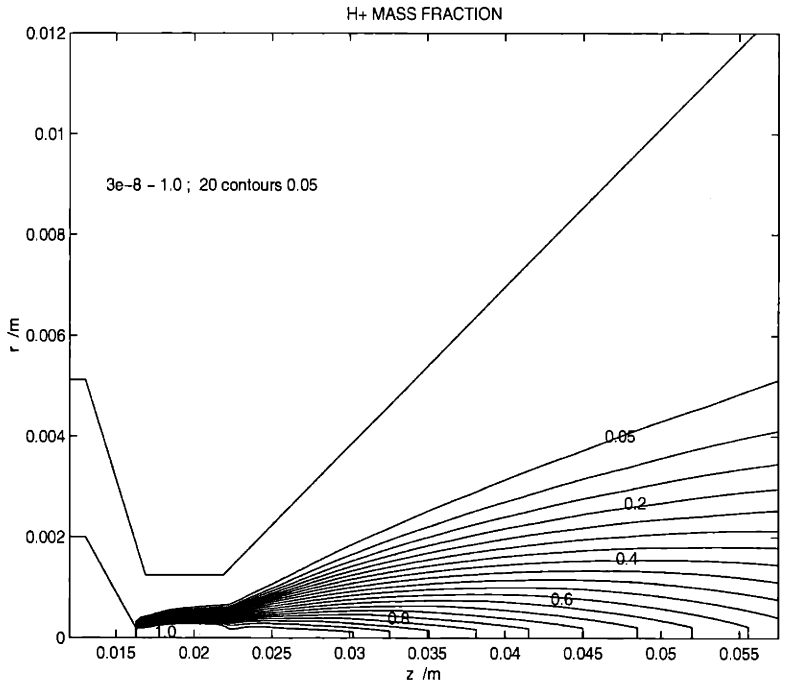

Figure 5-28: *H^+ Mass Fraction in a Conventional Arcjet*

In a conventional arcjet the gas is heated much more strongly in the core region, and so a significant temperature difference exists between the core and the walls. (Figures 5-7 and 5-22). In the seeded arcjet the temperatures experienced are much lower and so the temperature is much more uniformly distributed in the radial direction, except for right at the cathode tip where the heating is especially strong. This will also have been affected by the fact that so far zero temperature gradient conditions have been specified at the walls following the method of Oyerokun [93]. However in reality no material would be able to withstand the very high gas temperatures, and so the walls would have to be cooled: Probably by regenerative cooling with the incoming hydrogen. Thus in future, before a self consistent heat model with the anode block is incorporated, a more realistic boundary condition would be to impose a wall temperature of say 1000 K. This wall cooling should have the effect of creating a cooler, denser outer flow, but with a temperature drop of 2500 - 1000 K rather than of 20000 - 1000 K the seeded arcjet temperature will still be much more uniformly distributed.

The density (figures 5-1 and 5-16) follows the profile of the temperature in that higher temperature regions have lower density, and thus the argument as to the temperature distribution also applies to the density. Whilst the conventional arcjet has a low density, hot core and a high density cool outer flow, the flow inside a seeded arcjet is almost uniformly heated and radially distributed.

The heating is due to the current pushed through the plasma, and as shown in figures 5-9 and 5-24 there is a big contrast between seeded and conventional arcjet operation. In the conventional arcjet the current is confined to a narrow core region where ionized hydrogen is present, whereas for the seeded arcjet the current as the temperature is nearly uniformly distributed. One implication of this is that if the constrictor of a seeded arcjet was made of a conductor then the current would probably attach at the earliest possible location, at the entrance to the constrictor. If the current were allowed to attach in such a manner without passing down the length of the constrictor, then the propellant flowing through the plasma would just experience a very brief interval of passing through the strong current and would not be greatly heated. The seeded arcjet needs the comparatively long constrictor since the current and temperature are less, to supply the energy to the gas to heat it to a high temperature. In this run the heavy species are a couple of thousand Kelvin cooler than the electrons, indicating that a longer constrictor still, say with a length to diameter

ratio of twenty, would be preferable to allow the gas to heat up more closely to the electron temperature.

The hydrogen in the conventional arcjet is mostly molecular in the outer flow, transitioning to ionized in the core where the current flows as shown in figures 5-26, 5-27, 5-28. In a seeded arcjet at the operating conditions of table 5.1, the hydrogen is fully molecular throughout the flow, whereas the cesium rapidly transitions from fully atomic to fully ionized as it enters the constrictor where there is heating by the current. (figures 5-11 to 5-15). This was the desired operating condition which should produce minimum frozen losses.

The first run of the seeded arcjet only produced a specific impulse of 550 s compared to 1030 s for the conventional arcjet. This is mainly due to insufficient heating, suggesting the use of a longer constrictor or more applied current, but also due to the differing chemical composition. As already said, the addition of cesium reduces the specific impulse because of it's higher mass, but also since the hydrogen is undissociated for the seeded arcjet. In the conventional arcjet the hydrogen is appreciably dissociated in the exhaust plane, meaning that for the conventional arcjet a lot of the exhaust is atomic or ionized hydrogen with weighs half of molecular hydrogen.

5.3 Increased Current Run

Since the gas in the first run was not that strongly heated, and certainly not near to being dissociated or ionized, it was decided to turn up the current, since this was easier to do than stretching the constrictor. The new operating conditions were:

Seed Mass Fraction	2%
Inlet Pressure	8×10^5 Pa
Inlet Temperature	500 K
Applied Current	30 V

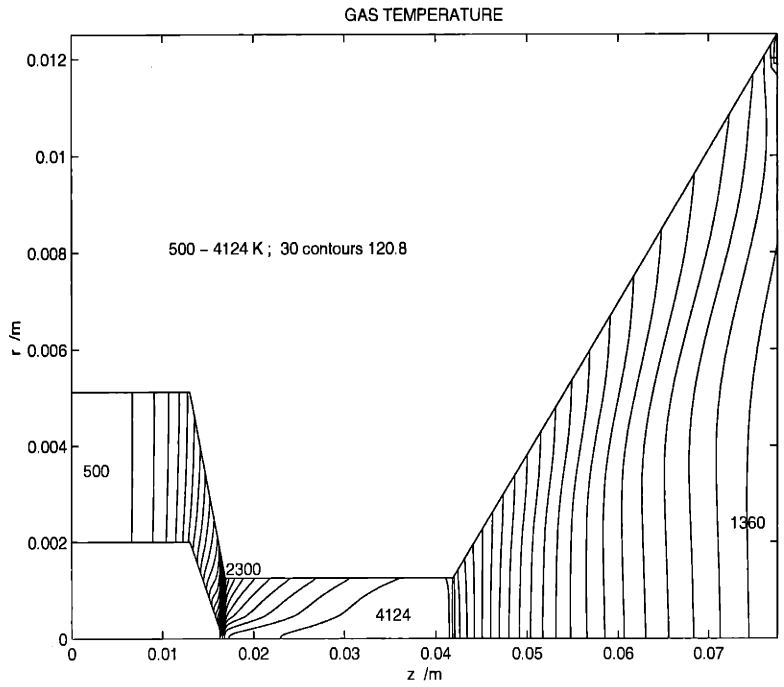

Figure 5-29: *Increased Current Run Gas Temperature*

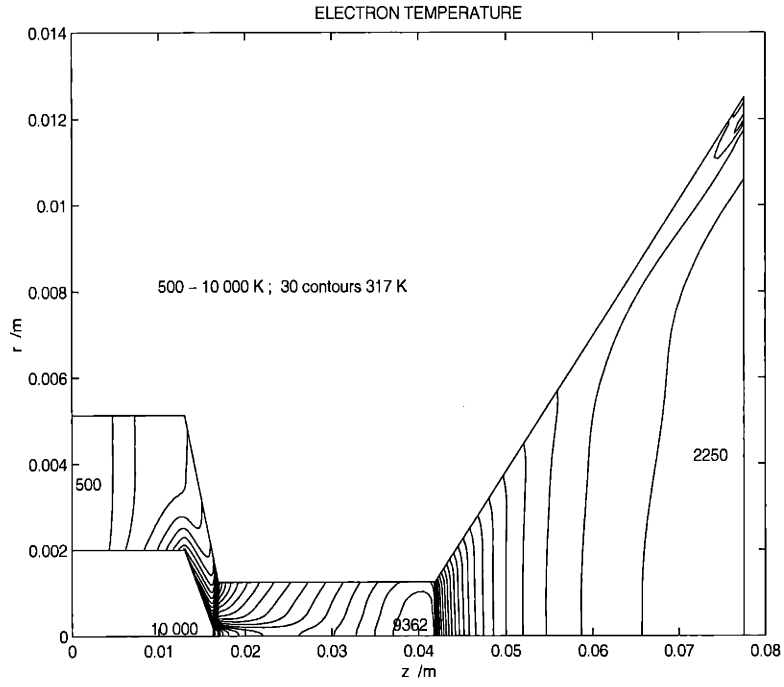

Figure 5-30: *Increased Current Run Electron Temperature*

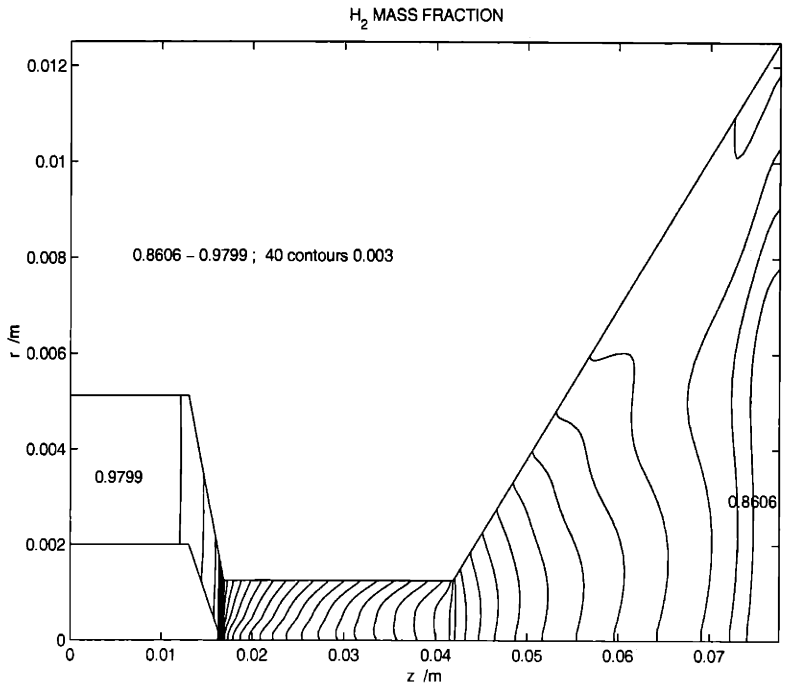

Figure 5-31: *Increased Current Run H_2 Mass Fraction*

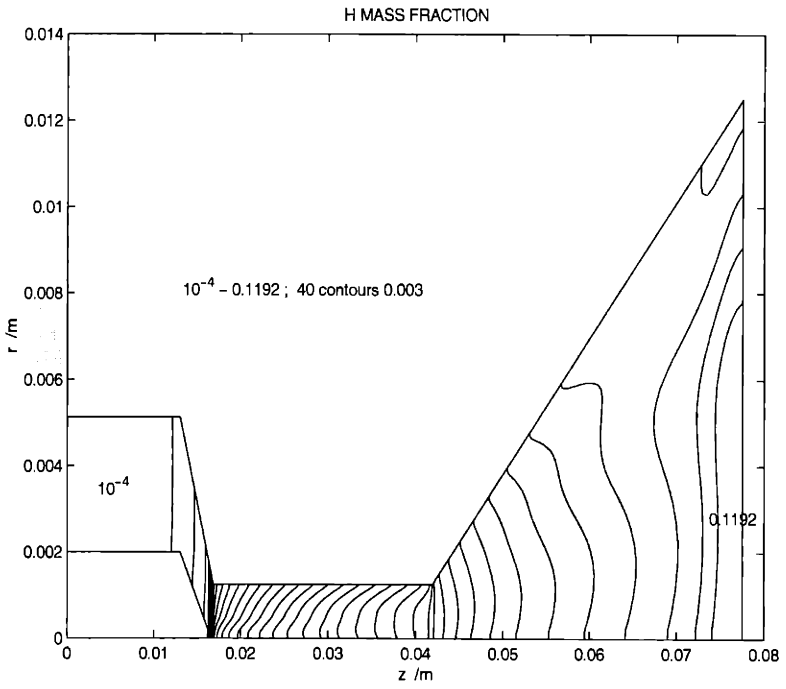

Figure 5-32: *Increased Current Run H Mass Fraction*

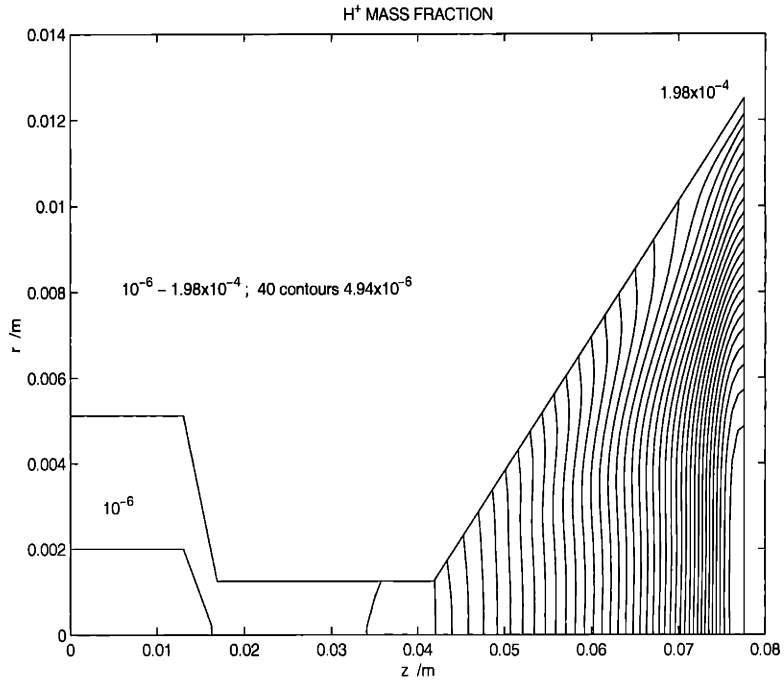

Figure 5-33: *Increased Current Run H^+ Mass Fraction*

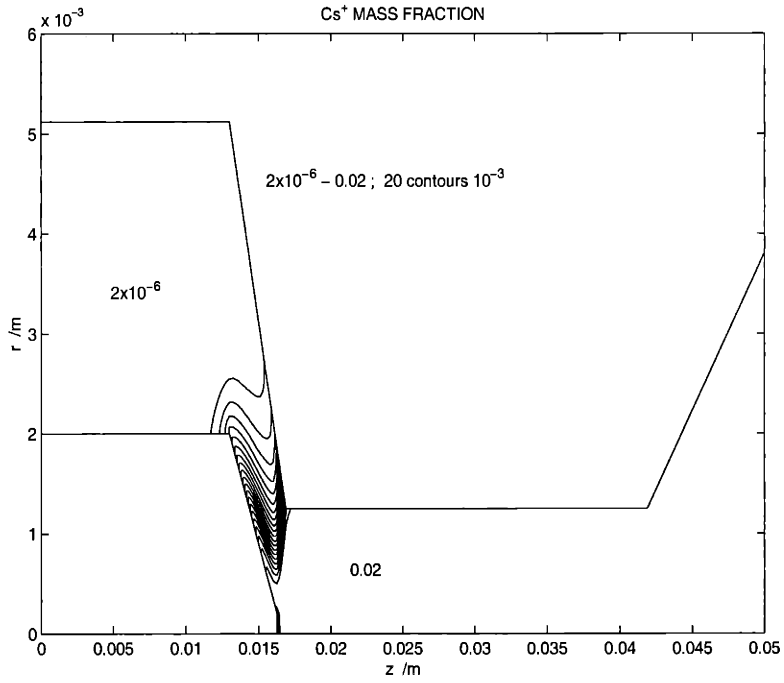

Figure 5-34: *Increased Current Run Cs^+ Mass Fraction*

A current of 30 Amps pushed to electron temperature up to 10000 K, and the gas temperature up to 4100 K, as can be seen in figure 5-30 and 5-29. Such high temperatures the cesium ionizes earlier in the arcjet and more fully, so is fully ionized by the time it reaches the inlet to the constrictor, which means that the current is even more uniformly distributed than in the first run. As the heavy species are heated by collisions with the hotter electrons, the gas temperature rises slowly through the constrictor, dissociating the hydrogen. The molecular hydrogen mass fraction drops slowly from 100% to 88% while the atomic hydrogen mass fraction climbs to 12%. (Figures 5-11 to 5-15). The hotter temperature and partially dissociated hydrogen produce a higher specific impulse, which for this run was found to be 755 s.

Despite the electron temperature in the arc attachment region of 9400 K, well in excess of Oyerokun's stability limit of 7000 K, [93] the ionized hydrogen is still seen to be at a minimal level. This may be due to the short residence time in this location, but needs further investigation. Oyerukun [93] said in his thesis that that diffusion, convection, and radiation would all help in damping out the instabilities, which is probably what we are seeing here where diffusion and convection are included.

Chapter 6

Experimental Design

Having demonstrated the basic proof of concept with the fluid model, the next step is to come up with an experimental design from which a prototype could be built and tested. The first stage in this work is a performance mapping of the thruster to obtain values for the variable parameters such as current, seed fraction, mass flow rate, constrictor length, etc which will give optimum performance.

The second stage is a thermal model of a proposed structure for the thruster. This includes a search for appropriate materials given the conditions expected in the arcjet. It is important that the temperature does not exceed the melting point of the materials used in any part of the flow, especially if lower melting point materials are to be used, such as incorporating a quartz window for spectroscopic measurements.

Finally myriad other issues such as the size and pumping requirements of a vacuum tank, extraction of cesium from the exhaust, and diagnostic equipment are addressed.

6.1 Performance Mapping

An important part of the experimental design is determining the conditions at which to run the seeded arcjet for optimum performance. Parameters include inlet pressure, mass flow rate, current, voltage, power, seeding fractions, and constrictor lengths, although many of these quantities are dependent upon others. Results such as the exit pressure and temperature, and exhaust velocity will determine the requirements of a vacuum tank, and pumping system, and any diagnostic equipment used to test a seeded arcjet in a laboratory. Alternatively, the availability of a specific vacuum tank and pumping capabilites, could be used to determine the size of the thruster.

For determining the performance, based on the variable parameters, it was decided to use the quasi one dimensional model of Oyerokun [91] [93], as the code could perform a run in under a minute, compared to the days/weeks required for the fully two dimensional code. Comparison of the fully 2-D model results and the results of the quasi 1-D model show good agreement not only in the gross properties, but also in the distributions of the state variables inside the thruster, so it was considered that the results of the quasi 1-D code would be accurate enough. This can be seen in figures 6-1 to 6-4. The quasi 1-D model appears to show a slightly more two dimensional behaviour than the full 2-D model, though this is merely an artifact of the boundary conditions used at the inlet to the quasi 1-D model. Using uniform inlet conditions will result in uniform heating. With some work the boundary conditions for the quasi 1-D model can be changed to better match the full 2-D profile.

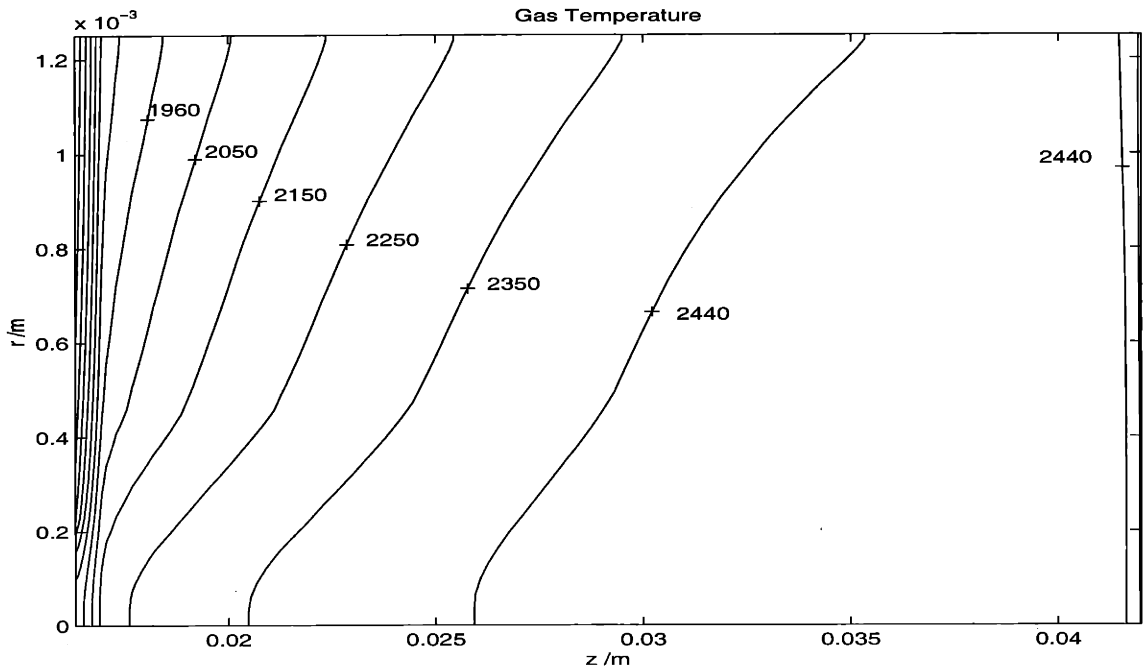

Figure 6-1: *Gas Temperature Distribution from the 2-D Model.*

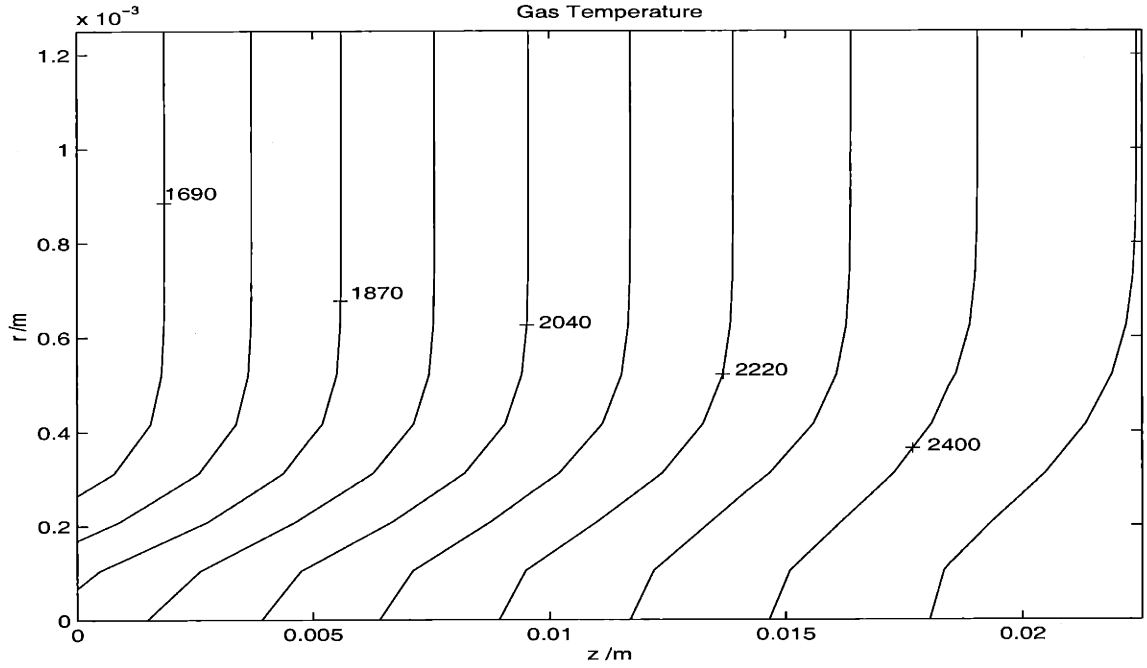

Figure 6-2: *Gas Temperature Distribution from the quasi 1-D Model.*

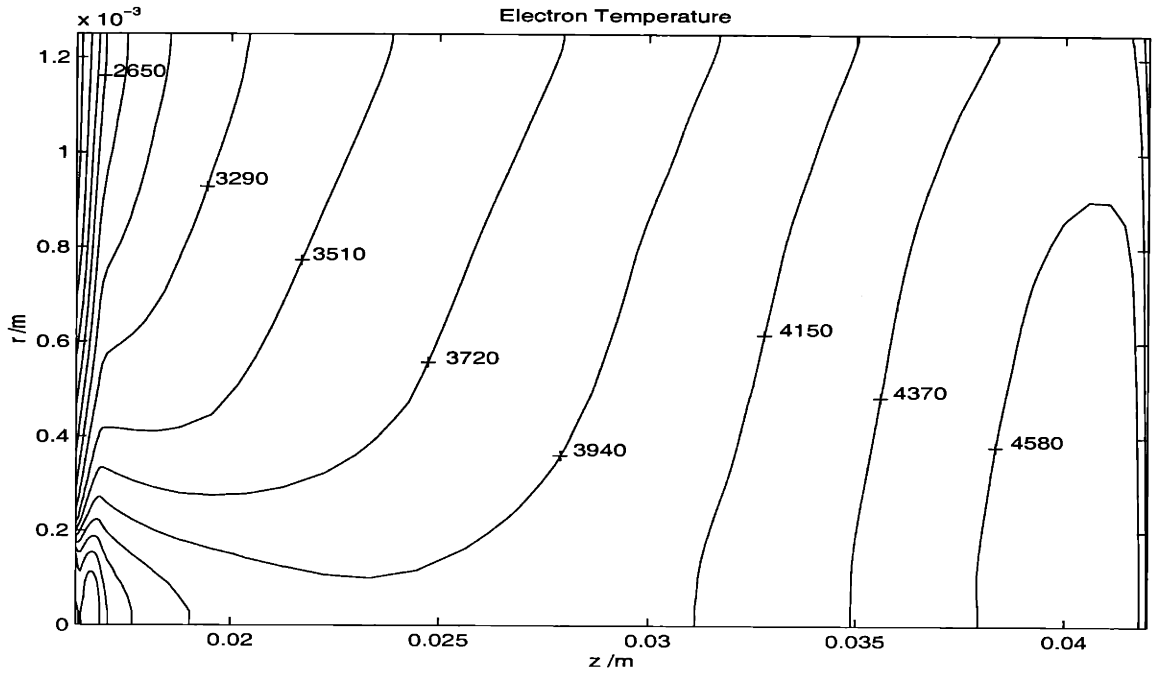

Figure 6-3: *Electron Temperature Distribution from the 2-D Model.*

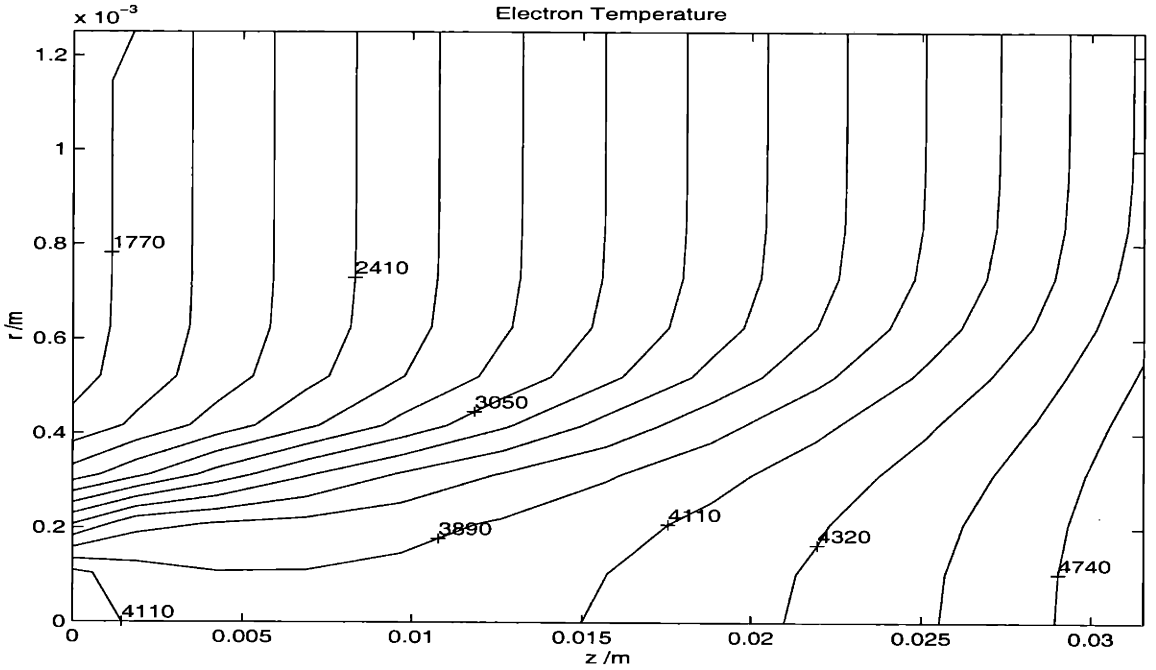

Figure 6-4: *Electron Temperature Distribution from the quasi 1-D Model.*

6.1.1 Simple One Dimensional Modelling

Most of the trends shown in seeded arcjets can be understood with a simple 1-D model of heat addition to a gas in a constant area pipe. The conservation equations written in terms of the conditions at the inlet and choked exit are

$$\rho^* u^* = \rho_o u_o = \left(\frac{\gamma}{R_g T_{To}}\right)^{\frac{1}{2}} P_{To} M_o, \tag{6.1}$$

$$P^* + \rho^* u^{*2} = P_o + \rho_o u_o^2 \approx P_{To}, \tag{6.2}$$

$$c_p T^* + \frac{1}{2} u^{*2} = c_p (T_{To} + \Delta T_T), \tag{6.3}$$

where $c_p \Delta T_T$ is the heat added per unit mass, and the approximations are valid for small M_o. Also $u^{*2} = \gamma R_g T^*$ and $P^*/\rho^* = R_g T^*$. Solving for ΔT_T gives

$$\frac{\Delta T_T}{T_{To}} = \frac{1}{2(\gamma+1)M_o^2} - 1, \tag{6.4}$$

which shows that the total temperature at the exit is directly proportional to that at the inlet, but inversely proportional to the Mach number. Since the thruster specific impulse scales as $\sqrt{T_T}$, this implies I_{sp} should vary as $1/M_o$ and be independent of other parameters.

The overall power balance for the heated flow is $IV = \dot{m}\Delta h_t$ which can be written as

$$V = \frac{\rho u \Delta h_t A}{I}. \tag{6.5}$$

Using this and equation 6.4 the voltage can be seen to scale as

$$V \propto \frac{P_{To}}{I/A}\left(\frac{1}{2(\gamma+1)M_o} - M_o\right). \tag{6.6}$$

In particular this shows the voltage is independent of the seed fraction.

Ohm's law states that $J = \sigma E$, and $V = EL$ so $V = \frac{1}{\sigma}\frac{I}{A}L$, and thus the constrictor length scales as

$$L \propto \frac{P_{To}\alpha}{(I/A)^2}\left(\frac{1}{2(\gamma+1)M_o} - M_o\right), \tag{6.7}$$

where α is the seed fraction.

To a first approximation the electron temperature, T_e, is proportional to E/P. Using

Ohm's law again, an approximate scaling of the electron temperature is

$$T_e \propto \frac{(I/A)T_{To}}{\alpha P_{To} M_o^2}. \tag{6.8}$$

6.1.2 Quasi One Dimensional Modelling

Summarizing the theory in Oyerokun's thesis as in reference [91], the model treats the flow in the constrictor as a quasi 1-D inviscid flow, coupled with a radial (Elenbaas-Heller) diffusion equation modified to allow convective energy transport. The overall conservation laws are:

Mass

$$\frac{d}{dx}\int_0^R 2\pi r \rho u dr = 0, \tag{6.9}$$

Momentum

$$\frac{d}{dx}\left(\rho u^2 A\right) + A\frac{d\rho}{dx} = 0, \tag{6.10}$$

Energy

$$\rho u \frac{\partial h_t}{\partial x} = \frac{1}{r}\frac{\partial}{\partial r}\left(r\frac{\partial \varphi}{\partial r}\right) + \sigma E^2, \tag{6.11}$$

Electric Potential

$$\frac{d}{dx}\int_0^R 2\pi r \sigma E dr = 0, \tag{6.12}$$

where $A = \pi R^2$, is the constrictor cross sectional area, h_t is the total enthalpy, $\varphi = \int_0^T K_{eff}(T)dT$ is the heat flux potential, and K_{eff} is the effective thermal conductivity which includes diffusive transport of the heats of reaction. The axial electric field is calculated from Ohm's law as

$$E = \frac{I}{\int_0^R 2\pi r \sigma dr}. \tag{6.13}$$

The governing equations are then simplified by assuming that the pressure, momentum flux ($q = \rho u^2$), and electric field are all uniform in the radial direction. Expressing all other function in terms of temperature and pressure, after some algebraic manipulation, the governing equations become

$$\frac{\partial h_t}{\partial x} = \frac{1}{\sqrt{q\rho}} \left(\frac{1}{r} \frac{\partial}{\partial r} \left(r \frac{\partial \varphi}{\partial r} \right) + \sigma E^2 \right), \tag{6.14}$$

$$\frac{dP}{dx} = \frac{\int_0^R \frac{r}{\beta\sqrt{\rho}} \left(\frac{\partial \rho}{\partial T} \right)_P \frac{\partial h_t}{\partial x} dr}{\frac{1}{q} \int_0^R r\sqrt{\rho} dr - \int_0^R \frac{r}{\sqrt{\rho}} \left(\frac{\alpha}{\beta} \left(\frac{\partial \rho}{\partial T} \right)_P + \left(\frac{\partial \rho}{\partial P} \right)_T \right) dr}, \tag{6.15}$$

$$\frac{\partial T}{\partial x} = \frac{\frac{\partial h_T}{\partial x} + \alpha \frac{dP}{dx}}{\beta}, \tag{6.16}$$

$$\frac{dE}{dx} = \frac{-E \int_0^R r \left(\left(\frac{\partial \sigma}{\partial T} \right)_P \frac{\partial T}{\partial x} + \left(\frac{\partial \sigma}{\partial P} \right)_T \frac{dP}{dx} \right) dr}{\int_0^R r\sigma dr}, \tag{6.17}$$

where

$$\alpha = \frac{1}{2\rho} - \left(\frac{\partial h}{\partial P} \right)_T + \frac{q}{2\rho^2} \left(\frac{\partial \rho}{\partial P} \right)_T, \qquad \beta = \left(\frac{\partial h}{\partial T} \right)_P + \frac{q}{2\rho^2} \left(\frac{\partial \rho}{\partial T} \right)_P.$$

These coupled ordinary differential equations are then integrated downstream from given initial conditions, with specified boundary conditions, until the flow becomes choked. The choking point is taken to be the end of the constrictor as well as the arc attachment point.

Specified quantities are the constrictor radius, seed fraction, and current. At the inlet to the constrictor the pressure, Mach number, and gaussian-like temperature profile with the peak at the core are prescribed. At the walls insulating boundary conditions are specified.

At each axial station $\frac{\partial h_T}{\partial x}(r)$ in equation 6.14 is computed. Substituting this into equation 6.15 and integrating in the radial direction gives $\frac{dP}{dx}$. Together with $\frac{\partial h_T}{\partial x}$ this gives $\frac{\partial T}{\partial x}$, which is then used to determine $\frac{dE}{dx}$. The step size is determined by local stability and accuracy. Once P, T, and E have been determined at a grid point, enthalpy and other variables can be computed. The above steps are repeated until sonic conditions are reached, which indicates the end of the constrictor, hence the constrictor length.

Thrust and specific impulse are calculated by assuming an isentropic frozen expansion in a nozzle to Mach 5, so

$$F = C_{th} P_T^* A \tag{6.18}$$

and

$$I_{sp} = \frac{F}{\dot{m} g}, \tag{6.19}$$

where the thrust coefficient, $C_{th} = 1.8$, which comes from assuming $\gamma = 1.3$ and $M_{exit} = 5$,

and P_T^* is the total pressure at the sonic point. The frozen losses are defined as

$$E_{frozen} = n_H \epsilon_d c A, \tag{6.20}$$

where $\epsilon_d = 4.478$ eV is the dissociation energy of hydrogen, and c is the exit gas velocity.

The inputs to Oyerokun's quasi 1-D code include the gas temperature at the wall and cathode at the constrictor inlet which were set to 500 K and 3500 K respectively for the the runs that were to be done. The constrictor radius was set to 1.4 mm, and the power to 10 kW.

This left the seed fraction, current, and the total pressure and Mach number at the constrictor inlet, as parameters which would be varied to find the optimum operating point of the 10 kW thruster.

6.1.3 Input Parameter Constraints

The parameters which can be varied to find the optimum operating point are the seed fraction, current, and the total pressure and Mach number at the constrictor inlet. However, these are not completely free to take any value that may lead to better performance as predicted by the quasi 1-D code.

Pressure

Increasing the pressure, P, at which the thruster is run, lowers dissociation level by lowering the temperature as seen in equation 6.8, and also by increasing the recombination rate in the nozzle. Unfortunately increasing the pressure also increases the stress on the walls and erosion of the throat due to higher arc temperatures. This leads to a shorter lifespan for the thruster. Higher pressures also increase the radiation losses. Given the currently available materials, the best compromise is considered to be in the range of 1 to 5 atmospheres for the chamber pressure (ref [56]).

Seed Fraction

For the seed fraction an initial guess may be that this should be selected to maximize the electric conductivity. This would allow the greatest heating in the shortest time, hence the

shortest constrictor and lowest viscous losses.

Figure 6-5 shows the variation of electrical conductivity with temperature at different seed fractions. It was calculated using the full conductivity calculation from the fluid code, but with the gas at equilibrium conditions. The plots all have the same high temperature asymptote since once the gas is fully ionized all collisions are Coulomb collisions, so the conductivity is same regardless of whether the ions are from cesium or hydrogen. If you look closely it can be seen that below 6000 K, the seed fraction for maximum conductivity is less than 100%.

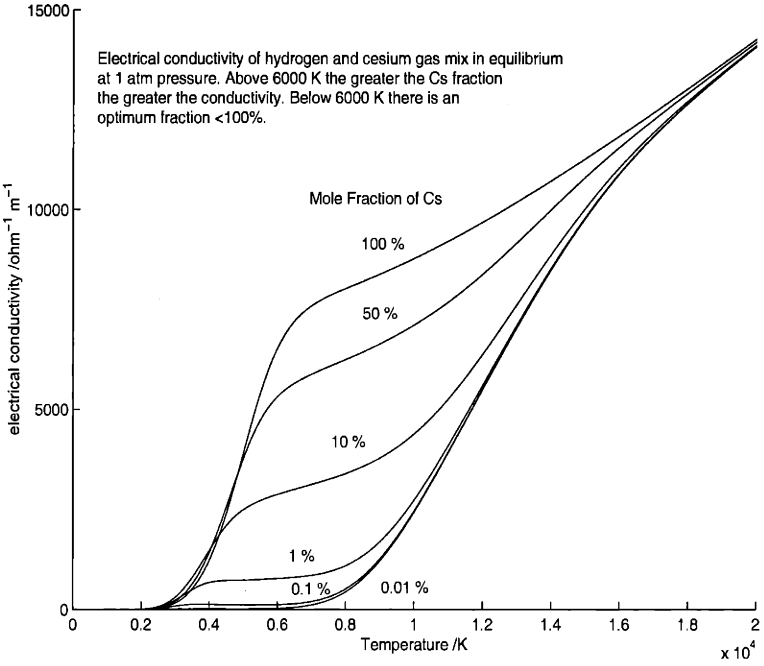

Figure 6-5: *Electrical Conductivity of Hydrogen Seeded with Cesium.*

This maximum can be explained by the fact that the collision cross section with electrons is much higher for cesium atoms than it is for hydrogen. Sutton and Sherman [123] combine the ionization given by Saha's equation

$$\frac{n_e n_i}{n_n} = \frac{2P_i}{P_n}\left(\frac{2\pi m_e kT}{h^2}\right)^{\frac{1}{2}} e^{-E_i/kT}, \tag{6.21}$$

and the resistivity,

$$\varrho = \frac{1}{\sigma} = \frac{m_e < c_e >}{n_e e^2}\left((n - n_n - 2n_e)Q_{eg} + n_n Q_{es}\right) + \alpha T^{\frac{3}{2}} \ln\left(\frac{\gamma T^{\frac{3}{2}}}{n_e^{\frac{1}{2}}}\right), \tag{6.22}$$

where the total number density is $n = n_g + n_n + n_i + n_e$. The number density of the buffer gas is n_g , and the rest are the neutral and ionized number densities of the seed, and the electron number density. Q_{eg} is the average cross section for the buffer. Equating the derivative with respect to n_n to zero, and approximating with $n_e \ll n$,

$$\frac{n_n}{n} = \frac{1 + \frac{\sigma_{en}}{2\sigma_{ei}\ln(\Lambda)}}{\frac{Q_{es}}{Q_{eg}} - 1}. \tag{6.23}$$

The total amount of seed atoms which must be added is $n_s = n_n + n_i$, and the fractional seeding is $(n_n + n_e)kT/P$.

The conductivity has a peak with respect to the seeding fraction. Although adding more seed atoms increases the number of charge carriers, due to the high cross section, if too much is added the conductivity goes down since the electrons can not travel as far before being absorbed. The electron cross section of cesium is much larger than that of hydrogen, so the seeding fraction for maximum conductivity is typically only a few percent. This can be seen in figure 6-6 for hydrogen seeded with cesium, which was also calculated using the fluid model code with equilibrium conditions.

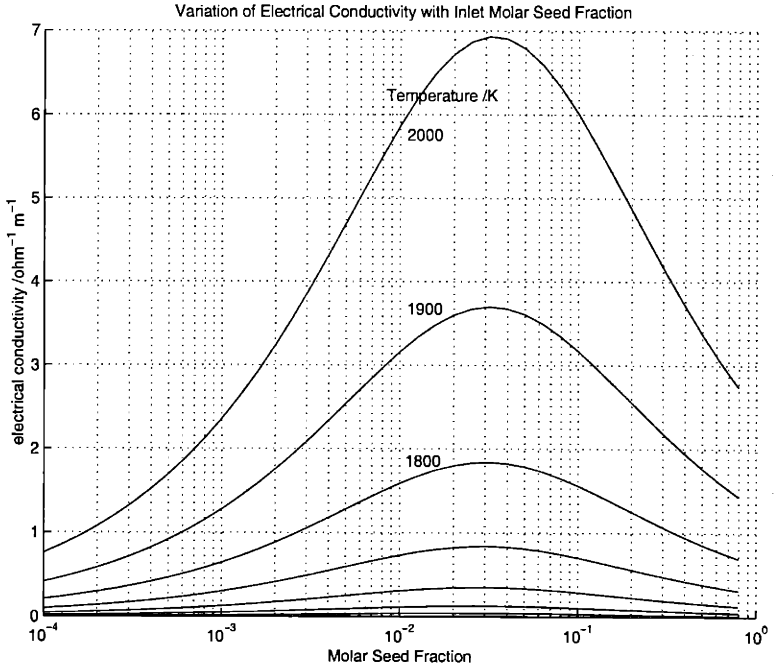

Figure 6-6: *Electrical Conductivity of Hydrogen Seeded with Cesium near 2000 K.*

Figure 6-7 shows the extension of this up to 5000 K, with the line of maximum conductivity as a function of temperature plotted.

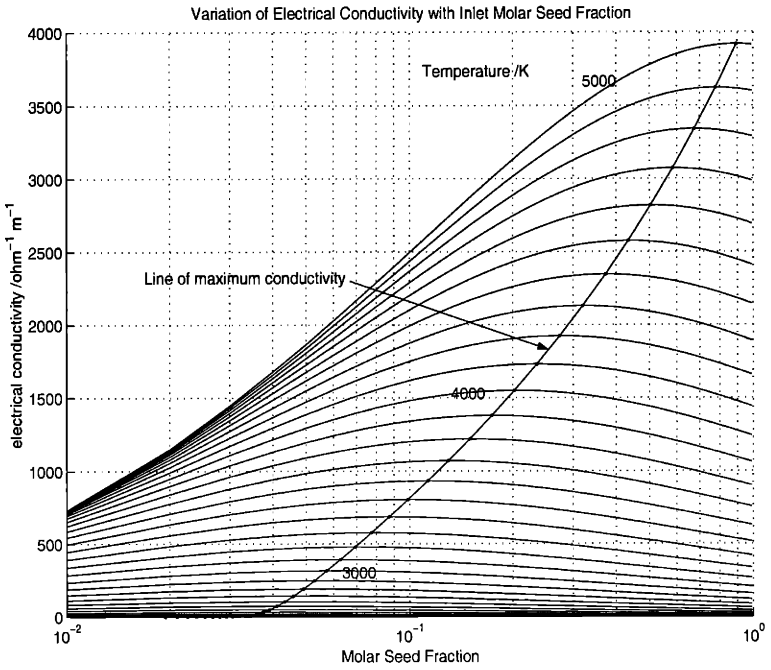

Figure 6-7: *Electrical Conductivity of Hydrogen Seeded with Cesium up to 5000 K.*

Figure 6-8 shows the seed fraction for maximum conductivity and the resultant conductivity as a function of temperature up to where it saturates out at 100% cesium. It should be noted however, that this is only maximizing conductivity, not the overall performance. It would not be desirable to run with a high fraction of cesium since its much greater mass which would greatly decrease the I_{sp}.

It turns out however that the maximum usable seed fraction is well below the few percent that maximize the conductivity at the conditions found in the seeded arcjet. This is shown by the stability analysis Oyerokun [93] [92] did, the result of which is shown in figure 6-9. Below the cesium stability line, the cesium is unstable with respect to ionization which will occur rapidly driving the cesium to nearly full ionization, and the electron temperature up to the cesium stability line. Similarly, above the hydrogen stability line, the hydrogen is unstable and will rapidly become near fully ionized. The desired operating point of the seeded arcjet is with the cesium fully ionized and the hydrogen unionized, and is thus between the two stability lines plotted. As can be seen Oyerokun predicts that at about a seed fraction of about 8×10^{-4}, the stability lines meet and as soon as the cesium ionizes,

hydrogen ionization would follow, which would result in the undesirable return of the frozen losses. Although Oyerokun did not account for several damping mechanisms which would make the hydrogen ionizational instability limit higher, it would be unwise to attempt to operate a seeded arcjet at molar seed fractions much above 8×10^{-4}.

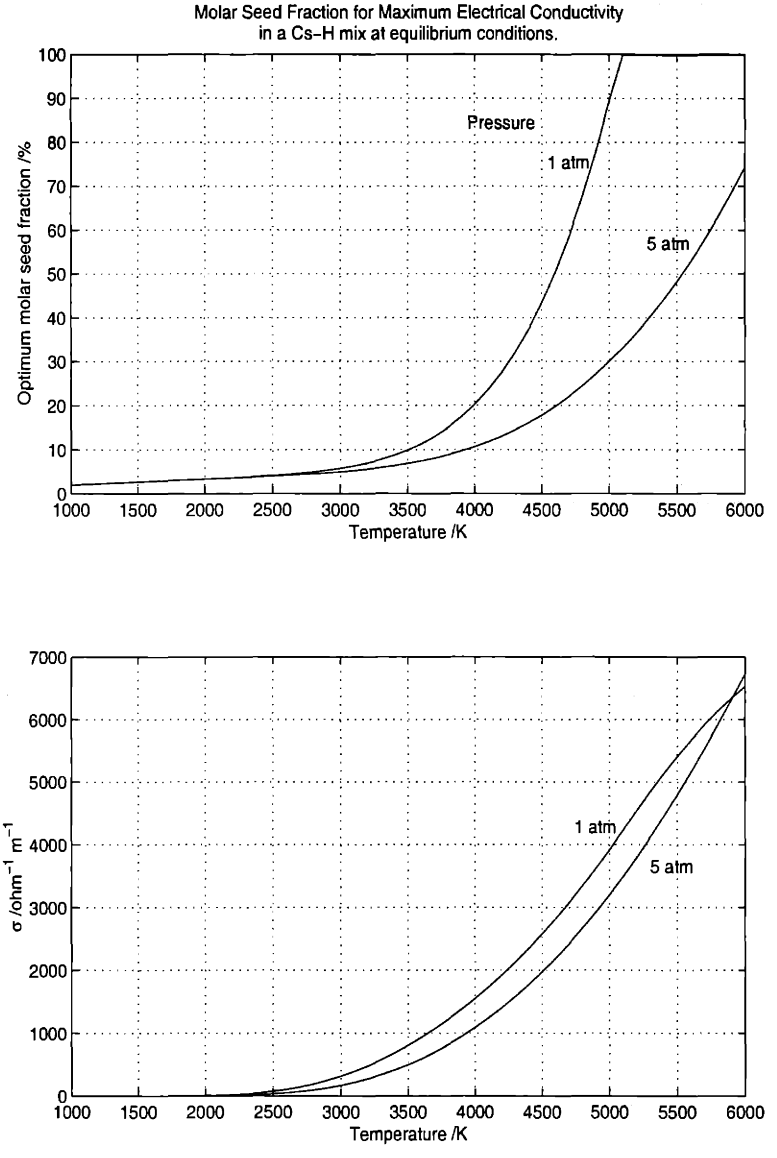

Figure 6-8: *Seed Fraction for Maximum Conductivity.*

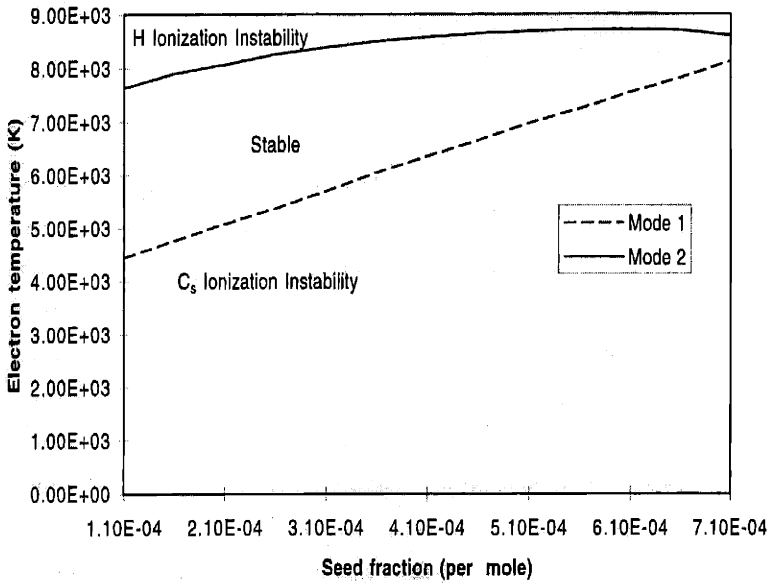

Figure 6-9: *Instability Threshold of Electron Temperature.*

Current and Mach Number

The Mach number at the inlet to the constrictor is related to the length of the constrictor as shown in section 6.1.1. The Mach number at the end of the constrictor must be 1 if the flow is thermally choked, so the lower the the constrictor inlet Mach number the longer the constrictor is. Viscous losses will place a limit on the length of the constrictor and hence the Mach number. Also since T_e scales as $\frac{1}{M_o^2}$ as the Mach number is decreased the electron temperature will eventually rise to a temperature where the hydrogen will begin to dissociate and the frozen losses will rise. Without actually calculating these limits the constrictor inlet Mach number is limited to being in the range 0 to 1. Similar arguments can be applied to the current using the simple one dimensional model of section 6.1.1.

6.1.4 Quasi One Dimensional Results

The fundamental aim is to obtain the most thrust for the minimum fuel ($\dot{m}$), and power (W). Minimum power implies the greatest efficiency hence minimum losses. Thus the quantities which act as figures of merit are the $I_{sp} = \frac{F}{\dot{m}g}$, which is the thrust per unit mass flow rate, and the efficiency $\eta = \frac{Thrust\ Power}{Input\ Power}$.

Approximately 1000 runs were done with the quasi one dimensional code to obtain a large database in which to examine the performance. The constrictor inlet Mach number was varied from 0.2 to 0.5; the current from 10 to 30 Amps; the pressure from 1 to 5 atmospheres; and the molar seed fraction from $2\text{x}10^{-4}$ to $9\text{x}10^{-4}$.

Figure 6-10 shows the I_{sp} of all the runs plotted against M_o. As predicted using simple heat addition in a pipe, the I_{sp} is independent of all quantities except M_o where it varies as $\frac{1}{M_o}$.

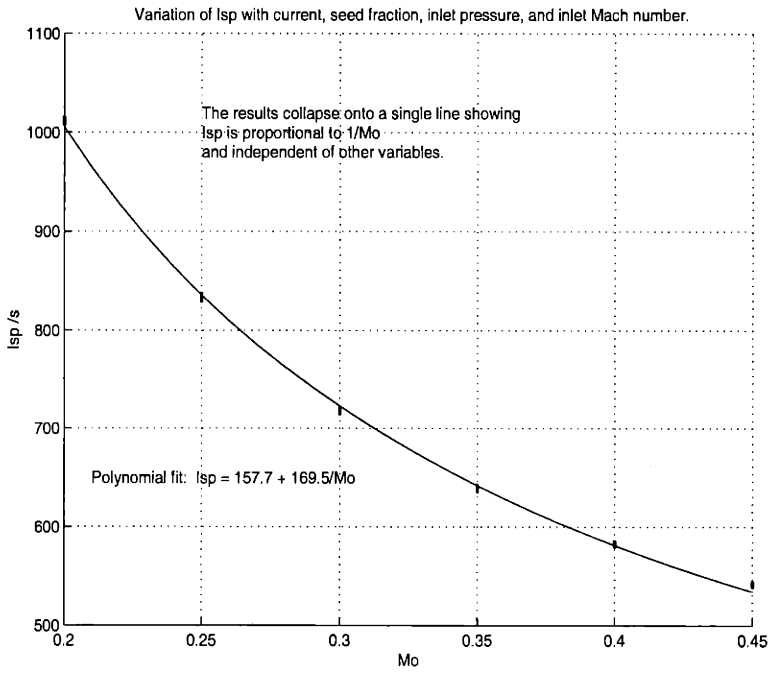

Figure 6-10: *I_{sp} versus Mach Number.*

Figure 6-11 also shows the variation of the frozen losses with Mach number. (I=17A, Molar seed fraction=$3\text{x}10^{-4}$, P_o=3 atm). Below a Mach number of about 0.25 the frozen losses begin to grow rapidly to an unacceptable level. As explained in section 6.1.1, this is because a lower M_o implies a longer constrictor, hence more time for heating and a higher electron temperature, which in turn creates dissociation of the hydrogen. There is thus a

tradeoff between I_{sp} and the frozen losses. Higher I_{sp} can be gained at the cost of lower efficiency, by heating the gas more and accepting more dissociated hydrogen. Conversely efficiency can be improved by running at a lower electron temperature. In practice this tradeoff will come through deciding the maximum amount of frozen losses that can be tolerated, such as say 1%, which in turn defines the constrictor inlet Mach number (0.24) and the I_{sp} (860).

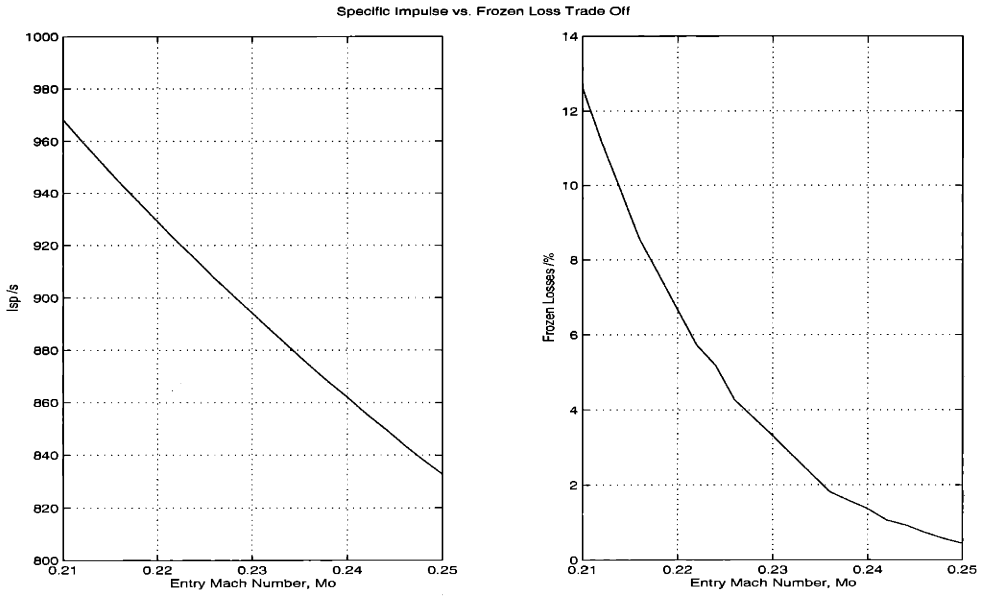

Figure 6-11: *Tradeoff between I_{sp} and Frozen Losses.*

Figure 6-12 shows the variation of the frozen losses for a selected subset of the database, and figure 6-13 is the same data plotted on a log scale. These graphs show a number of interesting features. As expected increasing M_o or the pressure, P_o, decreases the losses over the whole range investigated. Secondly at low M_o increasing the seed fraction decreases the losses, yet at higher M_o it increases the losses. Thirdly at low M_o decreasing the current decreases the losses, yet at M_o the effect is also reversed. The conclusion is that increasing M_o and P_o decreases the losses, but for a given M_o, P_o there is an optimum current and seed fraction.

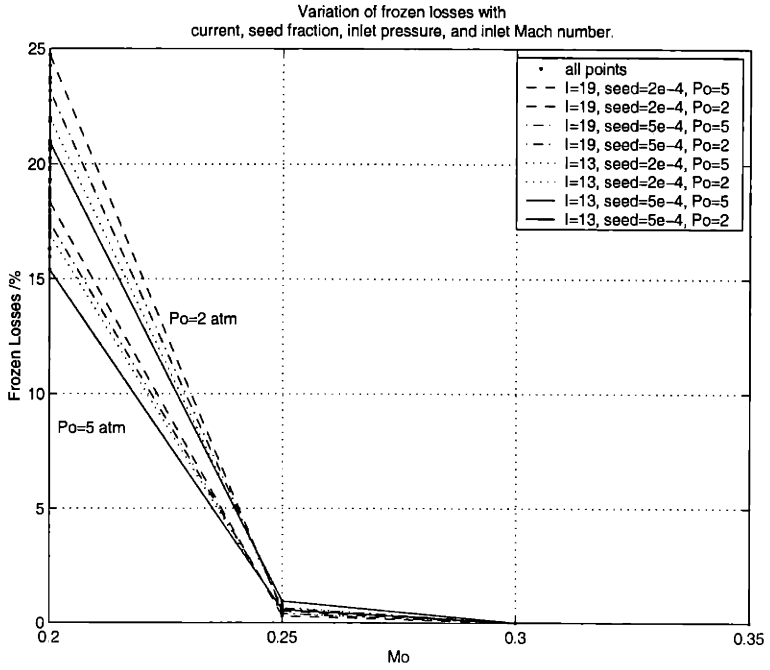

Figure 6-12: *Variation of Frozen Losses with Input Parameters.*

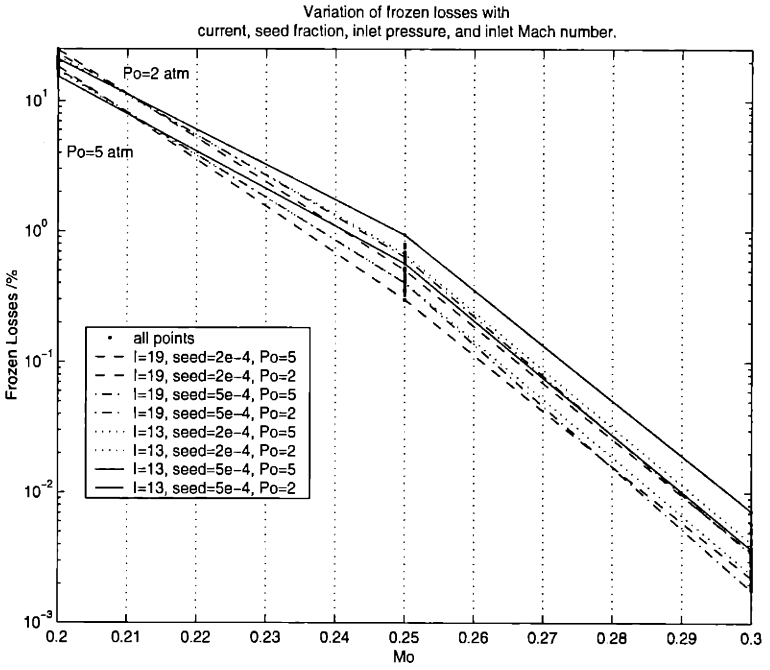

Figure 6-13: *Variation of Frozen Losses with Input Parameters (Log plot).*

For a few Mach numbers around the desired tradeoff point, contour plots of the frozen losses as a function of the current and seed fraction are plotted in figures 6-14 to 6-18. Rather than the frozen losses vs current and seed fraction being a rounded bowl with a well defined minimum, the function is more of an elongated valley, which can especially be seen in figure 6-18. The optimum seed fraction is always the maximum allowable, which should probably be kept below $6x10^{-4}$ for sake of having a margin of error. As the Mach number is increased the optimum current increases rapidly from less than 10 Amps for $M_o = 0.22$ to about 25 Amps for $M_o = 0.24$, although for higher Mach numbers up to 0.30 this optimum current remains at around 25 Amps.

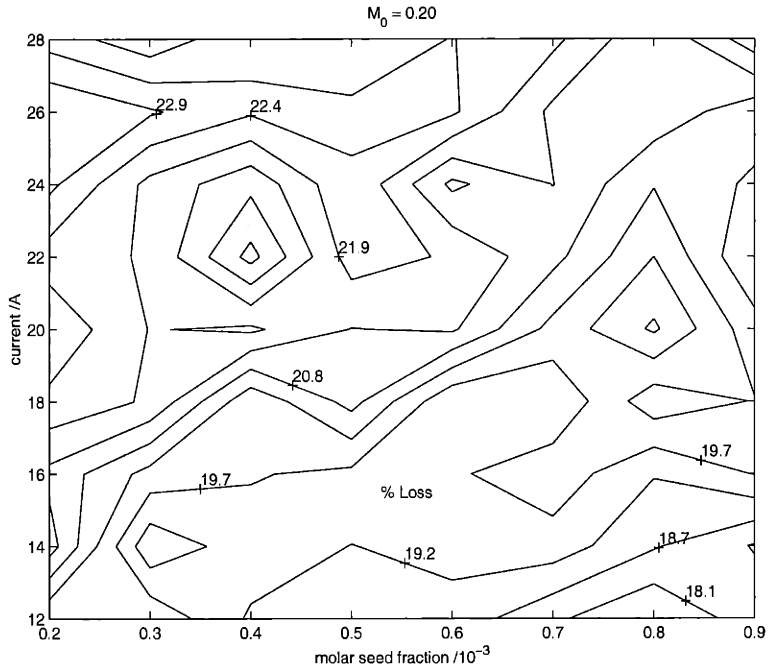

Figure 6-14: *Variation of Frozen Losses with Current and Seed Fraction at Mach 0.20.*

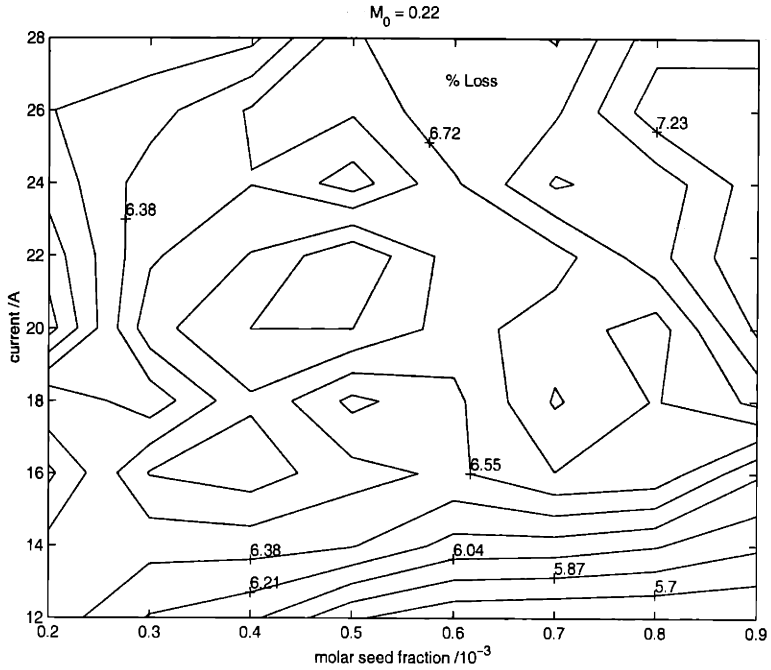

Figure 6-15: *Variation of Frozen Losses with Current and Seed Fraction at Mach 0.22.*

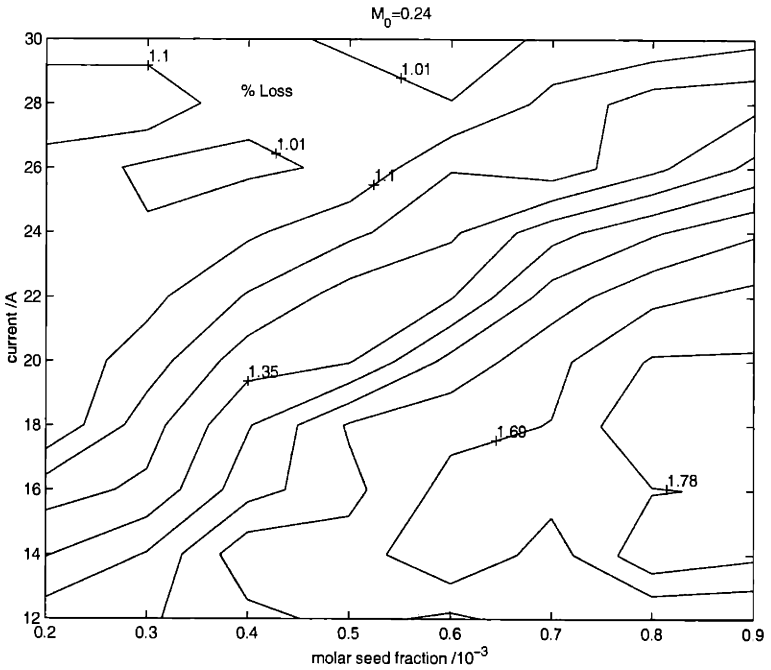

Figure 6-16: *Variation of Frozen Losses with Current and Seed Fraction at Mach 0.24.*

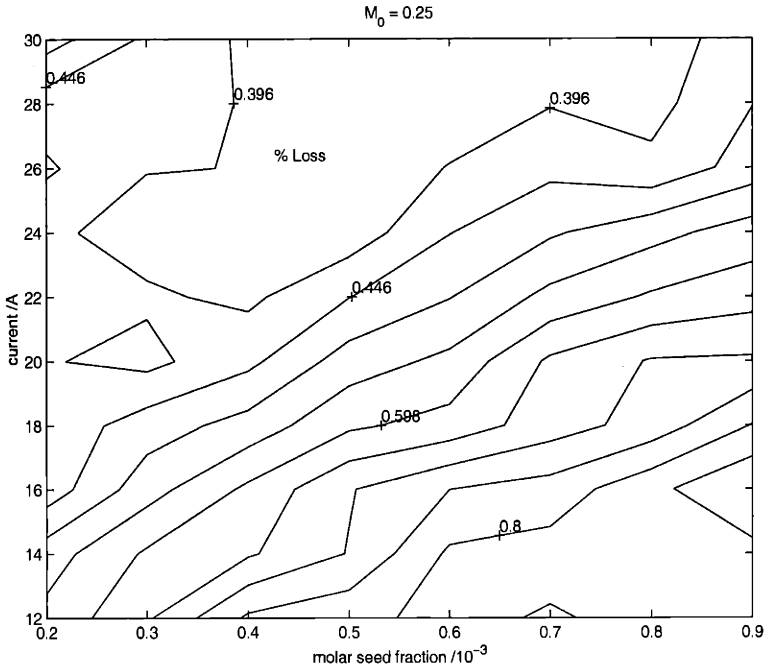

Figure 6-17: *Variation of Frozen Losses with Current and Seed Fraction at Mach 0.25.*

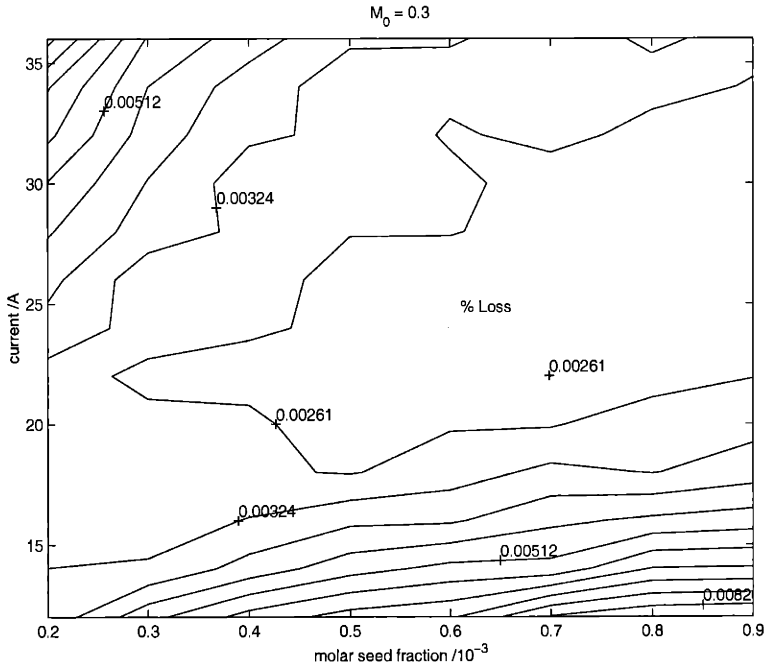

Figure 6-18: *Variation of Frozen Losses with Current and Seed Fraction at Mach 0.30.*

Following roughly along the valley in figure 6-16 the operating and performance parameters are very similar as can be seen in table 6.1

P_o /Pa	$3x10^5$				
M_o	0.24				
I /A	22	24	26	28	30
seed $/10^{-4}$	2	3	4	5	6
Power /W	9357	9495	9430	9339	9452
V /V	425	395	363	333	315
L/D	3.15	2.56	3.01	3.70	3.62
$\dot{m}$ /g s^{-1}	0.325	0.324	0.325	0.326	0.325
F /N	2.77	2.76	2.76	2.77	2.76
I_{sp}	869	870	868	866	867
Loss /%	1.05	1.02	0.99	1.05	0.93

Table 6.1: *Seeded Arcjet Characteristics along the Minimum Loss Valley.*

In conclusion, parameter variations using the quasi one dimensional code demonstrate the tradeoff between I_{sp} and frozen losses. For a thruster operating at 3 atmospheres pressure and a design point of 1% frozen losses, this requires a constrictor inlet Mach number of 0.24, which will give an I_{sp} of 860 s if the gas is expanded to Mach 5 in the nozzle. Given the desired Mach number, the contour plots of the frozen losses then specify the optimum current as about 26 A, with a molar seed fraction of around $3x10^{-4}$.

6.2 Materials

For the working structure of the thruster only two materials are needed. The first must be a good conductor as it will compose the cathode and the anode. It should also have a low work function so electrons can be readily emitted from the cathode. It must also have high thermal conductivity to be able to remove the heat loads from the arc attachment regions, and it must retain this high conductivity up to a melting point which should ideally be as high as possible, so the thruster can be run hotter. Finally if the thruster is to be cooled radiatively then it should be a good black body emitter. If need be this task could be taken care of by a suitable coating on the outside.

The second material will be used as the electrical insulation between the anode and the cathode, and will have to pass down the length of the constrictor. Consequently it will also require a high melting point, and good thermal conductivity to cope with the temperatures experienced. Perhaps most importantly it must maintain good resistivity up to very high temperatures. This could be a problem for some ceramics as they become semi-conducting at high temperature.

For the conductor, most metals should provide adequate conductivity, so the melting point and thermal conductivity of a range of metals was examined. Some potential metals are listed in table 6.2 from reference [53]. Tungsten was clearly the best choice as it has both the highest melting point and the highest heat transfer rate. In the arcjet literature tungsten is indeed the most commonly used anode material. For cathodes tungsten is often doped with two percent thorium to decrease the work function. Given this tungsten was selected as the metal for the seeded arcjet. Following another popular choice in the arcjet literature it was decided to make the outer casing along the propellant feed passages out of molybdenum because it is much lighter, and the temperatures at that point should be much lower.

	Density	Melting	Thermal Conductivity ($Wm^{-1}K^{-1}$) at various temperatures(K)									
Metal	/Kg m^{-3}	point /K	100	200	400	600	800	1000	1200	1500	2000	2500
Iridium	22500	2720	172	153	144	138	132	126	120	111		
Molybdenum	10240	2894	179	143	134	126	118	112	105	98	90	86
Niobium	8570	2741	55.2	52.6	55.2	58.2	61.3	64.4	67.5	72.1	79.1	
Tantalum	16600	3269	59.2	57.5	57.8	58.6	59.4	60.2	61.0	62.2	64.1	65.6
Tungsten	19300	3660	208	186	159	137	125	118	113	107	100	95

Table 6.2: *Thermal Conductivity of Various Metals*

Insulators are usually ceramics (often oxide ceramics) or plastics, and normally have resistivities in excess of 10^9 Ωm when cold and dry, although resistivity usually falls rapidly with temperature. For purer ceramics the resistivity reduces by a factor of about 100 when at 500 K, and higher factors for other materials. High potential gradients can also cause breakdown in a material. The capacity to resist this is called dielectric strength. Both plastics and ceramics deteriorate because of arcing along the surface. Essentially insulting characteristics can be retained to temperatures around 1000 K, but there is an increasing contribution to conductivity from ionic movement which acts as the ultimate limit on properties.

Figure 6-19 from reference [132] gives the thermal conductivity of various ceramics, and also includes aluminium and copper alloys and plastics for comparison.

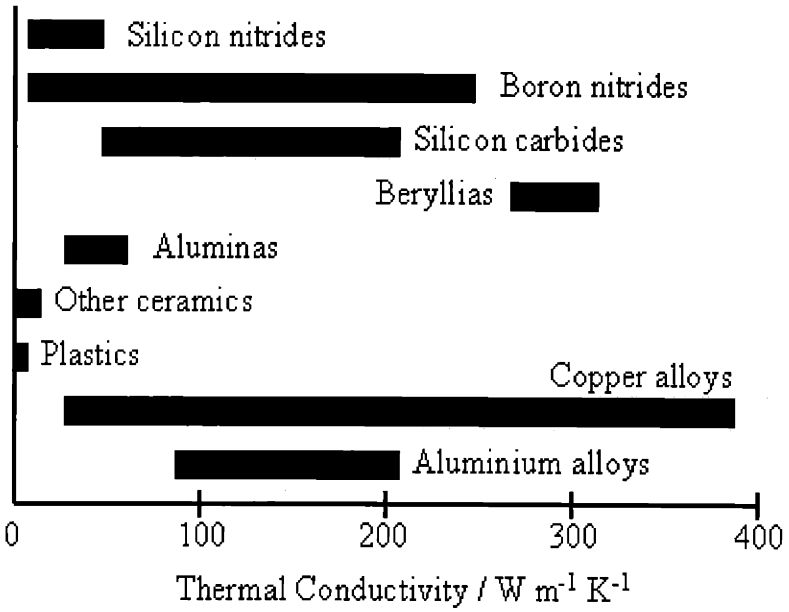

Figure 6-19: *Thermal Conductivity of Various Ceramics.*

Plastics were discounted as a potential insulator because of the low melting point. Using references [101], [116], [87], some high temperature ceramics were identified with their resistivities, and thermal conductivities. These are plotted in figures 6-20 and 6-21. The materials were selected for their high resistivity. Recall resistance, R, is given by,

$$R = \rho \frac{l}{S}, \tag{6.24}$$

where ρ is the resistivity, l the length, and S the cross section. There is not much difference in the resistivity of the materials selected, except for TiN, which is comparable at high temperatures, but significantly worse at low temperatures. Quartz (SiO_2) was included because of its optical transparency. The next most desirable property is high thermal conductivity, as shown in figure 6-21. This clearly shows BN and BeO, to have the best thermal conductivities as was expected.

There did not appear to be much difference in the performance between Boron Nitride and Beryllium Oxide, so various papers on electric propulsion were consulted. For the insulator the most popular choice in the literature is Boron Nitride, and no mention was found of BeO. Boron Nitride is fairly soft so can be easily machined, and is relatively inexpensive, so Boron Nitride was selected as the material for the insulator.

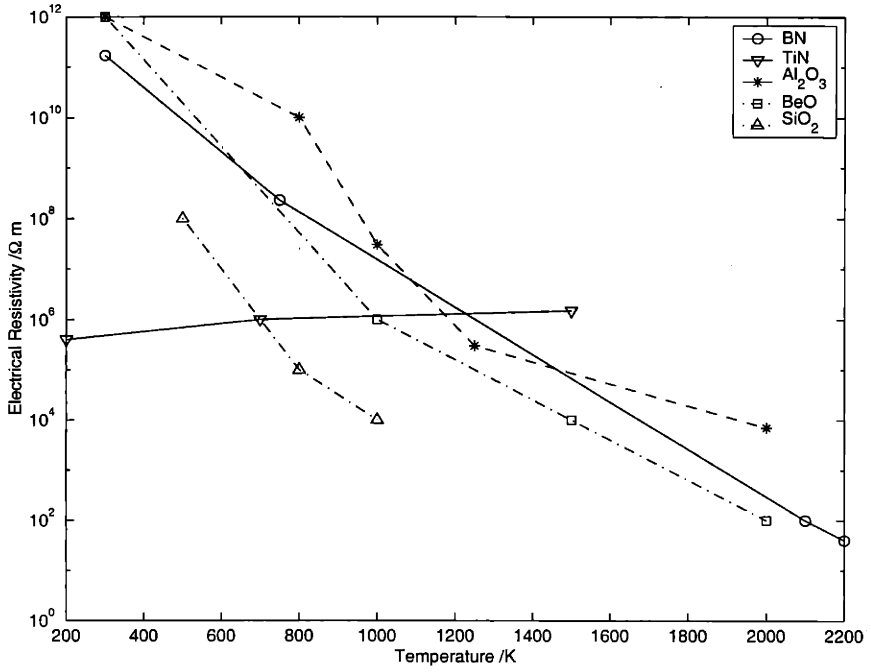

Figure 6-20: *Electrical Resistivity of Some High Temperature Ceramics.*

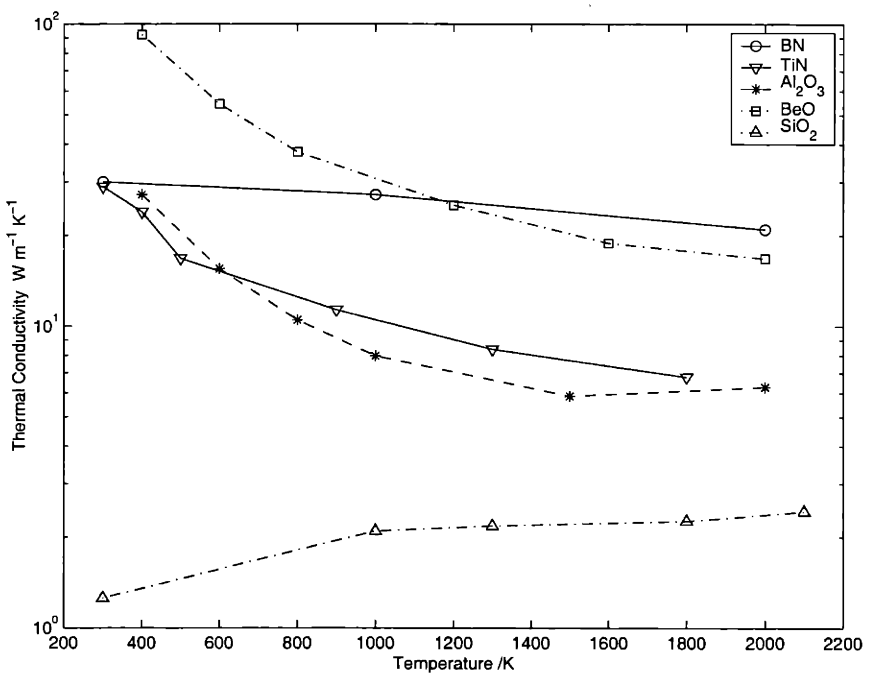

Figure 6-21: *Thermal Conductivity of Some High Temperature Ceramics.*

6.3 Thermal Model

6.3.1 Introduction to the Thermal Model

As part of the experimental design it was clear that a thermal model of the structure of the thruster would be required. This would determine materials that could be used and also the geometry. For example in a laboratory prototype if it was wished to include a quartz window for taking spectroscopic measurements then the temperature at that location must not exceed the melting point of quartz which is typically around 1000 K.

Some simple one dimensional calculations showed that the anode region would be nearly isothermal, and that radiative cooling was only a minor source of heat loss. Most heat would be conducted back through the structure to either a heat sink at the end (The spacecraft itself which would act as a high thermal capacity body), or would have to be taken up regeneratively by propellant being supplied to the thruster.

To obtain realistic estimates of the temperature distribution within the seeded arcjet structure a two dimensional model was created very similar to that by Miller [85].

For the initial structural design a generic radiatively cooled arcjet thruster was used based on the German TT1 thruster as did Miller. Boron nitride was used as the electrically insulating layer between the cathode and the anode as shown in figure 6-22.

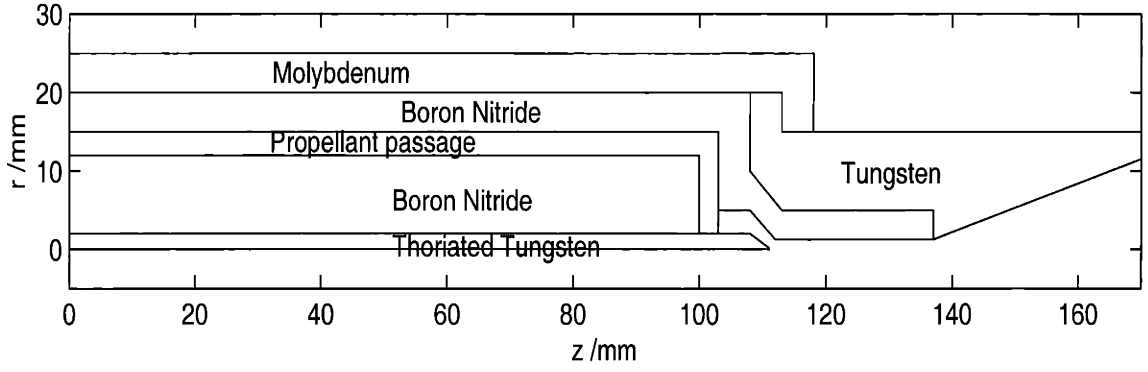

Figure 6-22: *Initial Structural Design.*

The propellant gas is injected at the rear of the assembly and flows through passages in the boron nitride. Heat is passed regeneratively from the feed pipe walls into the propellant. Heat is transfered from the hot plasma in the thruster itself to the walls, although the majority of this occurs at the arc attachments points on the cathode tip and on the anode at the very beginning of the nozzle where the wall first becomes conducting. The only other

source of heat in the model is the ohmic dissipation from the current being passed along the cathode, through the tungsten anode block, and back long the molybdenum casing. For a 10 kW arcjet the ohmic dissipation in the anode is only a few Watts compared to the 1 kW dissipated by the arc electrons in the attachment region, so this was ignored. In the cathode however, due to its small size, the ohmic dissipation is on the order of 5 W compared to the 100 W dissipated on the cathode tip. Therefore this source of heating was included in the cathode rod.

Heat flow is governed by the equation, (See reference [53] for a derivation):

$$\rho c_p \frac{\partial T}{\partial t} = \nabla \cdot k \nabla T + q' \qquad \left[\mathrm{W\,m^{-3}}\right]. \tag{6.25}$$

In axisymmetric cylindrical coordinates with steady state this is

$$\frac{1}{r}\frac{\partial}{\partial r}\left(rk\frac{\partial T}{\partial r}\right) + \frac{\partial}{\partial z}\left(k\frac{\partial T}{\partial z}\right) + q' = 0. \tag{6.26}$$

This is identical in form to the potential equation

$$\frac{1}{r}\frac{\partial}{\partial r}\left(r\sigma\frac{\partial \phi}{\partial r}\right) + \frac{\partial}{\partial z}\left(\sigma\frac{\partial \phi}{\partial z}\right) = \nabla\left(\psi \nabla P_e\right)$$

given in section 4.1.3, so the same Successive Over-Relaxation (SOR) scheme as described in section 4.4 can be used with

$$a\frac{\partial^2 T}{\partial \xi^2} + b\frac{\partial^2 T}{\partial \eta^2} + c\frac{\partial^2 T}{\partial \xi \partial \eta} + d\frac{\partial T}{\partial \xi} + e\frac{\partial T}{\partial \eta} = -q',$$

where

$$a = k(\xi_r^2 + \xi_z^2) \qquad b = k(\eta_r^2 + \eta_z^2) \qquad c = 2k(\xi_r\eta_r + \xi_z\eta_z)$$

$$d = k\left(\xi_{rr} + \xi_{zz} + \frac{\xi_r}{r}\right) + (\xi_r^2 + \xi_z^2)\frac{\partial k}{\partial \xi} + (\xi_r\eta_r + \xi_z\eta_z)\frac{\partial k}{\partial \eta}$$

$$e = k\left(\eta_{rr} + \eta_{zz} + \frac{\eta_r}{r}\right) + (\eta_r^2 + \eta_z^2)\frac{\partial k}{\partial \eta} + (\xi_r\eta_r + \xi_z\eta_z)\frac{\partial k}{\partial \xi}.$$

$$q' = \frac{J^2}{\sigma}. \tag{6.27}$$

For the thermal conductivity, k, of tungsten, molybdenum, and boron nitride curve fits

were done to the data quoted by Miller [85] which are from the Handbook of Physics and Chemistry for tungsten and molybdenum and from technical data from the Carborundum Company [15] for boron nitride. For the range of temperatures expected these are plotted in figure 6-23 with the valid ranges of the curve fits.

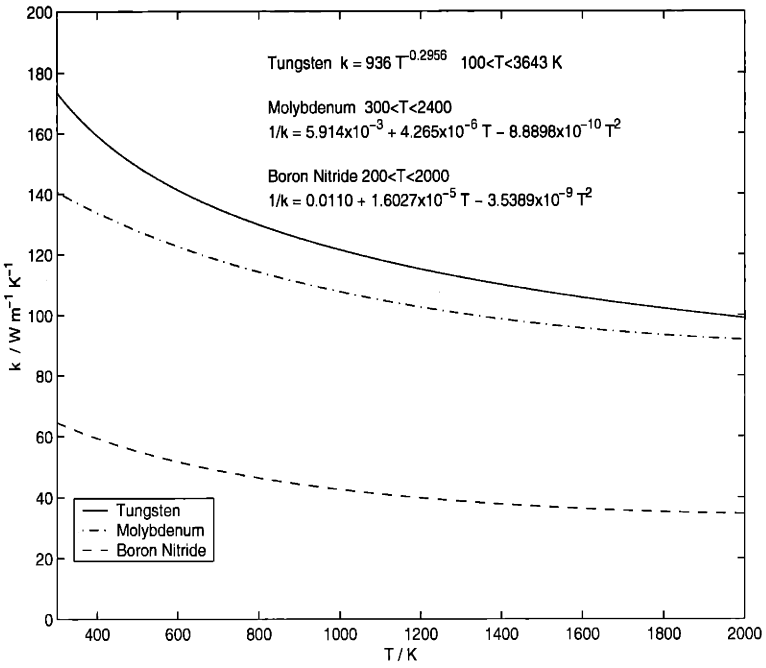

Figure 6-23: *Thermal Conductivities of Tungsten, Molybdenum and Boron Nitride.*

6.3.2 Thermal Model Boundary Conditions

At the backplate, there was assumed to be a heat sink at a constant 300 K, simulating the large structure of the rest of the spacecraft.

For the centreline which occurs along the length of the cathode rod, no vertical heat flux was imposed so

$$kA\frac{\partial T}{\partial r} = 0. \tag{6.28}$$

For the outer shell the temperature was calculated from the heat flux emitted by radiation into space, although the 3 Kelvin background was neglected so

$$k\frac{\partial T}{\partial n} = \varepsilon\sigma T^4, \tag{6.29}$$

where n is the vector normal to the surface. When discretised on horizontal surfaces this is

$-k(T_2 - T_1)/(r_2 - r_1) = \varepsilon\sigma T_2^4$, which has the disadvantage of containing the non-linear T^4 term, but can be readily solved using a Newton-Raphson iteration

$$J(X^{n+1} - X^n) = -R \qquad \text{or in 1-D} \qquad x^{n+1} = x^n - \frac{f(x^n)}{f'(x^n)}. \tag{6.30}$$

Solving for T_2 the iteration is

$$T_{n+1} = T_n - \frac{\frac{\varepsilon\sigma}{k}(r_2 - r_1)T_n^4 + T_n - T_1}{3\frac{\varepsilon\sigma}{k}T_n^3 + 1}. \tag{6.31}$$

However because $\frac{\varepsilon\sigma}{k}(r_2 - r_1)$ is so small, $T_2 \approx T_1$ is useful for an initial guess, and the gradient is roughly linear so only one iteration is needed to solve with high accuracy. This linearity also allows the iteration to be abandoned for the simpler

$$T_2^{(n+1)} = T_1 - \frac{\varepsilon\sigma}{k}(r_2 - r_1)T_2^{4(n)} \tag{6.32}$$

without any significant loss in accuracy.

For the heat flux from the hot plasma in the thruster itself, the heat flux to the wall was calculated from a nominal fluid flow simulation, given the temperature profile imposed in that run. This is therefore not a self-consistent model, but rather what would be the first step in an iterative process of running the thermal model of the structure and the fluid flow model. The wall temperature profile imposed in the original fluid flow simulation is fairly realistic, and the idea was to obtain realistic estimates of the temperature distribution in the structure, with a view to the experimental design. The fluid flow calculations showed that about 1kW was deposited at the anode arc attachment region at the entrance to the nozzle, and about 0.1kW was deposited onto the cathode tip, so this is what was specified as the boundary condition to the thermal model along the surfaces which were accounted for in the fluid model. The heat flux is given by

$$q = -k\frac{\partial T}{\partial n} \qquad \left[\mathrm{W\,m^{-2}}\right], \tag{6.33}$$

where

$$\frac{\partial T}{\partial n} = \hat{\underline{n}} \cdot \nabla T, \tag{6.34}$$

where in curvilinear coordinates

$$\nabla T = \frac{\partial T}{\partial z}\underline{\hat{z}} + \frac{\partial T}{\partial r}\underline{\hat{r}},$$

Vertically $\underline{\hat{n}} = \frac{r_\eta}{\sqrt{r_\eta^2 + z_\eta^2}}\underline{\hat{z}} - \frac{z_\eta}{\sqrt{r_\eta^2 + z_\eta^2}}\underline{\hat{r}}$, Horizontally $\underline{\hat{n}} = \frac{r_\xi}{\sqrt{r_\xi^2 + z_\xi^2}}\underline{\hat{z}} - \frac{z_\xi}{\sqrt{r_\xi^2 + z_\xi^2}}\underline{\hat{r}}$.

6.3.3 Regenerative Heat Transfer

The addition of heat to the propellant from the walls in the feed pipe was assumed to be essentially one dimensional to simplify calculations. Following Incropera and De Witt (reference [53]) consider flow in a pipe.

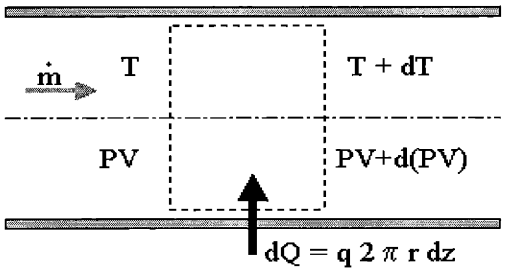

Figure 6-24: *Heat addition in a pipe.*

Recall that $\dot{E} = \dot{m}C_vT$ and $\dot{m} = \rho uA$. Applying conservation of energy to the control volume in figure 6-24

$$dQ + \dot{m}(c_vT_m + PV) - \left(\dot{m}(c_vT_m + PV) + \dot{m}\frac{d}{dz}(c_vT_m + PV)dz\right) = 0 \qquad (6.35)$$

so

$$dQ = \dot{m}d(c_vT_m + PV) \qquad [\mathrm{W}], \qquad (6.36)$$

or in other words the rate of heat transfer to the fluid is the rate at which thermal energy increases plus the rate at which work is done. For a perfect gas $Pv = RT_m$, $c_p = c_v + R$ so

$$dQ = \dot{m}c_pdT_m = q2\pi rdz. \qquad (6.37)$$

Now the heat flux into the gas,

$$q = k\frac{\partial T}{\partial r}\bigg|_{wall} \qquad \left[\mathrm{W\,m^{-2}}\right], \tag{6.38}$$

can be modelled as

$$q = h(T_w - T_m), \tag{6.39}$$

where h is called the Heat Transfer Coefficient, T_w is the temperature at the wall, and T_m is the mean temperature of the fluid at that axial location. Therefore

$$\dot{m}c_p\frac{dT_m}{dz} = 2\pi r h(T_w - T_m) \qquad \left[\mathrm{W\,m^{-1}}\right]. \tag{6.40}$$

The heat transfer coefficient, h, can be calculated in terms of a non-dimensional number known as the Nusselt number,

$$Nu = \frac{hD_h}{k} \qquad \text{where} \qquad D_h = \frac{4A}{P}. \tag{6.41}$$

k is the thermal conductivity of the gas, and D_h is the Hydraulic Diameter, which is four times the cross sectional area divided by the wetted perimeter. For pipes with circular cross sections this is simply the diameter. The Nusselt number is known empirically in a variety of flows, and is essentially the ratio of the diameter of the pipe to thickness of the thermal boundary layer. Incropera and De Witt [53] give the Nusselt numbers for fully developed laminar flow in tubes of different cross sections as in figure 6-25.

The propellant feed pipe was initially modelled as an annular pipe for which

$$\dot{m}c_p\frac{dT_m}{dz} \;=\; q_o 2\pi r_o + q_i 2\pi r_i \;=\; 2\pi r_o h_o(T_o - T_m) + 2\pi r_i h_i(T_i - T_m), \tag{6.42}$$

where the subscript o denotes the outer surface and i the inner surface. Incropera and De Witt [53] give a detailed formula for the inner and outer Nusselt numbers, but given the not insubstantial difference between the Nusselt numbers for constant heat flux or constant wall temperature, neither of which is correct for the situation being modelled, this was not used. Instead an average over several plausible Nusselt numbers was taken, which for the initial geometry gave a Nusselt number of about 6.

For the thermal conductivity of the gas, the fluid code uses a very complicated solver,

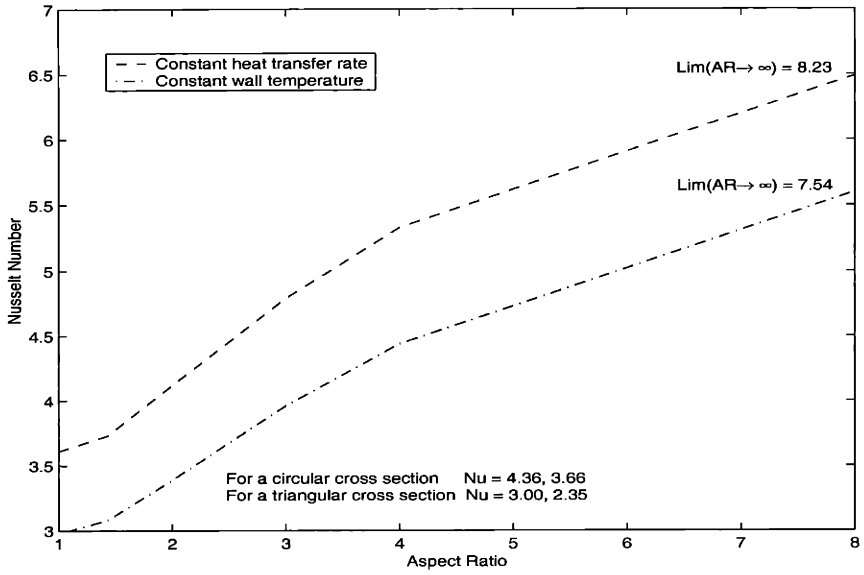

Figure 6-25: *Nusselt numbers for fully developed laminar flow in a pipe.*

based on chemical and thermal non-equilibrium and all the chemical species. Since the temperature of the gas from the backplate to the thruster inlet was not expected to exceed 1000 K, and any cesium would have a negligible effect, a simpler method was used. The thermal conductivity of an equilibrium mixture of pure hydrogen was calculated, and curve fitted up to 2000 K just to be sure. Within the range of feed pipe pressures anticipated pressure has a negligible effect below 2500 K, as can be seen in figure 6-26.

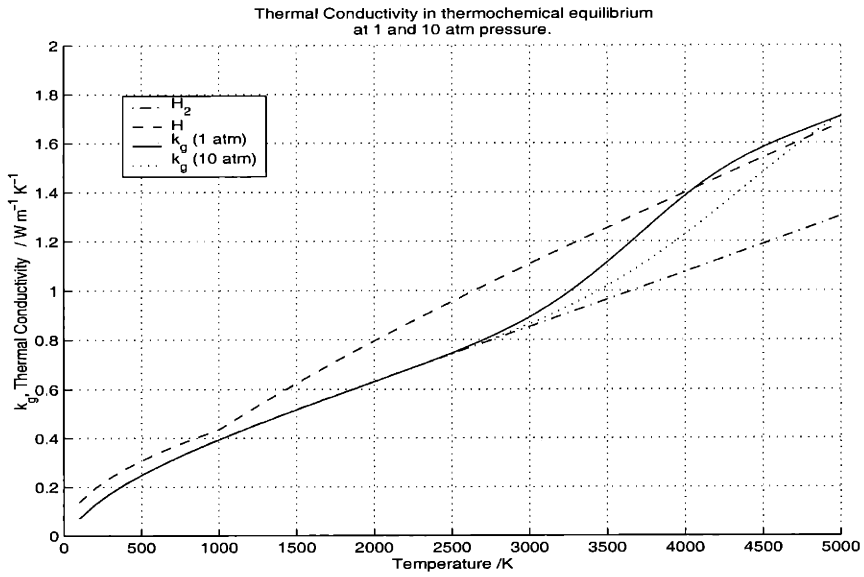

Figure 6-26: *Thermal Conductivity of Hydrogen.*

In a similar manner, the fluid code has a complicated scheme for calculating the specific heats, whereas for the feed pipe calculation treating the gas as if it were all H_2 will incur negligible errors. As in section 3.4.3

$$\begin{aligned} C_p &= C_v + R \\ &= R\left(1 + \frac{5}{2} + \frac{\left(\frac{\theta_v}{T}\right)^2 e^{\theta_v/T}}{\left(e^{\theta_v/T} - 1\right)^2}\right) \\ &= R\left(\frac{7}{2} + \left(\frac{\frac{\theta_v}{2T}}{\sinh\left(\frac{\theta_v}{2T}\right)}\right)^2\right), \end{aligned} \tag{6.43}$$

where $\theta_v = 6140$ K, and $R = 4157$ J K^{-1} Kg^{-1} (As opposed to the universal gas constant of 8.31435 J K^{-1} mol^{-1}).

Using equation 6.42 the mean propellant temperature, T_m, can be found by integrating along the passageway from a specified starting temperature. Although a simple second order accurate scheme should suffice, this integration was done using a fourth order Runge-Kutta scheme. I.e. for $\frac{dU}{dt} = f$,

$$\frac{U_{n+1} - U_n}{\Delta t} = \frac{1}{6}(k_1 + 2k_2 + 2k_3 + k_4), \tag{6.44}$$

with

$$\begin{aligned} k_1 &= f(U_n) \\ k_2 &= f(U_n + \frac{1}{2}k_1\Delta t) \\ k_3 &= f(U_n + \frac{1}{2}k_2\Delta t) \\ k_3 &= f(U_n + k_3\Delta t). \end{aligned}$$

For the gas/structure wall boundary the temperature can be found by matching the heat flux into the gas with that passed to the wall from the surrounding structure by conduction.

$$q_{into\ gas} = \frac{k_{gas}Nu}{D_h}(T_w - T_m) = q_{conduction} = k_{structure}\frac{dT}{dn}. \tag{6.45}$$

When discretised dT/dn is simply $(T_{w+1} - T_w)/\Delta n$ where T_{w+1} indicates the temperature

at one grid point away from the wall. The system is then readily solved for T_w.

6.3.4 Thermal Model Results and Modifications

A grid was made conforming to the initially specified geometry and the first step obtaining results from the thermal model was to test the basic scheme on this grid but assuming it to be a block of pure tungsten without any propellant feed pipes present or any ohmic dissipation in the cathode rod. A couple of extra programs were written to calculate the heat flux into and out of any subsection of the grid. With approximately 1 kW applied to the arc attachment region, the temperature varied smoothly from 300 K at the backplate to 1200 K at the arc attachment region. The converged solution was found to conserve energy to within 0.1%.

The thermal model was then run on the system including the different materials, and the propellant feed pipe, the results of which are shown in figure 6-27.

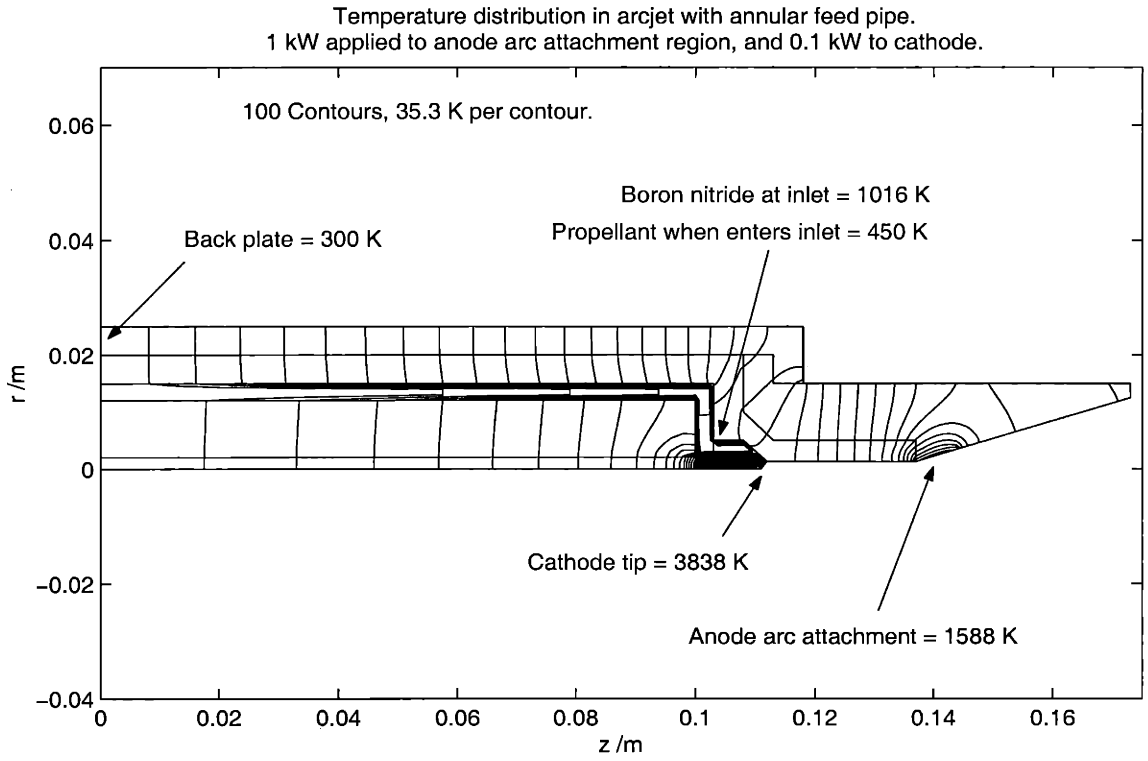

Figure 6-27: *Temperature distribution in arcjet with annular feed pipe.*

Along the feed pipe in the inner boron nitride block the temperature rises from 300 K to nearly 700 K. The propellant however only rises to a little over 400 K. The feed pipe also

acts to thermally insulate the cathode block from the anode block.

It was thought that it might be better to make the feed pipe into one or more channels through the boron nitride, and to make it spiral around to make the path longer. This would allow more time for regenerative heating and thermally connect the cathode and the anode. The drawback however would be a larger pressure drop required along the feed pipe.

The feed pipe was then modelled as spiraling around the core, so about half of the area at any section was occupied by the pipe, and half by solid boron nitride.

To avoid modelling the feed pipe in three dimensions, keeping the 2-dimensional model, the grid points in the feed pipe region were assumed to be those of the solid boron nitride, and the propellant temperature was dealt with in a 1-dimensional manner as before.

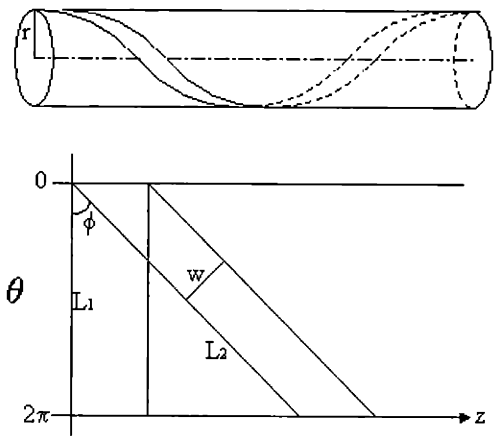

Figure 6-28: *Spiral feed pipe.*

From figure 6-28, the area of one spiral is the length of the spiral times the width. The total area is $2\pi r dz$ so the fraction of the total area occupied by the channel is

$$\frac{A_{channel}}{A_{total}} = \frac{w}{2\pi r \sin\phi}. \tag{6.46}$$

Accounting for top and bottom, assuming relatively thin channels, and 2 sides of height, h, and also assuming that the temperature of the boron nitride around the feed pipes does not vary significantly, the equation for heat transfer into the propellant becomes

$$\dot{m} c_p dT_m = qdA = 2\frac{k_{gas} Nu}{D_h}(T_{wall} - T_{gas})\left(\frac{w+h}{\sin\phi}\right) dz. \tag{6.47}$$

Changing the geometry of the propellant feed pipes changes the Nusselt number, so

the data from figure 6-25 was averaged and interpolated. Most increase in dT/dz comes from decreasing the hydraulic diameter, which for a given area of channel can be done by increasing the aspect ratio of the channel - wide and flat, or tall and narrow.

If multiple channels are used then the area ratio becomes

$$\frac{A_{channel}}{A_{total}} = \frac{nw}{2\pi r \sin\phi}. \tag{6.48}$$

Since the mass flux is split among each of the channels, they have to become straighter to maintain the same area ratio as before. These effects cancel each other, so there is no difference in the exit temperature at the same area ratio, whether one long highly wound channel, or many straight ones are used. The advantage of straight channels however would be a smaller pressure drop across the feed pipe length, and also greater ease of manufacture.

Using a specified wall temperature profile, numerous runs of the propellant temperature integration were done with a variety of channel sizes, area ratios, and number of channels, as illustrated in figures 6-29 to 6-32.

Figure 6-29 shows the effect decreasing the hydraulic diameter can have. Table 6.3 shows the calculated Nusselt number changes by less than a factor of 2, given the change in aspect ratio of 10. The hydraulic diameter does change by nearly a factor of 10 however, which causes a corresponding change in the temperature gradient at the feed pipe entrance.

w = 12.5 mm		
	h=3 mm	h=0.3 mm
w/h	4.17	41.7
Nu	4.9	7.88
D_h	4.8 mm	0.586 mm
$\left.\frac{dT}{dx}\right\|_{T=300K}$	3.8 K m^{-1}	41.6 K m^{-1}

Table 6.3: *Feedpipe Comparison*

A height of 0.3 mm however would be difficult to manufacture, so next, figures 6-30 and 6-31 show a comparison for a pipe of height 3 mm, with widths of 1mm to 25 mm. Good heat transfer is really only achieved for widths of around 1 mm or less.

Finally figure 6-32 (along with figure 6-30b) illustrates that there is no difference in the propellant temperature at the end of the feed pipe, whether one channel or many are used.

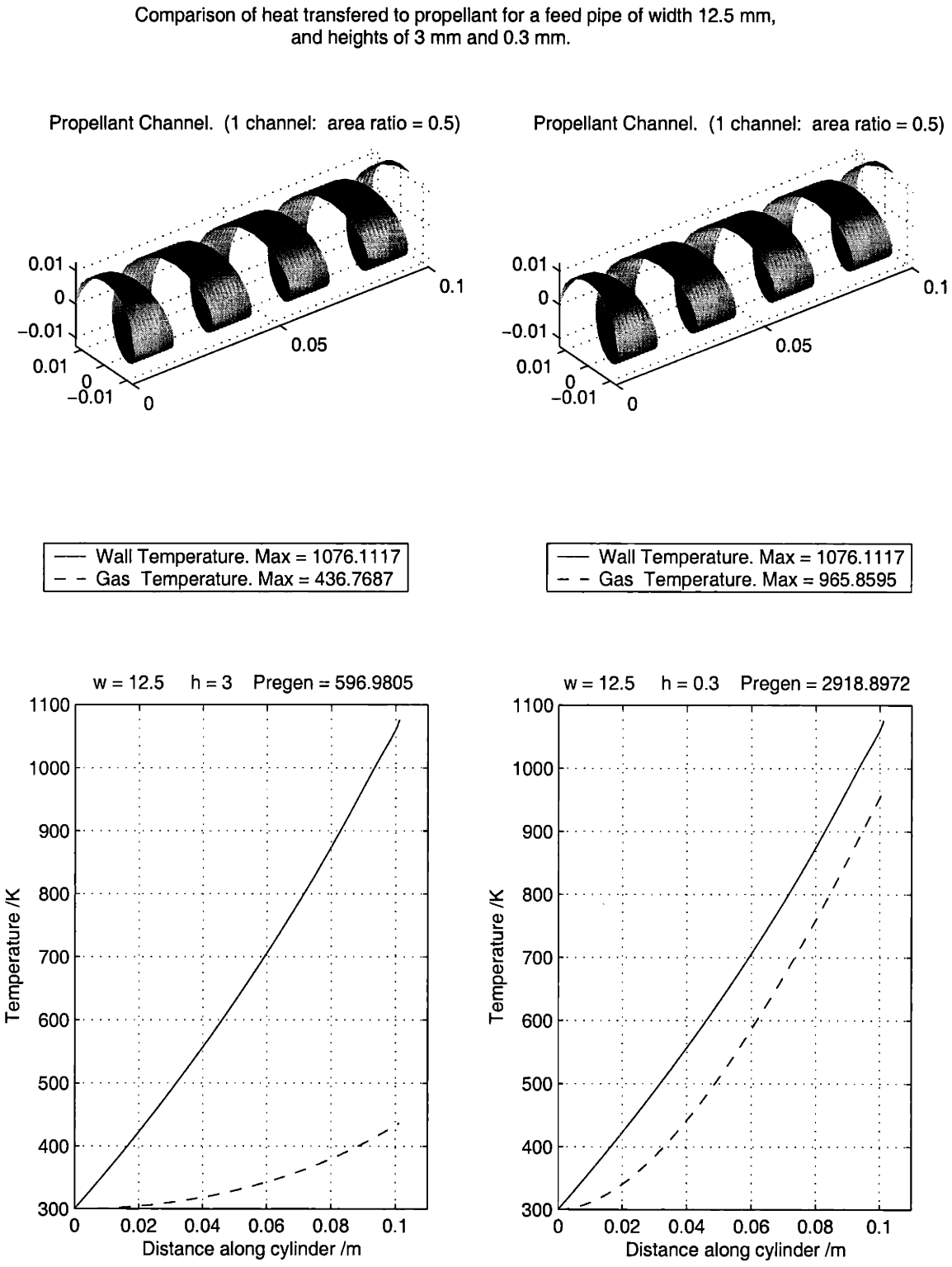

Figure 6-29: *Propellant temperature profile along feed pipe (1).*

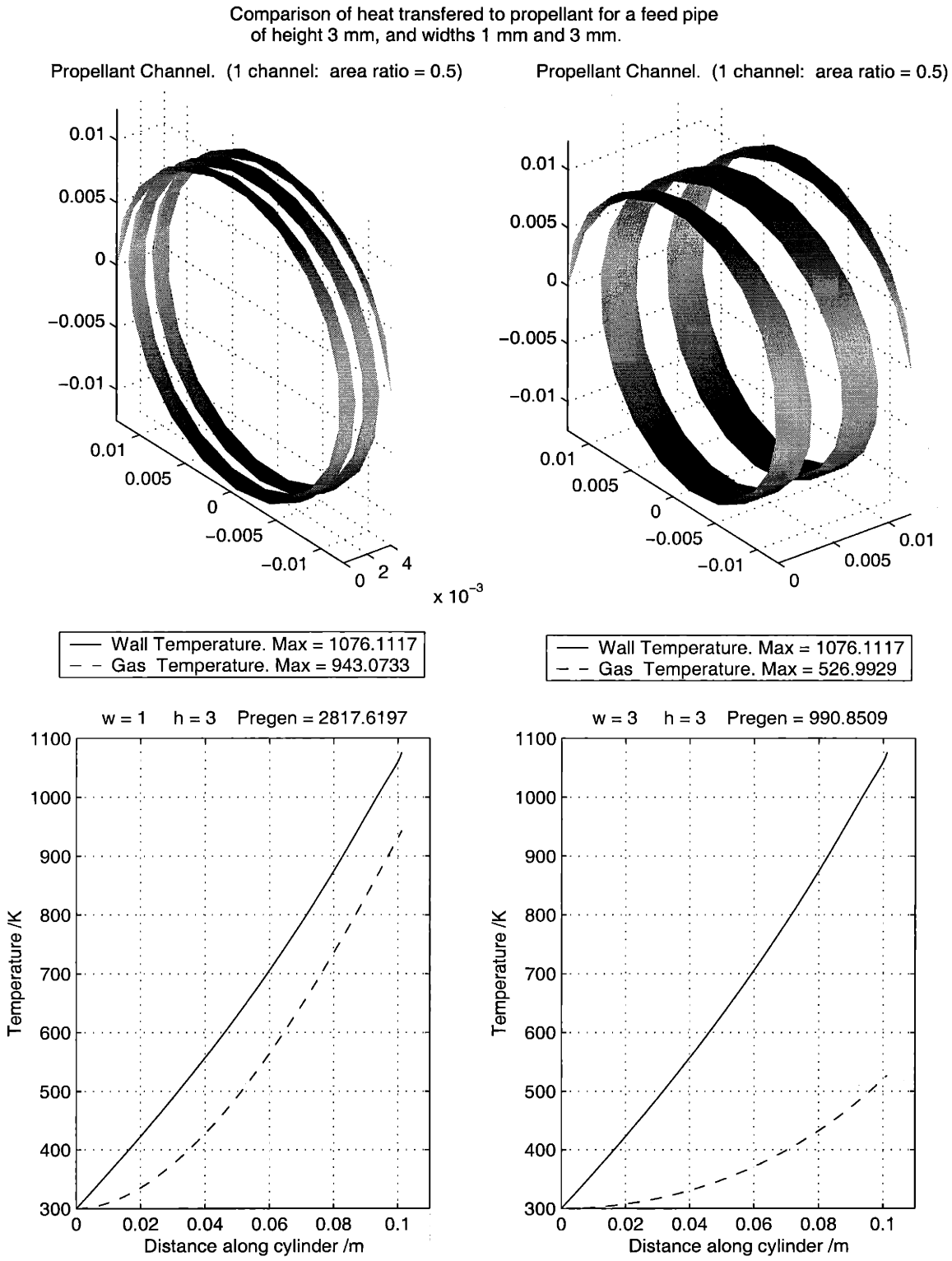

Figure 6-30: *Propellant temperature profile along feed pipe (2).*

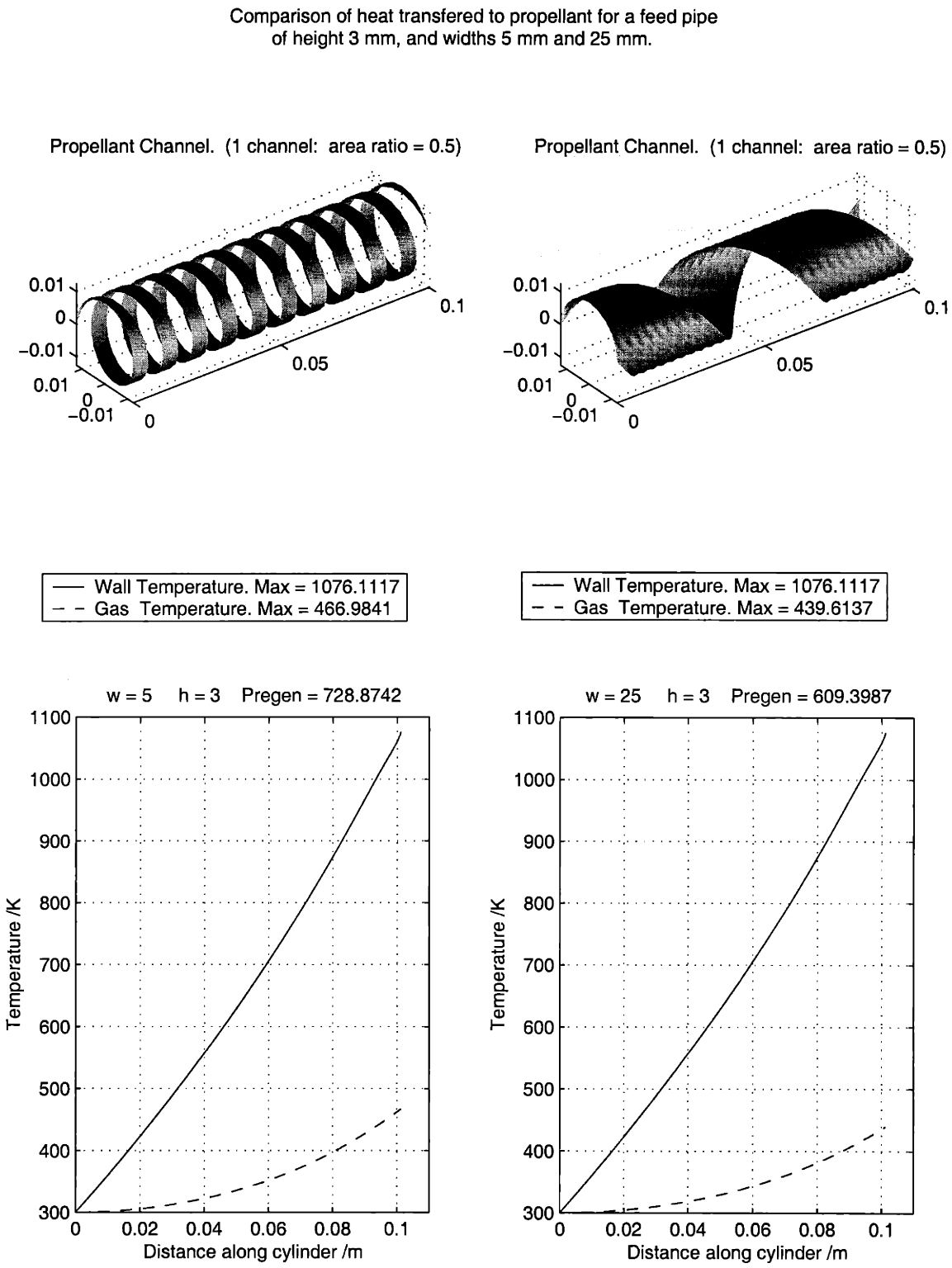

Figure 6-31: *Propellant temperature profile along feed pipe (3).*

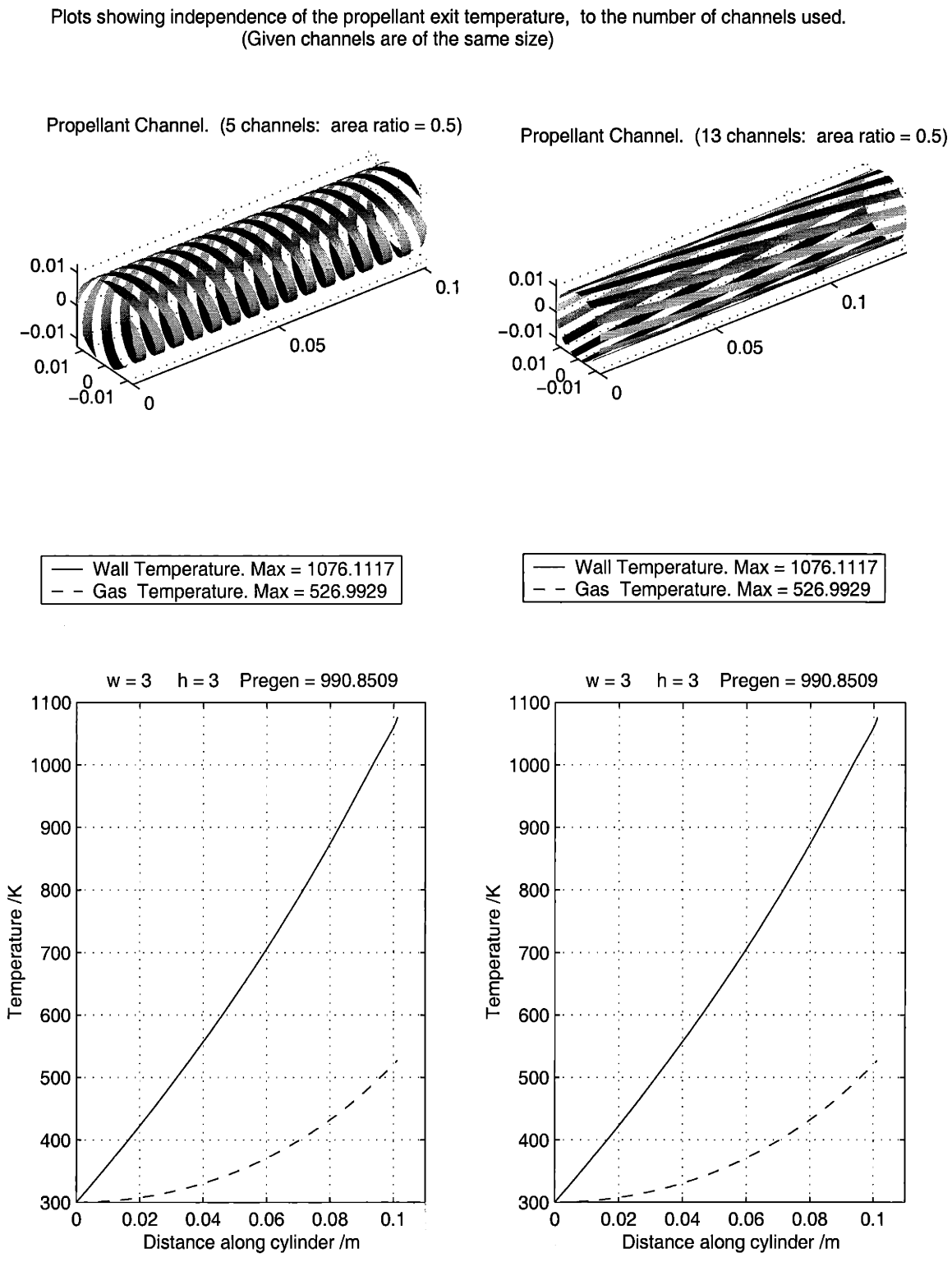

Figure 6-32: *Propellant temperature profile along feed pipe (4).*

In the end for a preliminary design, it was decided to use 36 straight channels, each 5 mm high and 1 mm wide. For the wall temperature profile specified in figures 6-29 to 6-32, this gives a maximum propellant temperature of 998 K, and a regenerative heat transfer of 3061 W.

Increasing the fraction of the volume occupied by the feed channels in that region, as expected does increase the amount of heat transfered regeneratively, but the effect is small. For the example above with channels 5 mm high and 1 mm wide, increasing this fraction from 50 % to 80 % only increases the maximum gas temperature to 1027 K, and the regenerative power to 3193 W. Also with 80 % of the channel region occupied by the feed pipes, the heat transfer between the inner and outer sections is greatly reduced and they start to become thermally isolated again, as can be seen in figures 6-33 and 6-34.

The modelling of feed pipes done here is really only the beginning of the development of a regenerative cooling system, aimed at reclaiming the last ten percent of energy losses, and can be continued much further along the lines of various models of heat exchangers. For an arcjet one example can be seen in figure 2-5.

The modelling also showed that for the initial geometry, the temperature predicted for the cathode tip is in excess of the melting point of tungsten (3643 K), so the geometry was redesigned to give a faster increase in area behind the tip, to more quickly decrease the power per unit area. The new geometry with the 5 mm high feed pipes is shown in figure 6-35. (The initial geometry is shown in figure 6-22).

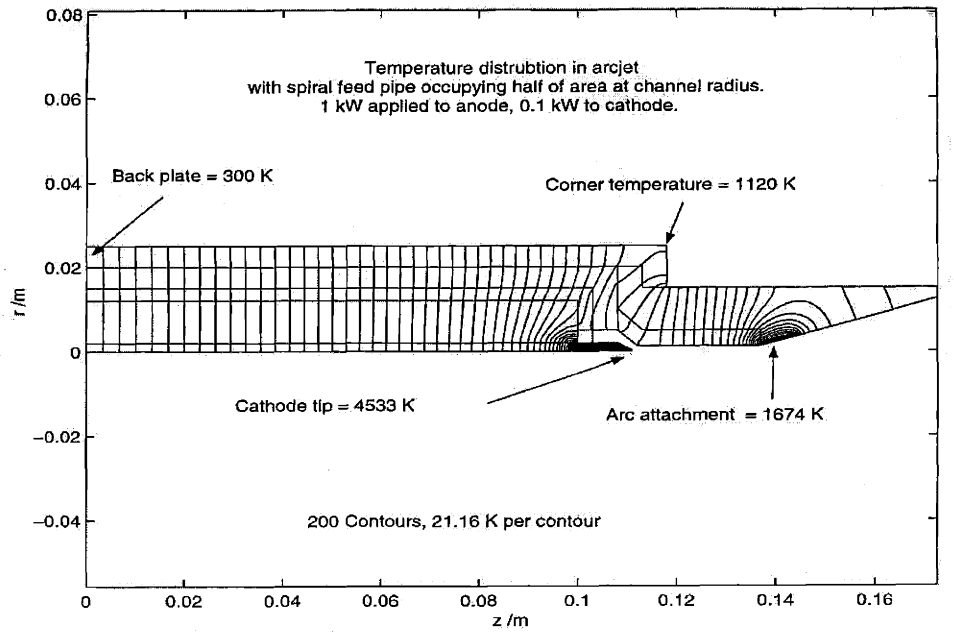

Figure 6-33: *Temperature distribution in arcjet with pipe area fraction 0.5.*

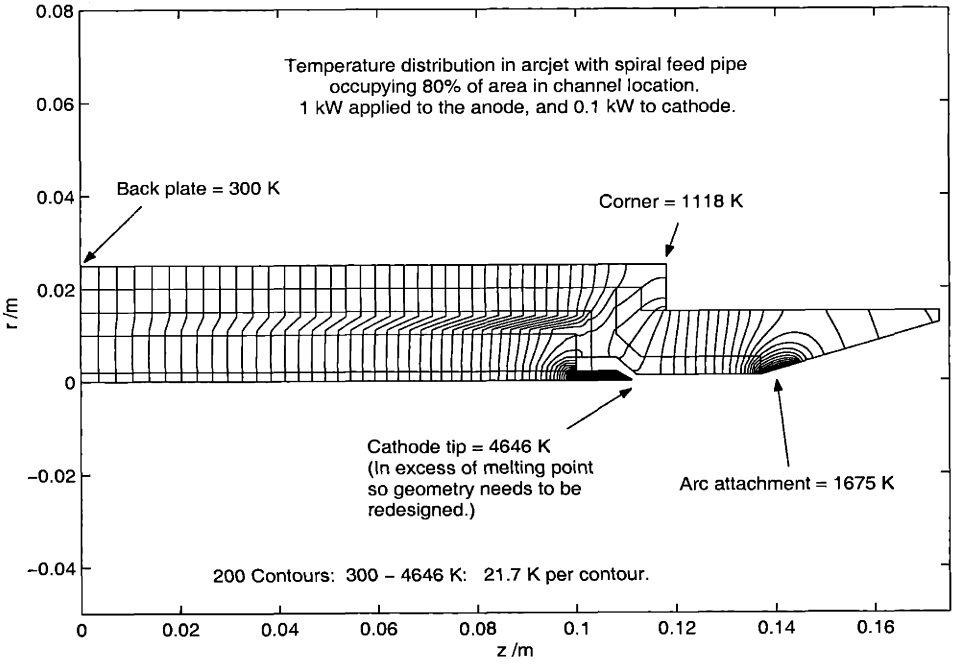

Figure 6-34: *Temperature distribution in arcjet with pipe area fraction 0.8.*

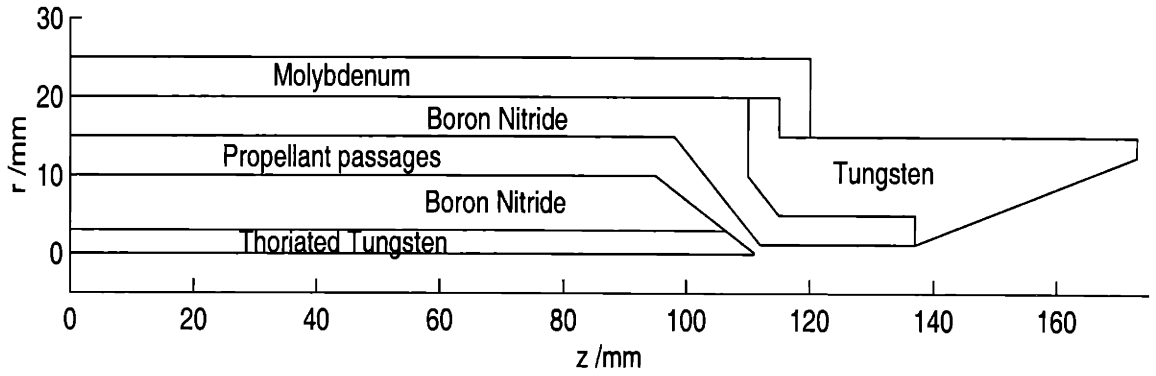

Figure 6-35: *Structural design with enlarged cathode and feed pipes.*

In conducting a full simulation of the thermal model, all the grid points were assumed to be structural and the temperature of the propellant in the feed pipes was integrated in 1-D as above. The presence of the feed pipes then act as an energy loss term to the boron nitride at the grid points in the channel area, rather than as boundary conditions.

In the heat flow equation 6.25, for the source term, $\dot{q}$, the heat passed regeneratively to the propellant must be modelled. (As well as the ohmic dissipation in the cathode, and the heat flux deposited by the arc attachments, already accounted for.), In the propellant

$$dQ = \dot{m} c_p dT_m = q dA \qquad [\mathrm{W}], \tag{6.49}$$

as in equation 6.37. Hence the heat loss from the material is,

$$q' = -\frac{dQ}{dV} \qquad \left[\mathrm{W\,m^{-3}}\right], \tag{6.50}$$

where the volume dV is the cross sectional area of the channel region, $\pi(r_o^2 - r_i^2)$, times the length of the cell on the numerical grid, dz.

To account for the reduction in area of the boron nitride in the feed pipe area, the thermal conductivity of the material there was reduced instead. For the feed pipe occupying a fraction of the area, $A_{channel}/A_{total}$, the thermal conductivity of the pipe structure was set to

$$k_{pipe\ structure} = \frac{k_{bn}}{(1 - \frac{A_{channel}}{A_{total}})}, \tag{6.51}$$

neglecting the thermal conductivity of the gas as negligible compared to that of the structure.

Using the full thermal structure model with the temperature in the propellant pipe integrated with every relaxation step, more simulations were run, a typical example of which is shown in figures 6-36 to 6-38.

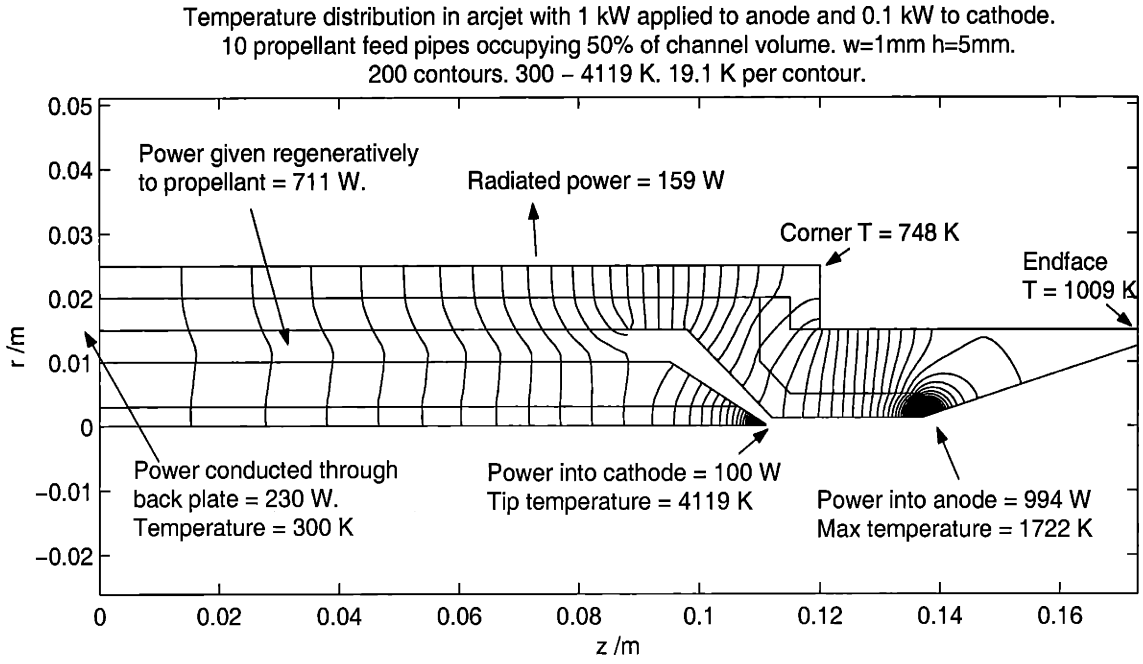

Figure 6-36: *Temperature distribution in arcjet with multiple feed pipes.*

Figure 6-37, shows that with feed pipes 1 mm wide and 5 mm high, occupying 50% of the channel volume, that 711 W of the incident 1094 W, is reclaimed regeneratively.

Figure 6-38, shows that with the enlarged cathode, and improved regenerative heating, that even in this case the temperature on the cathode tip is in excess of the melting point of tungsten. However the temperature drops much more rapidly that with the original cathode design, and that melting will stop less than 0.1 mm from the tip, at only a very slightly larger tip radius. It should also be pointed out however that the thermal model does not account for electron emission cooling of the cathode, which can be a strong source of cooling, that would keep the cathode below the melting point of tungsten.

Given the achievements of the current model, with 65% of the heat lost to the walls regained regeneratively, and that the cathode tip will not melt, the thermal modelling was left at this stage to continue other areas of the experimental design.

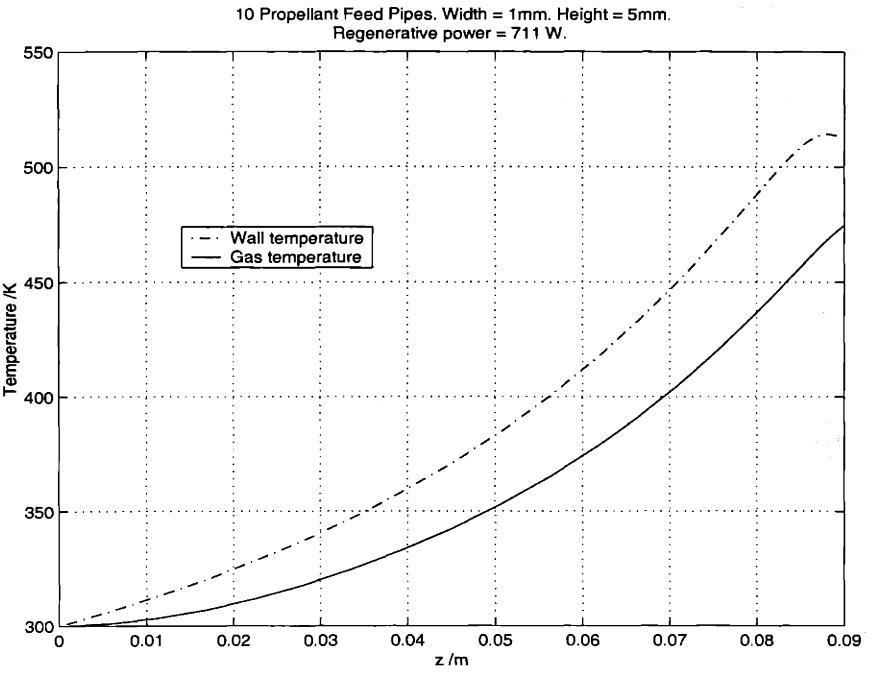

Figure 6-37: *Propellant temperature in final thermal model run.*

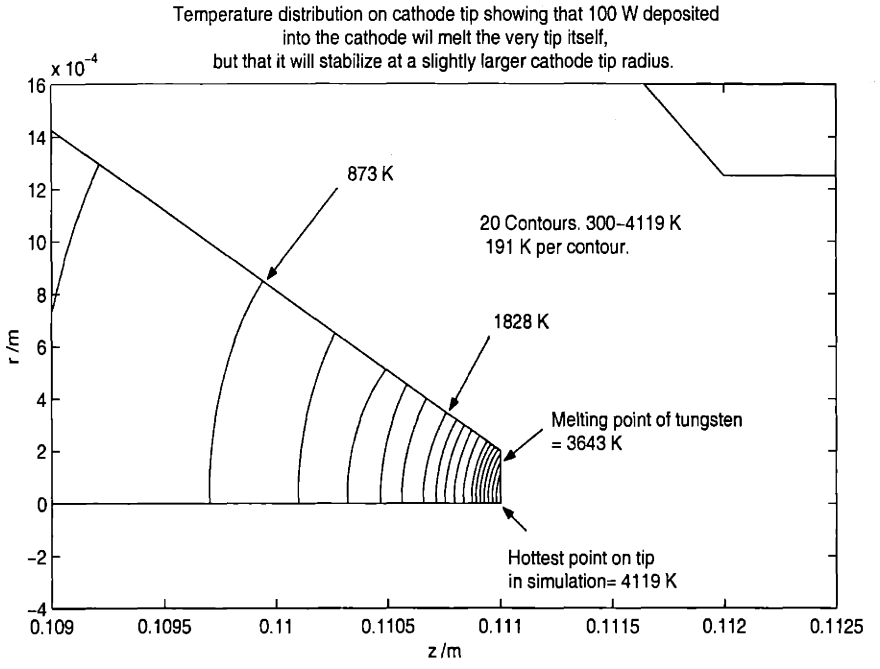

Figure 6-38: *Temperature distribution on cathode tip.*

6.4 Vacuum Tank Operation

Given the size and power of the thruster the vacuum tank needs to be able to house the thruster, a thrust measurement stand, and any other diagnostic equipment, and the pumps need to be able to extract the exhaust at the propellant flow rate and still maintain an acceptable background pressure. Fortunately for arcjets which have a much higher exit pressure than other types of electric thrusters such as Hall thrusters and ion engines, this background pressure can be fairly high. Alternatively if the size of the tank and pumping speed is fixed then the thruster needs to be scaled to fit.

6.4.1 Pumps

To measure long term operation of an arcjet the vacuum tank must be able to run in steady state with a tolerable background pressure. The ability of a pump to extract gas is measured by its pumping speed, which is the ratio of the throughput to the pressure, and is typically quoted in litres per second [40]. In general pumping speed is a function of pressure, and is fairly constant over a range, until the lowest attainable pressure with that pump is approached when the speed drops off rapidly, as illustrated in figure 6-39.

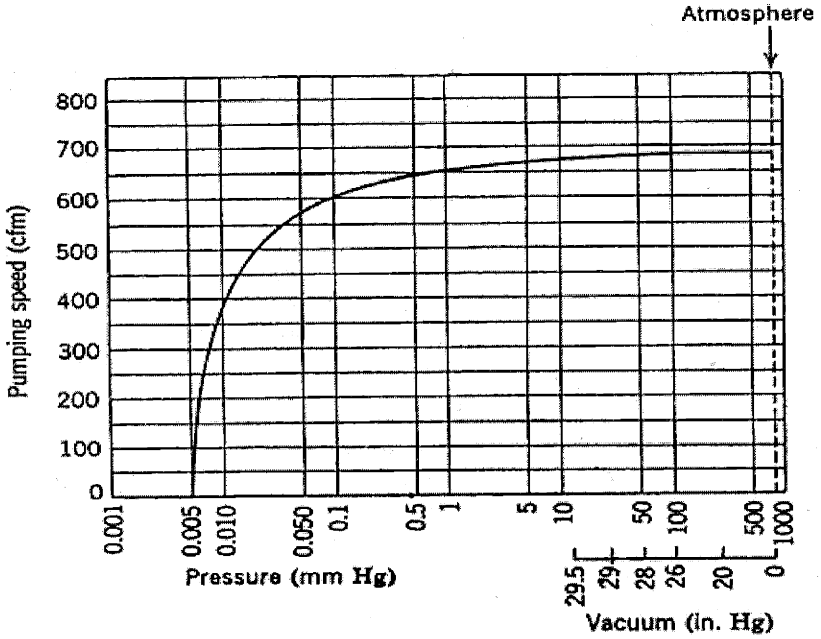

Figure 6-39: *Typical Pumping Speed Plot of a Mechanical Pump.*

In steady state operation, the pumping speed will match the rate at which gas is intro-

duced into the chamber. If the mass flow rate of into the chamber is $\dot{m}$ Kg s^{-1}, and the propellant weighs M Kg mol^{-1}, then it is introduced to the chamber at

$$\dot{n} = \frac{\dot{m}}{M} \qquad \text{mol } s^{-1}. \tag{6.52}$$

At chamber pressure P, the pumps can remove

$$\dot{n} = \frac{P\dot{V}_{pump}}{R_{univ}T} \qquad \text{mol } s^{-1}. \tag{6.53}$$

For steady state the pumping speed therefore needs to be capable of pumping at least

$$\dot{V}_{pump} \geq \frac{R_{univ}T}{P} \cdot \frac{\dot{m}}{M} \qquad m^3\ s^{-1}. \tag{6.54}$$

From the performance mapping of section 6.1, at the chosen optimum point the pressure at the end of the constrictor was found to be 1.126x10^5 Pa, and the mean gas temperature about 2000 K. Using an isentropic expansion the exit pressure was found to be 403 Pa for an expansion to Mach 5, and 51.5 Pa for an expansion to Mach 7. [2]. Similarly the exit temperature after expansion is approximately 400 K for Mach 5, and 200 K for Mach 7. Since a lower pressure places a greater requirement on the pumping speed it would be wise to use P=51.5Pa and T=200K, as the requirement. The design point mass flow rate is 3x10^{-4} Kg s^{-1}, and using H_2 which weighs 2x10^{-3} Kg mol^{-1}. Inserting this data into equation 6.54, gives a minimum pumping speed of

$$\dot{V}_{pump} \geq 5 \ \ m^3\ s^{-1}.$$

Fortunately this is a readily attainable pumping speed at the a pressure of 50 Pa.

6.4.2 Cesium Supply and Extraction

Extraction

The propellants themselves pose a number of problems for a laboratory experiment. Hydrogen is stored as a liquid so would require cryogenic equipment to store it, but more importantly it is also explosive. When running the thruster the lower the flow of hydrogen the better from a safety point of view. It should also be vented directly to the atmosphere,

so large quantities of hydrogen gas are not kept around.

Dealing with cesium is even more problematic. Cesium is toxic and explosive in the presence of water vapour. Even the moisture in the air could be enough to cause cesium combustion. It is also extremely reactive with carbon dioxide. Consequently cesium most be kept stored under vacuum or under a cover gas of a noble gas or nitrogen. (Nitrogen can not be used as a cover gas for lithium, but is often acceptable for other alkali metals). See reference [83].

To deal with these issues the cesium in the exhaust needs to captured. Since cesium melts at 28.5°C it could easily be cold trapped just using chilled water as a coolant. This could be applied to the vacuum chamber as a whole and simply have the cesium condense on the chamber walls, but this would then create severe problems with cleaning and general operation as you would not be able to open the chamber to the air. Consequently it was thought that the best method of dealing with cesium in the vacuum chamber would be to have a tank within a tank. The inner tank would just be a chilled liner where the majority of the cesium should be captured, and which could be sealed off independently. Opening the main tank would then be possible at any time, and the atmospheric pressure would hold the inner tank tightly shut. The inner tank could then be removed to access the thruster assembly.

For the cesium trap if the trap is cooled to between 0°C and 28.5°C, the cesium will freeze out onto the trap. Being a metal the cesium will not thermally insulate the cold trap, and as such the trap will not lose efficiency as cesium accumulates. Keeping the trap above 0°C will prevent any water vapour present from freezing onto the trap which could be hazardous due to its high reactivity with cesium.

The pumping speed of a cold trap is given by

$$\dot{V}_{cold\ trap} = \frac{\bar{c}}{4}\sqrt{\frac{29}{M}}\left(1 - \frac{P_2}{P_1}\right)A \qquad 1\,\mathrm{s}^{-1}, \tag{6.55}$$

where P_1 is the partial pressure of the gas in the chamber, and P_2 is the partial pressure of the gas at the temperature of the cold plates. If Cs is cooled to a solid state P_2 will be negligible. The thermal speed of the gas in the chamber which is given by $\bar{c} = \sqrt{\frac{8RT}{\pi M}}$, and depends on the temperature the tank is run at.

This gives the pumping speed assuming there is plenty of time for cesium to be captured,

whereas the aim here is to extract the cesium before it enters the main tank and the main pumps. For the thruster exhaust passing over a cold trap to extract the cesium, only the cesium in the boundary layer of the flow will be extracted, and the rest will pass by without encountering the surface. Thus the exhaust should ideally be passed through some sort of labyrinthine passages to extract as much cesium as possible before entering the chamber at large. This means the cesium cold trap should be designed along the lines of a heat exchanger, so it will have a very large surface area for capturing cesium.

If the trap can be fully enclosed such as by having walls with a hinged door on either end, then when the system is cleaned the trap can be closed keeping the cesium contained under vacuum. If the cesium is trapped by freezing it onto the surface of the cold trap, the coolant can then be replaced with hot water to melt the cesium which will then drain down to the bottom of the trap where it could be drained into a collecting can with a closing valve. The collected cesium could then be reused.

There are many different designs of heat exchangers, (see reference [6] for some examples), but it was decided that the simplest method given the containment and draining requirements would be a Shell and Tube design. With this design coolant is passed down tubes placed in a casing through which the propellant would pass, as illustrated in figure 6-40. With the tubes containing coolant mounted vertically, the cesium would then drain off under gravity when the coolant is replaced by hot water. In reality many more tubes would be used, and the trap could be sized to the vacuum tank being used. The tubes would be stacked in an array so the exhaust cannot pass directly through the trap without impinging on many tubes.

For cleaning of the inner chamber or any cesium spills or contamination of the main chamber Mausteller et al. [83] devote an entire chapter to post-operation cleaning techniques. In general this is done by reaction, and given the reactive character of the alkali metals it is important to design the system to minimize any low spots or pockets that will retain pools of cesium. Mausteller recommends that all runs should have a minimum slope of 3° to aid in drainage.

In the cleaning process provision should be made for venting off gas because most of the cleaning agents release hydrogen. The system should also be protected from the atmosphere, and cleaned under an inert atmosphere to exclude oxygen and so minimize the risk of the released hydrogen exploding. Atmospheric contamination can also result in the formation

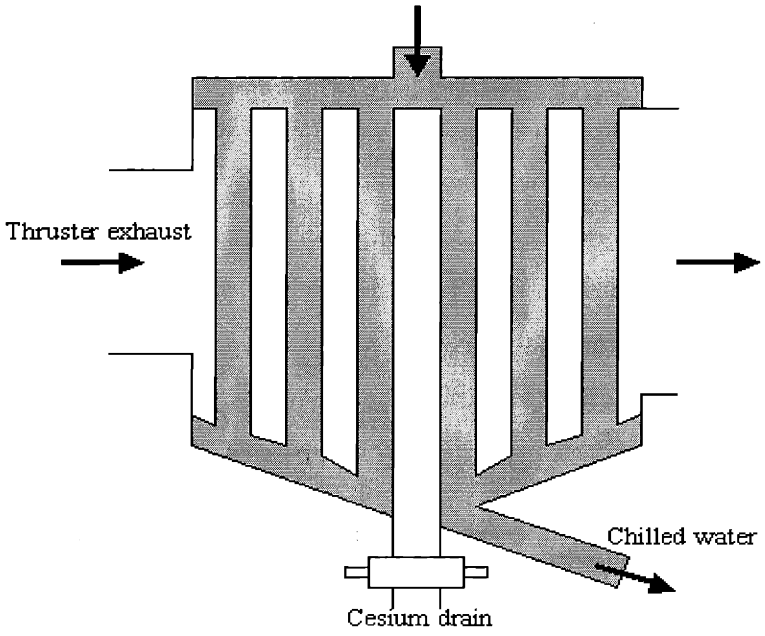

Figure 6-40: *Cold Trap for Cesium Removal.*

of hard crusts over the alkali metal, increasing the difficulty of cleaning.

Cleaning agents are either solvents such as liquid ammonia or reactants such as water, steam, or alcohol. For small systems Mausteller recommends using liquid ammonia. Although it requires refrigeration, no hydrogen is formed and there is no overheating. The colour of the ammonia can also be used as a rough indication of the cleaning process, as it changes from blue with low metal concentrations to a bronze colour with higher concentrations. The solubility of cesium in liquid ammonia is 173g per 100g NH_3 at -33.8°C. Since alkali metals and their hydroxides can cause severe thermal and chemical burns protective clothing is needed, including rubber gloves and eye protection. Simple cotton clothes should suffice although woolen and synthetic clothing should be avoided. Please see reference [83] for more details.

If kept cool, exposing cesium to the atmosphere will not undergo auto-combustion, unlike lithium or sodium. This is because cesium oxide is very soluble in cesium, so no crust is formed, and the cesium slowly turns to a golden hue and then bronze-black. Due to the presence of the oxides, the corrosion of the container will be much more severe than for other alkali metals.

Fires produced by exposing alkali metals to the atmosphere must be extinguished by

the removal of oxygen from the combustion zone. Ideally this would be done by displacing the oxygen with an inert gas but inorganic salts are the most widely used alkali metal fire extinguishants. Displacement with an inert gas minimizes cleanup procedures as no salt alkali-metal mixtures are formed. Any water or carbon dioxide based fire extinguisher must not be used as it would cause an explosion. The salts used must similarly be anhydrous otherwise they may exacerbate the fire rather than extinguish it. Sodium chloride is the most commonly used inorganic salt as it is stable at flame temperatures encountered in alkali metal fires. It is not effective for lithium fires however as it is denser than lithium and will sink to the bottom of any liquid lithium rather than forming a crust to exclude oxygen. For lithium fires, graphite has been used with good success, although graphite should only be used for fighting other alkali metal fires if they are very small. Other inert materials are potential extinguishants, and include resin covered NaCl, soda ash, $CaC0_3$, and polyurethane foam. Again, please see reference [83] for more details.

Supply

Some method of supplying the cesium to the flow is required, which also has to be able to regulate the seeding fraction. Monitoring of the seeding fraction could be done spectroscopically by measuring optical absorption of light tuned to a resonant line of cesium, as explained in section 6.4.3.

One option would be a diffuser composed of a cesium boiler with the hydrogen supply passed over the top. The lower pressure of the faster moving hydrogen would then pull out a stream of cesium vapour. If the passage from the boiler were placed in the structure where the temperature is above the boiling point of cesium (670°C), this would prevent cesium from condensing on the walls. The system would require calibrating of the seeding fraction to the power supplied to the boiler, the hydrogen mass flow rate, and the size of the opening at the top of the boiler. The last quantity would be the most controllable, simply needing an adjustable valve.

The alternative to the system described above, would be to use a mechanical or an electromagnetic pump to pump liquid cesium into the hot region of the thruster where it will boil and then be entrained in the propellant flow. Electromagnetic pumps are a popular choice for pumping alkali metals as they do not penetrate the walls of the system [83]. Current is fed into an electrode attached perpendicular to a magnetic field, and the

induced EMF forces liquid metal through the piping. There are many variations of EM pumps, some of which can be seen in figure 6-41, which all depend on the appropriately phased introduction of current and magnetic fields using either AC or DC.

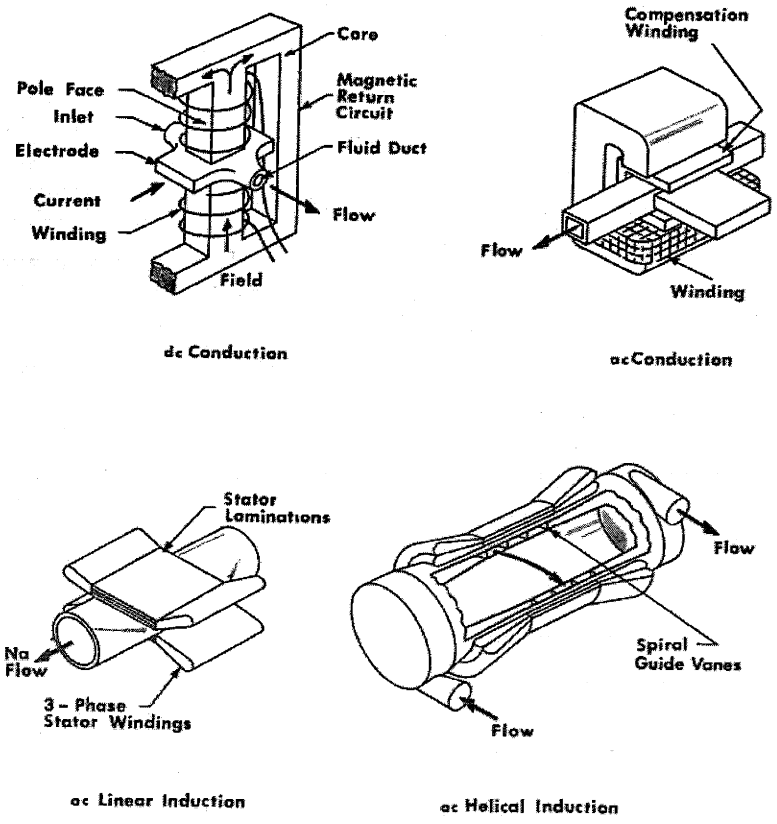

Figure 6-41: *Types of Electromagnetic Pumps.*

Three-phase AC induction pumps work slightly differently. A three phase winding produces a moving magnetic field in the liquid metal, and induces currents. Interaction of the current and magnetic field creates a pumping action.

A couple of Mechanical Induction pumps are shown in figure 6-42. The centrifugal pump works by rotating a set of electromagnets next to a pancake-shaped chamber, with a ring of high temperature magnetic iron on the other side. The helical rotor pump pumps liquid metal through an annulus between two cylinders by a motor driven rotor carrying helical poles.

The materials used for the storage and transfer of cesium are also extremely important due to its highly corrosive nature. The effects of corrosive action depend on the duration of exposure, and on impurities in the cesium which may accelerate or retard the rate of

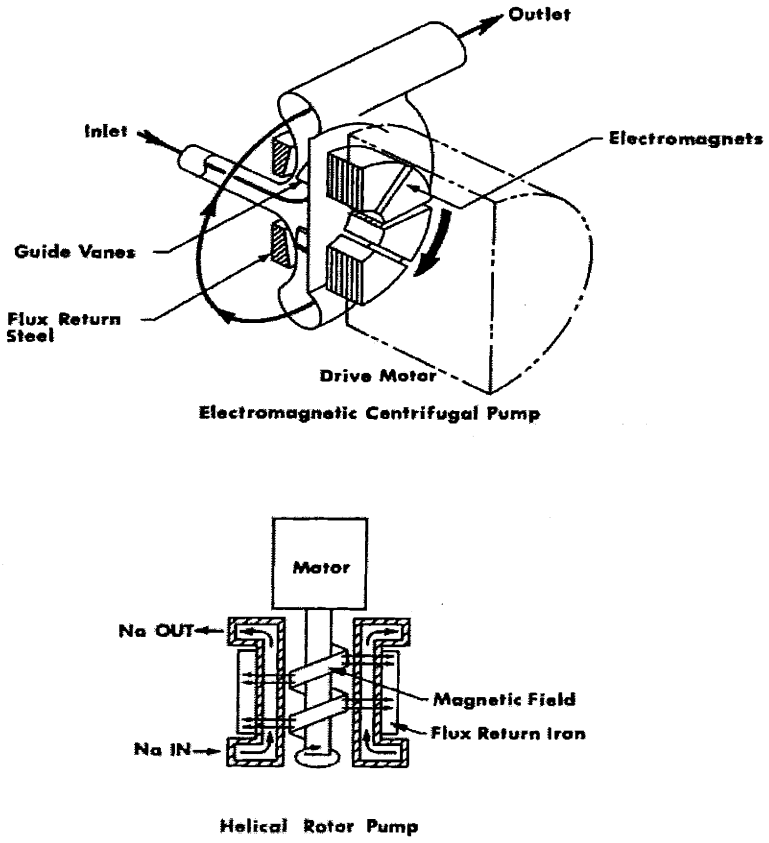

Figure 6-42: *Mechanical Induction Pumps.*

corrosion. The effects of corrosion by cesium can be seen in tables 6.4 and 6.5. [122]

As a rule, cesium at room temperature can be stored in containers made of glass or numerous metals. At elevated temperatures oxygen-free copper, stainless steel (316 and 347), tungsten, tantalum, and molybdenum are recommended. Up to 1300 K, stainless steel 19-9DL, tantalum, and tungsten are still compatible with cesium. In one study the only metal that was not attacked by cesium, even after 7000 hours at 1275 K was tungsten [49]. Consequently the cesium feed system on the arcjet should ideally be made out of tungsten for a spaceflight model. The cold trap however can be made out of one of a number of metals.

2 mmHg vapour pressure for 100 hours at 575 K

Metal	Percentage mass change
Copper	-2.1
Aluminium	-0.76
Silver solder	-0.32
18-8 Stainless	-0.25
Nichrome	-0.12
Nickel	-0.1
Mild steel	-0.04
Brass	+0.13
Porous tungsten	+0.34

Table 6.4: *Corrosive Action of Cesium Vapour on Metals*

2 mmHg vapour pressure for 100 hours at 480 K

Material	Percentage mass change
Nylon cloth	-27.8
Asbestos cloth	-15.7
Teflon	-9.7
Natural rubber	-1.8
Tungsten glass	-0.2
Soft glass	-0.1
Graphite teflon	+0.1
Pyrex glass	+0.2
Zirconium oxide	+0.5
Aluminium oxide	+2.6

Table 6.5: *Corrosive Action of Cesium Vapour on Non-Metals*

6.4.3 Experimental Setup

Mechanical Layout

There are two possible designs for the mechanical layout. The first is a simulated flight model as was simulated in the thermal model of section 6.3. The second is a laboratory test model which may well include features, such as water cooling passages for measuring heat transfer rates, that a flight model would not.

A model of the flight version of the thruster thruster was built in the machine shop at MIT, using aluminium and acrylic to produce a to scale model and examine some of the issues of manufacturing the thruster. Two main difficulties were found in the machining the thruster shown in figure 6-35. The first is the length, and narrowness of the propellant feed pipes. Drilling these with a 1mm diameter bit, has problems because it is difficult to find a drill bit long enough, and to match up the holes if drilled from each direction. A better design would be to split the propellant feed pipe into regions if the material is to be drilled. Alternatively the section with the feed pipe could be split from the outer annulus, and then easily machined, although there may then be leakage and thermal contact problems with the outer casing. The alternative would be to mould the insulator with rods for the feed pipes inserted, and simply removed once the mould had set.

The other problem encountered in machining a model was the constrictor being recessed into the anode block. Drilling out a hole in the back of the anode block is straightforward, but then machining that surface flat on the inside of the relatively narrow hole proved to be difficult. This problem could be easily overcome however by a simple redesign of the thruster to extend the insulator block up to the end of the constrictor, and have a flat interface between the insulator and the anode. A step could be included to aid in fitting together, but this could then be done with a much larger radius.

Glocker et al. [35] built a laboratory test model of an arcjet which would serve as a very useful basis for designing and testing a prototype seeded arcjet. The mechanical layout can be seen in figure 6-43

The TT1 thruster consists of a thoriated tungsten cathode rod with a coaxial ring segments which stack up to build the inlet, constrictor, and nozzle. All the segments are individually water cooled. In order to avoid any unforeseen arcing, the segments are

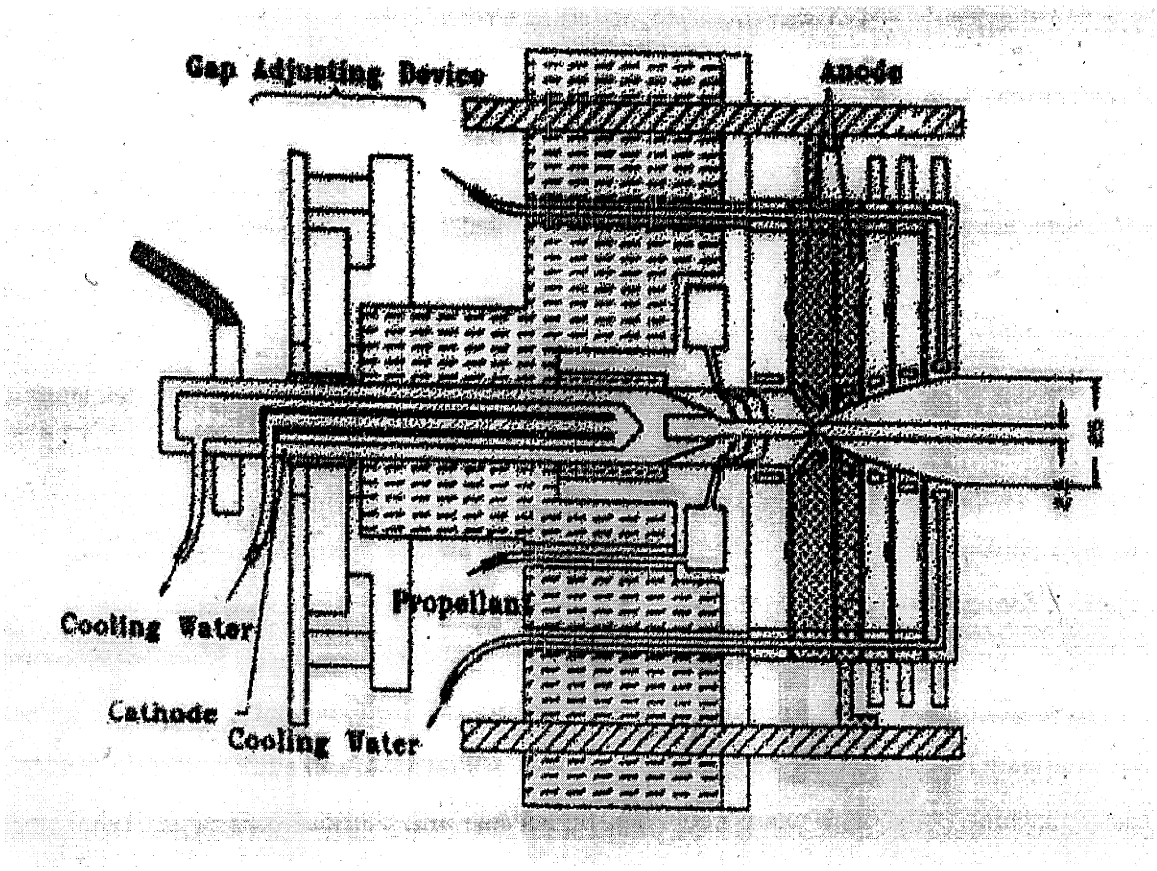

Figure 6-43: *TT1 Thruster.*

insulated from each other by ceramic washers, leaving 0.5 mm between each segment. Any or all of the segments can be connected to form the anode. The propellant enters a ring shaped pre-plenum via a gas supply tube. From there it flows through four bore holes which are oriented tangentially to induce swirl in the flow. In conventional arcjets this swirl helps stabilize the arc, and forces it to attach to the cathode tip. For spot attachment on the anode, swirl also causes the attachment spot to rotate thereby preventing any localised overheating. The constrictor segment is designed as a screwable insert so that it can be easily changed.

For testing the current was supplied by a dozen current regulated power units. The thruster was mounted on a thrust balance and cooling water was supplied through semicircular hoses to minimize stiffness. Thermocouples were inserted into each of the water tubes for each segment to measure the temperature difference between the inlet and outlet. From this the heat flux into each segment can be calculated given the mass flow rate of the water.

The modifications required for the seeded arcjet would basically be the addition of the

cesium supply system, and the extension of the constrictor. The constrictor segments would have to be built of an insulator such as boron nitride.

The individual segments of the constrictor and nozzle allow a great deal of information to be gained about the heat fluxes and current distributions, and also easily allow for changes in the geometry. Inserting a quartz window for taking spectroscopic measurements for example would be straightforward, as would including strips of boron nitride between the blocks to electrically insulate them. A similar setup to that used by Curran et al. [23], for which the circuit diagram is shown in figure 2-2, and some results in figure 2-3, could then be used for current distribution measurements.

Spectroscopic Diagnostics

For the plasma diagnostics, three important quantities to be measured are the electron temperature and number density, and the cesium concentration. This can be done spectroscopically as explained by Sharma [117].

During the discharge some electrons recombine with cesium ions and emit continuum radiation. The intensity of the radiation at a given wavelength is related to the electron number density, the cesium ion number density, and the electron temperature by

$$I_\nu \propto \frac{n_e^2}{T_e^{\frac{3}{2}}} \left(\exp\left(\frac{hc}{kT_e} \left(\lambda_{6P}^{-1} - \lambda^{-1} \right) \right) + 2.22 \exp\left(\frac{hc}{kT_e} \left(\lambda_{5D}^{-1} - \lambda^{-1} \right) \right) \right), \tag{6.56}$$

where I_ν is proportional to the continuum radiation from the plasma and $\lambda_{6P,5D}$ are the wavelengths of the lower levels of the electron transitions from the continuum. See reference [117] for a derivation. If the radiation is monitored at two wavelengths, then the ratio of intensities is

$$\frac{I_{\nu 1}}{I_{\nu 2}} \propto \frac{\exp\left(\frac{hc}{kT_e} \left(\lambda_{6P}^{-1} - \lambda_1^{-1} \right) \right) + 2.22 \exp\left(\frac{hc}{kT_e} \left(\lambda_{5D}^{-1} - \lambda_1^{-1} \right) \right)}{\exp\left(\frac{hc}{kT_e} \left(\lambda_{6P}^{-1} - \lambda_2^{-1} \right) \right) + 2.22 \exp\left(\frac{hc}{kT_e} \left(\lambda_{5D}^{-1} - \lambda_2^{-1} \right) \right)} \tag{6.57}$$

which may be used to calculate the electron temperature. This can then be substituted back into 6.56 to find the electron number density.

Sharma monitored the radiation at 4904Å and 4285Å, and used a spectral lamp (GE 6.6A/T4Q/1CL-200W) to calibrate the radiation recording system, the fibre optics, and the photomultiplier tubes.

Sharma measured the cesium concentration by measuring optical absorption of light tuned to a resonant line of cesium at 4550Å. Using a cesium spectral lamp the amplitude of the resonant line was compared directly from the lamp to that passed through the plasma. The difference in amplitude directly gives the cesium concentration. To minimize noise and record a reference on each oscilloscope trace, the light from the spectral lamp was chopped at about 15 kHz. The optical arrangement is shown in figure 6-44. The housing of the lamp is heated to maintain the cesium vapour in the lamp at the same temperature at which calibration was done. For calibration two quartz test chambers were sealed off as shown in figure 6-45.

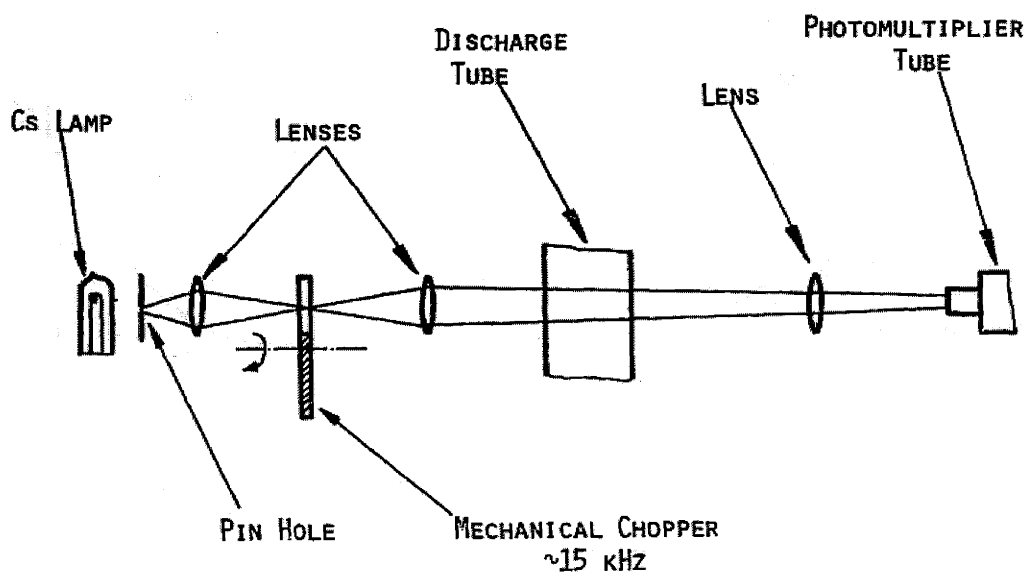

Figure 6-44: *Cesium Diagnostic System.*

This and a host of other methods for diagnosing the properties of a plasma can be found in reference [52], "Principles of Plasma Diagnostics".

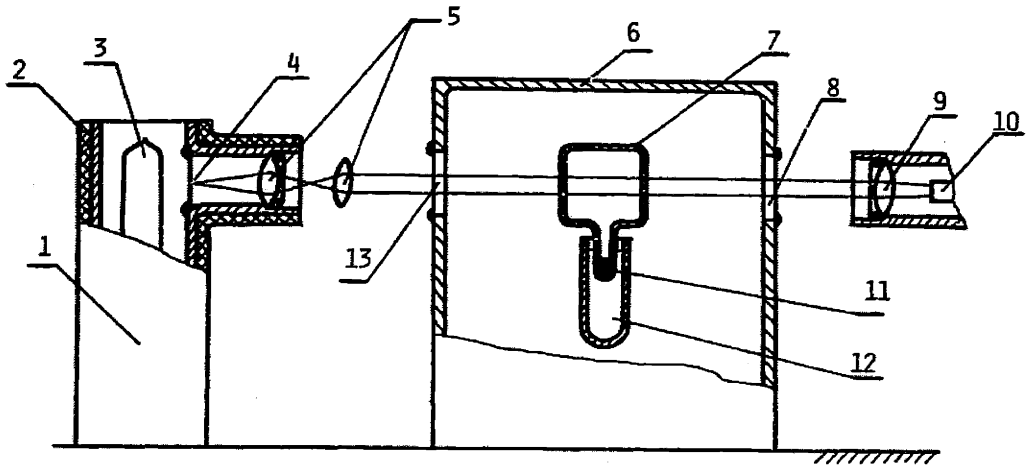

Cs Absorption Diagnostics Calibration Experiment

1. Lamp Holder
2. Heating Tape & Insulator
3. Cs Lamp
4. Pin Hole
5. Lenses
6. Oven
7. Test Chamber
8. Quartz Window
9. Lens
10. Photomultiplier Tube
11. Cs Pool
12. Oil Bath
13. Quartz Window

Figure 6-45: *Calibration of Cs Absorption Diagnostics.*

Chapter 7

Mission Analysis

The aim of this chapter is examine in more detail the potential use of a seeded arcjet thruster. With the thruster as designed using hydrogen as a propellant, cryo tanks will be required as well as a cryostat, consuming power and weight. For a given mission the aim would be to minimize the mass of the propulsion system, and thereby maximize the mass of the payload.

An alternative would be to not cool the hydrogen, but instead once the thruster is switched on it wouldn't be switched off until the propellant had run out. The requirement would then be that the mass flow rate into the thruster (the fuel consumption) be greater than the evaporation rate (which could be controlled by insulation). This would save on the weight of the cryostat, but limit operation to missions such as orbital insertion at the beginning of a spacecraft's life.

Another alternative would be to use a propellant which does not require cryogenic storage. Methane, ammonia, and hydrazine are popular choices of arcjet propellants which could all be seeded with cesium. Argon is another popular arcjet propellant, and could be easily pre-mixed with xenon seeding as both are noble gases. Helium would give better performance than argon, but again is a cryogenic fuel. Since none of these combinations has yet been numerically modelled to find their performance in a seeded arcjet, they will not be analysed here. Other than ammonia the likelihood is too low I_{sp} since $T_g \leq 4000K$, and the molecular mass should be small.

Traditionally costs of things like the satellite launch mass, power requirement, and time for orbital insertion are treated in a linear fashion with a cost per unit mass, power, or

time. This fails to take into account how satellites are really built and operated. [90]. The launch vehicle used specifies the maximum mass of the satellite that can be used, and the launch cost steps up when the next size launcher is required, rather than having a linear relationship.

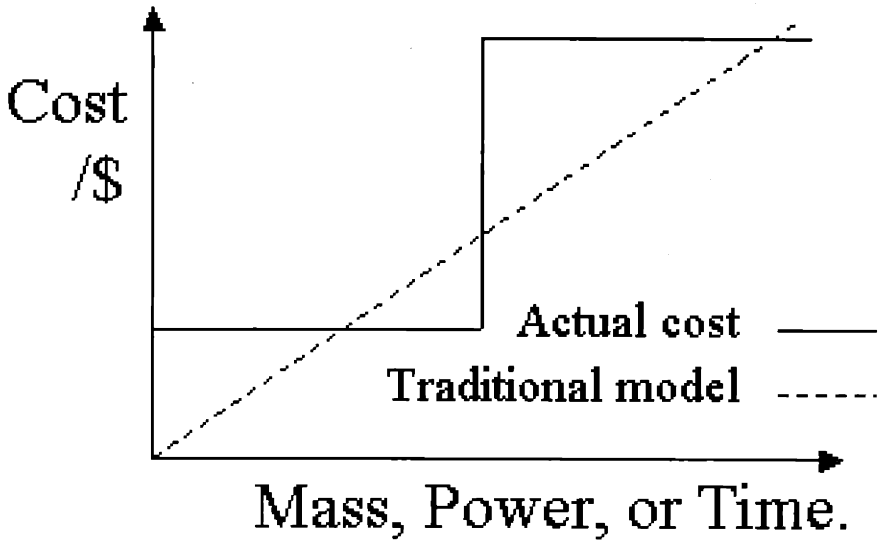

Figure 7-1: *Actual Costs of Satellite Mass, Power, and Mission Time.*

Similarly for the cost of power, a linear relationship is valid when the electric propulsion dominates the power budget for the mission, but in practice commercial missions use excess power for orbit raising. Providing additional power beyond that is very expensive so is not acceptable for commercial missions. Since real missions use excess power for manoeuvres, it can assumed that the power demands will be met by the power to be used later for the payload. Thus the power requirement will not contribute to the cost or weight of the propulsion system since it will be on board anyway.

The same argument applies for the time required for orbital insertion. Most commercial missions are constrained by cash flow, and have a fixed need date, rather than the insertion costing more the longer it takes. Thus any gains from a shorter mission time should be ignored.

The arguments above effectively remove any monetary arguments from the study, and the mission analysis reduces to maximizing the payload mass by minimizing the mass of

the propulsion unit.

7.1 Traditional Mission Study

7.1.1 Electric Mission Theory

Traditional analysis of electric thruster missions assume they are powered separately rather than making synergistic use the power plant for the whole spacecraft, and assume either constant thrust or constant acceleration [122]. Consider a constant power and thrust mission with a prescribed duration. The final mass of the spacecraft is given by the rocket equation:

$$\frac{m_f}{m_o} = e^{-\Delta V/c}, \tag{7.1}$$

where m_f is the final mass, m_o the original mass, ΔV the required change in velocity, and c the exhaust velocity. The propellant mass is thus

$$m_p = m_o(1 - e^{-\Delta V/c}). \tag{7.2}$$

With a separately power thruster the structural mass is comprised of a part m_{so} independent of the power level plus a part αP, with α the mass per unit power of the powerplant of power P. The power can be described in terms of the jet kinetic power, and an efficiency as

$$P = \frac{\frac{1}{2}\dot{m}c^2}{\eta_p}. \tag{7.3}$$

For constant power and thrust flight $\dot{m} = m_p/t$, so

$$m_s = m_{so} + \frac{\alpha}{2\eta_p}\frac{m_p}{t}c^2. \tag{7.4}$$

The payload mass is $m_l = m_f - m_s$, hence

$$\frac{m_l}{m_o} = e^{-\Delta V/c} - \frac{m_{so}}{m_o} - \frac{\alpha c^2}{2\eta_p t}(1 - e^{-\Delta V/c}). \tag{7.5}$$

Figure 7-2 shows $\frac{m_l}{m_o}$ vs. $\frac{c}{v_p}$, where v_p is defined as

$$v_p = \sqrt{\frac{2\eta_p t}{\alpha}}. \tag{7.6}$$

If $\frac{\Delta V}{c}$ is a small quantity then by expanding the exponentials in equation 7.5 the optimum

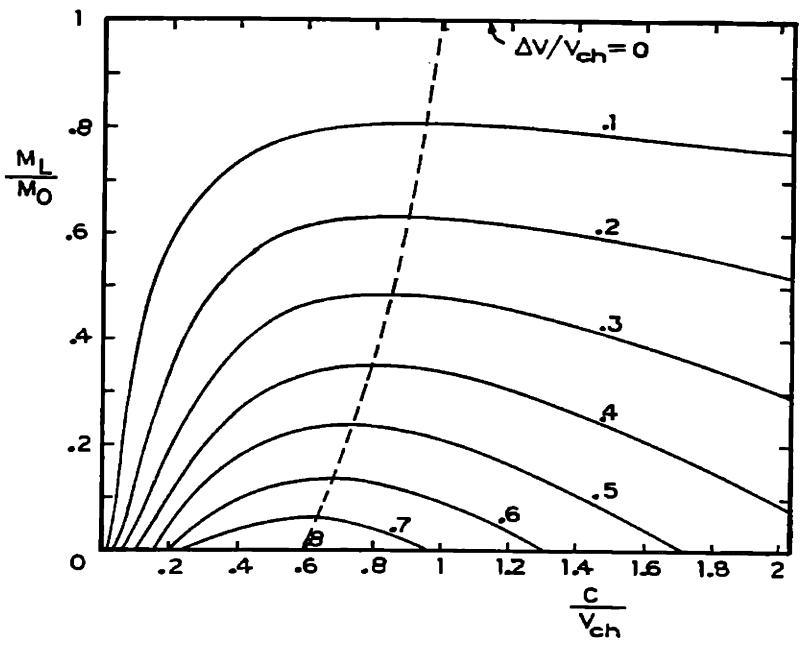

Figure 7-2: *Payload Fraction vs. Specific Impulse.*

exhaust velocity is

$$c_{opt} \approx v_p - \frac{\Delta V}{2} \tag{7.7}$$

and

$$\left(\frac{m_l}{m_o}\right)_{max} \approx \left(1 - \frac{\Delta V}{c}\right)^2 . \tag{7.8}$$

Figure 7-2 also shows that the maximum ΔV for which any payload can be carried is about 0.8 v_p.

Figure 7-3 then shows the mass breakdown for the optimum c.

The effects of power plant mass per unit power, propulsive efficiency of the thruster, and mission time are all accounted for in the characteristic velocity v_p. Equation 7.7 therefore shows that for a light power plant and/or a long mission duration, that a high specific impulse is better. ($I_{sp} = c/g$, with the acceleration due to gravity, g = 9.8 m s^{-2}). From figure 7-3 it can then be seen that with a long mission time and a high I_{sp}, a high mass fraction can be the payload. Conversely with a short mission time and a low I_{sp}, only a small mass fraction will be payload, and the majority will be propellant.

These results however assume a constant efficiency, whereas in general the efficiency is

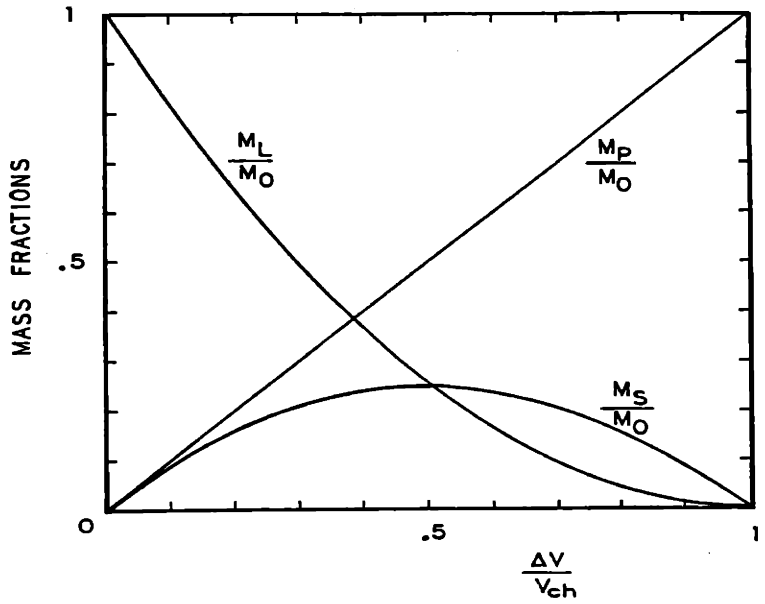

Figure 7-3: *Mass fractions at Optimum Exhaust Velocity.*

a function of the specific impulse. This function also depends upon the type of thruster being used. For ion engines and MPD thrusters the efficiency increases with c, whereas in arcjet it typically decays beyond a certain c.

In ion engines for example, the ions are accelerated through a voltage drop $\Delta\phi$, and so the energy spent per ion is $\frac{1}{2}m_ic^2 + e\Delta\phi$, where m_i si the mass of the ion, and e the charge on the electron. Of the energy spent only $\frac{1}{2}m_ic^2$ is thrust. Thus the efficiency can be written as

$$\eta_p = \eta_o \frac{c^2}{c^2 + \frac{2e\Delta\phi}{m_i}}. \tag{7.9}$$

The effect this has on the optimization is to increase the optimum c to take advantage of the higher efficiency. This reduces the fuel fraction, but increases the structural fraction due to the increased size of the power plant. This in turn reduces the maximum possible payload. However for long flight time missions, these losses are felt the least.

For MPD thrusters, the losses are much more complicated, but a simple equation useful for curve fitting experimental data can be obtained as follows: The thrust is usually dominated by the electromagnetic component so $F = bI^2$, where I is the discharge current, and b is a constant of order 10^{-7} N A^{-2}. The jet velocity is $c = bI^2/\dot{m}$, so the jet power is $P_{jet} = \frac{1}{2}\dot{m}c^2$. The ohmic power dissipated is $P_\Omega = RI^2 = \dot{m}cR/b$. Thus for an MPD

thruster the efficiency can be written as

$$\eta_p = \frac{\eta_o}{1 + \frac{2R}{bc}}. \tag{7.10}$$

7.1.2 LEO-GEO Mission Study

Mission	ΔV / km s^{-1}
Earth Surface to LEO	7.6
LEO to GEO	4.2
LEO to GEO with 28.5° plane change	5.2
LEO to Earth Escape	3.2
LEO to Lunar Orbit (7 days)	3.9
LEO to Mars Orbit (0.7 years)	5.7
LEO to Mars Orbit (40 days)	85.0
LEO to Neptune Orbit (29.9 years)	13.4
LEO to Neptune Orbit (5.0 years)	70.0
LEO to Solar Escape	8.7
LEO to 1000 AU (50 years)	142.0
LEO to Alpha Centauri (50 years)	30000.0

Table 7.1: *Typical Mission Velocity Requirements using Impulsive Burns.*

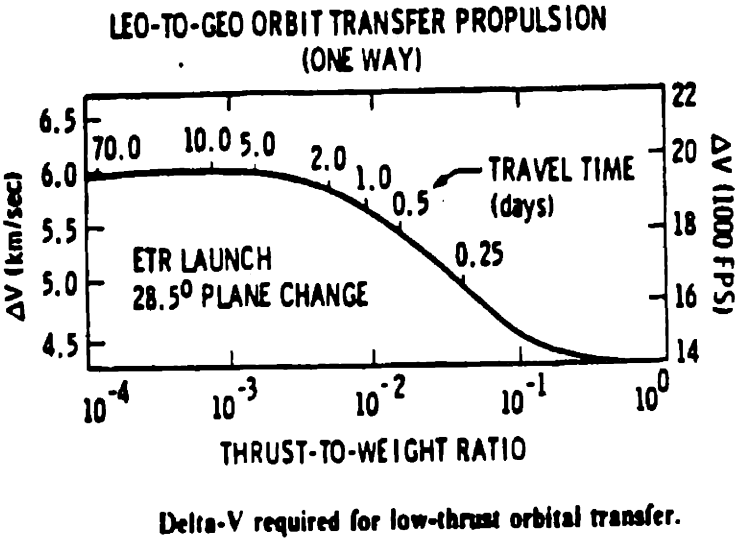

Figure 7-4: *LEO-GEO ΔV variation with time taken.*

This section presents an example of a mission study for a LEO to GEO orbit raising with a 28.5° plane change, as is typically used for satellites launched from within the continental United States. This work closely follows that of Kaufman and Robinson as presented in reference [62].

First some performance data was required for any propulsion system to be modelled. For ion engines, MPD thrusters, and arcjets this was taken from reference [62], although the efficiency of a conventional arcjet was reduced to 35%, more in line with current performance. For the seeded arcjet, the same data was used but with an efficiency of 80%, and a slightly increased mass per unit power to account for the cesium supply. Finally data for Hall (SPT) thrusters was added from reference [11]. The efficiency data is shown in figure 7-5.

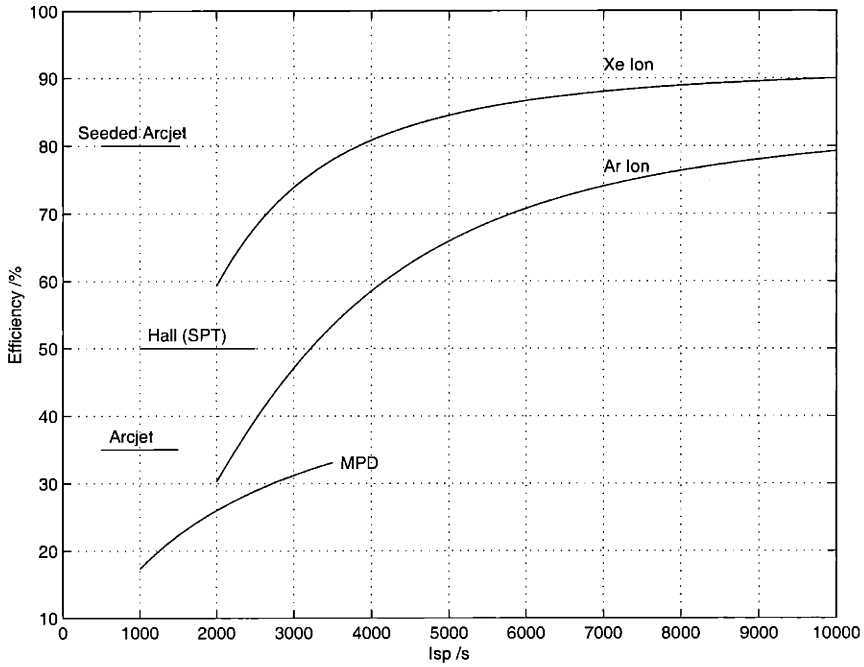

Figure 7-5: *Efficiencies of Various Electric Thrusters.*

A mass of 0.1 times the initial mass is assumed for the required structure, guidance, tanks, etc, and the masses of the propulsion systems are summarized in table 7.2

Ion Engine	Thruster	Table 7.3
1500<Isp<10000	Power Processor	$\eta_{ppu} = 0.9$ 10 kg/kW
	Power Source	15 kg/kW
	Other	5 kg/kW
MPD	Thruster	Table 7.4
1000<Isp<3500	Power Processor	$\eta_{ppu} = 0.9$ 2.5 kg/kW
	Power Source	15 kg/kW
	Other	2.5 kg/kW
Arcjet	Thruster	$\eta_p = 0.35$ 2.5 kg/kW
500<Isp<1200	Power Source	15 kg/kW
	Other	2.5 kg/kW
Seeded Arcjet	Thruster	$\eta_p = 0.80$ 2.5 kg/kW
500<Isp<1200	Power Source	15 kg/kW
	Other	5.0 kg/kW
Hall	Thruster	$\eta_p = 0.50$ 3.0 kg/kW
1000<Isp<3000	Power Processor	$\eta_{ppu} = 0.9$ 2.5 kg/kW
	Power Source	15 kg/kW
	Other	2.5 kg/kW

Table 7.2: *System Specific Masses and Efficiencies.*

	Argon		Xenon	
I_{sp} /s	Efficiency η_p	Specific Mass / kg/kW	Efficiency η_p	Specific Mass / kg/kW
1462	0.251	4.34	0.469	7.12
1950	0.328	3.32	0.589	3.36
2438	0.400	2.47	0.672	2.68
2925	0.466	1.88	0.731	2.16
3900	0.570	1.57	0.806	1.50
4875	0.647	1.30	0.848	1.11
5850	0.704	1.11	0.874	0.90
6825	0.746	0.96	0.891	0.73
7800	0.779	0.84	0.902	0.61
9750	0.824	0.67	0.918	0.47

The efficiency data is fitted very well by equation 7.9 with

Ar: $\Delta\phi = 150\ V$, $\eta_o = 0.85$

Xe: $\Delta\phi = 150\ V$, $\eta_o = 0.92$,

so these curve fits were used.

The specific masses also curve fit well to functions of the form $y = \frac{A}{x} + \frac{B}{x^2}$.

Table 7.3: *Ion Engine Efficiencies and Specific Masses.*

I_{sp} /s	Efficiency η_p	Specific Mass / kg/kW
1000	0.18	2.25
1200	0.20	2.25
1500	0.22	2.25
2000	0.25	2.25
2500	0.29	2.25
3000	0.31	2.25
3500	0.32	2.25

The efficiency data is fitted very well by equation 7.10 with $b = 10^{-7}$ N A^{-2}, and $R = 10^{-3}\Omega$.

Table 7.4: *MPD Efficiencies and Specific Masses.*

The ΔV requirement is 5.2 km s^{-1} for impulsive burns as would be done with chemical propulsion, and 5.9 km s^{-1} for a low thrust mission.

The first step was to calculate the mass to power ratios for the propulsion system as a whole, using the data from table 7.2.

$$\alpha = \frac{M}{P} = M_{powersupply} + M_{processor} + M_{other} + \frac{M_{thruster}}{\eta_{ppu}}. \tag{7.11}$$

Next the thrust to mass ratio was calculated. From Newton's Second Law $F = \dot{m}c$, and power is given by equation 7.3. Combining these with a little algebra gives the thrust to mass ratio,

$$\frac{F}{m} = \frac{2\eta_p}{\alpha c}. \tag{7.12}$$

The thrust to mass ratios calculated are plotted in figure 7-6. This reproduces figure 1 from Kaufman and Robinson [62], with seeded arcjets and Hall thrusters added. For a given thrusting time, hence same vehicle acceleration, the thruster with the highest thrust to mass ratio will have the lowest propulsion system mass and hence highest payload mass. The propellant mass is not included since for two spacecraft with the same initial mass, thrust, and acceleration, the propellant mass will be the same.

For the mission study itself, two steps are required. The first is to find the optimum specific impulse for a given mission duration and ΔV, which in this case is 5.9 km s^{-1}. For a given ΔV and duration, the optimum I_{sp} was found numerically from the maximum of the payload mass, $\frac{m_l + m_{so}}{m_o}$, in equation 7.5. A mass of $m_{so} = 0.1 m_o$ was then subtracted.

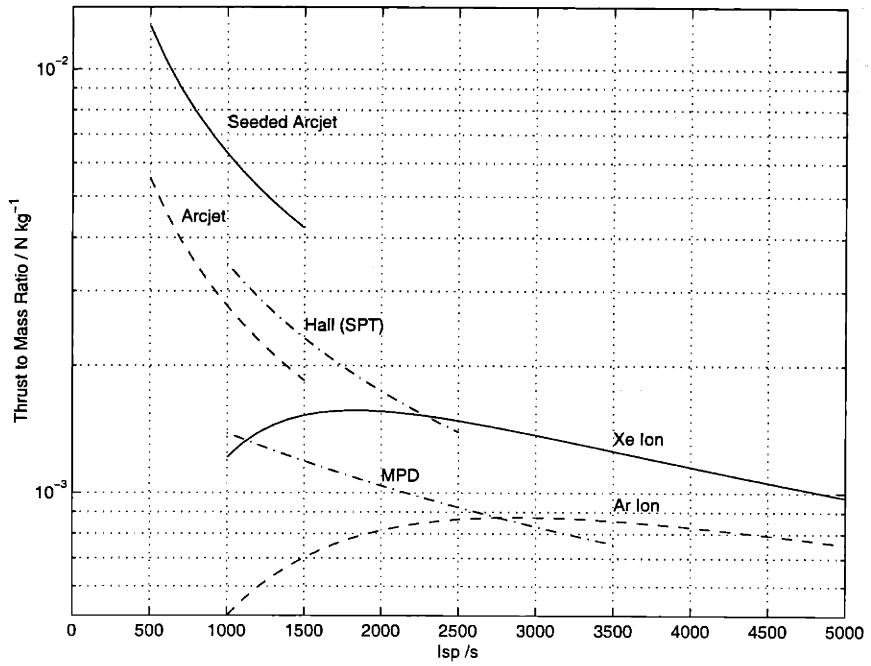

Figure 7-6: *Thrust to Mass Ratios of Electric Thrusters.*

The second step is to scan across a range of mission times, which in this study was from 10 to 300 days. The results are shown in figures 7-7 and 7-8.

It should be noted that a chemical propulsion system can deliver a payload fraction of about 0.25. Figure 7-7 therefore shows that up to a mission time of about 40 days, a chemical system will deliver the most payload. For mission times of 40 to 160 days, the seeded arcjet gives the best performance, and for longer missions, the high I_{sp} of the ion engine finally pays off the best. This also reproduces figure 2 from Kaufman and Robinson [62].

Figure 7-8 shows the results if the power source is considered part of the payload, which can be a reasonable assumption given the power demands of many payloads. Here chemical thrusters are best up to about 15 day missions, after which the seeded arcjet is best up to 80 days. For 80 to 160 days the Hall thruster is the best option, after which the ion engine takes over.

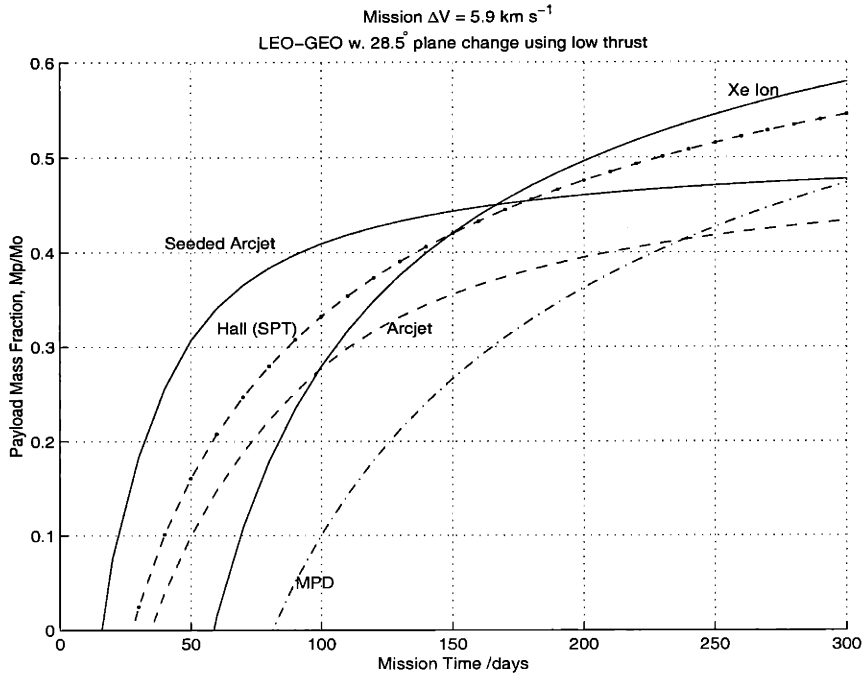

Figure 7-7: *Payload delivered with propulsion unit having its own power source.*

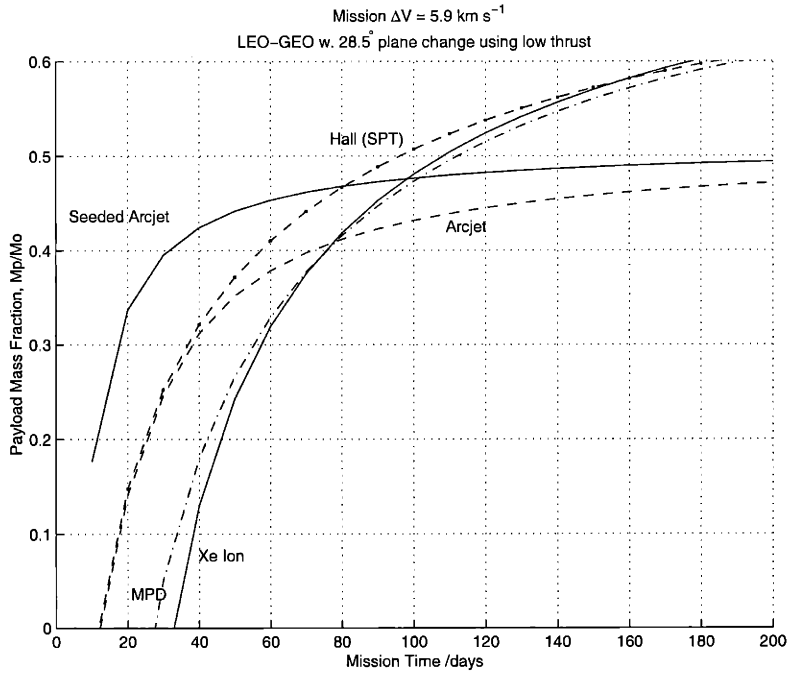

Figure 7-8: *Payload delivered with power source considered part of payload.*

7.2 Combined Chemical and Electric Mission Study

7.2.1 Combined Mission Theory

Following Oh's optimization of combined chemical and electric missions in reference [90], the chemical stage of a mission is done first and the remainder completed with electric propulsion.

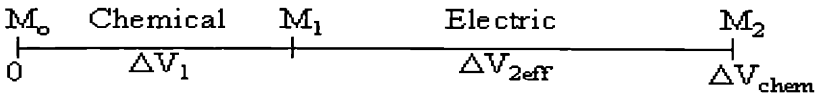

For example a LEO (Low Earth Orbit) to GEO (Geostationary Earth Orbit) might be done by a chemical boost to an intermediate orbit with an exhaust velocity of 3100 m s^{-1} and lasting one orbit, followed by an electric orbit raising at 10 kW and lasting 90 days.

For a chemical only mission it is governed by the rocket equation (Eqn 7.1). For a chemical orbit raising the minimum ΔV is given by the Hohmann transfer

$$\Delta V_{Hohmann} = \sqrt{\frac{GM}{r_1}}\left(\left(\frac{2r_2}{r_1+r_2}\right)^{\frac{1}{2}}\left(1-\frac{r_1}{r_2}\right)+\left(\frac{r_1}{r_2}\right)^{\frac{1}{2}}-1\right). \tag{7.13}$$

For a combined chemical/electric mission, the actual ΔV required can be written in terms of the ΔV required if the mission were done completely by chemical means. The total mission requires ΔV_{chem} if done completely by chemical propulsion. The first stage of the mission is done by a chemical thruster and requires ΔV_1. The remaining stage if also done by chemical thruster requires ΔV_{2eff}, but if done by an electric thruster requires

$$\Delta V_2 = \frac{\Delta V_{2eff}}{\eta_v}, \tag{7.14}$$

where η_v is the mission planning efficiency. Now,

$$\Delta V_{chem} = \Delta V_1 + \Delta V_{2eff}. \tag{7.15}$$

Using the rocket equation 7.1

$$\frac{m_1}{m_0} = e^{-\Delta V_1/c_1}, \qquad \frac{m_2}{m_1} = e^{-\Delta V_2/c_2}, \tag{7.16}$$

so

$$\Delta V_{chem} = c_1 \ln\left(\frac{m_0}{m_1}\right) + \eta_v c_2 \ln\left(\frac{m_1}{m_2}\right). \tag{7.17}$$

With the beam power defined as

$$P = \frac{\frac{1}{2}\dot{m}_2 c_2^2}{\eta_p}, \tag{7.18}$$

and the mass flow

$$m_2 = m_1 - \dot{m}_2 t, \tag{7.19}$$

then

$$\frac{\Delta V_{chem}}{c_1} = \ln\left(\frac{m_0}{m_2 + \frac{2\eta_p P t}{c_2^2}}\right) + \frac{\eta_v c_2}{c_1} \ln\left(\frac{m_2 + \frac{2\eta_p P t}{c_2^2}}{m_2}\right), \tag{7.20}$$

so

$$\exp\left(-\frac{\Delta V_{chem}}{c_1}\right) = \frac{m_2}{m_0}\left(\frac{1}{\frac{\eta_p P t}{\frac{1}{2}m_2 c_2^2} + 1}\right)^{\left(\frac{\eta_v c_2}{c_1} - 1\right)}. \tag{7.21}$$

Equation 7.21 is the rocket equation for a combined chemical/electric mission. For chemical only this would be

$$\exp\left(-\frac{\Delta V_{chem}}{c_1}\right) = \frac{m_2}{m_0}$$

so the term

$$\left(\frac{1}{\frac{\eta_p P t}{\frac{1}{2}m_2 c_2^2} + 1}\right)^{\left(\frac{\eta_v c_2}{c_1} - 1\right)}$$

represents any savings to be gained by using electric propulsion.

The optimum I_{sp} is given at $\frac{dm_2}{dc_2} = 0$. For a short flight time with $\frac{\eta_p P t}{\frac{1}{2}m_2 c_2^2} \ll 1$, using the binomial expansion $(1+x)^n \approx 1 + nx$ and rearranging,

$$m_0 e^{-\Delta V_{chem}/c_1} = m_2 + \frac{B}{c_2^2} - \frac{AB}{c_2}, \qquad A \equiv \frac{\eta_v}{c_1}, \qquad B \equiv 2Pt\eta_p. \tag{7.22}$$

Differentiating this and solving for c_2 yields the

$$\text{short flight time optimum } c_2 = \frac{2c_1}{\eta_v}. \tag{7.23}$$

The general solution is given by

$$2B(1 - Ac_2) + c_2(AB + Am_2c_2^2) \ln\left(\frac{B}{m_2c_2^2} + 1\right) = 0, \tag{7.24}$$

which can be solved numerically. Oh [90] plotted I_{sp} vs. time and η_v for a given m_2, P, η_p, c_1, ΔV_{chem}, which is shown in figure 7-9 for the conditions below:

m_2	4000 kg
Power	10 kW
η_p	0.5
I_{sp}	310 s
ΔV_{chem}	1800 m s^{-1}

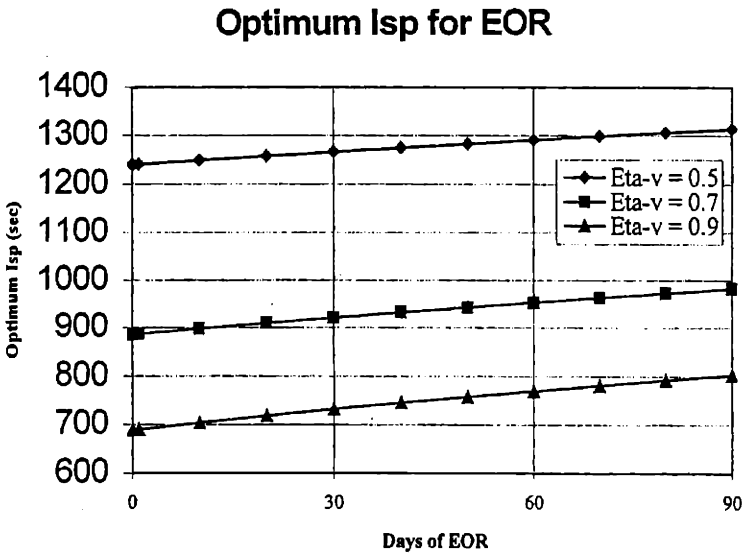

Figure 7-9: *Optimum I_{sp} for Combined Chemical/Electric Missions.*

Oh also plotted the mass delivered to orbit vs specific impulse in figure 7-10 for the conditions:

m_0	6000 kg
Power	10 kW
time	90 days
c_1	3100 m s^{-1}
ΔV_{chem}	1800 m s^{-1}
η_v	0.5
η_p	0.5

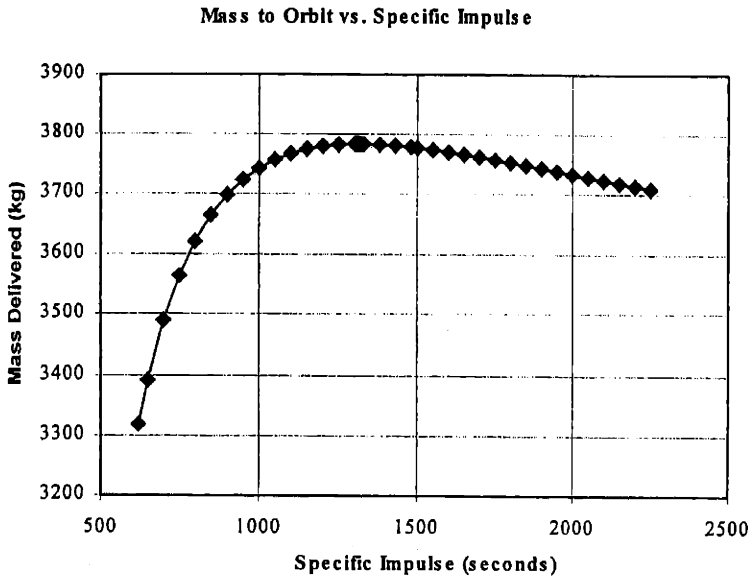

Figure 7-10: *Mass Delivered into Orbit vs. Specific Impulse.*

7.2.2 LEO-GEO Combined Mission Study

This section presents a similar mission study to that done in section 7.1.2. The major difference is that to simplify calculation of the mission planning efficiency (equation 7.14), the 28.5° plane change was omitted. Also due to the structure of the equations, specific values were chosen for the power and initial mass.

For a combined chemical and electric mission, the simplest thing to take most advantage of both systems seemed to be a Hohmann transfer to an intermediate orbit followed by a low thrust spiral out to the final radius. Many other options are available but for now the study was restricted to this mission plan.

The ΔV for circular coplanar orbit raising using continuous low thrust can be calculated as follows. Applying the thrust, F, along the flight path of a vehicle of mass, m, the energy per unit mass is increased at a rate Fv/m, so

$$\frac{d}{dt}\left(-\frac{GM}{2r}\right) = \frac{F}{m}v. \tag{7.25}$$

With low thrust the orbital speed is $\sqrt{\frac{GM}{r}}$, therefore,

$$\sqrt{\frac{r}{GM}}\frac{d}{dt}\left(-\frac{GM}{2r}\right) = \frac{F}{m} = \frac{1}{2}\sqrt{\frac{GM}{r^3}}\frac{dr}{dt}. \tag{7.26}$$

Thus

$$\sqrt{\frac{GM}{r}} = -\int \frac{F}{m}dt + Const. \tag{7.27}$$

Now $\int_o^t \frac{F}{m}\ dt$ is the ΔV for the manoeuvre, which is related to the fuel consumption by $\Delta V = c\ \ln\left(\frac{M_o}{M(t)}\right)$. Hence

$$\Delta V_{low\ thrust} = \sqrt{\frac{GM}{r_1}} - \sqrt{\frac{GM}{r_2}}. \tag{7.28}$$

For an orbital radius ratio, $\rho = r_2/r_1$, and velocity at the lower radius $v_1 = \sqrt{\frac{GM}{r_1}}$, the Hohmann and Low Thrust ΔVs can be written as,

$$\text{Hohmann} \quad \frac{\Delta V_H}{v_1} = \sqrt{\frac{2\rho}{1+\rho}} + \frac{1-\sqrt{\frac{2}{1+\rho}}}{\sqrt{\rho}} - 1, \tag{7.29}$$

$$\text{Low Thrust} \quad \frac{\Delta V_{LT}}{v_1} = 1 - \frac{1}{\sqrt{\rho}}. \tag{7.30}$$

This difference is not much until large ratios are reached. Some values are given in table 7.5.

ρ	1	1.1	1.5	2	4	6.3
$\Delta V_H/V_1$	0	0.04651	0.1816	0.2845	0.4487	0.5036
$\Delta V_{LT}/V_1$	0	0.04654	0.1835	0.2929	0.5000	0.6015

Table 7.5: ΔV *for Hohmann and Low Thrust Transfers.*

In Oh's system of equations ΔV_{chem} is defined as the ΔV for the mission if it were done

completely by chemical propulsion, and ΔV_{2eff} is defined as the ΔV for the second stage if it were done by chemical thrusters. Consequently for the LEO-GEO orbit raising under consideration it is important to know the total ΔV for reaching GEO using two successive Hohmann transfers. Using a final $r_2 = 6.3r_0$, and an intermediate orbit at r_1, the total ΔV is plotted in figure 7-11.

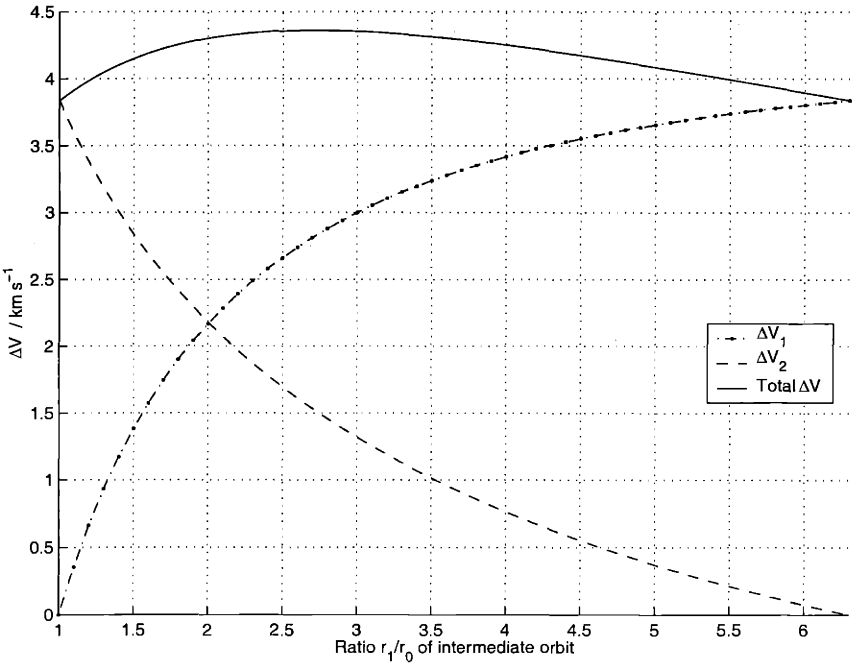

Figure 7-11: *Total ΔV for LEO-GEO using two Hohmann Transfers.*

The mission study then proceeded using the following algorithm:

Step 1. Specify the mission duration, initial mass, and power.

Step 2. Guess a planning efficiency η_v, and total ΔV.

Step 3. Guess an optimum Isp.

Step 4. Calculate the mass delivered into orbit, m_2. This can be obtained from the combination equation 7.21, rearranged to give $\frac{m_2}{m_0}$, and solved iteratively.

$$\frac{m_2}{m_0} = \frac{e^{-\Delta V_{chem}/c_1}}{\left(\frac{\eta_p P t}{\frac{1}{2} m_2 c_2^2} + 1\right)^{\left(1-\frac{\eta_v c_2}{c_1}\right)}}. \tag{7.31}$$

Step 5. Subtract off the mass of the propulsion system $= \alpha P$, as in the traditional mission study, to obtain the useful payload.

Step 6. Repeat steps 3 to 5 scanning over Isp, to obtain the Isp which maximizes the

payload.

Step 7. At the optimum Isp, calculate ΔV_1, using

$$\Delta V_1 = c_1 \ln\left(\frac{m_0}{m_2 + \frac{2\eta_p P t}{c_2^2}}\right) \tag{7.32}$$

Step 8. Given ΔV_1, calculate ΔV_{2eff} and ΔV_{chem}, as in figure 7-11. Calculate the low thrust ΔV from equation 7.30, and then η_v using equation 7.14.

Step 9. Repeat steps 3 to 8 using the new values of η_v and ΔV_{chem}, until a converged solution is obtained.

The chemical exhaust velocity was taken to be 3100 m s^{-1}, and a Xenon Ion Engine, Seeded Arcjet, and Hall Thruster were modelled. For an initial mass of 6000 kg, and a power of 10 kW, the result is shown in figure 7-12. It should be noted however that the payload fractions here are 0.1 higher than in the study in section 7.1.2, because a structural mass of $0.1m_0$ was not subtracted.

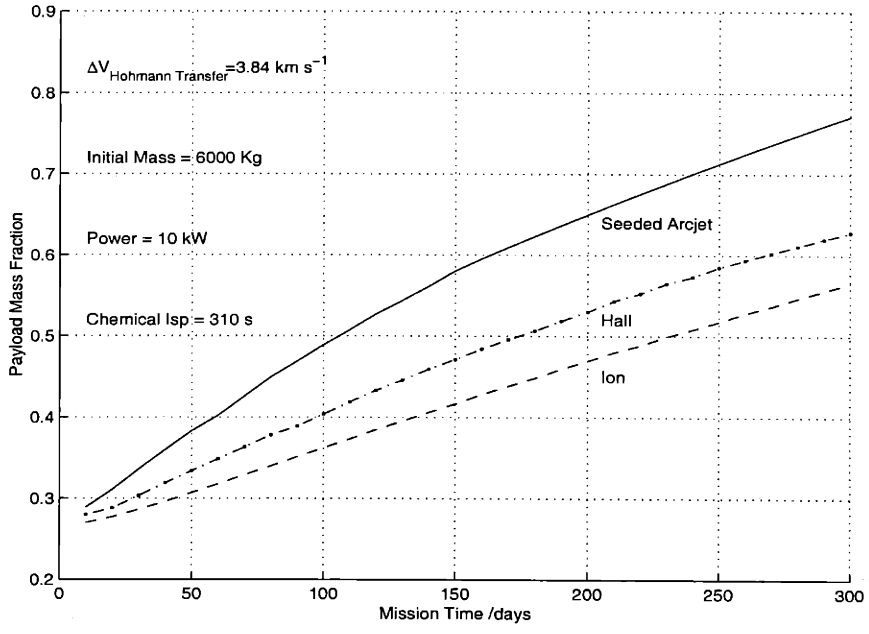

Figure 7-12: *Payload Fraction for Combined Chemical/Electric Mission.*

As can be seen for a combined chemical and electric mission, the seeded arcjet is the best choice for mission times greater than about 30 days, and always gives a higher payload

fraction than either Hall thrusters or ion engines. The reason for this is because the I_{sp} of the electric stage (as indicated towards in figures 7-9 and 7-10, and shown specifically for this mission in figure 7-13) optimizes at around the I_{sp} that arcjets deliver, and the seeded arcjet gives the highest efficiency and thrust to mass ratio of any thrusters at this I_{sp}.

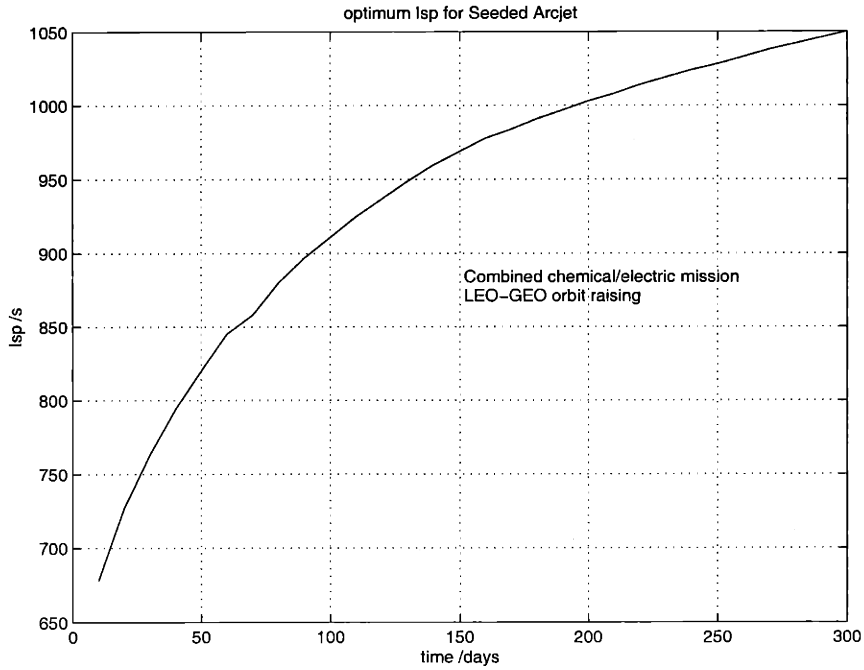

Figure 7-13: *Optimum Isp for Seeded Arcjet for the Combined Mission.*

Chapter 8

Conclusions

8.1 Summary and Conclusions

The two dimensional code developed proves to within the limitations of the code, that it is indeed possible to run a cesium seeded hydrogen arcjet thruster in a regime where the hydrogen is fully molecular, yet the cesium is fully ionized, due to the difference in the dissociation and ionization energies of hydrogen and the ionization energy of cesium, and also the electron-heavy temperature disparity which favours ionization rather than dissociation. This leads to much higher efficiencies since the frozen losses are greatly reduced.

No ionizational instability was encountered at the arc attachment region on the anode, even when the electron temperature there was increased to $9000K$. This is in excess of Oyerokun's stability limit of $7000K$, [93] above which it was predicted that any significant dissociation would then lead to runaway ionization.

As predicted by Oyerokun [93] the current density was nearly uniformly distributed in the constrictor, which means there is much more even heating of the propellant. An implication of this is that the constrictor must be made of an insulator. Due to the high temperatures encountered in the seeded arcjet this poses a problem since few materials are able to withstand such high temperatures and ceramics which can withstand the heat become semiconducting at those temperatures.

With the current supplied over a much larger distance than conventional arcjets and the conductivity being less, the electric potential drop is much larger. This has the effect of making the potential drop at the the sheaths much less significant. Whereas in a conventional arcjet this loss may be ten percent it is only about one percent in a seeded

arcjet.

The performance mapping demonstrates the trade off between I_{sp} and frozen losses, and suggests the constrictor inlet Mach number where a useful compromise is reached. At that Mach number and the desired inlet pressure, there is then an optimum current and seeding fraction, to minimize the frozen losses, although the seeding fraction is limited due to a stability constraint. These parameters are sufficient to calculate any other flow properties from, using the quasi one dimensional model.

The materials study showed that tungsten is the best choice for the electrodes due to its high melting point and high thermal conductivity. For the insulating constrictor Boron Nitride or Beryllium Oxide have the highest electrical resistivity and thermal conductivity at high temperatures. Extensive regenerative cooling, especially within the constrictor would help.

The thermal model led to an improved geometry to reduce heat loads to prevent melting of the cathode tip in particular. It predicted the temperature distribution in the thruster and suggested ways to optimize the regenerative cooling, thereby regaining some of the energy lost from the plasma in the constrictor and nozzle.

The rest of the experimental design then included a couple of ways of supplying and removing the cesium, and dealing with its toxicity, corrosivity, and rapid oxidation. A mechanical layout for the thruster which enables the most parameters to be diagnosed and provide the greatest flexibility was found. The size and pumping requirements for a vacuum tank were then determined, and some of the diagnostic equipment considered.

A mission study, using electric propulsion only, showed that for LEO to GEO orbit raising that the seeded arcjet, provides the highest payload ratio for mission times between 30 and 160 days with the power source considered part of the propulsion system, and between 15 and 80 days when considered part of the payload. Finally a combined chemical and electric propulsion mission study using an initial mass of 6000 Kg and a power of 10 kW, showed that the seeded arcjet gave the highest payload ratio for transfers lasting from 30 days to in excess of 300 days, when compared to Hall thrusters and Ion Engines.

8.2 Future Recommendations

The overall performance characteristics are a slight overestimate since radiation is also source of loss, especially with cesium present in the flow. It also provides another mechanism for energy transport, so it would be useful for a radiation model to be including in future.

In terms of results produced, more runs need to be done with a fully two dimensional code to obtain a more accurate performance mapping than was obtained with the quasi one dimensional code. This will however require work on the integration algorithm to provide a faster, more stable scheme, that can produce results in a reasonable time span. Splitting off the chemical reactions and electron temperature from the flow equations appears to be the best way to do this.

As mentioned in section 4.5, some of the boundary conditions on the mass fractions were simplified for stability during startup. Returning to the more physically correct boundary conditions, should improve the accuracy of the code. At the walls the temperature should ideally be calculated simultaneously with the thermal model of the arcjet structure to obtain a self-consistent solution.

One question which could be investigated with more numerical simulations would be the transition from conventional to seeded behaviour as the seeding fraction is increased from zero. In a conventional arcjet the current forms a narrow core, whereas in an optimally seeded arcjet the current is distributed much more uniformly through the constrictor. Whether this transition is abrupt or smooth is not yet known.

Another question would be stability limit where the electron temperature is raised to the point when the hydrogen would rapidly ionize, reintroducing the frozen losses. This limit was not yet reached but was shown to be above 9400 K.

Apart from changes in constrictor length future work could examine alternative geometries such as constrictor width, cathode location, and nozzle geometries. For the nozzle, the effects of bi-angle designs and of including an energy recovery chamber (see figure 2-4) could be explored.

Another future line of inquiry might be the use of alternative propellants. Potential seed materials include any of the alkali or earth-alkali metals, and also the larger noble gases. Xenon might be a good choice as mixing could be done a priori, and a single tank used. Also if other forms of electric propulsion such as an ion engine were to be on-board, xenon could

be used for both. The noble gases also have the advantage of being gaseous so no system is required to evaporate it, as is required for the alkali metals. Noble gases are also non-toxic. Other potential buffer materials include helium, nitrogen, hydrazine, ammonia, and methane to name just the more commonly used options. Helium and nitrogen unfortunately require cryogenic cooling for containment, but avoid the sooting problems associated with hydrocarbon fuels. Apart from cesium seeded hydrogen, probably the most interesting combination to examine would be xenon seeded helium.

Finally whilst more work needs to be done on the numerical model, I believe that this work together with the work of Oyerokun [93] has proved that the basic concept of seeding an arcjet with an alkali metal works, and has a practical importance to spacecraft propulsion. The next major step is the building and testing of a prototype for comparison of actual and predicted performance. I would be greatly interested to see the results of experimental work.

Appendix A

Fundamental Constants

Pi	$\pi = 3.1415926536$	
Boltzmann's constant	$k = 1.380658 \times 10^{-23}$	JK^{-1}
Planck's constant	$h = 6.6261 \times 10^{-34}$	$J\,s$
Stefan-Boltzmann constant	$\sigma_{SB} = 5.6705 \times 10^{-8}$	$Wm^{-2}K^{-4}$
Avogadro's number	$L = N_A = 6.0221367 \times 10^{23}$	mol^{-1}
Universal gas constant	$\hat{R} = N_A k = 8.31435$	$JK^{-1}mol^{-1}$
Electronic Charge	$e = 1.6022 \times 10^{-19}$	C
Permittivity of vacuum	$\epsilon_0 = 8.854187817 \times 10^{-12}$	Fm^{-1}
Permeability of vacuum	$\mu_0 = 4\pi \times 10^{-7}$	Hm^{-1}
Atomic mass unit	$m_u = 1.6605402 \times 10^{-27}$	kg
Gravitational acceleration	$g_e = 9.81$	$m\,s^{-2}$
Electron mass	$m_e = 9.1093897 \times 10^{-31}$	kg
Hydrogen atomic mass	$m_H = 1.6737 \times 10^{-27}$	kg
Nitrogen atomic mass	$m_N = 2.3258 \times 10^{-26}$	kg
Cesium atomic mass	$m_{Cs} = 2.2069 \times 10^{-25}$	kg
Dissociation energy (H_2)	7.236×10^{-19}	J
Dissociation energy (N_2)	1.570×10^{-18}	J
Ionization energy (H)	2.179×10^{-18}	J
Ionization energy (N)	2.329×10^{-18}	J
Ionization energy (Cs)	6.200×10^{-19}	J
Vibrational Temperature (H_2)	6160	K
Energy of 1 Kelvin	$k/e = 8.6174 \times 10^{-5}$	eV
Temperature of 1 eV	$e/k = 1.1604 \times 10^{4}$	K
Atmospheric pressure	$p_0 = 1.01325 \times 10^{5}$	Pa

Appendix B

Equilibrium Constants

Table B.1: *Equilibrium Constants for the Hydrogen and Nitrogen Dissociation Reactions (from JANAF Thermochemical Tables)*

Temperature (K)	$\log K_p$	
	$\frac{1}{2}H_2 \rightleftharpoons H$	$\frac{1}{2}N_2 \rightleftharpoons N$
200	-54.325	-120.419
400	-25.876	-58.710
600	-16.335	-38.084
800	-11.538	-27.746
1000	-8.644	-21.530
1200	-6.705	-17.377
1400	-5.313	-14.407
1600	-4.264	-12.175
1800	-3.446	-10.437
2000	-2.788	-9.045
2200	-2.249	-7.905
2400	-1.798	-6.954
2600	-1.415	-6.148
2800	-1.087	-5.457
3000	-0.801	-4.857
3200	-0.551	-4.332
3400	-0.330	-3.867
3600	-0.133	-3.455
3800	0.044	-3.085
4000	0.203	-2.751

Table B.1: *continued*

Temperature (K)	$\log K_p$	
	$\frac{1}{2}H_2 \rightleftharpoons H$	$\frac{1}{2}N_2 \rightleftharpoons N$
4200	0.347	-2.449
4400	0.478	-2.175
4600	0.598	-1.923
4800	0.708	-1.693
5000	0.809	-1.480
5200	0.902	-1.283
5400	0.989	-1.101
5600	1.069	-0.931
5800	1.144	-0.773
6000	1.213	-0.625

Appendix C

Collision Cross Sections

Table C.1: *Total Collision Cross Sections for Electron Collisions*

Temperature (K)	Q_{ij} ($\mathring{A}^2$)			
	$e - H_2$	$e - N_2$	$e - H$	$e - N$
1000	10.1	5.05	-	-
2000	11.3	7.70	-	30.7
3000	12.6	8.85	26.01	21.8
4000	13.4	9.50	24.54	19.3
5000	14.2	9.85	23.20	17.7
6000	14.8	10.1	21.96	16.7
7000	15.5	10.2	20.83	16.3
8000	15.9	10.2	19.80	15.9
9000	16.4	10.0	18.86	15.5
10000	16.9	9.90	17.99	15.3
11000	17.3	9.80	17.18	15.0
12000	17.6	10.0	16.44	14.8
13000	17.8	10.5	15.76	14.7
14000	18.0	10.8	15.11	14.6
15000	18.2	11.2	14.52	14.4
16000	18.3	11.5	13.96	14.3
17000	18.4	11.9	13.43	14.2
18000	18.5	12.4	12.93	14.0
19000	18.5	13.1	12.47	13.8
20000	18.4	13.8	12.02	13.7

Table C.1: *continued*

Temperature (K)	Q_{ij} ($\mathring{A}^2$)			
	$e - H_2$	$e - N_2$	$e - H$	$e - N$
21000	18.3	15.7	-	13.5
22000	18.2	18.9	-	13.3
23000	18.0	24.8	-	13.1
24000	17.8	26.8	-	13.0
25000	17.6	27.9	-	12.8
26000	17.4	28.9	-	-
27000	17.2	29.5	-	-
28000	17.0	29.8	-	-
29000	16.7	30.0	-	-
30000	16.4	29.8	-	-
31000	16.3	29.1	-	-
32000	16.0	27.8	-	-
33000	15.7	25.4	-	-
34000	15.4	23.0	-	-
35000	15.2	21.0	-	-

Appendix D

Collision Integrals

Table D.1: *Diffusion Collision Integrals for Hydrogen Interactions*

Temp (K)	$\langle \Omega_{ij}^{(1,1)} \rangle$ $(\mathring{A}^2)$					
	$H_2 - H_2$	$H_2 - H$	$H_2 - e$	$H - H$	$H - H+$	$H - e$
1000	5.21	4.16	3.81	5.24	-	-
2000	4.37	3.27	4.58	4.13	-	-
3000	3.79	2.80	4.99	3.57	-	-
4000	3.42	2.49	5.23	3.23	-	-
5000	3.14	2.27	5.33	3.03	27.7	6.85
6000	2.93	2.09	5.35	2.88	27.0	6.29
7000	2.75	1.94	5.30	2.76	26.4	5.82
8000	2.60	2.37	5.21	2.62	26.0	5.43
9000	2.47	2.25	5.09	2.48	25.5	5.09
10000	2.36	2.14	4.95	2.36	25.2	4.80
11000	2.26	2.04	4.81	2.25	24.8	4.54
12000	2.17	1.95	4.67	2.15	24.5	4.31
13000	2.09	1.87	4.52	2.07	24.2	4.11
14000	2.02	1.80	4.37	1.99	24.0	3.92
15000	1.95	1.74	4.23	1.92	23.7	3.76
16000	-	-	4.10	-	23.5	3.61
17000	-	-	3.97	-	23.3	3.47
18000	-	-	3.85	-	23.1	3.34
19000	-	-	3.73	-	22.9	3.23
20000	-	-	3.62	-	22.8	3.12

Table D.1: *continued*

Temp (K)	$\langle \Omega_{ij}^{(1,1)} \rangle$ $(\mathring{A}^2)$					
	$H_2 - H_2$	$H_2 - H$	$H_2 - e$	$H - H$	$H - H+$	$H - e$
21000	-	-	3.51	-	22.6	3.03
22000	-	-	3.41	-	22.4	2.94
23000	-	-	3.32	-	22.3	2.86
24000	-	-	3.23	-	22.1	2.79
25000	-	-	3.14	-	22.0	2.72
26000	-	-	3.06	-	21.9	2.66
27000	-	-	2.99	-	21.8	2.60
28000	-	-	2.92	-	21.6	2.55
29000	-	-	2.85	-	21.5	2.51
30000	-	-	2.79	-	21.4	2.46
31000	-	-	2.73	-	21.3	2.43
32000	-	-	2.67	-	21.2	2.39
33000	-	-	2.62	-	21.1	2.36
34000	-	-	2.56	-	21.0	2.33
35000	-	-	2.51	-	21.0	2.31

Table D.2: *Diffusion Collision Integrals for Nitrogen Interactions*

Temp (K)	$\langle \Omega_{ij}^{(1,1)} \rangle$ $(\mathring{A}^2)$			
	$N_2 - N_2$	$N_2 - N$	$N - N$	$N - N+$
1000	9.13	8.21	6.46	34.3
2000	7.55	6.84	5.36	31.4
3000	6.76	6.10	4.83	30.0
4000	6.24	5.60	4.48	29.0
5000	5.87	5.22	4.21	28.3
6000	5.59	4.93	4.00	27.7
7000	5.34	4.68	3.82	27.3
8000	5.16	4.48	3.68	26.9
9000	5.00	4.30	3.52	26.5
10000	4.86	4.15	3.43	26.2
11000	4.73	4.01	3.33	25.9
12000	4.62	3.88	3.24	25.7
13000	4.52	3.77	3.15	25.4
14000	4.43	3.67	3.06	25.2
15000	4.35	3.58	2.99	25.0
16000	-	-	2.92	24.8
17000	-	-	2.85	24.6
18000	-	-	2.79	24.5
19000	-	-	2.74	24.3
20000	-	-	2.69	24.2
21000	-	-	-	24.0
22000	-	-	-	23.9
23000	-	-	-	23.8
24000	-	-	-	23.7
25000	-	-	-	23.6
26000	-	-	-	23.5
27000	-	-	-	23.4
28000	-	-	-	23.3
29000	-	-	-	23.2
30000	-	-	-	23.1
31000	-	-	-	23.0
32000	-	-	-	22.9
33000	-	-	-	22.8
34000	-	-	-	22.7
35000	-	-	-	22.6

Table D.3: *Viscosity Collision Integrals for Hydrogen Interactions*

Temp (K)	$\langle\Omega_{ij}^{(2,2)}\rangle$ $(\mathring{A}^2)$					
	$H_2 - H_2$	$H_2 - H$	$H_2 - e$	$H - H$	$H - H+$	$H - e$
1000	6.00	5.13	4.18	5.95	-	-
2000	5.33	4.10	4.94	4.74	-	-
3000	4.73	3.55	5.31	4.12	-	-
4000	4.29	3.35	5.44	3.74	-	-
5000	3.97	2.91	5.42	3.50	13.6	5.81
6000	3.71	2.69	5.30	3.28	12.5	5.27
7000	3.50	2.52	5.13	3.06	11.6	4.83
8000	3.32	2.37	4.92	2.88	10.8	4.47
9000	3.17	2.25	4.71	2.73	10.2	4.15
10000	3.03	2.14	4.49	2.60	9.60	3.89
11000	2.91	2.04	4.28	2.50	9.10	3.65
12000	2.81	1.95	4.08	2.42	8.66	3.44
13000	2.71	1.87	3.89	2.34	8.26	3.27
14000	2.62	1.80	3.71	2.25	7.90	3.11
15000	2.54	1.74	3.55	2.18	7.57	3.00
16000	-	-	3.39	2.09	7.27	2.84
17000	-	-	3.25	2.02	6.99	2.73
18000	-	-	3.12	1.96	6.74	2.63
19000	-	-	3.00	1.89	6.50	2.54
20000	-	-	2.89	1.84	6.27	2.46
21000	-	-	2.79	1.78	6.07	2.40
22000	-	-	2.70	1.73	5.87	2.33
23000	-	-	2.61	1.68	5.69	2.27
24000	-	-	2.54	1.63	5.51	2.23
25000	-	-	2.46	1.59	5.35	2.19
26000	-	-	2.40	1.55	5.19	2.15
27000	-	-	2.33	1.51	5.04	2.12
28000	-	-	2.27	1.48	4.90	2.10
29000	-	-	2.22	1.45	4.77	2.08
30000	-	-	2.17	1.42	4.64	2.06
31000	-	-	2.12	1.39	4.52	2.05
32000	-	-	2.07	1.36	4.41	2.04
33000	-	-	2.03	1.34	4.30	2.04
34000	-	-	1.99	1.31	4.19	2.04
35000	-	-	1.95	1.29	4.09	2.04

Table D.4: *Viscosity Collision Integrals for Nitrogen Interactions*

Temp (K)	$\langle \Omega_{ij}^{(2,2)} \rangle$ $(\mathring{A}^2)$			
	$N_2 - N_2$	$N_2 - N$	$N - N$	$N - N+$
1000	10.4	9.82	7.24	13.3
2000	8.86	8.27	5.97	10.5
3000	8.07	7.43	5.36	9.15
4000	7.55	6.85	4.96	8.33
5000	7.17	6.42	4.70	7.74
6000	6.87	6.08	4.46	7.26
7000	6.64	5.80	4.28	6.85
8000	6.43	5.56	4.14	6.48
9000	6.26	5.36	4.01	6.15
10000	6.11	5.17	3.89	5.84
11000	5.98	5.01	3.79	5.56
12000	5.86	4.87	3.70	5.31
13000	5.75	4.73	3.61	5.07
14000	5.65	4.61	3.53	4.86
15000	5.56	4.50	3.45	4.66
16000	-	-	3.38	4.48
17000	-	-	3.32	4.31
18000	-	-	3.26	4.15
19000	-	-	3.20	4.00
20000	-	-	3.14	3.87
21000	-	-	-	3.74
22000	-	-	-	3.62
23000	-	-	-	3.52
24000	-	-	-	3.41
25000	-	-	-	3.32
26000	-	-	-	3.24
27000	-	-	-	3.16
28000	-	-	-	3.07
29000	-	-	-	2.99
30000	-	-	-	2.91
31000	-	-	-	2.85
32000	-	-	-	2.79
33000	-	-	-	2.73
34000	-	-	-	2.67
35000	-	-	-	2.61

Table D.5: *Non-dimensional Collision Integrals for Charged Particle Interactions*

$\psi_{i,j}$	$F_{Paq}^{(1,1)}$	$F_{Paq}^{(2,2)}$	$F_{Mac}^{(1,1)}$	$F_{Mac}^{(2,2)}$
-7.0	-6.051	-5.102	-5.532	-4.887
-6.8	-5.897	-4.947	-5.372	-4.725
-6.6	-5.745	-4.792	-5.212	-4.563
-6.4	-5.593	-4.638	-5.053	-4.401
-6.2	-5.442	-4.485	-4.894	-4.238
-6.0	-5.292	-4.332	-4.734	-4.074
-5.8	-5.142	-4.181	-4.573	-3.911
-5.6	-4.994	-4.030	-4.410	-3.749
-5.4	-4.846	-3.881	-4.245	-3.588
-5.2	-4.700	-3.732	-4.077	-3.430
-5.0	-4.554	-3.584	-3.906	-3.276
-4.8	-4.409	-3.437	-3.733	-3.126
-4.6	-4.265	-3.291	-3.558	-2.980
-4.4	-4.123	-3.146	-3.382	-2.840
-4.2	-3.981	-3.002	-3.206	-2.704
-4.0	-3.840	-2.859	-3.030	-2.572
-3.8	-3.700	-2.717	-2.855	-2.443
-3.6	-3.561	-2.576	-2.683	-2.316
-3.4	-3.422	-2.436	-2.514	-2.189
-3.2	-3.285	-2.297	-2.348	-2.063
-3.0	-3.149	-2.158	-2.187	-1.934
-2.8	-3.013	-2.011	-2.029	-1.803
-2.6	-2.878	-1.884	-1.876	-1.669
-2.4	-2.743	-1.748	-1.727	-1.531
-2.2	-2.609	-1.612	-1.582	-1.390
-2.0	-2.475	-1.477	-1.441	-1.246
-1.8	-2.341	-1.341	-1.305	-1.098

Table D.5: *continued*

$\psi_{i,j}$	$F_{Paq}^{(1,1)}$	$F_{Paq}^{(2,2)}$	$F_{Mac}^{(1,1)}$	$F_{Mac}^{(2,2)}$
-1.6	-2.207	-1.205	-1.171	-0.9478
-1.4	-2.071	-1.069	-1.041	-0.7956
-1.2	-1.935	-0.9320	-0.914	-0.6418
-1.0	-1.797	-0.7940	-0.7880	-0.4865
-0.8	-1.657	-0.6524	-0.6640	-0.3299
-0.6	-1.514	-0.5084	-0.5406	-0.1718
-0.4	-1.366	-0.3605	-0.4171	-0.01189
-0.2	-1.213	-0.2074	-0.2926	0.1504
0.0	-1.053	-0.04749	-0.1657	0.3160
0.2	-0.8833	0.1209	-0.03529	0.4858
0.4	-0.7026	0.2999	0.1003	0.6612
0.6	-0.5078	0.4920	0.2427	0.8435
0.8	-0.2960	0.6996	0.3940	1.034
1.0	-0.06429	0.9251	0.5563	1.235
1.2	0.1900	1.170	0.7315	1.445
1.4	0.4680	1.435	0.9213	1.667
1.6	0.7686	1.715	1.127	1.898
1.8	1.087	2.006	1.347	2.137
2.0	1.416	2.297	1.582	2.380
2.2	1.741	2.580	1.827	2.625
2.4	2.049	2.848	2.078	2.869
2.6	2.330	3.100	2.330	3.108
2.8	2.588	3.338	2.579	3.343
3.0	2.829	3.567	2.821	3.571

Bibliography

[1] Anderson, Dale A., John C. Tannehill, and Richard H. Pletcher. *Computational Fluid Mechanics and Heat Transfer.* Series in Computational and Physical Processes in Mechanics and Thermal Sciences. Hemisphere Publishing Corporation, 1984.

[2] Anderson, John D., Jr. *Fundamentals of Aerodynamics.* McGraw-Hill, New York, 2nd edition, 1991.

[3] Aston, G. and M.B. Aston. "Integrated Design Arcjets for High Performance". IEPC, 25th International Electric Propulsion Conference, Cleveland, August 1997.

[4] Belov, V.A. "Viscosity of Partially Ionized Hydrogen". *High Temperature*, Vol. 5:pp. 31–6, 1967.

[5] Benson, Guy B. An Improved Numerical Model for Flow Computations Of Electrothermal Arcjet Thrusters. Master's thesis, Massachusetts Institute of Technology, 1996.

[6] Bhatia, M. V. and P. N. Cheremisinoff. *Heat Transfer Equipment*, volume Vol. 2 of *Process Equipment Series.* Technomic Publishing Co.,Inc., Westport, CT, 1980.

[7] Bittencourt, J. A. *Fundamentals of Plasma Physics.* Pergamon Press, New York, 1986.

[8] Boyd, I.D. "Extensive Validation of a Monte Carlo Model for Hydrogen Arcjet Flowfields". *AIAA Journal of Propulsion and Power*, Vol. 13(No. 6):pp. 775–782, November-December 1997.

[9] Brode, R. B. "The Qualitative Study of the Collisions of Electrons with Atoms". *Review of Modern Physics*, Vol. 5(No. 4):pp. 257, 1933.

[10] Bromaghim, D.R. *et al.* "An Overview of the On-Orbit Results from the ESEX Flight Experiment". AIAA 99-2706, AIAA/ASME/SAE/ASSEE 35th Joint Propulsion Conference, Los Angeles, June 1999.

[11] Brophy, J.R. *et al.* "Performance of the Stationary Plasma Thruster: SPT-100". AIAA 92-3155, AIAA/ASME/SAE/ASSEE 28th Joint Propulsion Conference, Nashville, July 1992.

[12] Bullis, R. N. "Low Energy Cesium Ion-Atom Collision Cross Sections". *Rept. on Thermionic Conversion Specialists Conf., Gatlinburg Tenn.*, page pp. 1, 1963.

[13] Butler, G.W., B.A. Kashiwa, and D.Q. King. "Numerical Modeling of Arcjet Performance". AIAA 93-1474, AIAA 21st Fluid Dynamics, Plasma Dynamics, and Lasers Conference, Seattle, June 1990.

[14] Butler, G.W. and D.Q. King. "Single and Two Fluid Simulations of Arcjet Performance". AIAA 92-3104, AIAA/SAE/ASME/ASEE 28th Joint Propulsion Conference, Nashville, July 1992.

[15] Carborundum Company. "Combat Boron Nitride Technical Data". Niagara Falls, New York, 1991.

[16] Chapman, Sydney and T. G. Cowling. *The Mathematical Theory of Non-Uniform Gases.* Cambridge University Press, Cambridge, 3rd edition, 1970.

[17] Chase, Jr., M. W. et. al. *Journal of Physical and Chemical Reference Data Supplement No. 1: JANAF Thermochemical Tables*, volume 14. American Chemical Society and American Institute of Physics for the National Bureau of Standards, Washington D.C., 3rd edition, 1985.

[18] Chen, Francis F. *Introduction to Plasma Physics and Controlled Fusion; Volume 1: Plasma Physics.* Plenum Press, New York, 2nd edition, 1984.

[19] Cruciani, G. and W.D. Deininger. "Development Testing of a 1kW Class Arcjet Thruster". AIAA 92-3114, AIAA/SAE/ASME/ASEE 28th Joint Propulsion Conference, Nashville, July 1992.

[20] Cruciani, G., W.D. Deininger, and C. Petagna. "Development of a 1N, Radiatively Cooled Arcjet". AIAA 90-2536, AIAA/DLGR/JSASS 21st International Electric Propulsion Conference, Orlando, July 1990.

[21] Cubley, S. J. and E. A. Mason. "Atom-molecule and Molecule-molecule Potentials and Transport Collision Integrals for High-temperature Air Species". *Physics of Fluids*, Vol. 18(No. 9):pp. 1109–1111, September 1975.

[22] Curran, F.M. and T.W. Haag. "An Extended Life and Performance Test of a Low-Power Arcjet". NASA Technical Memorandum 100942, July 1988.

[23] Curran, F.M., D.H. Manzella, and E.J. Pencil. "Performance Characterization of a Segmented Anode Arcjet Thruster". AIAA 90-2582, AIAA/DLGR/JSASS 21st International Electric Propulsion Conference, Orlando, July 1990.

[24] Curran, F.M. and S. Nakanishi. "Low Power dc Arcjet Operation with Hydrogen/Nitrogen Propellant Mixture". AIAA 86-1505, AIAA/SAE/ASME/ASEE 22nd Joint Propulsion Conference, Huntsville, June 1986.

[25] Curran, F.M. and C.J. Sarmiento. "Low PowerArcjet Performance Characterization". AIAA 90-2578, AIAA/DLGR/JSASS 21st International Electric Propulsion Conference, Orlando, July 1990.

[26] Curran, F.M., A.J. Sovie, and T.W. Haag. "Arcjet Nozzle Design Impacts". NASA Technical Memorandum 102050, May 1989.

[27] Daybelge, U. "Transport Coefficients of Two-Temperature Partially Ionized Gases". Stanford University Institute for Plasma Research Report Number 263, December 1968.

[28] Devoto, R. S. "Transport Coefficients of Partially Ionized Hydrogen". *Journal of Plasma Physics*, Vol. 2:pp. 617–31, 1968.

[29] Drawin, H. W. and P. Felenbok. *Data for Plasmas in Local Thermodynamic Equilibrium.* Gauthier-Villars, Paris, 1965.

[30] Ducati, A.C., H. Humpal, J.Meltzer, E. Muehlberger, J.P. Todd, and H. Waltzer. "1-kw Arcjet-Engine system-Performance Test". *Journal of Spacecraft*, Vol. 1(No. 3):pp. 327–332, May-June 1964.

[31] Fujita, K. and Y. Arakawa. "Numerical Prediction of Arcjet Performance Based on the Chemical Kinetics and Electron Temperature Disparity". IEPC 95-25, 24th International Electric Propulsion Conference, Moscow, Russia, September 1995.

[32] Glocker, B. and M. Autweter-Kurtz. "Numerical and Experimental Constrictor Flow Analysis of a 10kW Thermal Arcjet". AIAA 92-3835, AIAA/SAE/ASME/ASEE 28th Joint Propulsion Conference, Nashville, July 1992.

[33] Glocker, B. and M. Autweter-Kurtz. "Radiation Cooled Medium Power Arcjet Experiments and Thermal Analysis". AIAA 92-3834, AIAA/SAE/ASME/ASEE 28th Joint Propulsion Conference, Nashville, July 1992.

[34] Glocker, B., M. Autweter-Kurtz, T.M. Goelz, H.L. Kurtz, and H.O. Schrade. "Medium Power Arcjet Thruster Experiments". AIAA 90-2531, AIAA/DLGR/JSASS 21st International Electric Propulsion Conference, Orlando, July 1990.

[35] Glocker, B., Th. Rosgen, and A. Laxander. "Medium Power Arcjet Analysis and Experiments". IEPC 91-016, AIDAA/AIAA/DGLR/JSASS 22nd Electric Propulsion Conference, Viareggio, Italy, October 1991.

[36] Glocker, B., H.O. Schrade, and P.C. Sleziona. "Numerical Prediction of Arcjet Performance". AIAA 90-2612, AIAA/DLGR/JSASS 21st International Electric Propulsion Conference, Orlando, July 1990.

[37] Gölz, T., M. Autweter-Kurtz, H.L. Kurtz, and H.O. Schrade. "High Power Arcjet Analysis Thruster Experiments". IEPC 91-072, AIDAA/AIAA/DGLR/JSASS 22nd Electric Propulsion Conference, Viareggio, Italy, October 1991.

[38] Goodfellow, K.D. and J.E. Polk. "Throttling Capability of a 30 kw Class Ammonia Arcjet". AIAA 91-2577, AIAA/SAE/ASME/ASEE 27th Joint Propulsion Conference, Sacramento, June 1991.

[39] Grier, Norman T. *Calculation of Transport Properties of Ionizing Atomic Hydrogen.* Technical Report TN D-3186, NASA, April 1966.

[40] Guthrie, Andrew. *Vacuum Technology.* Wiley, New York, 1963.

[41] Haag, T.W. and F.M. Curran. "High Power Arcjet Performance". AIAA 91-2456, AIAA/SAE/ASME/ASEE 27th Joint Propulsion Conference, Sacramento, June 1991.

[42] Hardy, T.L. and F.M. Curran. "Low Power dc Arcjet Operation with Hydrogen/Nitrogen/Ammonia Mixtures". AIAA 87-1948, AIAA/SAE/ASME/ASEE 23rd Joint Propulsion Conference, San Diego, June 1987.

[43] Hastings, Daniel and Henry Garrett. *Spacecraft-Environment Interactions.* Cambridge University Press, Cambridge, 1996.

[44] Heimerdinger, D. J. *Fluid Mechanics in a Magnetoplasmadynamic Thruster*, Doctoral thesis. Massachusetts Institute of Technology, 1988.

[45] Heimerdinger, D.J. *An Approximate Two-Dimensional Analysis of a MPD Thruster.* Master's thesis, Massachusetts Institute of Technology, 1984.

[46] Hinnov, Einar and Joseph G. Hirschberg. "Electon-Ion Recombination in Dense Plasmas". *Physical Review*, Vol. 125(No. 3):pp. 795–801, February 1, 1962.

[47] Hirsch, C. *Numerical Computation of Internal and External Flows, Volume 2: Computational Methods for Inviscid and Viscous Flows.* John Wiley and Sons, Inc., New York, 1988.

[48] Hirschfelder, Joseph O., Charles F. Curtiss, and R. Byron Bird. *Molecular Theory of Gases and Liquids.* John Wiley and Sons, Inc., New York, 1954.

[49] Holley, J.H. *et al.* "Corrosivity and Contamination of Cesium in Ion Propulsion". ARS Electric Propulsion Conference, Berkeley, California. March 1962. Also in Electric Propulsion Development, vol. 9 of Progress in Astronatuics and Aeronautics. Academic Press, New York. 1963.

[50] Hoskins, W.A., G.W. Butler, and A.E. Kull. "A Comparison of Regenerative and Conventional Arcjet Performance". AIAA 92-3240, AIAA/SAE/ASME/ASEE 28th Joint Propulsion Conference, Nashville, July 1992.

[51] Hoskins, W.A., A.E. Kull, and G.W. Butler. "Measurement of Population and Temperature Profiles in an Arcjet Plume". AIAA 92-3240, AIAA/SAE/ASME/ASEE 28th Joint Propulsion Conference, Nashville, July 1992.

[52] Hutchinson, I.H. *Principles of Plasma Diagnostics.* Cambridge University Press., 1987.

[53] Incropera, Frank P. and David P. DeWitt. *Introduction to Heat Transfer.* John Wiley and Sons Inc., New York, 1985.

[54] Itikawa, Y. "Momentum-Transfer Cross Sections for Electron Collisions with Atoms and Molecules ". *Atomic Data and Nuclear Data Tables*, Vol. 21(No. 1):pp. 69–75, January 1978.

[55] Jack, J. R. Theoretical perfomance of propellants suitable for electrothermal jet engines. *ARS J.*, Vol. 31:pp. 1685, 1961.

[56] Jahn, R. G. *Physics of Electric Propulsion.* McGraw-Hill Book Company, New York, 1968.

[57] Janev, R. K., W. D. Langer, K. Evans Jr., and D. E. Post Jr. *Elementary Processes in Hydrogen-Helium Plasmas.* Springer-Verlag, New York, 1987.

[58] Janson, S.W., R.P. Welle, D.R. Schulthess, and R.B. Cohen. "Arcjet Plume Characterization Part II: Optical Diagnositic Results". AIAA 90-2643, AIAA/DLGR/JSASS 21st International Electric Propulsion Conference, Orlando, July 1990.

[59] John, R.R., S. Bennett, L.A. Cross, M.M. Chen, and J.F. Connors. "Energy Addition and Loss Mechanisms in the Thermal Arc Jet Engine". AIAA 63-022, AIAA Electric Propulsion Conference, Colorado Springs, March 1963.

[60] John, R.R., M. Chen, J. Connors, and J. Megrue. "Arc Jet Performance - Experiment and Theory iv". ARS 2345-62, ARS Electric Propulsion Conference, Berkeley, March 1962.

[61] John, R.R., J.F. Connors, and S. Bennett. "Thirty Day Endurance Test of a 30 kw Arc Jet Engine". AIAA 63-274, AIAA Summer Meeting, Los Angeles, June 1963.

[62] Kaufman, H.R. and R.S. Robinson. "Electric Thruster Performance for Orbit Raising and Maneuvering". Orbit-Raising and Maneuvering Propulsion: Research Status and Needs. Leonard Caveny (Ed.). Vol. 89 of Progress in Astronautics and Aeronautics, AIAA, 1984.

[63] Kestin, J. and Dorfman, J. *A Course in Statistical Thermodynamics.* Academic Press Inc., New York, 1971.

[64] King, D.Q. and G.W. Butler. "Modelling and Measurement of N_2 Arcjet Performance". AIAA 90-2626, AIAA/DLGR/JSASS 21st International Electric Propulsion Conference, Orlando, July 1990.

[65] Knowles, S.C., W.W. Smith, F.M. Curran, and T.W. Haag. "Performance Characterization of a Low Power Hydrazine Arcjet". AIAA 87-1057, AIAA/DGLR/JSASS 19th Electric Propulsion Conference, Colorado Springs, May 1987.

[66] Knowles, S.C., S.E. Yano, and R.S. Aadland. "Qualification and Life Testing of a Flight Design Hydrazine Arcjet System". AIAA 90-2576, AIAA/DLGR/JSASS 21st International Electric Propulsion Conference, Orlando, July 1990.

[67] Kovitya, P., D.A. Scott, and G.N. Haddad. "Two-dimensional Modelling of Plasma Torches". CSIRO Division of Applied Physics, Final Report for AWRA Contract No. 123, July 1988.

[68] Krier, Herman, Rodney L. Burton, T. W. Megli, S.A. Bufton, and N.T. Tiliakos. *Arcjet Plasma Modeling with Experimental Validation.* Technical Report UILU-ENG 94-4011, University of Illinois at Urbana-Champaign, Department of Mechanical and Industrial Engineering, 1994.

[69] Kurtz, H.L., D.M. Zube, B. Glocker, and M. Autweter-Kurtz. "Low Power Hydrazine Arcjet Thruster Study". AIAA 92-3116, AIAA/SAE/ASME/ASEE 28th Joint Propulsion Conference, Nashville, July 1992.

[70] Kutler, P., L. Sakell, and G. Aiello. "On the Shock-On-Shock Interaction Problem". AIAA 74-524, AIAA 7th Fluid and Plasma Dynamics Conference, June 1974.

[71] Langan, W. T., J. D. Cresswell, and W. G. Browne. "Effect of Ablation Products on Ionization in Hypersonic Wakes". *AIAA Journal*, Vol. 3(No. 12), December 1965.

[72] Lichtin, D.A., S.W. Janson, J.E. Pollard, D.R. Schulthess, and R.B. Cohen. "Arcjet Plume Characterization Part I: Mass/Velocity Analyzer Results". AIAA 90-2642, AIAA/DLGR/JSASS 21st International Electric Propulsion Conference, Orlando, July 1990.

[73] Liebeskind, J.G., R.K. Hanson, and M.A. Cappelli. "Velocity Measurements in a Hyfrogen Arcjet Using LIF". AIAA 91-2112, AIAA/SAE/ASME/ASEE 27th Joint Propulsion Conference, Sacramento, June 1991.

[74] MacCormack, Robert W. "The Effect of Viscosity in Hypervelocity Impact Cratering". AIAA 69-354, AIAA Hypervelocity Impact Conference, April 30 - May 2 1969.

[75] MacCormack, Robert W. "Numerical Solution of the Interaction of a Shock Wave with a Laminar Boundary Layer," Proceedings from the Second International Conference on Numerical Methods in Fluid Dynamics. In *Lecture Notes in Physics*, pages 151–63. Springer-Verlag, New York, 1971.

[76] MacCormack, Robert W. and B. S. Baldwin. "A Numerical Method for Solving the Navier-Stokes Equations with Application to Shock-Boundary Layer Interactions". AIAA 75-1, AIAA 13th Aerospace Sciences Meeting, January 1975.

[77] MacDonald, James. "Accurate Collision Iintegrals for the Attractive Static Screened Coulomb Potential with Application to Electrical Conductivity ". *Astrophysical Journal Supplement Series*, Vol. 76:pp. 369–382, May 1991.

[78] Maecker, Heinz M. "Principles of Arc Motion and Displacement". *Proceedings of the IEEE*, Vol.59(No. 4):pp. 439–449, 1971.

[79] Manzella, D.H. and M.A. Cappelli. "Vacuum Ultraviolet Absorption in a Hydrogen Arcjet". AIAA 92-3564, AIAA/SAE/ASME/ASEE 28th Joint Propulsion Conference, Nashville, July 1992.

[80] Manzella, D.H., F.M. Curran, R.M. Myers, and D.M. Zube. "Preliminary Plume Characteristics of an Arcjet Thruster". AIAA 90-2645, AIAA/DLGR/JSASS 21st International Electric Propulsion Conference, Orlando, July 1990.

[81] Martinez-Sanchez, M. "Arcjet Modeling: Status and Prospects". AIAA 94-2653, 25th AIAA Plasmadynamics and Lasers Conference, June 20-23 1994.

[82] Martinez-Sanchez, M. and A. Sakamoto. "Simplified Analysis of Arcjet Thrusters". AIAA 93-1904, AIAA/SAE/ASME/ASEE 29th Joint Propulsion Conference, Monterey, June 1993.

[83] Mausteller, J. W., F. Tepper, and S. J. Rodgers. *Alkali Metal Handling and Systems Operating Techniques.* American Nuclear Society and U.S. Atomic Energy Commision, Monograph Series on Nuclear Science and Technology. Gordon and Breach, Science Publishers, New York, 1967.

[84] Megli, T.W., H. Krier, and R.L. Burton. "A Plasmadynamics Model for Nonequilibrium Processes in N_2/H_2 Arcjets". AIAA 95-1961, AIAA 26th Plasmadynamics and Lasers Conference, San Diego, June 1995.

[85] Miller, S.A. *Multifluid Nonequilibrium Simulation of Arcjet Thrusters.* PhD thesis, Massachusetts Institute of Technology, 1994.

[86] Mitchner, M. and Charles H. Kruger, Jr. *Partially Ionized Gases.* John Wiley and Sons, Inc., 1973. Reprints available from authors.

[87] Munz, D. and T. Fett. *Ceramics: Mechanical Properties, Failure Behaviour, Materials Selection.* Springer-Verlag, Berlin, 1999.

[88] Nakanishi, S. "Experimental Performance of a 1-Kilowatt Arcjet Thruster". NASA Technical Memorandum 87131, October 1985.

[89] Nighan, W.L. "Electron Energy Distributions and Collision Rates in Electrically Excited N_2, CO and CO_2". *Phys. Rev. A.*, Vol. 2(No. 5):pp. 1989–2000, November 1970.

[90] Oh, David. "Optimization of Combined Electric/Chemical Orbit Raising Missions". AIAA/SAE/ASME/ASEE 37th Joint Propulsion Conference, Salt Lake City, July 2001.

[91] Oyerokun, F. and M. Martinez-Sanchez. "A Study of Alkali-Seeded Hydrogen Arcjet Performance". IEPC 95-236, 24th International Electric Propulsion Conference, Moscow, Russia, September 1995.

[92] Oyerokun, F., D. Robertson, and M. Martinez-Sanchez. "Stability of Alkali-Seeded Hydrogen Arcjets". IEPC 97-012, 25th International Electric Propulsion Conference, Cleveland, Ohio, August 1997.

[93] Oyerokun, Folusho T. A Theoretical Study On Alkali Seeding Of Arcjet Thrusters. Master's thesis, Massachusetts Institute of Technology, 1997.

[94] Paquette, C., C. Pelletier, G. Fontaine, and G. Michaud. "Diffusion Coefficients for Stellar Plasmas". *Astrophysical Journal Supplement Series*, Vol. 61:pp. 177–95, May 1986.

[95] Pfender, E. "Electric Arcs and Arc Gas Heaters". In M. N. Hirsch and H. J. Oskam, editors, *Gaseous Electronics*, volume 1, chapter 5. Academic Press, 1978.

[96] Pipkin, A. C. "Electrical Conductivity of Partially Ionized Gases". *Physics of Fluids*, Vol. 4(No. 1):pp. 154–58, January 1961.

[97] Pivirotto, T.J. and W.D. Deininger. "Velocity Measurements in the Plume of an Arcjet Engine". AIAA 87-1063, AIAA/DGLR/JSASS 19th Electric Propulsion Conference, Colorado Springs, May 1987.

[98] Pivirotto, T.J., D.Q. King, and W.D. Deininger. "Long Duration Test of a 30 kw Class Thermal Arcjet Engine". AIAA 87-1947, AIAA/SAE/ASME/ASEE 23rd Joint Propulsion Conference, San Diego, June 1987.

[99] Polk, J.E. and K.D. Goodfellow. "Results of a 1462 Hour Ammonia Arcjet Endurance Test". AIAA 92-3833, AIAA/SAE/ASME/ASEE 28th Joint Propulsion Conference, Nashville, July 1992.

[100] Press, William H., Saul A. Teukolsky, William T. Vetterling, and Brian P. Flannery. *Numerical Recipes in Fortran.* Cambridge University Press, New York, 2nd edition, 1992.

[101] Purdue University, Thermophysical Research Center. *Thermophysical Properties of High Temperature Solid Materials.* Macmillan, New York, 1967.

[102] Rainwater, James C., Louis Biolsi, Kevin J. Biolsi, and Paul M. Holland. "Transport Properties of Ground State Nitrogen Atoms". *Journal of Chemical Physics*, Vol. 79(No. 3):pp. 1462–1468, August 1983.

[103] Rhodes, R. and D. Keefer. "Numerical Modeling of an Arcjet Thruster". AIAA 90-2614, AIAA/DLGR/JSASS 21st International Electric Propulsion Conference, Orlando, July 1990.

[104] Rhodes, R. and D. Keefer. "Comparison of Model Calculations With Experimental Data From Hydrogen Arcjets". IEPC 91-111, 22nd International Electric Propulsion Conference, Viareggio, Italy, October 1991.

[105] Rhodes, R. and D. Keefer. "Modeling Arcjet Space Thrusters". AIAA 91-1994, AIAA/SAE/ASME/ASEE 27th Joint Propulsion Conference, Sacramento, June 1991.

[106] Richter, R. "Development Work on Plasma Arc Jet Engines". ARS 2347-62, ARS Electric Propulsion Conference, Berkeley, March 1962.

[107] Richtmyer, R. D. and K. W. Morton. *Difference Methods for Initial-Value Problems.* Interscience Publishers, Wiley, New York, 2nd edition, 1967.

[108] Robertson, D.K. A Two-Dimensional, Non-Equilibrium, Numerical Model of an Alkali Seeded Hydrogen Arcjet Thruster. Master's thesis, Massachusetts Institute of Technology, 1998.

[109] Robertson, D.K. and M. Martinez-Sanchez. "Two-Dimensional Numerical Simulations of a Cesium Seeded Hydrogen Arcjet". AIAA 98-4036, AIAA/ASME/SAE/ASEE 34th Joint Propulsion Conference, Cleveland, July 1998.

[110] Rogers, R. C. and C. J. Schexnayder Jr. "Chemical Kinetic Analysis of Hydrogen-Air Ignition and Reaction Times". NASA Technical Paper 1856, 1981.

[111] Rogoff, Gerald L. "Ambipolar Diffusion Coefficients for Discharges in Attaching Gases". *J. Phys. D: Appl. Phys.*, Vol. 18:pp. 1533–1545, 1985.

[112] Rosa, R. J. *Magnetohydrodynamic Energy Conversion.* Hemisphere Publishing Corporation, 1987.

[113] Sankovic, J.M. "Investigation of the Arcjet Plume Near Field Using Electrostatic Probes". NASA Technical Memorandum 103638, October 1990.

[114] Sankovic, J.M. and F.M. Curran. "Arcjet Thermal Characteristics". AIAA 91-2456, AIAA/SAE/ASME/ASEE 27th Joint Propulsion Conference, Sacramento, June 1991.

[115] Sears, Francis W. and Salinger, Gerhard L. *Thermodynamics. Kinetic Theory, and Statistical Thermodynamics.* Addison-Wesley Publishing Company, Reading, Massachusetts, 3rd edition, 1975.

[116] Shackelford, J.F. and W. Alexander. *CRC Materials Science and Engineering Handbook.* CRC Press, Boca Raton, Florida, 3rd edition, 2001.

[117] Sharma, Surendra P. *Experimental Investigation of the Physical Processes in a Magnetohydrodynamic Laser.* PhD thesis, Massachusetts Institute of Technology, 1978.

[118] Sheppard, Eric J. *Nonequilibrium Ionization in Electromagnetic Accelerators*, Doctoral thesis. Massachusetts Institute of Technology, 1994.

[119] Smith, W.W.., R.D. Smith, S.E. Yano, K. Davies, and D. Lichtin. "Low Power Hydrazine Arcjet Flight Qualification". IEPC 91-148, AIDAA/AIAA/DGLR/JSASS 22nd Electric Propulsion Conference, Viareggio, Italy, October 1991.

[120] Spurrett, R. and R.A. Bond. "Modelling Arcjet Thruster Performance". IEPC 91-110, 22nd Electric Propulsion Conference, Viareggio, Italy, October 1991.

[121] Stallcop, James R., Harry Partridge, and Eugene Levin. "Resonance Charge Transfer, Transport Cross Sections, and Collision Integrals for $N^+(^3P) - N(^4S^0)$ and $O^+(^4S^0) - O(^3P)$ Interactions". *Journal of Chemical Physics*, Vol. 95(No. 9):pp. 6429–6439, November 1991.

[122] Stuhlinger, E. *Ion Propulsion for Space Flight.* McGraw-Hill, New York, 1964.

[123] Sutton, G. W. and A. Sherman. *Engineering Magnetohydrodynamics.* McGraw-Hill, New York, 1965.

[124] Sutton, George P. *Rocket Propulsion Elements, An Introduction to the Engineering of Rockets.* John Wiley and Sons, Inc., New York, 6th edition, 1992.

[125] Tahara, H., T. Sakakibara, K. Onoe, and T. Yoshikawa. "Discharge Characteristics and Inner Plasma Features of a High Power DC Arcjet Thruster". AIAA 90-2534, AIAA/DLGR/JSASS 21st International Electric Propulsion Conference, Orlando, July 1990.

[126] Tahara, H., T. Sakakibara, K. Onoe, and T. Yoshikawa. "Experimental and Numerical Studies of a 10kW Water-cooled Arcjet Thruster". IEPC 91-015, 22nd Electric Propulsion Conference, Viareggio, Italy, October 1991.

[127] Thompson, Philip A. *Compressible Fluid Dynamics.* McGraw-Hill, New York, 1972.

[128] Todd, J.P. and R.E. Sheets. "Development of a Regeneratively Cooled 30-kw Arcjet Engine". AIAA 64-671, AIAA 4th Electric Propulsion Conference, Philadelphia, August 1964.

[129] Vanderslice, J.T., Stanley Weissman, E.A. Mason, and R.J. Fallon. "High-Temperature Transport Properties of Dissociating Hydrogen". *Physics of Fluids*, Vol. 5(No. 2):pp. 155–64, February 1962.

[130] Vincenti, Walter G. and Charles H. Kruger, Jr. *Introduction to Physical Gas Dynamics.* Robert E. Krieger Publishing Co., Inc., Malabar, Florida, 1965.

[131] Wang, Joseph Jiong. *Electrodynamic Interactions Between Charged Space Systems and the Ionospheric Plasma Environment*, Doctoral thesis. Massachusetts Institute of Technology, 1991.

[132] Waterman, N.A. and M.F. Ashby. *The Materials Selector.* Chapman and Hall, London, 2nd edition, 1997.

[133] Watson, V.R. and E.B. Pegot. "Numerical Calculations for the Characteristics of a Gas Flowing Axially Through a Constricted Arc". NASA Technical Note TN D-4042, June 1967.

[134] Yamada, T., Y. Shimizu, K. Toki, and K. Kuriki. "Thermal Analysis and Thrust Performance of a Low Power Arcjet Thruster". AIAA 90-2581, AIAA/DLGR/JSASS 21st International Electric Propulsion Conference, Orlando, July 1990.

[135] Yamada, T., K. Toki, and K. Kuriki. "Behavior of Arc Column in Arcjet Constrictor". IEPC 93-184, 23rd International Electric Propulsion Conference, Seattle, 1993.

[136] Yee, H.C. "A Class of High Resolution Explicit and Implicit Shock Capturing Methods". NASA Technical Memorandum TM 101088 (or N89-25652), February 1989.

[137] Yoshikawa, T., K. Onoe, S. Tsuri, M. Ishii, and K. Uematsu. "Development of a Low Power Arcjet Thruster - Thrust Performance and Life Evaluation". IEPC 91-043, 22nd Electric Propulsion Conference, Viareggio, Italy, October 1991.

[138] Yun, K. S. and E. A. Mason. "Collision Integrals for the Transport Properties of Dissociating Air at High Temperatures". *Physics of Fluids*, Vol. 5(No. 4):pp. 380–386, April 1962.